

Award Number: W81XWH-15-1-0236

TITLE: Phosphoproteomic assessment of therapeutic kinases for personalized therapy in castration resistant prostate cancer

PRINCIPAL INVESTIGATOR: Justin M. Drake

CONTRACTING ORGANIZATION: State University of New Jersey, Rutgers  
NEW BRUNSWICK, NJ 08903

REPORT DATE: October 2018

TYPE OF REPORT: Final

PREPARED FOR: U.S. Army Medical Research and Materiel Command  
Fort Detrick, Maryland 21702-5012

DISTRIBUTION STATEMENT: Approved for Public Release;  
Distribution Unlimited

The views, opinions and/or findings contained in this report are those of the author(s) and should not be construed as an official Department of the Army position, policy or decision unless so designated by other documentation.

<b>REPORT DOCUMENTATION PAGE</b>			<i>Form Approved</i> <i>OMB No. 0704-0188</i>		
Public reporting burden for this collection of information is estimated to average 1 hour per response, including the time for reviewing instructions, searching existing data sources, gathering and maintaining the data needed, and completing and reviewing this collection of information. Send comments regarding this burden estimate or any other aspect of this collection of information, including suggestions for reducing this burden to Department of Defense, Washington Headquarters Services, Directorate for Information Operations and Reports (0704-0188), 1215 Jefferson Davis Highway, Suite 1204, Arlington, VA 22202-4302. Respondents should be aware that notwithstanding any other provision of law, no person shall be subject to any penalty for failing to comply with a collection of information if it does not display a currently valid OMB control number. <b>PLEASE DO NOT RETURN YOUR FORM TO THE ABOVE ADDRESS.</b>					
<b>1. REPORT DATE</b> October 2018		<b>2. REPORT TYPE</b> Final		<b>3. DATES COVERED</b> 15 Sep 2015 - 14 Sep 2018	
<b>4. TITLE AND SUBTITLE</b> Phosphoproteomic assessment of therapeutic kinases for personalized therapy in castration resistant prostate cancer				<b>5a. CONTRACT NUMBER</b>	
				<b>5b. GRANT NUMBER</b> W81XWH-15-1-0236	
				<b>5c. PROGRAM ELEMENT NUMBER</b>	
<b>6. AUTHOR(S)</b> Justin M. Drake  E-Mail: jdrake@umn.edu				<b>5d. PROJECT NUMBER</b>	
				<b>5e. TASK NUMBER</b>	
				<b>5f. WORK UNIT NUMBER</b>	
<b>7. PERFORMING ORGANIZATION NAME(S) AND ADDRESS(ES)</b> State University of New Jersey, Rutgers NEW BRUNSWICK, NJ 08903				<b>8. PERFORMING ORGANIZATION REPORT NUMBER</b>	
<b>9. SPONSORING / MONITORING AGENCY NAME(S) AND ADDRESS(ES)</b> U.S. Army Medical Research and Materiel Command Fort Detrick, Maryland 21702-5012				<b>10. SPONSOR/MONITOR'S ACRONYM(S)</b>	
				<b>11. SPONSOR/MONITOR'S REPORT NUMBER(S)</b>	
<b>12. DISTRIBUTION / AVAILABILITY STATEMENT</b> Approved for Public Release; Distribution Unlimited					
<b>13. SUPPLEMENTARY NOTES</b>					
<b>14. ABSTRACT</b> Determining which biomarkers are most accurate for therapy responses in cancer is still challenging. We have started to develop a quantitative proteomics assay using targeted MS to develop a panel of peptide biomarkers that connect to their genomic alterations in cancer. We have started to biosynthesize these protein and protein domain biomarkers in bacterial or animal expression systems with uniform <sup>15</sup> N-enrichment in house and assess the applicability of our protein biomarkers in identifying the protein levels of two commonly observed genetic alterations in cancer: HER2 and BRAF in clinical tissues. Initially, this was done using pre-clinical xenograft tumors with genetic alterations to these genes followed by the development of a panel of protein biomarkers towards these same proteins. We have begun preliminary analyses of these proteins in clinical tissues and have found that they can be detected in fresh frozen human tumors and display increased protein amounts compared to the normal tissue controls. These data will provide proof-of-concept and key preliminary results needed to support our long-term goal of applying a targeted MS platform to a broader panel of cancer associated mutations for clinical applications.					
<b>15. SUBJECT TERMS</b> Phosphoproteomics, metastatic, castration resistant prostate cancer, kinase, mass spectrometry					
<b>16. SECURITY CLASSIFICATION OF:</b>			<b>17. LIMITATION OF ABSTRACT</b>	<b>18. NUMBER OF PAGES</b>	<b>19a. NAME OF RESPONSIBLE PERSON</b> USAMRMC
<b>a. REPORT</b> U	<b>b. ABSTRACT</b> U	<b>c. THIS PAGE</b> U			<b>19b. TELEPHONE NUMBER</b> (include area code)
			UU	95	

## Table of Contents

	<u>Page</u>
<b>1. Introduction.....</b>	<b>4</b>
<b>2. Keywords.....</b>	<b>4</b>
<b>3. Accomplishments.....</b>	<b>4</b>
<b>4. Impact.....</b>	<b>6</b>
<b>5. Changes/Problems.....</b>	<b>6</b>
<b>6. Products, Inventions, Patent Applications, and/or Licenses.....</b>	<b>7</b>
<b>7. Participants &amp; Other Collaborating Organizations.....</b>	<b>8</b>
<b>8. SpecialReportingRequirements.....</b>	<b>9</b>
<b>9.Appendices.....</b>	<b>9</b>

## INTRODUCTION

Prostate cancer is the most common diagnosed cancer among men in the U.S with approximately 180,000 newly diagnosed cases year and the third leading cause of epithelial cancer-related death in men with an estimated 26,700 deaths in 2017 (Siegel et al., 2017). One of the biggest challenges during cancer treatment is to define the patient subsets that will best respond to appropriate therapies. In prostate cancer, all patients are essentially treated the same and there are currently no subtypes to stratify for therapy purposes.

Molecular targets for metastatic castration resistant prostate cancer (CRPC) include translocations (Tomlins et al., 2005), somatic mutations (Grasso et al., 2012), and DNA amplifications (Taylor et al., 2010) but targeting AR is still the main focus for current therapies. As resistance to AR therapeutic agents become more common, AR independent pathways such as kinase signaling need to be considered as new therapeutic options, although activating mutations of kinases in metastatic CRPC are very rare (Grasso et al., 2012). This is a major clinical problem and the development of new biomarkers that can either predict disease progression (diagnostic) or to stratify patients for effective personalized therapy (predictive) are urgently needed. Our strategy is to develop biomarkers geared towards the activated kinases in metastatic CRPC using targeted mass spectrometry (T-MS) approaches for clinical diagnostics. Our goal is to generate a minimal set, but if necessary up to 100 unique phosphopeptides that behave as surrogates for kinase activation that can be used pre-clinically and clinically to evaluate endogenous kinase signaling, as resistance mechanisms to conventional therapies, and as biomarkers for patient stratification leading to therapy decisions.

## KEYWORDS

- Castration resistant prostate cancer
- Phosphoproteomics
- Metastasis
- Kinase
- Targeted Mass spectrometry
- Biomarker

## ACCOMPLISHMENTS

### What were the major goals of the project?

The major aims of the project are to:

Aim 1: To establish quantitative methods to detect activated kinases for clinical diagnostics.

Aim 2: To measure activated kinases in pre-clinical xenograft models of prostate cancer.

Aim 3: To assess efficacy of targeted SIM MS in clinical CRPC tissues for personalized therapy.

### What was accomplished under these goals?

#### Aim 1:

Task 1: We have designed and obtained phosphopeptides for up to 111 different kinases of interest (including several phosphosites for a few select kinases) for testing by MS. We have identified 82/111 (74%) of these peptides via MS and 39/111 (35%) were detected at 400 attomoles; nearly sensitive enough for detection in biopsy tissues. We now have generated a list of our phosphopeptides for targeted MS. Task 1 is completed.

Task 2: We have purchased a SpikeMix heavy labeled kinase activation loops pool from JPT Innovative Peptide Solutions as an alternative to the in house standards. These peptides are labeled at the C terminal using Arg U-13C6; U-15N4 or Lys U-13C6; U-15N2. The JPT peptide pool contains 466 total peptides (288 phospho and 178 non-phosphopeptides) from which, we have generated a list of 56 phosphopeptides of interest for detection by targeted-MS. Of these, 34/56 peptides (61%) are identical to the custom peptides from the 111 non-heavy labeled phosphopeptide pool (mentioned above in Task 1). The remaining 22 evaluate either the same phosphoresidue (just a different peptide sequence usually at the termini where trypsin cleaves) or a different

phosphoresidue to the same protein. We spiked in serial dilutions of the heavy-labeled peptide pool in the range from 10fmol/ul to 80amol/ul along with 0.25ug/ul grape lysate tryptic digest. Of the list of 56 heavy labeled peptides we are interested in, we detected 42 (75%) via targeted-MS (**Table 1**). 17/42 (40%) were detected at 160 amol and higher while 19/42 (45%) were detected at 800 amol and higher. Task 2 is still underway and we plan on expanding the list of heavy labeled peptides for detection, although this has not been done to date due to my transition to the University of Minnesota.

**Task 3:** We are also evaluating phosphopeptide enrichment strategies to determine the best sample preparation that is necessary to achieve optimum sensitivity using N<sup>15</sup> heavy labeled phosphopeptides corresponding to kinase activation loops while simultaneously developing our final targeted phosphopeptide list. The purpose is to determine when to spike in the heavy labeled phosphopeptides and whether phosphopeptide enrichment is necessary (**Figure 1, presented last reporting period**). The samples we propose to use are cell line-derived xenografts and we have generated tumors from LNCaP, C4-2, 22Rv1, DU-145, PC3 and NCI-H660 cell lines and flash frozen for targeted-MS analyses (see **Aim 2**). We have lysed these tumor samples and are in the process of performing enrichment techniques followed by analysis via MS as outlined in **Figure 1** using the heavy labeled phosphopeptides from **Table 1**.

#### **Aim 2:**

**Task 4:** While we are still highly interested in phosphopeptide analyses, we also wanted to see if our targeted MS approaches could be used for total protein. We have, as an alternative, analyzed cell line protein lysates for the detection of total HER2 and BRAF using HCC1954 and HCC202 breast cancer cell lines and UACC903 melanoma cell lines (**Figure 2**). HER2 is amplified in HCC1954 and low/absent in HCC202 cell lines as determined by western blot analysis while BRAF is high in the UACC903 cell line (**Figure 2**). Protein lysates from the same cell lines were spiked in with heavy-labeled HER2 protein domain standard followed by filter aided sample preparation (FASP) and tryptic digestion for the detection and quantification of HER2 by targeted MS (see **Figure 7** for workflow). **Figure 3A** shows the chromatogram peak intensity for the tryptic peptide VLGSGAFGTVYK and **Figure 3A** shows the relative abundance in both cell lines. The relative abundance correlates between western blot and MS analyses, i.e. approximately 400 fold higher in HCC1954 cell line compared to HCC202 (**Figure 2** vs **Figure 3C**).

Along the lines of evaluating total proteins, we have started to develop an in house platform where we can purify <sup>15</sup>N enriched protein domains for targeted MS. To develop the most clinically relevant and actionable protein target list, we proceeded to identify and list the 50 most common mutations observed across three different targeted genomic sequencing panels (Foundation One (company Rutgers Cancer Institute uses for PMI), IMPACT (MSKCC), and CGMP\_50 (Cornell), **Figure 4**). Our approach is to develop protein-based biomarkers that can accurately measure the protein expression level of these mutated genes in cancer tissues to aid in the prioritization of targeted therapies. Central to this is the capability to synthesize and heavy label each individual protein standard for targeted MS assays, which will allow us to control production and amounts used for our assays (**Figure 5**).

**Task 5:** Has yet to begin as my transition to the University of Minnesota put a halt to the animal experiments shortly after Year 2 progress report was submitted.

#### **For Aim 3:**

**Tasks 6 and 7:** To begin an attempt at human samples, we measured the concentrations of 5 cancer-associated proteins in samples of human tumors. Fresh frozen tumor tissue and Adjacent Normal Tissue (ANT), was obtained from the Rutgers Cancer Institute of New Jersey Biospecimen Repository. Tissue extracts were prepared using the Filter-Aided Sample Preparation (FASP)(Ostasiewicz et al., 2010; Wisniewski et al., 2011) protocol. Using *E. coli* expression vectors, one or more domains from each of these 5 cancer-associated human

proteins were produced with uniform (>98%) <sup>15</sup>N-enrichment, purified to >98% homogeneity, and protein concentrations were determined. <sup>15</sup>N-T-MS was then used to measure endogenous levels of HER2, BRAF, EE2FK, ANXA7, and DLV3, in tumor and ANT tissue. Representative targeted MS results for BRAF are presented in **Figure 6A**. A <sup>15</sup>N-BRAF domain (residues 149–232) was prepared at 4 dilutions, added to the tissue extracts, and the resulting mixtures were processed by trypsin hydrolysis followed by targeted MS analysis. Data for the four most dilute standards are shown (red line for tumor sample and purple line for ANT sample), demonstrating the excellent linearity of our standard curves. From these data, the amount of BRAF was determined to be  $0.39 \pm 0.02$  fmol / 0.5 μg lysate and  $0.03 \pm 0.01$  fmol / 0.5 μg lysate, for the tumor and ANT tissue samples, respectively. Hence BRAF is elevated ~13-fold in this tumor compared to control tissue (**Figure 6B**). A survey of the results for the 5 proteins studied (**Figure 6B**) demonstrates that BRAF, EE2FK, and ANXA7 are all significantly and reproducibly elevated in the tumor tissue. These data demonstrate that our methods are sufficiently sensitive and quantitative to measure several targets simultaneously from clinical samples without sophisticated sample workup, and establish feasibility for developing an in house targeted MS platform.

**What opportunities for training and professional development has the project provided?**

Nothing to report.

**How were the results disseminated to communities of interest?**

Nothing to report.

**What do you plan to do during the next reporting period to accomplish the goals?**

I transitioned from Rutgers University to the University of Minnesota and during this transition, all of my lab members at Rutgers University moved on to find other positions. Therefore, I was not able to finish my anticipated project timelines mentioned in the Year 2 progress report due to lack of personnel and had to terminate my grant early. Since there is not another reporting period remaining on this grant, I will continue the project using my own funds.

**IMPACT**

**What was the impact on the development of the principal discipline(s) of the project?**

Therapeutic targeting of tyrosine kinases in late stage prostate cancer are still underdeveloped. We have begun investigation into new ways that we can detect activated, non-mutated kinases in pre-clinical and clinical tissues for potential biomarkers leading to better prognosis and therapies.

**What was the impact on other disciplines?**

To date, this is minimal, but we anticipate the results of our studies have the broad capability of expanding to other cancer types where detection of activated kinases might be important. This could include ovarian cancer, triple negative breast cancer, and osteosarcomas.

**What was the impact on technology transfer?**

Nothing to report.

**What was the impact on society beyond science and technology?**

Nothing to report.

**CHANGES/PROBLEMS**

**Changes in approach and reasons for change.**

Nothing to report.

**Actual or anticipated problems or delays and actions or plans to resolve them.**

In early 2016, I hired a postdoctoral fellow to work on this project but after 3 months left for another position. I then hired another postdoc to work on this project that began January 1, 2017. After 4 months, this new hire became adjusted to the new environment, was trained on the project, and started to engage on this project. However, since I accepted a new position at the University of Minnesota nearly 12 months after this postdoc started, it was difficult to gain any momentum finishing the project as we anticipated. While it isn't the timeline I anticipated throughout the grant period, I feel the project will continue beyond the current DoD support and a publication will result from this work. If I was able to be granted a one year no cost extension, I feel we could have finished the desired tasks related to the project as well.

Further, an unanticipated setback was that we were unable to detect a significant amount of the custom peptides designed and obtained from JPT, even after multiple rounds of synthesis from JPT. From the first batch of custom peptides we had synthesized from JPT, we detected 39/52 (75%) at 400amol. However, subsequent batches of a new set of 59 phosphopeptides were not detected at all here at Rutgers. We believe several issues may have been at play here including but not limited to improper reconstitution of the lyophilized peptides, low phosphopeptide yields after synthesis, or difficulty solubilizing the phosphopeptides. This unexpected problem has set us back approximately four months as we had to re-order and re-analyze this batch of phosphopeptides. After this length of troubleshooting with JPT, we decided to move on from this and proceeded forward using a commercially available heavy labeled peptide pool from JPT for targeted MS analyses of a select number of phosphorylated kinases. This pool consisted of both total and phosphopeptides mapping to several proteins. From this pool, we selected 56 out of the 288 phosphopeptides in the pool for which there were overlap with our initial list of 111 phosphopeptides. The 56 phosphopeptides we selected and subsequently detected via MS cover a vast range of activated signaling pathways that are relevant to cell cancer biology. We plan on adding to our list of phosphopeptides of interest (from the JPT pool) to expand our targets, for which we will design and obtain new custom labeled standards to use in Task 7.

**Changes that had a significant impact on expenditures**

I transitioned from Rutgers University to the University of Minnesota and during this transition, all of my lab members at Rutgers University moved on to find other positions. Therefore, I was not able to finish my anticipated project timelines due to lack of personnel and had to terminate my grant early.

**Significant changes in use or care of human subjects, vertebrate animals, biohazards, and/or select agents.**

Nothing to report.

**Significant changes in use or care of human subjects.**

Nothing to report.

**Significant changes in use or care of vertebrate animals.**

Nothing to report.

**Significant changes in use of biohazards and/or select agents.**

Nothing to report.

**PRODCUTS**

**Publications, conference papers, and presentations.**

**Journal publications (Note: These publications were not a direct result of this project but related.)**

1. Lue HW, Podolak J, Kolahi K, Cheng L, Rao S, Garg D, Xue CH, Rantala JK, Tyner JW, Thornburg KL, Martinez-Acevedo A, Liu JJ, Amling CL, Truillet C, Louie SM, Anderson KE, Evans MJ, O'Donnell VB, Nomura DK, **Drake JM**, Ritz A, Thomas GV (2017) Metabolic Reprogramming Ensures Cancer Cell Survival Despite Oncogenic Signaling Blockade. *Genes Dev.* 31(20):2067-2084. PMID: PMC5733498.
2. de Leeuw R, McNair CM, Schiewer MJ, Neupane NP, Brand LJ, Augello MA, Li Z, Cheng LC, Yoshida A, Diehl JA, Hazard ES, Courtney SM, Hardiman GT, Hussain MH, **Drake JM**, Kelly WK, Knudsen KE (2018) MAPK Reliance via Acquired CDK4/6 Inhibitor Resistance in Cancer. *Clin. Cancer Res.* 24(17):4201-4214. PMID: PMC6125187.
3. Cheng LC, Li Z, Graeber TG, Graham NA, **Drake JM** (2018) Phosphopeptide Enrichment Coupled with Label-Free Quantitative Mass Spectrometry to Investigate the Phosphoproteome in Prostate Cancer. *J. Vis. Exp.* 138:e57996.
4. Ramroop JR, Stein MN, **Drake JM** (2018) Phosphoproteomics in the Era of Precision Medicine for Prostate Cancer. *Front. Oncol.* 8(28):1-18. PMID: PMC5820335.
5. Xianjuan K, Li B, Olayanju JB, **Drake JM**<sup>#</sup>, Chen N<sup>#</sup> (2018) Nutraceutical or Pharmacological Potential of *Moringa oleifera Lam.* *Nutrients.* 10(3):E343. <sup>#</sup>Co-corresponding author. PMID: PMC5872761.

**Books or other non-periodical, one time publications.**

Nothing to report.

**Other publications, conference papers, and presentations.**

Invited Presentations

PPCR/SPORE Seminar, Fred Hutchinson Cancer Research Center, Seattle, WA, "Phosphoproteomics-based analyses to identify signaling pathways in lethal prostate cancer." April 2018

NIH-Sponsored Frontiers in Stem Cells in Cancer Advanced Training Course, Xavier University, New Orleans, LA, "Phosphoproteomics in prostate cancer." May 2018

**Website(s) or other Internet site(s)**

Nothing to report.

**Technologies or techniques.**

Nothing to report.

**Inventions, patent applications, and/or licenses.**

Nothing to report.

**Other products.**

Nothing to report.

**PARTICIPANTS & OTHER COLLABORATING ORGANIZATIONS**

**What individuals have worked on the project?**

Name:	Johnny Ramroop
Project Role:	Postdoctoral Fellow, Dr. Drake Laboratory



Researcher Identifier (e.g. ORCID ID):	NA
Nearest person month worked:	4
Contribution to Project:	<i>Dr. Ramroop attempted to finish the wet lab targeted MS experiments but due to my change in institutions, he had to find a new opportunity and wasn't able to accomplish the required tasks.</i>
Funding Support:	NA

**Has there been a change in the active other support of the PD/PI(s) or senior/key personnel since the last reporting period?**

Nothing to report.

**What organizations were involved as partners?**

Dr. Peter Lobel

**Organization Name:** Rutgers University

**Location of Organization:** Piscataway, NJ

**Partner's Contribution to the Project:** Collaboration

**SPECIAL REPORTING REQUIREMENTS**

None

**APPENDICES (see attached)**

- Supporting Data (Figures 1-7 and Table 1)
- Publication in *Genes and Development*
- Publication in *Clinical Cancer Research*
- Publication in *Journal of Visual Experiments*
- Publication in *Frontiers in Oncology*
- Publication in *Nutrients*

**REFERENCES**

Grasso, C.S., Wu, Y.M., Robinson, D.R., Cao, X., Dhanasekaran, S.M., Khan, A.P., Quist, M.J., Jing, X., Lonigro, R.J., Brenner, J.C., *et al.* (2012). The mutational landscape of lethal castration-resistant prostate cancer. *Nature* 487, 239-243.

Ostasiewicz, P., Zielinska, D.F., Mann, M., and Wisniewski, J.R. (2010). Proteome, phosphoproteome, and N-glycoproteome are quantitatively preserved in formalin-fixed paraffin-embedded tissue and analyzable by high-resolution mass spectrometry. *J Proteome Res* 9, 3688-3700.

Siegel, R.L., Miller, K.D., and Jemal, A. (2017). Cancer Statistics, 2017. *CA Cancer J Clin* 67, 7-30.

Taylor, B.S., Schultz, N., Hieronymus, H., Gopalan, A., Xiao, Y., Carver, B.S., Arora, V.K., Kaushik, P., Cerami, E., Reva, B., *et al.* (2010). Integrative genomic profiling of human prostate cancer. *Cancer Cell* 18, 11-22.

Tomlins, S.A., Rhodes, D.R., Perner, S., Dhanasekaran, S.M., Mehra, R., Sun, X.W., Varambally, S., Cao, X., Tchinda, J., Kuefer, R., *et al.* (2005). Recurrent fusion of TMPRSS2 and ETS transcription factor genes in prostate cancer. *Science* 310, 644-648.

Wisniewski, J.R., Ostasiewicz, P., and Mann, M. (2011). High recovery FASP applied to the proteomic analysis of microdissected formalin fixed paraffin embedded cancer tissues retrieves known colon cancer markers. *J Proteome Res* 10, 3040-3049.

**Table 1**

Peptide ID	Peptide Modified Sequence	Precursor M/Z	Peptide RT (Average)
ABL1 Y412	LMTGDTpYTAHAGAK	762.835823	21.23
BTK Y551	YVLDDepYTSVSGSK	825.854933	29.12
CHEK2 S379	IYNGDYpYR	577.233106	23.6
CHEK2 S379	ILGETpSLMR	555.268634	37.7
CSF1R Y809	DIMNDSNpYIVK	700.306367	35.05
DDR1 Y796	NLYAGDpYR	612.751663	29.59
DDR2 Y740	NLYSGDpYR	620.74912	28.07
ERBB4 Y1056	SEIGHSPPPApYTPMSGNQFVYR	842.378003	37.53
<b>FGFR1 Y653</b>	<b>DIHHIDpYRK</b>	<b>431.19146</b>	<b>23.31</b>
<b>FGFR1 Y654</b>	<b>DIHHIDpYRK</b>	<b>431.19146</b>	<b>22.84</b>
FGFR2 656	DINNIDpYRK	623.267568	30.04
FGFR2 657	DINNIDpYRK	623.267568	27.91
FGFR3 647	DVHNLDPYRK	627.767735	26
FGR Y412	DDEpYNPCQGSK	700.749414	19.19
FLT3 Y842	DIMSDSNpYVVR	694.793202	32.83
FRK Y387	VDNEDIpYESR	665.265331	21.47
FYN Y420, LCK Y394, SRC Y419, YES Y426	LIEDNEpYAR	657.286067	22.36
FYN Y440, YES1 Y446, SRC Y439	WTAPEAALpYGR	662.801687	36.48
HCK Y411, LYN Y397	VIDNEpYAR	650.278242	20.92
ITK Y512	FVLDDQpYTSSTGK	825.362925	31.49
JAK1 Y1034	EYpYSVHNK	564.236071	19.14
KIT Y823	NDSNpYVVK	513.722796	20.69
MAP2K1 S218, MAP2K2 S222	LCDFGVSGQLIDpSMANSFVGTR	822.035248	59.18
<b>MAPK1 Y187</b>	<b>VADPDHDTGFLTEpYVATR</b>	<b>745.331158</b>	<b>35.12</b>
MAPK11 Y182	QADEEMTGpYVATR	780.817405	24.75
MAPK14 Y182	HTDDEMTGpYVATR	793.31503	22.63
<b>MAPK3 T198</b>	<b>IADPEHDHpTGFLETVVATR</b>	<b>754.674925</b>	<b>40.01</b>
<b>MAPK3 T202</b>	<b>IADPEHDHTGFLpTEYVATR</b>	<b>754.674925</b>	<b>42.77</b>
<b>MAPK3 Y204</b>	<b>IADPEHDHTGFLTEpYVATR</b>	<b>754.674925</b>	<b>36.23</b>
MET Y1234	EpYYSVHNK	564.236071	19.83
MET Y1235	EYpYTVK	445.692976	21.2
NTRK2 Y706	DVYSTDPYR	636.24641	25.44
PDGFRA Y849	DIMHDSNpYVSK	698.788342	23.86
PDGFRB Y857	DSNpYISK	457.690965	19.38
PTK6 Y342	EDVpYLSHDHNIPYK	606.604369	28.18
PTK6 Y342 and Y351	EDVpYLSHDHNIPpYK	633.259813	26.97
PTK6 Y351	EDVYLSHDHNIPpYK	606.604369	26.86
RET Y900	DVpYEEDSYVK	667.767598	25.03
<b>RET Y905</b>	<b>DVYEEESpYVK</b>	<b>667.767598</b>	<b>23.93</b>
RPS6KA5 Y212	AYpSFCGTIEYMAPDIVR	1041.950636	55.74
TYK2 Y1054	AVPEGHEpYR	655.775669	20.96
VEGFR2 Y1059, FLT4 Y1068	DPDpYR	427.66961	19.94

**Table 1. List of heavy labeled peptides detected by targeted MS.**

Selected peptides from the JPT kinase activation loops pool that were detected by targeted MS. The precursor M/Z and average peptide retention times for each peptide are shown. Results for the highlighted peptides are shown in Figures 1-7.

# Figure 1

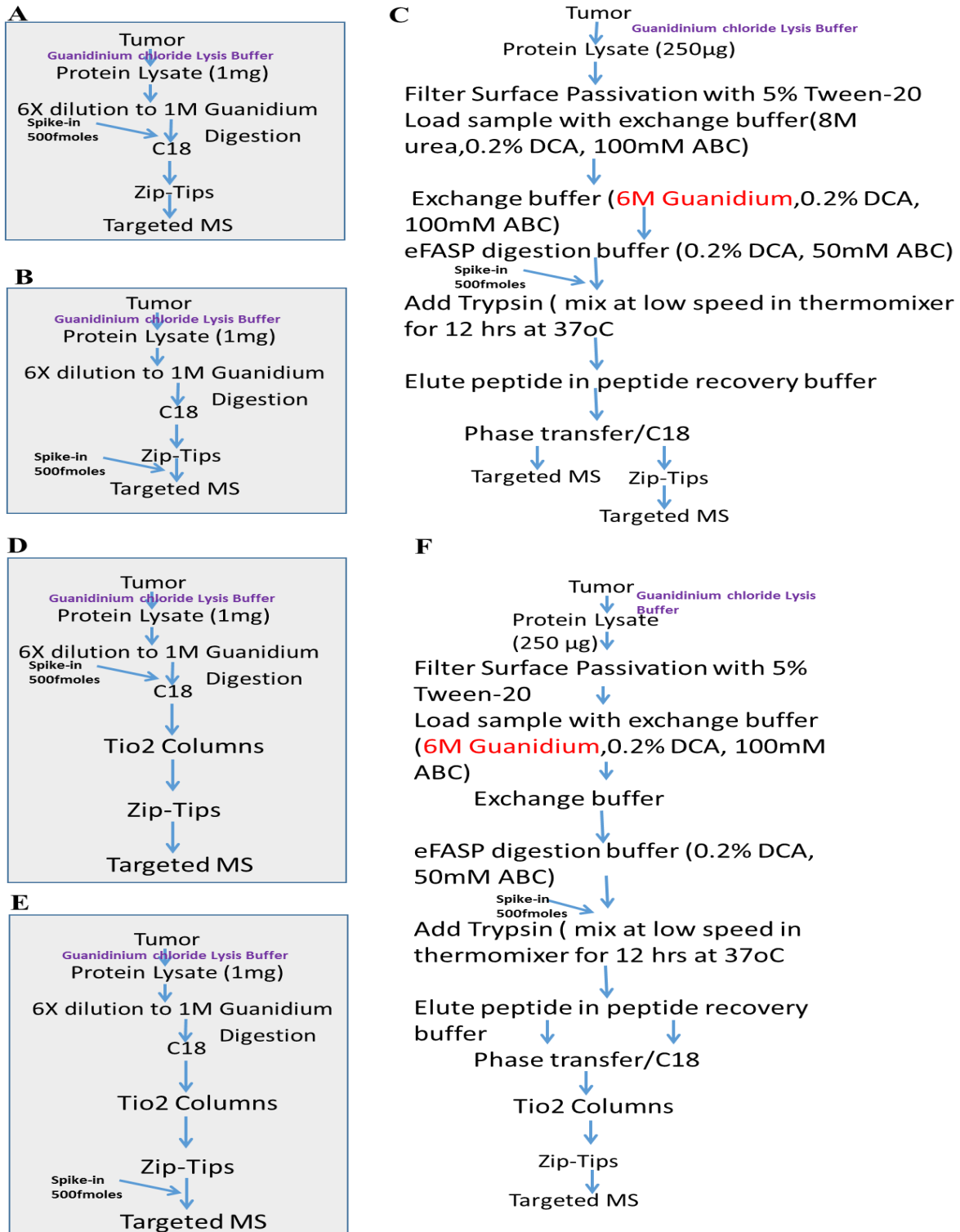


**Figure 1. Proposed methods for phosphopeptide spike in and enrichment for Targeted MS.** Different methods will be used to determine the optimum sensitivity and when to spike in the heavy labeled phosphopeptides (A-C) and when to perform enrichment protocols (D-F). These will be tested on our generated cell line derived xenografts.

**Figure 2**

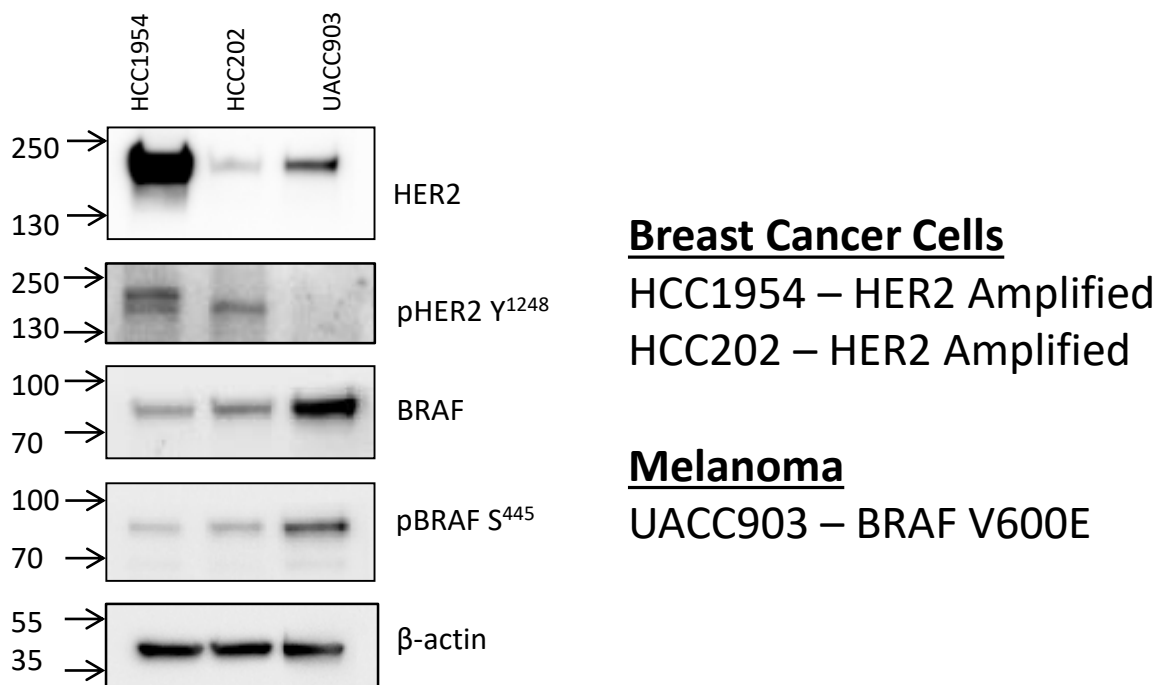


**Figure 2. Western blot of amplified HER2 does not always connect to protein expression.** Western blot analysis of 2 breast cancer cell lines (HCC1954, HCC202) and a melanoma cell line (UACC903) of 2 key proteins related to their genomic information. When analyzing HER2 overexpression, only HCC1954 overexpressed HER2 while the other HER2 genomically amplified cell line, HCC202, did not. This demonstrates that genetic amplification of a key driver event in breast cancer, HER2, would benefit from a complementary proteomic assay to confirm HER2 protein levels for targeted therapies.

# Figure 3

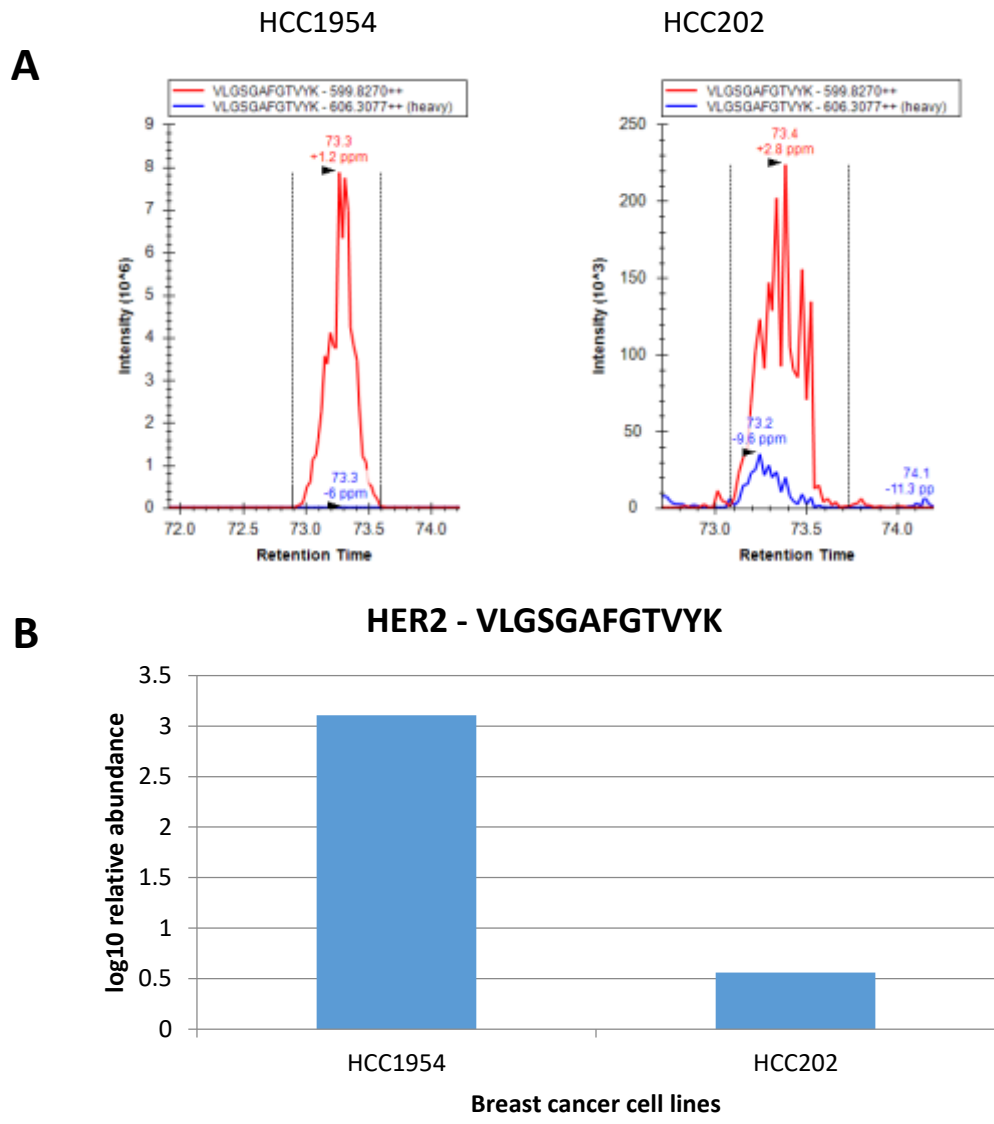


**Figure 3. Western blot and Targeted MS/MS quantification of HER2.**

(A) Western blot analysis of protein lysate from HCC1975 and HCC202 breast cancer cell lines probed for total HER2 protein. (B) Mass spectrum chromatograms of HER2 – VLGSQAFGTVYK tryptic peptide. (C) Log<sub>10</sub> relative abundance of the HER2 peptide in both cell lines showing approximately 400 fold higher in HCC1954 compared to HCC202.

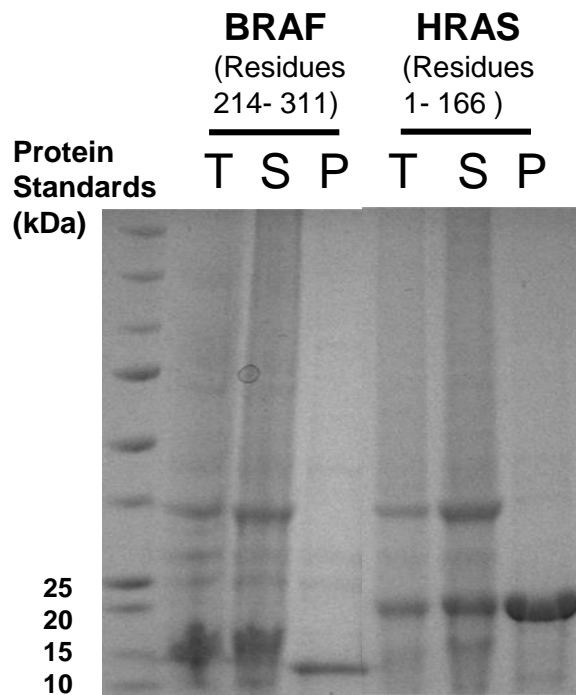
**Figure 4**

**List of 50 Proteins Selected for Targeted MS**

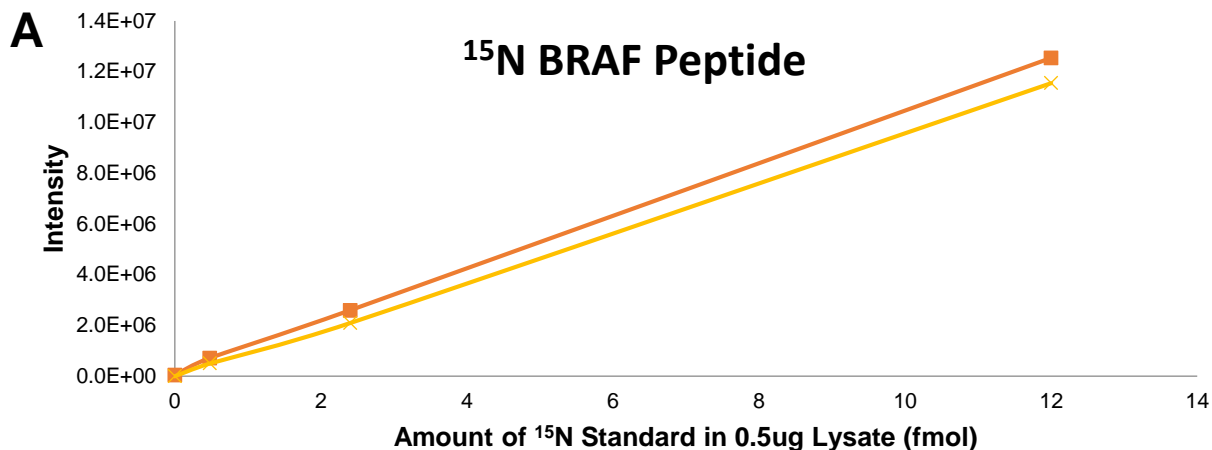
ABL1	AKT2	ALK	APC	ATM	<b>BRAF</b>	CDH1	CDKN2A	CSF1R	CTNNB1
EGFR	<b>ERBB2</b>	ERBB4	EZH2	FBXW7	<b>FGFR1</b>	FGFR2	FGFR3	FLT3	GNA11
GNAQ	GNAS	HNF1A	HRAS	IDH1	IDH2	JAK2	JAK3	KDR	KIT
<b>KRAS</b>	MET	MLH1	MPL	NPM1	NRAS	NOTCH1	PDGFRA	PIK3CA	PTEN
PTPN11	RB1	RET	SMAD4	SMARCB1	SMO	SRC	STK11	TP53	VHL

**Figure 4. Selection of protein targets for generation of  $^{15}\text{N}$  peptide standards and availability of expression vectors.** 50 targets were selected based on the overlap of these genes between three different targeted genomic sequencing panels (Foundation One, IMPACT\_MSKCC, and CGMP\_50). The genes marked in boxes are the four we will initially analyze to validate our  $^{15}\text{N}$ -T-MS approach. *E. coli* protein expression vectors for one or more domain (and/or full-length) constructs are available at Rutgers for 20 of the corresponding proteins (highlighted in red). Protocols for producing domain (and/or full-length) constructs of 30 additional proteins in *E. coli* (blue), HEK293 (green), and CHO or insect (black) cells are published for the corresponding 3D protein structures deposited in the Protein Data Bank ([www.pdb.org](http://www.pdb.org)).

**Figure 5**



**Figure 5. One-step Purification of  $^{15}\text{N}$ -enriched Protein Domains Under Denaturing Conditions.** Domain constructs of BRAF and HRAS were expressed with N-terminal hexa-His tags, solubilized in 8 M urea, and purified using NiNTA affinity columns under denaturing conditions. T – total cell pellet, S – water soluble fraction of total cell pellet, P – NiNTA purified sample. Yields were 24 mg/L and 44 mg/L for HRAS and BRAF constructs, respectively. Although these two constructs can also be purified without urea solubilization, the yield of human proteins expressed in *E. coli* with poor solubility can be significantly improved by purification under solubilizing conditions. Where required, target proteins can be further purified using gel filtration chromatography.

**Figure 6**

**B Summary of Pilot <sup>15</sup>N-based Targeted MS Study**

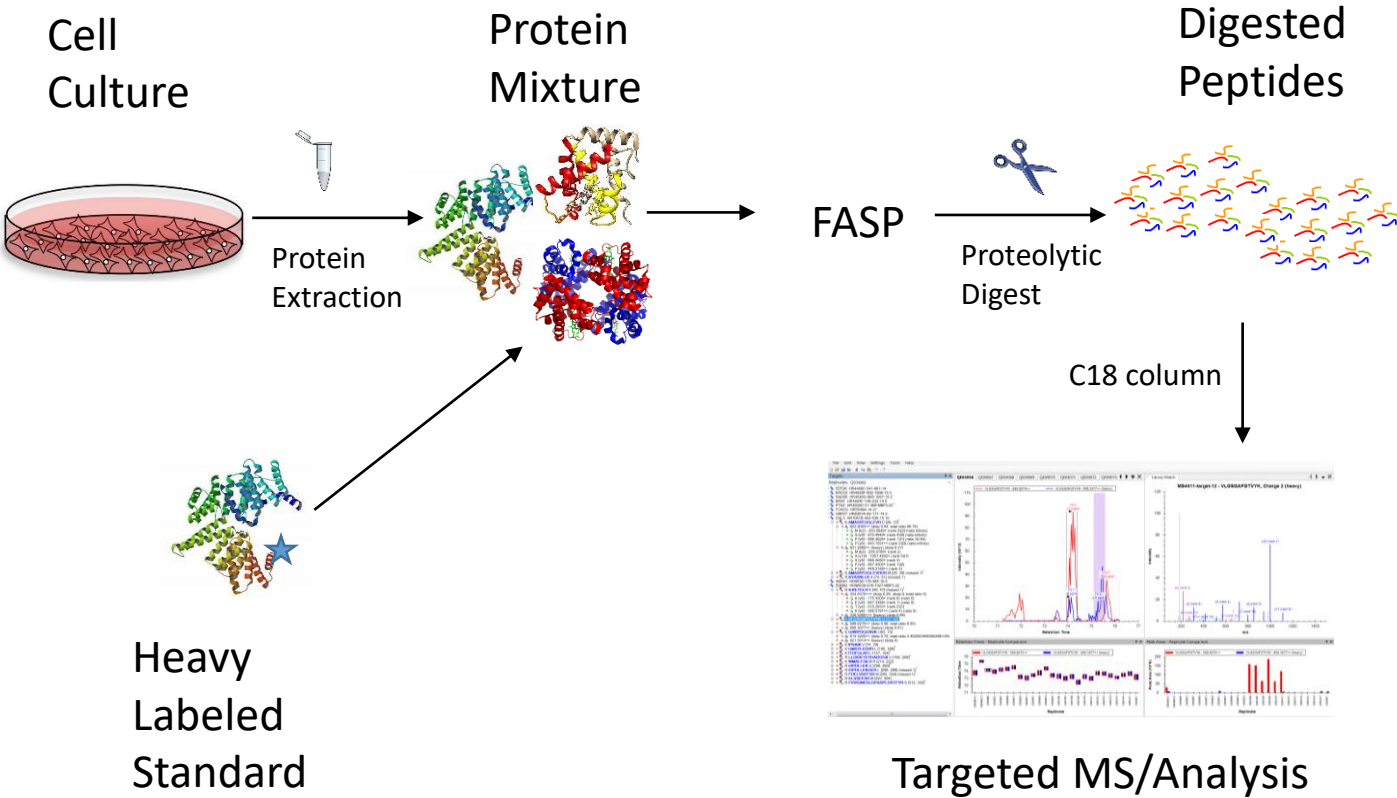
<u>Protein</u>	<u>Peptide</u>	<u>ANT (fmol)</u>	<u>Tumor (fmol)</u>	<u>Ratio Tumor/ANT</u>	<u>Unique Peptide</u>	<u>Reported Isoforms</u>
HER2	EILDEAYVMAGVGSPYVSR	N.D.	1.05±0.57	Undefined	yes	yes
	GMSYLEDVR	0.21±0.10	0.95±0.04	4.5	yes	yes
BRAF	GLIPECCAVYR	0.03±0.01	0.39±0.02	13.0	yes	no
EEF2K	GFDYLLK	0.04±0.01	0.36±0.05	9.0	yes	no
	AFDSGQNLSPDR	0.06±0.03	0.42±0.12	7.0	yes	no
ANXA7	PAANFDAIR	0.20±0.02	2.36±0.08	11.8	yes	no
	EFSGYVESGLK	0.99±0.08	6.08±0.33	6.1	yes	no
DVL3	AMASPESGLEVR	N.D.	0.30±0.07	Undefined	yes	no

**Figure 6. <sup>15</sup>N-based SID-MRM mass spectrometry results for a panel of proteins.** A. Standard curve dilution analysis of heavy labeled BRAF peptide spiked into both normal (purple line) and tumor (red line) tissue. B. Summary of five different proteins and their respective peptides observed in both normal and tumor tissue. ANT = adjacent normal tissue, fmol = femto-moles. N.D. = not detectable.



**Figure 7**

**Targeted MS workflow**



# Metabolic reprogramming ensures cancer cell survival despite oncogenic signaling blockade

Hui-wen Lue,<sup>1</sup> Jennifer Podolak,<sup>1</sup> Kevin Kolahi,<sup>2</sup> Larry Cheng,<sup>3</sup> Soumya Rao,<sup>1</sup> Devin Garg,<sup>1</sup> Chang-Hui Xue,<sup>1</sup> Juha K. Rantala,<sup>1</sup> Jeffrey W. Tyner,<sup>1</sup> Kent L. Thornburg,<sup>2</sup> Ann Martinez-Acevedo,<sup>4</sup> Jen-Jane Liu,<sup>4</sup> Christopher L. Amling,<sup>4</sup> Charles Truillet,<sup>5</sup> Sharon M. Louie,<sup>6</sup> Kimberly E. Anderson,<sup>6</sup> Michael J. Evans,<sup>5</sup> Valerie B. O'Donnell,<sup>7</sup> Daniel K. Nomura,<sup>6</sup> Justin M. Drake,<sup>3</sup> Anna Ritz,<sup>8</sup> and George V. Thomas<sup>1,9</sup>

<sup>1</sup>Knight Comprehensive Cancer Institute, Oregon Health and Science University, Portland, Oregon 97239, USA; <sup>2</sup>Knight Cardiovascular Institute, Oregon Health and Science University, Portland, Oregon 97239, USA; <sup>3</sup>Rutgers Cancer Institute of New Jersey, Rutgers, The State University of New Jersey, New Brunswick, New Jersey 08903, <sup>4</sup>Department of Urology, Oregon Health and Science University, Portland, Oregon 97239, USA; <sup>5</sup>Department of Radiology, University of California at San Francisco School of Medicine, San Francisco, California 94107, <sup>6</sup>University of California at Berkeley, Berkeley, California 94720, USA; <sup>7</sup>Systems Immunity Research Institute, Cardiff University, Cardiff CF14 4XN, United Kingdom; <sup>8</sup>Department of Biology, Reed College, Portland, Oregon 97202, USA; <sup>9</sup>Department of Pathology and Laboratory Medicine, Oregon Health and Science University, Portland, Oregon 97239, USA

**There is limited knowledge about the metabolic reprogramming induced by cancer therapies and how this contributes to therapeutic resistance. Here we show that although inhibition of PI3K–AKT–mTOR signaling markedly decreased glycolysis and restrained tumor growth, these signaling and metabolic restrictions triggered autophagy, which supplied the metabolites required for the maintenance of mitochondrial respiration and redox homeostasis. Specifically, we found that survival of cancer cells was critically dependent on phospholipase A2 (PLA2) to mobilize lysophospholipids and free fatty acids to sustain fatty acid oxidation and oxidative phosphorylation. Consistent with this, we observed significantly increased lipid droplets, with subsequent mobilization to mitochondria. These changes were abrogated in cells deficient for the essential autophagy gene *ATG5*. Accordingly, inhibition of PLA2 significantly decreased lipid droplets, decreased oxidative phosphorylation, and increased apoptosis. Together, these results describe how treatment-induced autophagy provides nutrients for cancer cell survival and identifies novel cotreatment strategies to override this survival advantage.**

[*Keywords:* autophagy; cancer; metabolism; phospholipid; resistance; signaling]

Supplemental material is available for this article.

Received July 25, 2017; revised version accepted October 26, 2017.

Despite significant advances in precision cancer therapies, tumor regressions are variable and rarely complete. Although the molecular basis of how cancer cells survive therapies that are designed to kill them (i.e. drug-tolerant “persister” cells) is likely due to a mixed set of mechanisms, we reasoned that at its root are subpopulations of drug-tolerant cancer cells that can rewire their signaling and metabolic networks to adapt to treatment-imposed proliferative, survival, and nutrient restrictions. While rewired compensatory oncogenic signaling (e.g., mediated through bypass pathways, receptor amplification, and second site mutations) have been well documented, little is known about the metabolic reprogramming induced by treatment and how this contributes to resistance.

To better understand the metabolic consequences of anti-cancer treatment, we studied metabolic reprogram-

ming in the context of PI3K pathway inhibition. The PI3K pathway, which includes the PI3K holoenzyme and its truncal effector kinases, AKT and mTOR, is essential for cell growth, proliferation, survival, and metabolism. However, clinical responses to PI3K–AKT–mTOR inhibitors have been modest to date (Fruman and Rommel 2014; Toska and Baselga 2016). We hypothesized that the limited ability of PI3K–AKT–mTOR inhibitors to induce cancer cell death was due to the autophagy-mediated metabolic reprogramming that enabled drug-tolerant cells to survive despite therapy-enforced nutrient restrictions. Our hypothesis was based on the knowledge that nutrients derived from autophagic degradation are reused to maintain macromolecular synthesis and or oxidized to

Corresponding author: [thomasge@ohsu.edu](mailto:thomasge@ohsu.edu)

Article published online ahead of print. Article and publication date are online at <http://www.genesdev.org/cgi/doi/10.1101/gad.305292.117>.

© 2017 Lue et al. This article is distributed exclusively by Cold Spring Harbor Laboratory Press for the first six months after the full-issue publication date (see <http://genesdev.cshlp.org/site/misc/terms.xhtml>). After six months, it is available under a Creative Commons License (Attribution-NonCommercial 4.0 International), as described at <http://creativecommons.org/licenses/by-nc/4.0/>.

maintain bioenergetics (Galluzzi et al. 2015). Additionally, due to the central role that the PI3K–AKT–mTOR pathway has in regulating cellular growth, we reasoned that small molecule inhibitors that converge directly or indirectly on this pathway would similarly induce autophagy to sustain drug-tolerant cells, therefore extending the reach of this mechanism of resistance beyond specific PI3K–AKT–mTOR inhibitors.

Thus far, the therapeutic reflex to block autophagy is to add anti-malarial lysosomotropic inhibitors such as chloroquine, but the clinical responses to these drugs have been variable and noncurative (Goldberg et al. 2012; Shanware et al. 2013; Rosenfeld et al. 2014; Towers and Thorburn 2016). Therefore, it would be clinically impactful to directly target the metabolic enzymes mediating autophagy-fueled metabolic processes on which drug-tolerant cells are dependent. However, there have not been any therapeutically tractable metabolic enzymes identified in the setting of therapy-induced autophagy.

Here, we identify CYT387, a JAK inhibitor that induces autophagy by inhibiting mTOR complex 1 (mTORC1). Consequently, by relieving the inhibitory signal transmitted from mTORC1 to PI3K, treatment with CYT387 leads to activation of the PI3K–mTORC2/AKT pathway. Combining CYT387 with MK2206, an allosteric AKT inhibitor, did not induce any tumor regressions despite effectively inhibiting PI3K–AKT–mTORC1/2 activation. Notably, the combination treatment further increased autophagy. This suggested that inhibition of signaling pathways alone would be insufficient to kill all tumor cells. Subsequently, we performed global metabolic profiling to systematically document the immediate metabolic adaptations effected by the therapy-induced autophagic processes. We show that autophagy-mediated metabolic adaptations supported cancer cell survival. Autophagy was required for these metabolic adaptations because these changes were abrogated in cells deficient for the essential autophagy gene *ATG5*. Subsequently, we identified that phospholipase A2 (PLA2), the rate-limiting enzyme responsible for catalyzing the breakdown of phospholipids to lysophospholipids and fatty acids, had an important role in the survival of cancer cells. Pharmacological inhibition of this enzyme dampened oxidative phosphorylation (OXPHOS) and further increased apoptosis when combined with CYT387–MK2206 combination treatment. Our findings highlight a previously unappreciated role for PLA2 in conferring a survival advantage to drug-tolerant cancer cells in metabolically restricted environments, demonstrate that this enzyme supports autophagy-induced metabolic reprogramming, and, importantly, provide a path forward for novel cotreatment strategies.

## Results

### *CYT387 induces autophagy through the modulation of the PI3K–AKT–mTOR pathway*

To precisely identify which cancer drugs induce autophagic flux by inhibiting the mTORC1 pathway, we used a library of 116 clinically focused and mechanistically

annotated compounds that included activity against two-thirds of the tyrosine kinome as well as other nontyrosine kinase pathways on a human renal cell carcinoma (RCC) cell line, ACHN (Leonard et al. 2016; Maxson et al. 2013, 2016) (see Supplemental Fig. S1A for a schematic of the workflow; see Supplemental Table 1 for a list of drugs and known targets). We monitored mTORC1 activity through phosphorylation of S6 and combined this with a measurement of p62 steady-state levels as an initial screen of autophagy flux (Joachim et al. 2015) in a high-content imaging screen.

Remarkably, the screen identified several structurally different Janus kinase (JAK) inhibitors as potent inducers of autophagic flux; namely, pan-Jak inhibitor (JAK1, JAK2, and JAK3), Go6978 (JAK 2), ruxolitinib (Jak1 and Jak2), and CYT387 (JAK1 and JAK2). All four drugs potently inhibited S6 phosphorylation, pointing to a mTORC1-dependent mechanism. Since JAK inhibitors as a class of compounds scored highly in our screen and because CYT387 was the most potent JAK inhibitor to induce autophagic flux and simultaneously decrease S6 phosphorylation in solid tumor cells in our screen, we selected this small molecule for further validation. CYT387 (momelutinib) is an orally available JAK1–2 inhibitor that has improved splenomegaly and reduced anemia in myeloproliferative neoplasia (MPN) patients (Patel et al. 2016; Winton and Kota 2017). In support of this, CYT387 suppressed the phosphorylation of JAK; its substrate, STAT3; and S6 in human RCC and MPN cell lines (Supplemental Fig. S1B,C). CYT387 induces autophagy that is reversible—as seen by the reduction in LC3B lipidation within 24 h of removal of drug—and correlated with reversal of the p-STAT3, p-S6, and p-AKT phosphorylation patterns (Supplemental Fig. S1D).

CYT387 treatment of ACHN human RCC cells plated on coverslips resulted in decreased p62 protein expression and phosphorylated S6 levels by immunofluorescence staining, confirming our high-content imaging finding (Fig. 1A). Accordingly, we observed that treatment with CYT387 induced autophagy in multiple human RCC and MPN cell lines and was primarily cytostatic (Supplemental Fig. S1E,F). Immunoblots confirmed the induction of autophagy by CYT387, as seen by the conversion of LC3-I to LC3-II, the degradation of p62, and inhibition of mTORC1 (as seen by decrease in phosphorylated S6) (Fig. 1B). We additionally confirmed that CYT387 treatment induced autophagic flux by several different methods. (1) We stably expressed a mCherry-EGFP-LC3 reported in ACHN cells, which takes advantage of the fact that EGFP fluorescence is quenched in the acidic environment of the autolysosome relative to mCherry (Debnath 2008). CYT387 treatment resulted in decreased expression of green–yellow cells and increased expression of red cells (Supplemental Fig. S2A). (2) We stained CYT387-treated ACHN cells with the autofluorescent compound monodansylcadaverine (MDC), a marker of autolysosomes, and found that CYT387 increased MDC autofluorescence (Supplemental Fig. S2B; Turcotte et al. 2008). (3) CYT387 increased LC3-II levels in ACHN cells, and this increase was more pronounced in the presence of

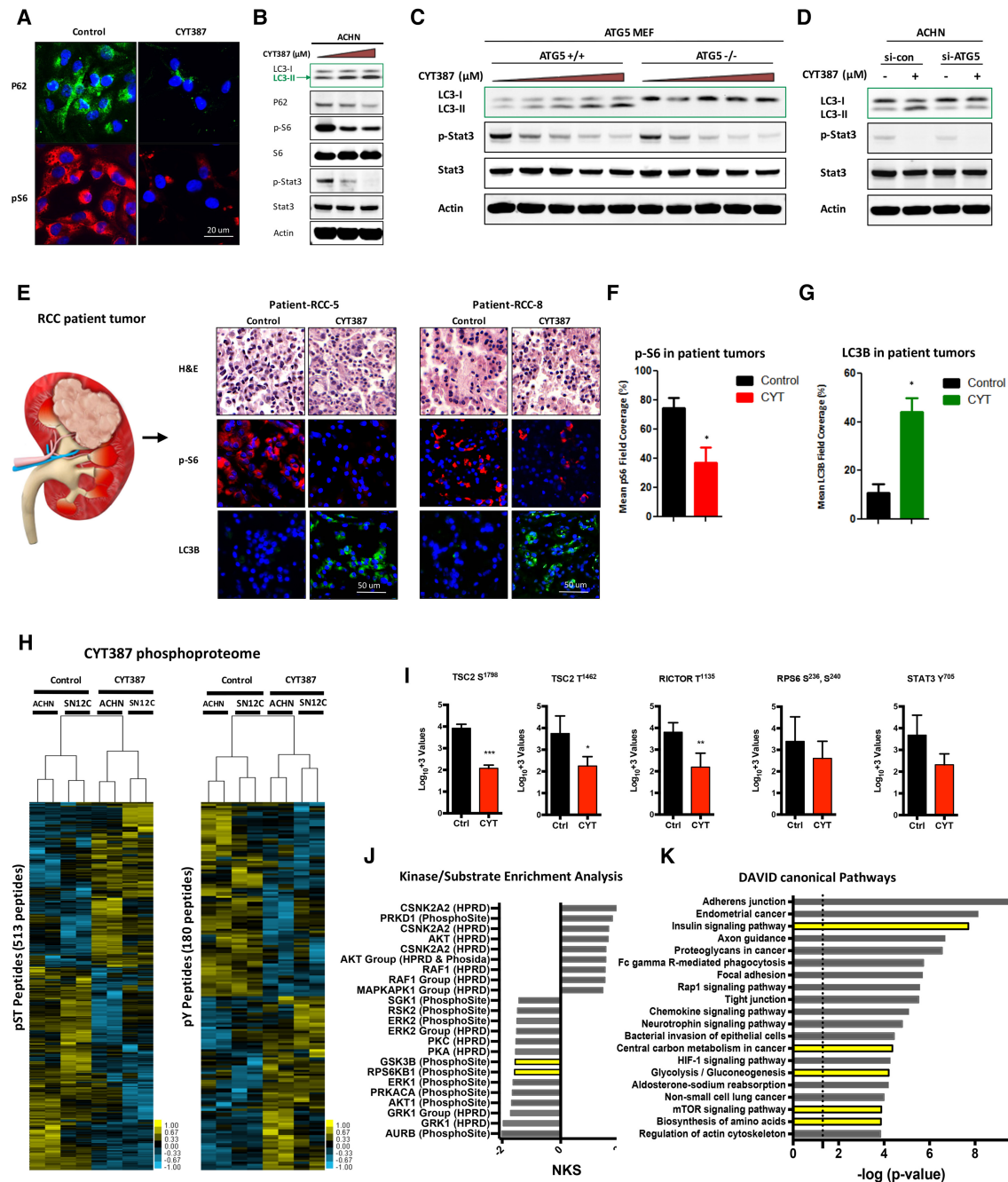


**Figure 1.** CYT387 induces autophagy in human cancer cell lines and patient-derived models. (A) ACHN cells were grown on coverslips, treated with CYT387 for 24 h, and stained p62 and p-S6. (B) ACHN cells were treated with increasing doses of CYT387 (0–2  $\mu$ M) and immunoblotted with LC3, p62, p-S6, total S6, p-STAT3, total STAT3, and  $\beta$ -actin. (C) *ATG5*<sup>+/+</sup> and *ATG5*<sup>-/-</sup> MEFs were treated with 0–3  $\mu$ M CYT387 for 24 h, and LC3 processing was evaluated by immunoblotting. (D) Immunoblot for LC3 and p-STAT3 and *ATG5* in ACHN cells transiently transfected with siRNA against *ATG5*.  $\beta$ -Actin was used as a loading control. (E) Patient-derived organotypic cultures were treated with CYT387 for 24 h and stained with p-S6 and LC3B (images from two different patient tumors are shown). (F,G) Quantification of p-S6 (F) and LC3B (G) staining in patient-derived organotypic cultures (bar graph).  $n = 10$  patients. (H) Supervised hierarchical clustering heat maps of phosphoserine and phosphothreonine (pST) peptides and phosphotyrosine (pY) peptides identified from CYT387-treated and untreated ACHN and SN12C human RCC cells with two technical replicates. Five-hundred-thirteen unique pST phosphopeptides (rows) and 180 unique pY phosphopeptides were either fourfold more enriched or fourfold less enriched, on average ( $t$ -test,  $P < 0.2$ ), in CYT387-treated cells compared with untreated cells (phosphopeptide lists are in Supplemental Tables 2, 3). (I) Relative phosphorylation abundance between ACHN and SN12C CYT387-treated and untreated cells. RPS6 S<sup>236</sup>, S<sup>240</sup> was found in the pST unsupervised heat map. (Ctrl) Control; (CYT) CYT387. (\*)  $P < 0.05$ ; (\*\*)  $P < 0.01$ ; (\*\*\*)  $P < 0.001$ , unpaired  $t$ -test. (J) Kinase substrate enrichment analysis (KSEA) of CYT387-treated and untreated pST data. Hits  $> 5$ ; false discovery rate [FDR]  $< 0.05$ . A positive NKS (normalized Kolmogorov-Smirnov score) infers greater kinase activity in CYT387-treated cells, while a negative NKS indicates greater activity in untreated cells (unfiltered summary is in Supplemental Table 4). (K) KEGG (Kyoto Encyclopedia of Genes and Genomes) pathways found from DAVID analysis of relatively active genes due to CYT387 treatment. The DAVID input list was generated by interpreting functional annotations of pSTY data (the complete pathway list is in Supplemental Table 2).

E64D/pepstatin (which inhibits the protease-induced re-conversion of LC3-II into LC3-I), consistent with an increase in autophagosome formation (Supplemental Fig. S2C; Tanida et al. 2005). (4) CYT387 increased the number of double-membraned autophagosomes, which are pathognomonic of autophagy as determined by transmission electron microscopy (Supplemental Fig. S2D; Klionsky et al. 2016). Notably, CYT387 was able to induce autophagy in a dose-dependent manner in murine embryonic fibroblasts (MEFs) that retained the essential autophagy gene *ATG5* (*ATG5<sup>+/+</sup>*), as seen by the lipidation of LC3 (Fig. 1C) (Cecconi and Levine 2008; Fung et al. 2008). Conversely, CYT387 did not induce autophagy in *ATG5*-deficient cells (*ATG5<sup>-/-</sup>*). Likewise, CYT387-induced autophagy was abrogated with siRNA depletion of *ATG5* in ACHN cells (Fig. 1D). To extend our studies into clinical samples, we exposed patient-derived RCC organotypic cultures to CYT387 treatment for 24 h. Importantly, CYT387 significantly induced LCB expression while simultaneously reducing phosphorylated S6 levels (Fig. 1E,F). Taken together, these results indicate that CYT387 treatment induces autophagic flux in both human RCC cell lines and patient-derived tumors.

To obtain further insight into the signaling pathways affected by CYT387 treatment, we studied changes in the phosphoproteome of two different human RCC cells (ACHN and SN12C) after CYT387 treatment using quantitative phosphoproteomics (Rush et al. 2005; Moritz et al. 2010; Zhuang et al. 2013). Supervised hierarchical clustering revealed that 513 phosphoserine and phosphothreonine (pST) peptides and 180 phosphotyrosine (pY) peptides significantly differed between treated and untreated cells (Fig. 1H; Supplemental Tables 2–9). We observed two phosphopeptides to be hypophosphorylated at inhibitory residues T1462 and S1798 in tuberous sclerosis complex 2 (TSC2) in CYT387-treated cells (Manning et al. 2002; Roux et al. 2004). Rapamycin-insensitive companion of mTOR (RICTOR) in CYT387-treated cells was hypophosphorylated at T1135. RICTOR is a subunit of mTORC2 (Kim et al. 2017), but the phosphorylation of T1135 is mediated by mTORC1 via induction of the p70S6 kinase (Julien et al. 2010) and impedes the ability of mTORC2 to phosphorylate AKT on S473 (Fig. 1I; Dibble et al. 2009). As expected, ribosomal protein S6 at residues S236 and S240 and STAT3 Y705 trended toward hypophosphorylation, and p70S6 kinase (RPS6KB) was significantly less active in CYT387-treated cells based on kinase substrate enrichment analyses (KSEAs) (Fig. 1J; Drake et al. 2012). However, KSEAs of AKT motifs were inconclusive, as some motifs trended toward increased activity and others trended toward decreased activity in CYT387-treated cells. DAVID analysis of genes corresponding to the phosphopeptides and activated in CYT387-treated cells (Supplemental Tables 10, 11) also revealed several KEGG (Kyoto Encyclopedia of Genes and Genomes) pathways that are biologically relevant to CYT387 treatment, including glycolysis, amino acid biosynthesis, and central carbon metabolism (Fig. 1K; Huang et al. 2009a,b). In support of these phosphoproteomics findings, mRNA analysis of CYT387-treated ACHN cells

using gene set enrichment analysis (GSEA) of multiple independent data sets revealed significant enrichment of genes involved in several metabolic pathways, while biological modules associated with mTOR (e.g., cell cycle and protein synthesis) were anti-correlated with CYT387 treatment. (Supplemental Tables 12, 13).

Collectively, the phosphoproteome and transcriptome data provide strong evidence that CYT387 treatment reduces mTORC1 signaling to increase TSC2 and mTORC2 signaling leading to AKT activation and is coupled with changes in metabolic pathways.

#### *PI3K–AKT–mTOR inhibition treatment restrains tumor growth but does not induce tumor regression*

We reasoned that the CYT387-induced inhibition of mTORC1 would relieve the inhibitory feedback signal normally transmitted from mTORC1 to PI3K, as the phosphoproteomic data suggested via KSEA, and that this would result in hyperactivation of PI3K and AKT, with consequent prosurvival signaling. Consistent with this interpretation, CYT387 treatment caused an increase in AKT T308, the PDK-1-catalyzed site that serves as readout for PI3K signaling in a time-dependent manner (Supplemental Fig. S3A,B). Notably, CYT387 did not dephosphorylate ERK (Supplemental Fig. S3C). Therefore, we sought to identify PI3K–AKT pathway inhibitors that would effectively cooperate with CYT387 to induce apoptosis. We used GDC-0941, a pan-PI3K inhibitor (Sarker et al. 2015); BX795, a PDK-1 inhibitor (Dangelmaier et al. 2014); and MK2206 (Yap et al. 2011), an allosteric AKT inhibitor, to chemically deconstruct this signaling pathway, as depicted in the schematic (Supplemental Fig. S3D–F). We first assessed the biologic effects of these inhibitors on proliferation and apoptosis in human RCC cells singly and in combination with CYT387 (Fig. 2A–D). While GDC-0941, BX795, and MK2206 alone exhibited some anti-proliferative effects, the combination with CYT387 resulted in significantly greater inhibition of proliferation in ACHN and SN12C cells. In marked contrast, all drugs as single agents had little or no effect on apoptosis, but the combination of either agent with CYT387 resulted in increased apoptosis. This was most striking in the CYT387 and MK2206 combination (Fig. 2B,D), and we therefore selected MK2206 for further *in vivo* studies. We investigated the mechanisms by which MK2206 and CYT387 cooperated to suppress tumor growth in RCC cells (Fig. 2E,F). MK2206 effectively inhibited AKT activation, as documented by dephosphorylation of both p-AKT Thr308 and p-Ser473 and the AKT substrate PRAS40. Consistent with prior results, suppression of AKT induced autophagy, as seen by the conversion of LC3-I to LC3-II. Suppression of mTORC1 by CYT387 led to feedback activation of PI3K, as seen by the increase in phosphorylation of p-AKT Thr308 (which serves as a readout for PI3K activity) and mTORC2 (as monitored by AKT Ser473 phosphorylation). Subsequently, combining MK2206 with CYT387 effectively inhibited both AKT and mTORC1 to almost undetectable levels and induced apoptosis (cleaved caspase 3). Thus, by inhibiting the PI3K–AKT–

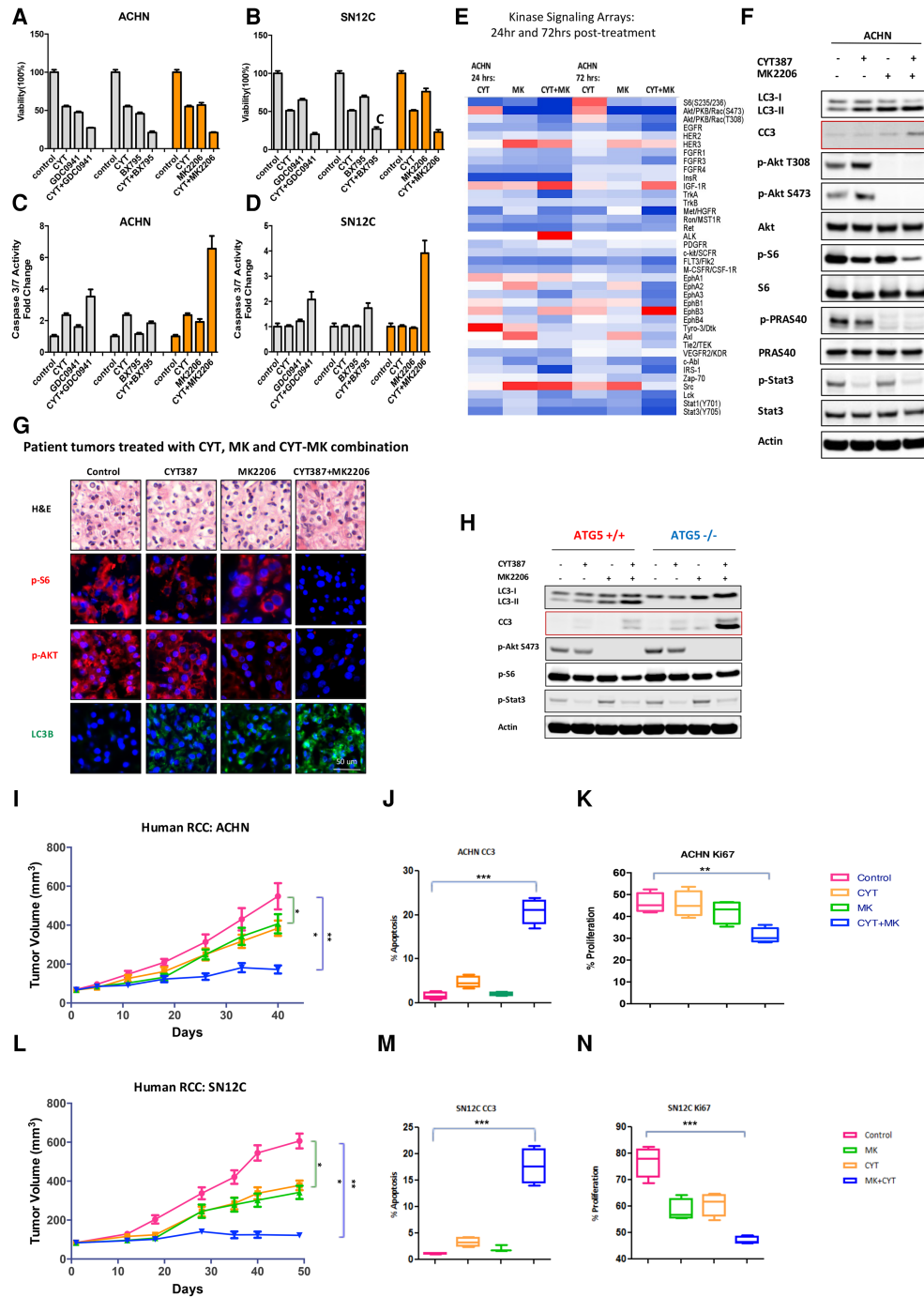


**Figure 2.** CYT387 combines with MK2206 to effectively inhibit PI3K-AKT-mTOR signaling in human cancer cell lines and xenografts but does not induce tumor regression. (A,B) Combination treatment with GDC0941, BX795, and MK2206 with measurement of cell viability in two human RCC cell lines: ACHN (A) and SN12C (B). (C,D) The same combinations as in A, with measurement of apoptosis by cleaved caspase 3/7 in ACHN (C) and SN12C (D) cells. (E) A heat map of signaling kinase arrays shows the effects of CYT387, MK2206, and CYT387+MK2206 cotreatment in ACHN cells at 24 h and 72 h after treatment. (F) Immunoblot for LC3, p-AKT Thr308, p-AKT Ser473, total AKT, p-PRAS40, total PRAS40, p-S6, total S6, p-STAT3, total STAT3, and  $\beta$ -actin. (G) Patient-derived organotypic cultures treated with DMSO (control), CYT387, MK2206, and the CYT387+MK2206 combination for 24 h exhibit an increase in LC3B (green) and a decrease in p-S6 (red) and p-AKT (red). (H) ATG5<sup>+/+</sup> and ATG5<sup>-/-</sup> MEFs were treated with 2  $\mu$ M CYT387, 10  $\mu$ M MK2206, and the combination for 24 h, and LC3, cleaved caspase 3, p-AKT, p-S6, p-STAT3, and  $\beta$ -actin were evaluated by immunoblotting. (I) ACHN xenografts treated with vehicle, 50 mg/kg CYT387, 60 mg/kg MK2206, and a 50 mg/kg CYT387 + 60 mg/kg MK2206 combination. Tumor volume is shown. Error bars represent mean  $\pm$  SEM. Control versus CYT387+MK2206, (\*\*\*\*)  $P < 0.01$ . (J,K) The effect on apoptosis (CC3) (J) and proliferation (KI67) (K) in ACHN xenograft tumors. Error bars represent mean  $\pm$  SEM. (J) Control versus CYT387+MK2206,  $P < 0.0001$ . (K) Control versus CYT387+MK2206,  $P = 0.0018$ . (L) SN12C xenografts treated with vehicle, 50 mg/kg CYT387, 60 mg/kg MK2206, and a 50 mg/kg CYT387 + 60 mg/kg MK2206 combination. Tumor volume is shown. Error bars represent mean  $\pm$  SEM. Control versus CYT387+MK2206, (\*\*\*\*)  $P < 0.0001$ . (M,N) The effect on apoptosis (CC3) (M) and proliferation (KI67) (N) in SN12C xenograft tumors. Error bars represent mean  $\pm$  SEM. (M) Control versus CYT387+MK2206,  $P < 0.0001$ . (N) Control versus CYT387+MK2206  $P < 0.0001$ .

mTOR pathway at proximal and distal nodes, CYT387 and MK2206 combine to shut down PI3K oncogenic signaling. However, autophagy still persisted in the combination treatment, pointing to a survival signal that sustains subpopulations of drug-tolerant cancer cells. Notably, the CYT387–MK2206 combination induced autophagy in patient-derived organotypic RCC cultures (Fig. 2G).

To further define the role of treatment-induced autophagy in mediating survival, we assessed the effects of CYT387 and MK2206 combination treatment on *ATG5*<sup>-/-</sup> and *ATG5*<sup>+/+</sup> MEFs. The CYT387–MK2206 cotreatment induced more apoptosis in *ATG5*<sup>-/-</sup> MEFs than it did in wild-type controls (demonstrated by an increase in cleaved caspase 3), indicating that autophagy protects cells from apoptosis (Fig. 2H). Collectively, these results suggest that despite effective inhibition of PI3K–AKT–mTOR signaling with the resultant induction of apoptosis, cancer cells are able to simultaneously induce an autophagic-fueled survival pathway.

We next examined the safety and efficacy of CYT387 and MK2206 cotreatment in vivo in two xenograft tumor models. While CYT387 or MK2206 alone exhibited an anti-tumor effect on ACHN and SN12C xenografts, the combination of CYT387 with MK2206 resulted in significantly greater tumor growth inhibition in ACHN and SN12C tumor xenografts ( $P < 0.001$ ) (Fig. 2I,L). Importantly, combination treatment was well tolerated, with no weight loss recorded (Supplemental Fig. S3G,H). Pharmacodynamic studies demonstrated that combination therapy led to the suppression of S6 and AKTS473 phosphorylation (Supplemental Fig. S3I). Consistent with our in vitro finding, CYT387 alone had a minimal impact on apoptosis. In marked contrast, combination treatment with CYT387 and MK2206 resulted in a significant increase in apoptosis (established by an increase in cleaved caspase 3;  $P < 0.001$ ) (Fig. 2J [ACHN xenograft tumors], M [SN12C xenograft tumors]) and a reduction in proliferation (demonstrated by a decrease in Ki-67;  $P < 0.001$ ) (Fig. 2K [ACHN xenograft tumors], N [SN12C xenograft tumors]). However, despite effective inhibition of PI3K–AKT–mTOR signaling, the combination treatment did not induce tumor regression.

#### *Metabolic reprogramming is supported by redox homeostasis*

The lack of tumor regression despite effective inhibition of PI3K–AKT–mTOR signaling led us to question whether metabolic reprogramming may sustain the survival of the treated cancer cells. The PI3K–AKT–mTOR pathway regulates multiple steps in glucose uptake and metabolism (Duvel et al. 2010). Therefore, we hypothesized that CYT387 and MK2206 treatment singly and in combination would negatively impact glucose uptake, aerobic glycolysis, and, subsequently, biosynthetic pathways, resulting in a drug-enforced reduction in glucose availability in the microenvironment. To determine the contribution of CYT387 and MK2206 treatment on the regulation of glycolysis, we measured glucose uptake by <sup>18</sup>F-fluoro-

deoxyglucose (<sup>18</sup>FDG), lactate excretion, and the extracellular acidification rate (ECAR) as readouts for glycolysis. CYT387, MK2206, and the combination significantly decreased glucose uptake and reduced lactate production in vitro (Fig. 3A,B). The dramatic difference between lactate/glucose ratio in extracellular medium further supports the finding that CYT387 and MK2206 cotreatment inhibits glycolysis (control: 1.51; CYT387: 0.65; MK2206: 0.81; CYT387+MK2206: 0.37). This impaired carbon metabolism with treatment also resulted in a reduction of cell size (Fig. 3C). Consistent with the above finding, CYT387, MK2206, and the CYT387–MK2206 combination significantly reduced the ECAR (Fig. 3D,E).

Decreased glucose availability with cotreatment might also be reflected in changes with OXPHOS activity, as measured by oxygen consumption rate (OCR; an indicator of OXPHOS). However, we found that the OCR/ECAR ratio increased after cotreatment, suggesting a predominant decrease in glycolysis with the maintenance of mitochondria-driven OXPHOS (Fig. 3F). Consistent with glucose limitation and decreased glycolysis, we observed increased AMPK phosphorylation at Thr172, an established indicator of metabolic stress (Fig. 3G). Importantly, in the setting of glucose deprivation and impairment of the pentose phosphate pathway (PPP), AMPK has been shown to increase NADPH levels from increased fatty acid oxidation. Specifically, we noted increased levels of NADPH, maintenance of GSSG/GSH ratios, and a resultant mitigation of reactive oxygen species (ROS) (Fig. 3H–J). These findings are consistent with the role of AMPK in mitigating metabolic stress and promoting cancer cell survival (Jeon et al. 2012). Additionally, AMPK would be predicted to further inhibit mTOR (Inoki et al. 2003; Gwinn et al. 2008). By comparison, we did not see any reduction in PKM2 levels, suggesting that the metabolic switch from aerobic glycolysis to OXPHOS is not dependent on pyruvate kinase activity (Christofk et al. 2008).

Overall, these findings suggest that by decreasing glucose levels, CYT387–MK2206 cotreatment severely reduces the glycolytic capacity needed to supply the bioenergetics needs of the RCC cells. Importantly, this treatment-induced nutrient-depleted condition, while suppressing proliferation, simultaneously promotes survival by regulating NADPH homeostasis and maintaining mitochondrial-driven oxidation.

#### *PI3K–AKT–mTOR treatment-induced autophagy promotes phospholipid metabolism*

Therefore, to comprehensively determine how autophagy contributes to the metabolic needs, we performed global metabolic analysis using a liquid chromatography-tandem mass spectrometry (LC-MS/MS)-based platform (Louie et al. 2016). These studies revealed that CYT387 and MK2206, singly and in combination, effected changes across multiple pathways (Fig. 4A; Supplemental Table 14). Consistent with the role of the PI3K–AKT–mTOR pathway in the regulation of glycolysis, treatment with these agents was accompanied by reductions in glucose, glucose-6-phosphate, DG3P, PEP, pyruvate, and lactate,

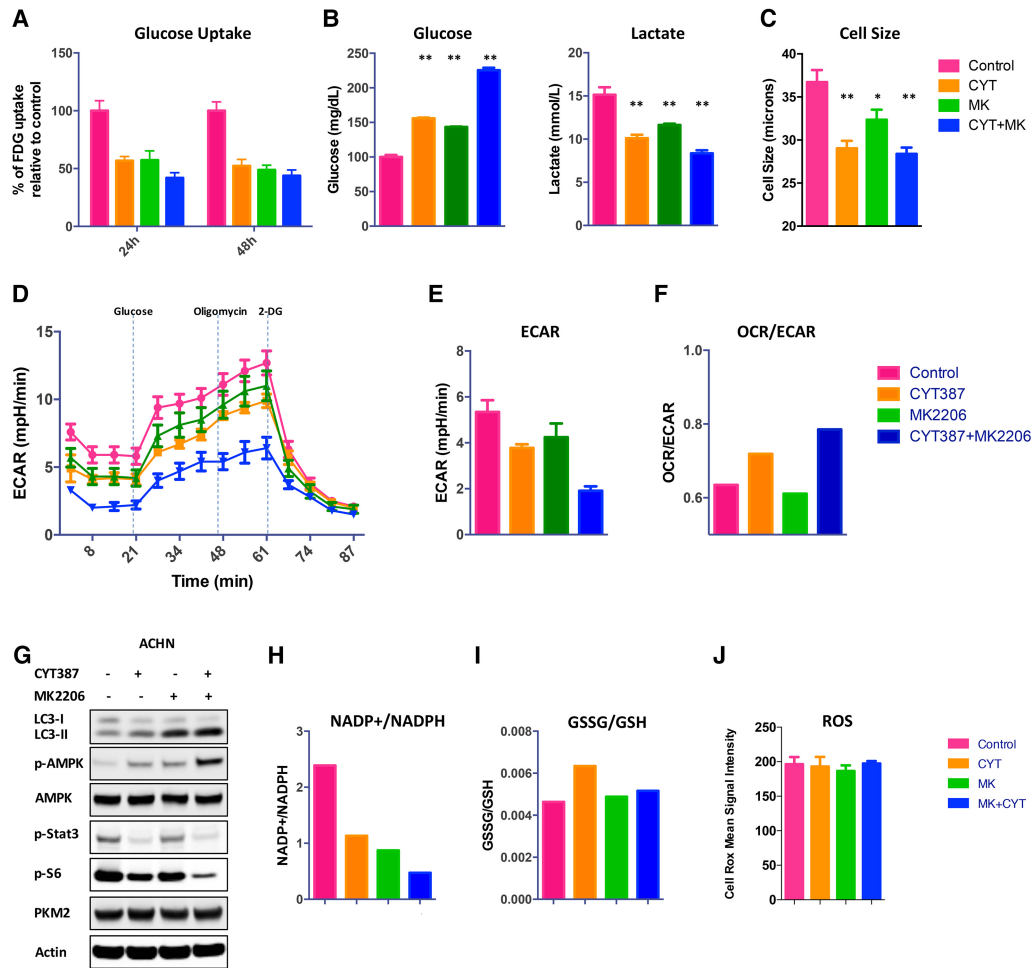


**Figure 3.** The effects of treatment on metabolism. (A) The treatment effects of control, CYT387, MK2206, and CYT387+MK2206 on glucose uptake over time, measured by  $^{18}\text{F}$ FDG. (B) Glucose and lactate levels in culture medium were measured in control and treated cells and normalized to cell number. (C) Qualitative analysis of cell diameter changes of ACHN cells treated with CYT387, MK2206, CYT387 + MK2206, or vehicle (DMSO). (\*)  $P < 0.02$ . (D) Glycolysis in ACHN cells was measured using a XF-96 extracellular flux analyzer after preincubation with drugs or DMSO. Shown are ECAR means  $\pm$  SD of experimental triplicates. (E) The effects of treatment on basal ECAR, measured in real time and presented as change in milli-pH per unit time. Representative results are shown.  $n = 2$ . (F) Ratios of oxygen consumption rate (OCR; an indicator of OXPHOS) to ECAR (an indicator of aerobic glycolysis at baseline) of treated ACHN cells. Representative results are shown.  $n = 2$ . (G–J) Treatment activates p-AMPK and increases NADPH levels, maintains GSSG/GSH ratios, and mitigates reactive oxygen species (ROS). (G) ACHN cells were treated with control, 2  $\mu\text{M}$  CYT387, 10  $\mu\text{M}$  MK2206, and CYT387 + MK2206 for 24 h and probed with the indicated antibodies. (H) NADP $^+$ /NADPH levels were measured. (I) GSSG and GSH levels were measured in lysates ( $n = 4$ ) using liquid chromatography-tandem mass spectrometry (LC-MS/MS). (J) The normalized abundance of these metabolites is shown. Cells were stained with the ROS sensor CellRox.  $n = 3$ ; three independent experiments.  $P = \text{ns}$ .

consistent with the inhibition of glycolysis (Supplemental Fig. S4A), as described above and also concordant with the gene expression data. Similarly, we also observed reductions in PPP intermediates, amino acids, tricarboxylic acid (TCA) cycle intermediates, and ribose biosynthesis and corresponding increases in purine breakdown products guanine and hypoxanthine (Supplemental Fig. S4B–E). These findings are in keeping with a nutrient-deprived state (i.e., decreased anabolism) with subsequent increased autophagic catabolism to maintain survival (Mizushima et al. 2001). Cells adapt to glucose deprivation by subsisting on fatty acids—mobilized through glycerolipid remodeling—for oxidation, and this is consistent with our

observation that the most significant metabolite changes were in lipid intermediates, including phospholipids, triacylglycerol (TAG), cholesterol esters, diacylglycerol (DAG), and fatty acids (C16:0, C18:0, and C18:1) (Fig. 4A; Supplemental Fig. S4F; Kerner and Hoppel 2000; Eaton 2002; Finn and Dice 2006).

We further investigated the lipid substrates that were catabolized by autophagy to produce fatty acids for fatty acid oxidation. Steady-state metabolite profiling showed significant increases in lysophospholipids and arachidonic acid (C20:4), with corresponding decreases in their phospholipid precursors (Fig. 4B). Phospholipids, which include phosphatidylcholine (PC), phosphatidylethanolamine (PE),



Lue et al.

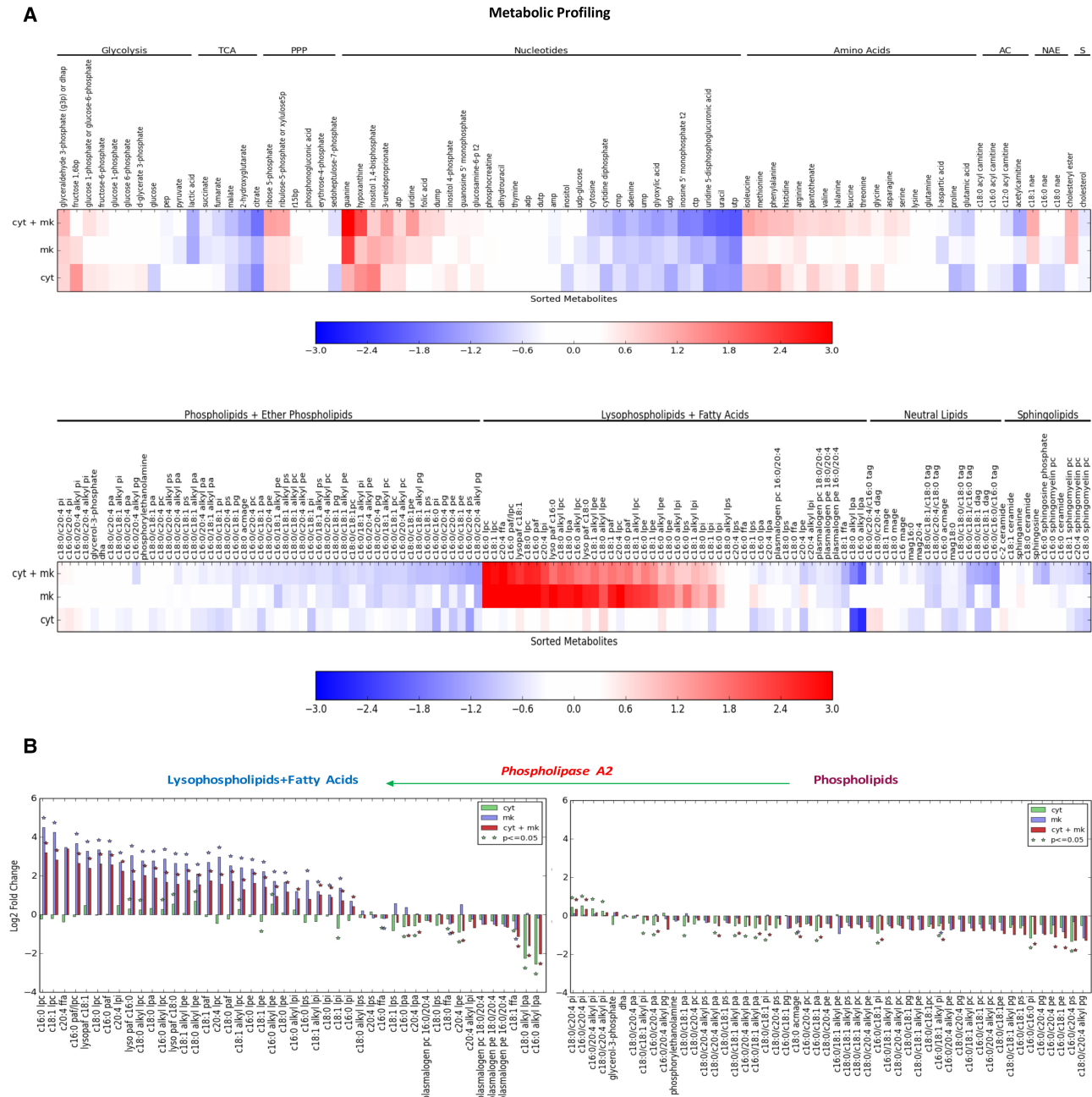


**Figure 4.** PI3K–AKT–mTOR signaling inhibition induces metabolic reprogramming. (A) Heat map of metabolomic profiling of treated cells (CYT387, MKK2206, and CYT387+MMK2206) compared with ACHN cells treated with vehicle (DMSO) using LC-MS/MS (see the Materials and Methods for details). Log fold changes of profiled metabolites are shown. Metabolites are ordered within each category: glycolysis, TCA cycle, PPP, nucleotide metabolism, amino acid metabolism, phospholipids, ether phospholipids, lysophospholipids, fatty acids, neutral lipids, acyl carnithines (SL), and sphingolipids (S), and n-acyl ethanolamines (NAE). (B) PLA2 catalyzes the hydrolysis of phospholipids to lysophospholipids and arachidonic acid. Waterfall plot demonstrating relative levels of phospholipids, lysophospholipids, and fatty acids in treated cells (CYT387, MK2206, and CYT387+MK2206) compared with ACHN cells treated with vehicle (DMSO). Asterisks denote a significant difference of treated cells compared with vehicle ( $t$ -test,  $P$ -value  $\leq 0.05$ ).

phosphatidylserine (PS), phosphatidylglycerol (PG), and phosphatidylinositol (PI), are major structural components of cellular membranes. PLA2 is the enzyme that catalyzes the hydrolysis of the phospholipid sn-2 ester bond with subsequent release of lysophospholipids; e.g., lysophosphatidylcholine (LPC), alkyl-lysophosphatidylcho-

line (alkyl-LPC), and free fatty acids (Murakami et al. 2011). Accordingly, we found elevated levels of C16:0 LPC, C18:0 LPC, C18:1 LPC, and C18:0 alkyl-LPC and corresponding decreases in their phospholipid precursors. Notably, we observed significant decreases in free fatty acids (C16:0, C18:0, and C18:1), supporting the idea that

phospholipids are hydrolyzed to supply fatty acids for fatty acid oxidation. Consistent with increased arachidonic acid levels in CYT387–MK2206-cotreated cells, we observed increased levels of 14,15-EET, 11,12-EET, 8,9-EET, and 5-HETE, pointing to arachidonic acid P450-mediated generation of eicosanoids (Supplemental Fig. S5).

*PI3K–AKT–mTOR treatment-induced autophagy facilitates lipid droplet (LD) formation and mitochondrial respiration*

To protect cells from the destabilizing effects of excess lipids, free fatty acids mobilized by autophagy and destined for oxidation are stored in an intermediate intracellular pool: LDs (Thiam et al. 2013). We reasoned that the large changes in glycerolipid redistribution identified by our metabolomics profiling of treated cells would result in an increased number of LDs to support fatty acid oxidation, with subsequent mobilization of fatty acids to mitochondria under these nutrient-depleted conditions (Rambold et al. 2015). Consistent with this, we observed that CYT387 and MK2206 singly and in combination incrementally and significantly increased the number and size of Bodipy 493/503-labeled (Fig. 5A–C, green) LDs. Additionally, we incubated ACHN human RCC cells with Bodipy-C12-HPC (a phospholipid containing green fluorescent long chain fatty acid) followed by treatment with vehicle or the CYT387–MK2206 combination. CYT387–MK2206 cotreatment led to a greater degree of incorporation of Bodipy-C12-labeled fatty acids into LDs relative to vehicle-treated cells. This suggests that CYT387–MK2206 treatment-induced autophagy results in phospholipid hydrolysis that releases fatty acids, which are subsequently incorporated into new LDs (Supplemental Fig. S6).

To determine whether the increase in LDs occurred in vivo, we stained the vehicle, CYT387, MK2206, and CYT387–MK2206-cotreated xenograft tumors for adipophilin, which belongs to the perilipin family, members of which coat intracellular lipid storage droplets and facilitate metabolic interactions with mitochondria (Sztalryd and Kimmel 2014). Consistent with the in vitro data, the number of adipophilin-positive LDs significantly and incrementally increased with treatment (as measured on treatment day 40 in ACHN xenograft tumors; CYT387<MK2206<CYT387+MK2206;  $P=0.0046$ ) (Fig. 5D), indicating that these drug treatments stimulate the formation of LDs in vivo. Collectively, these data suggest that the early adaptive and survival changes effected by the initial drug treatment continues to support the maintenance of long-term in vivo tumor growth.

Next, to further determine whether autophagy contributed to LD numbers, we treated  $ATG5^{+/+}$  and  $ATG5^{-/-}$  MEFs with CYT387, MK2206, and the combination. Autophagy-competent  $ATG5^{+/+}$  MEFs were able to significantly increase LD numbers (Fig. 5E). In marked contrast, none of the treatments was able to increase LDs in  $ATG5^{-/-}$  MEFs, confirming that autophagy is required to sustain LD levels (Fig. 5F). To investigate the metabolic ramifications of this, we compared oxygen consumption

by  $ATG5^{-/-}$  and  $ATG5^{+/+}$  MEFs when treated with CYT387, MK2206, and the combination. We found that CYT387–MK2206 cotreatment profoundly decreased the  $ATG5^{-/-}$  MEFs mitochondrial OCR and spare respiratory capacity (SRC; the quantitative difference between the maximal OCR and the initial basal OCR), indicating that  $ATG5^{-/-}$  MEFs function near their maximal rate and are unable to maintain an adequate level of mitochondrial respiration with CYT387+MK2206 cotreatment due to a deficit in their metabolic compensatory mechanisms (Fig. 5G,H). In contrast, we observed no decrease in mitochondrial OCR and SRC in CYT387–MK2206-cotreated  $ATG5^{+/+}$  MEFs.

The extent of the metabolic difference between vehicle-treated  $ATG5^{-/-}$  and CYT387+MK2206-cotreated MEFs was apparent in the overall ratio of OXPHOS to aerobic glycolysis (OCR/ECAR), which was twofold higher in vehicle-treated than in CYT387–MK2206-cotreated  $ATG5^{-/-}$  MEFs, reflective of the need for autophagy to supply the nutrients to maintain mitochondrial OCR under treatment-enforced metabolic restrictions (Fig. 5I).

This is in line with a model in which autophagy of cellular organelles and membranes during nutrient deprivation produces fatty acids that supply the LD pool, where they are then transferred into mitochondria for  $\beta$ -oxidation. In support of this, we observed that treated RCC cells had significantly increased numbers of mitochondria (Fig. 5J). Accordingly, dual staining of treated ACHN cells with a mitochondrial marker (Mitotracker orange) and LDs with Bodipy (Fig. 5K, green) revealed that the LDs were closely associated with the mitochondria, potentially enabling the fatty acids released from LDs to traffic directly from LDs to mitochondria and maximizing the fatty acid oxidation (Fig. 5K; Rambold et al. 2015).

Importantly, cancer cells become increasingly dependent on mitochondrial fatty acid oxidation in nutrient-depleted conditions (Fig. 5L; Cabodevilla et al. 2013). Consistent with this, using the Mito Fuel Flex test, we found that human ACHN RCC cells' dependence on fatty acid doubled with CYT387–MK2206 cotreatment (Fig. 5M). Consequently, oxidation of endogenous fatty acids significantly contributed to the OXPHOS rate in MK2206+CYT387-cotreated cells compared with control (>2.5-fold increase;  $P < 0.0001$ ) (Fig. 5N). Consistent with this, induction of fatty acid oxidation by CYT387–MK2206 cotreatment was attenuated in  $ATG5^{-/-}$  MEFs (Supplemental Fig. S7). In contrast, glutamine-supported OCR represented a minority of total OCR in CYT387–MK2206-cotreated ACHN cells (Supplemental Fig. S8). Taken together, this suggested that cellular lipid remodeling by the autophagy–lysosome system may supply a considerable fraction of the intracellular lipids–fatty acids irrespective of their external availability.

*Inhibiting PLA2 activity decreases autophagy-induced LDs, limits OXPHOS, and increases apoptosis*

Our data implicated hydrolysis of phospholipids as a critical mechanism for the generation of lysophospholipids

Lue et al.

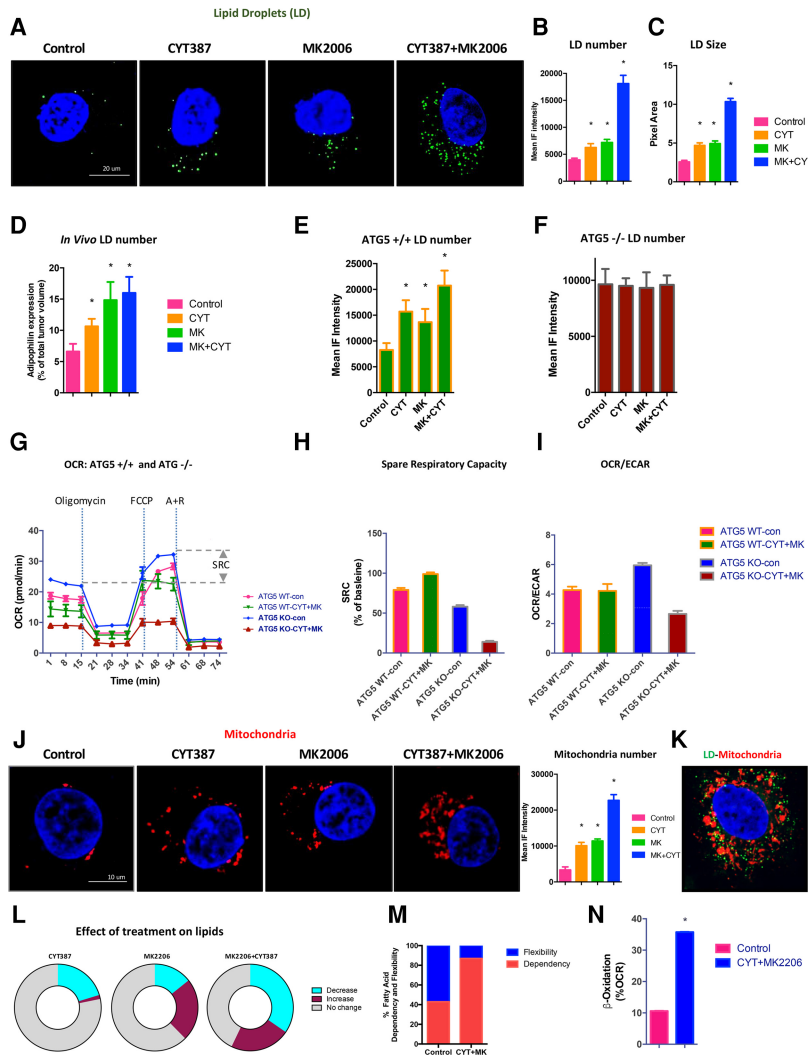


**Figure 5.** Autophagy is required for LD growth and fatty acid oxidation. (A) ACHN cells were treated with control, CYT387, MK2206, and CYT387+MK2206 for 24 h, and Bodipy 493/503 (green) was added to visualize LDs. Representative images are shown.  $n = 5$  experiments. (B,C) Bar graphs quantify the increase in number (B) and size (C) of LDs, respectively. Data are expressed as means  $\pm$  SEM. (\*)  $P < 0.001$  for control versus CYT387, control versus MK2206, and control versus CYT387+MK2206. (D) Adipophilin staining in xenograft tumors quantifies the increase in LDs in vivo.  $n = 9$ . Data are expressed as means  $\pm$  SEM. (\*)  $P < 0.01$  for control versus CYT387 and control versus MK2206, measured in tumors resected after 40 d of treatment. (E)  $ATG5^{+/+}$  MEFs were treated with 2  $\mu$ M CYT387, 10  $\mu$ M MK2206, and the combination for 24 h. Bodipy was added, and the LD number was measured.  $n = 500$  cells. (\*)  $P < 0.001$  for control versus CYT387 and control versus CYT387+MK2206;  $P < 0.005$  for control versus MK2206. (F)  $ATG5^{-/-}$  MEFs treated as in E. Bodipy was added, and the LD number was measured.  $n = 500$  cells.  $P = \text{NS}$  (no significance between treatment groups). (G)  $ATG5^{+/+}$  and  $ATG5^{-/-}$  MEFs were treated with DMSO (control), CYT387, MK2206, and CYT387+MK2206 for 24 h, and then OCRs (indicator of OXPHOS) were determined using a XF-96 extracellular flux analyzer during sequential treatments (dotted vertical lines) with oligomycin, FCCP, and rotenone/anti-mycin (A+R). Spare respiratory capacity (SRC) is the quantitative difference between maximal uncontrolled OCR (top horizontal dashed line) and the initial basal OCR (bottom horizontal dashed line). Shown are OCR means  $\pm$  SD of experimental triplicates. For ease of viewing, only control and CYT387 + MK2206 data are graphed. (H) SRC (the percentage maximum OCR after FCCP injection of baseline OCR) of  $ATG5^{+/+}$  and  $ATG5^{-/-}$  MEFs after the indicated treatments.

Shown are means  $\pm$  SD of experimental triplicates. (I) Ratios of OCR to ECAR (indicator of aerobic glycolysis) at baseline of  $ATG5^{+/+}$  and  $ATG5^{-/-}$  MEFs after the indicated treatments. (J) ACHN cells were treated with control, CYT387, MK2206, and CYT387+MK2206 for 24 h, and Mitotracker orange was added to visualize mitochondria. Representative images are shown.  $n = 5$  experiments. Mitochondria number was measured, and data are expressed as means  $\pm$  SEM. (\*)  $P < 0.001$  for control versus CYT387, control versus MK2206, and control versus MK2206+CYT387. (K) Dual staining of Bodipy and Mitotracker orange demonstrate close proximity of LDs with mitochondria in CYT387+MK2206-cotreated ACHN cells (a representative image is shown). (L) Global metabolite profiling reveals a preferential decrease in lipids. (Decrease) Abundance  $< 0.5$ -fold in treated cells compared with the vehicle; (increase) abundance greater than twofold in treated cells compared with the vehicle. (M) Fatty acid fuel dependency measures the reliance of ACHN cells on fatty acids to maintain baseline respiration. ACHN cells were treated with DMSO (control) or CYT387+MK2206 for 24 h, and OCR was measured during the Seahorse XF Mito Fuel Flex assay. The percentage of dependence on fatty acids was calculated by quantifying the change in basal OCR after fatty acid oxidation was blocked using 4  $\mu$ M CPT-1a inhibitor etomoxir divided by the total change in OCR from baseline after combined inhibition of fatty acid, glutamine, and pyruvate oxidation using 4  $\mu$ M etomoxir, 3  $\mu$ M BPTES, and 2  $\mu$ M UK5099, respectively (representative graph).  $n = 2$ . Fatty acid fuel flexibility was calculated by measuring the change in sensitivity to etomoxir's inhibition of OCR after blockade of glutamine and glucose oxidation and represents the ability of ACHN cells to increase oxidation of fatty acid when glutamine and pyruvate utilization is precluded. (N) Measurement of fatty acid-driven OCR, measured by acute inhibition of CPT-1a using 4  $\mu$ M etomoxir (\*\*)  $P < 0.01$ ) and represented as a percentage of total mitochondrial OCR calculated using mitochondrial complex I and III inhibitors 1  $\mu$ M rotenone and 1  $\mu$ M anti-mycin, respectively.

and fatty acids for fatty acid oxidation in treated RCC cells, and, therefore, inhibition of this enzymatic activity would negatively impact OXPHOS and subsequently limit the survival of these cells. To test this directly, we added the PLA2 inhibitor oleyloxyethylphosphocholine

(OOEPC; which inhibits secretory PLA) (Slatter et al. 2016) to CYT387, MK2206, and CYT387+MK2206-cotreated cells and measured LD numbers. Addition of OOEPC significantly reduced the LD abundance in CYT387, MK2206, and CYT387+MK2206-cotreated cells

(Fig. 6A,B). Since several isoforms of PLA2 exist, we determined their role in reducing LDs. We found that inhibition of calcium-sensitive PLA2 (with cPLA2i) and calcium-insensitive PLA2 (with bromoenol lactone [BEL]) was also able to reduce LD number, consistent with the rate-limiting role of PLA2 in mediating phospholipid hydrolysis (Supplemental Fig. S9). To document the kinetics of the new pool of CYT387–MK2206-induced LDs, we performed a time-course experiment to monitor the appearance of LDs following CYT387–MK2206 cotreatment and ascertained that LDs appeared 2 h after treatment and then continuously increased in number during the next 24 h of monitoring. In contrast, simultaneous addition of OOPEC to the CYT387–MK2206 combination at the start of treatment completely blocked the appearance of LDs. Similarly, addition of OOPEC at 2 h after cotreatment with CYT387+MK2206 completely inhibited any further increase in LDs. Subsequently, the addition of etomoxir at 8 h (which blocks the utilization of fatty acids) resulted in LD accumulation in OOPEC+CYT387+MK2206-treated cells. These results demonstrate that PLA2 activity is required for LD generation after CYT387–MK2206 cotreatment and that OOPEC is able to inhibit PLA2 activity (Supplemental Fig. S10).

To directly test the metabolic impact of OOPEC treatment, we first assessed changes in the OCR. We observed a marked decrease in the basal OCR when OOPEC was added to the CYT387–MK2206 combination. Importantly, the addition of OOPEC profoundly reduced the SRC, indicating that the inhibition of PLA2 decreases mitochondrial oxidation by reducing fatty acid supply and impedes the cells' capacity to respond to increased energetic demands (Fig. 6C,D). The marked reduction in SRC was similar to our earlier observations in CYT387–MK2206-treated *ATG5*<sup>-/-</sup> MEFs and is consistent with the model in which autophagy-supplied LDs are required to support mitochondrial OCR in metabolically restricted environments (Fig. 5G–I). Next, by plotting OCR versus ECAR, we determined the effect of PLA2 inhibition by OOPEC on CYT387–MK2206-treated tumors; this measurement highlighted that untreated ACHN human RCC cells have higher OXPHOS and glycolysis compared with CYT387–MK2206-cotreated cells (Fig. 6E). The addition of OOPEC markedly decreased OCR in ACHN cells, indicating that these treatments diminished the overall metabolic activity of the cancer cells.

This observed reduction in bioenergetic metabolism led us to determine whether PLA2 inhibition would have an impact on proliferation and apoptosis. Cotreatment with OOPEC had a minimal additional effect on proliferation (Fig. 6F). In contrast, the addition of OOPEC significantly increased apoptosis, consistent with its ability to reverse autophagy-supplied fatty acids that enable survival (Fig. 6G). To further verify that PLA2 inhibition impacted cancer cell survival, we tested a distinct PLA2 inhibitor, varespladib, which has been clinically developed for cardiovascular diseases (Rosenson et al. 2010). Similar to OOPEC, the addition of varespladib to CYT387–MK2206-treated cells decreased LDs and increased apo-

ptosis (Fig. 6H–J). Collectively, these data indicate that treatment-induced autophagy provides lysophospholipids and free fatty acids to maintain cancer cell survival despite nutrient depletion.

## Discussion

It is now generally accepted that autophagy is cytoprotective in the setting of cancer therapies by enabling cancer cells to mitigate metabolic and therapeutic stresses, thereby ensuring survival (Amaravadi et al. 2011; Sehgal et al. 2015; Rebecca and Amaravadi 2016). To date, the therapeutic reflex to block autophagy is to add antimetastatic lysosomotropic inhibitors such as chloroquine. However, the clinical responses to these have been underwhelming (Goldberg et al. 2012; Shanware et al. 2013; Rosenfeld et al. 2014; Towers and Thorburn 2016). While the role of autophagy in tumor initiation and progression has been well-documented, little is known about how treatment-induced autophagy mediates cytoprotection and resistance.

Our results demonstrate that cancer cells, when acutely exposed to small molecule inhibitors, activate the autophagic process to ensure early and lasting metabolic adaptations designed to enhance survival in a nutrient-depleted environment. We first observed the maintenance of OXPHOS when glucose became limiting due to treatment. Likewise, the coordinate activation of AMPK signaling ensures protective redox homeostasis to mitigate increased ROS produced by OXPHOS. Finally, we demonstrated activation of autophagy-mediated membrane glycerophospholipid metabolism with subsequent fatty acid oxidation to generate energy. Accordingly, we found that therapy-induced autophagy purposefully harnesses core biological processes to secure tumor cell fitness and survival. Our experiments involving autophagy-incompetent *ATG5*<sup>-/-</sup> MEFs demonstrate that autophagy is required under conditions of nutrient depletion to generate LDs and maintain mitochondrial OCR and SRC. It is not coincidental that LD depletion by pharmacological PLA2 inhibition achieved similar results. This is consistent with the model that autophagic digestion of phospholipids, with subsequent hydrolysis within the autolysosome, provides LDs with a constant supply of lipids, which can then be trafficked to the mitochondria to maintain mitochondrial respiration. The subsequent release of these fatty acids from LDs to fuel  $\beta$ -oxidation may occur independently of lipophagy, as others have observed (Rambold et al. 2015). Additionally, another possible source of fatty acids and amino acids may come from extracellular lysophospholipids and proteins through macropinocytosis.

This study further addresses the wider question of how cancer cells survive despite the inhibition of mTOR (an evolutionarily conserved master regulator of cell metabolism, proliferation, growth, and survival) and AKT (a committed prosurvival kinase that positively regulates these same processes in both normal and cancer cells) (Manning and Cantley 2007; Laplante and Sabatini 2012).

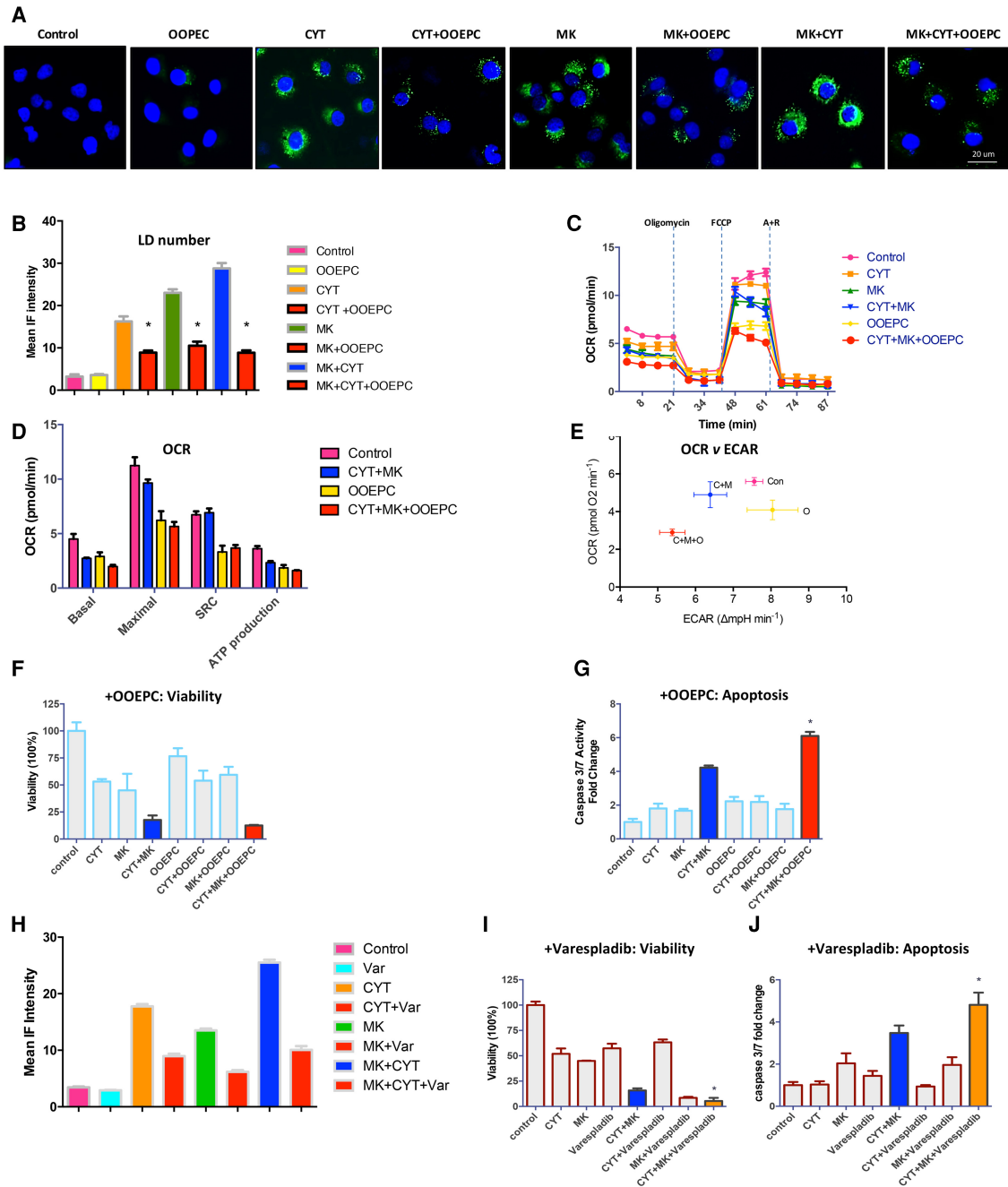


**Figure 6.** Hydrolysis of phospholipid supplies lysophospholipids and fatty acids for cancer cell survival. (A) ACHN cells were treated with control, OOEPC, CYT387, CYT387+OOEPC, MK2206, MK2206+OOEPC, CYT387+MK2206, and CYT387+MK2206+OOEPC for 24 h. Bodipy 493/503 (green) was added to visualize LDs. Representative images are shown.  $n = 3$  experiments. (B) Bar graphs quantify the number of LDs. Data are expressed as means  $\pm$  SEM. (\*)  $P < 0.0001$  for CYT387 versus CYT387+OOEPC, MK2206 versus MK2206+OOEPC, and CYT387+MK2206 versus CYT387+MK2206+OOEPC. (C,D) ACHN cells were treated with DMSO (control), OOEPC, CYT387, CYT387+OOEPC, MK2206, MK2206+OOEPC, CYT387+MK2206, and CYT387+MK2206+OOEPC for 24 h, and then OCR was determined using a XF-96 extracellular flux analyzer during sequential treatments with oligomycin, FCCP, and rotenone/anti-mycin (A+R). (D) Initial basal OCR, maximal OCR, SRC (the quantitative difference between maximal uncontrolled OCR and the initial basal OCR), and ATP production are depicted in the plot. Shown are OCR means  $\pm$  SD of experimental triplicates. For ease of viewing, only control, OOEPC, CYT387+MK2206, and CYT387+MK2206+OOEPC data are graphed. (E) OCR versus ECAR (means  $\pm$  SEM, experimental triplicates) after the addition of OOEPC to the CYT387–MK2206 combination. (Con) Control; (O) OOEPC; (C+M) CYT387+MK2206; (C+M+O) CYT387+MK2206+OOEPC. (F,G) Cell viability (F) and caspase 3/7 activity (G) with addition of OOEPC to CYT387, MK2206, and CYT387+MK2206.  $n = 3$ . Data are expressed as means  $\pm$  SD. (F)  $P = ns$  for CYT387+MK2206 versus CYT387+MK2206+OOEPC. (G) (\*)  $P < 0.001$  for CYT387+MK2206 versus CYT387+MK2206+OOEPC. (H) The effect of adding varespladib, a distinct PLA2 inhibitor, to CYT387, MK2206, and CYT387+MK2206 on LD numbers was evaluated with Bodipy staining (I,J) Cell viability (I) and caspase 3/7 activity (J) with the addition of varespladib, a distinct PLA2 inhibitor, to CYT387, MK2206, and CYT387+MK2206.  $n = 3$ . Data are expressed as means  $\pm$  SD. (I) (\*)  $P < 0.01$  for CYT387+MK2206 versus CYT387+MK2206+varespladib. (J) (\*)  $P < 0.1$  for CYT387+MK2206 versus CYT387+MK2206+varespladib.

Undoubtedly, the combination of attenuated proliferation signals, nutrient depletion, and metabolic competition for remaining nutrients kills many cells. Accordingly, our data demonstrate that glucose, which is tightly regulated by the PI3K–AKT–mTOR pathway at multiple steps, became limiting with treatment, with a resultant decrease in glycolysis (Engelman et al. 2006; Yecies and Manning 2011; Hu et al. 2016). However, the very same conditions that give rise to these nutrient-deprived microenvironments also induced autophagy. Consequently, the autophagic catabolism of membrane phospholipids provides a ready source of free fatty acids that maintains respiration in subpopulations of cancer cells, therefore enabling their survival in a low-glucose environment. The increase in fatty acid oxidation and OXPHOS requires redox homeostasis, and this is provided by the concomitant activation of AMPK, which increases NADPH, with a subsequent mitigation of ROS. Collectively, treatment-enforced metabolic reprogramming supports cancer cell fitness by providing fatty acids and NADPH to maximize survival.

Since the rate of autophagic release of fatty acids does not match the rate of mitochondrial consumption, these LDs serve a dual purpose: first, as a buffer to reduce lipotoxicity by storing lipid intermediates and, second, to transport these lipids to the mitochondria (Singh et al. 2009; Unger et al. 2010; Rambold et al. 2015). Consequently, these energy-strapped residual cancer cells increase fatty acid oxidation, as it is the most energetically efficient way to generate ATP. Long-lived cell types such as cardiac myocytes and memory T cells (Pearce et al. 2009; Chung et al. 2010) depend on fatty acid metabolism for survival, and we see this as yet another example of cancer cells hijacking normal physiological processes to their benefit.

Our screen identified several structurally different Janus family kinase inhibitors that inhibited mTORC1 and induced autophagic flux. While serendipitous, these findings are not unexpected, as small molecules inhibit several kinases and would directly and/or indirectly interdict the PI3K–AKT–mTOR pathway. To date, JAK inhibitors have been approved for and/or are undergoing late stage clinical trials in MPN, including the focus of this study, CYT387 (momelutinib) (Patel et al. 2016; Winton and Kota 2017). However, complete cytogenetic or molecular responses with JAK inhibitors have not been observed, with clinical benefit mainly resulting from improved performance status due to reduced cytokine levels rather than the elimination of cancer cells (Verstovsek et al. 2012; Vannucchi et al. 2015). Therefore, our finding that JAK inhibitors induce autophagy in both solid tumors and MPN cells, which then maintain residual disease potentially through the hydrolysis of phospholipids, may offer an explanation of why this class of inhibitors has not been able to eliminate drug-tolerant cancer cells and effect durable responses.

Combination therapies come with the increased risk of side effects. Notably, CYT387, MK2206, and varespladib have all been tested in human clinical trials, and their maximum tolerated doses have been established; the challenge ahead will be to develop optimal dosing schedules

that balance target engagement with side effects. However, most small molecule inhibitors have favorable toxicity profiles, and metabolic targets would be non-cross-resistant and predicted to have different side effects that are not overlapping. The experience with infectious diseases highlights the importance of combinations to achieve rapid efficient cancer suppression; i.e., HAART (highly active anti-retroviral therapy) in HIV, which is routinely used to produce durable clinical responses and prevent the emergence of resistance. Polytherapy in cancer is similarly justified and achievable, and here we outline the molecular roadmap for interdicting signaling and metabolism to override treatment-induced autophagy.

## Materials and methods

### Cell lines

ACHN, Caki-1, RCC10, SN12C, TK-10, U031, 786-0, UKE-1, SET-2, and HEL were used in this study and were obtained from American Type Culture Collection. *ATG5<sup>+/+</sup>* and *ATG5<sup>-/-</sup>* MEFs were a kind gift from Jay Debnath (University of California at San Francisco). Cell lines were maintained in Dulbecco's modified Eagle's medium (DMEM) supplemented with 10% fetal bovine serum (FBS) at 37°C in a 5% CO<sub>2</sub> incubator.

### Patient tumor ex vivo organotypic culture

Tumor tissue samples were collected at the time of surgical removal from consented patients and transported in IMEM + FBS + PS. The tissue was sliced into thin sections using a surgical knife. Sections were cultured on an organotypic insert (EMD, PICMORG50) for 24 h in IMEM, 10% FBS, 1% PS, and 50 µg/mL holo-transferrin with drug. A section of each tumor was immediately fixed in 10% buffered formalin to confirm tissue viability. After culture, treated tissue sections were fixed in 10% buffered formalin and embedded in paraffin. Paraffin-embedded tumors were evaluated for morphology (H&E) and immunofluorescent signaling.

### Cell viability and apoptosis analysis

Cell viability assays were performed by plating  $3 \times 10^3$  cells per well in 24-well plates in triplicate and treating them the following day with the indicated agents. The experiment was continued for 5 d, and then the cells were fixed using 4% formaldehyde and stained for 1 h with Syto60. Fluorescence was measured and quantified, and photographs were obtained using a LiCor Odyssey infrared imager. The effect of CYT387, MK2206, and the CYT387 +MK2206 combination on cell number was assessed as fold of DMSO-treated control cells. Experimental results are the average of at least three independent experiments. Apoptosis was determined using caspase 3/7 Glo assay kit (Promega) following the manufacturer's instructions. Briefly, 2000 cells per well were plated in 96-well plates and cultured for 72 h. Cells were treated with CYT387, MK2206, and the combination of CYT387 and MK2206 for 72 h, and then 100 µL of reagent was added to each well and incubated for 30 min at room temperature. Caspase 3/7 activity was measured using a luminometer. Luminescence values were normalized by cell numbers. The effect of CYT387, MK2206, and the CYT387+MK2206 combination on caspase 3/7 activation was assessed as fold of DMSO-treated control cells.

Lue et al.

*High-content imaging*

A seven-point dilution series of 116 small molecule inhibitors covering a 1000× concentration range was plated into three 384-well plates using the EP Motion automated dispensing system. Control wells with equal volumes of DMSO were included as negative controls. ACHN cells were grown, trypsinized, counted, and plated directly into warm drug plates using a Multidrop Combi dispenser. Plates were incubated for 72 h and subsequently imaged on an Olympus ScanR Platform at 10× magnification, performing four images per well in 384-well plates. Single-cell nuclear and cytoplasmic fluorescent intensities were calculated using the Olympus ScanR analysis software: The DAPI-positive region of each cell was used as a boundary to quantitate nucleus counts for analysis of cell growth, and integrated nuclear DNA staining intensity was used for cell cycle analysis. A 10-pixel extension of the nuclear region (and not including the nuclear region) was used to quantitate cytoplasmic signal of immunofluorescent staining of p62 protein and phosphorylation of S6. The mean signal intensity of each marker in all cells per well was used as the metric for cytoplasmic marker expression (average intensity of pS6 and p62). Unsupervised hierarchical clustering was used to identify compounds that produced similar pS6 and p62 dose response phenotypes after treatment.

*Western blotting*

Cells were plated in six-well dishes and treated the following day with the indicated agents. Treatments were for 24 h, after which cells were washed with ice-cold PBS and lysed with RIPA buffer (Sigma). Phosphatase inhibitor cocktail set II and protease inhibitor cocktail set III (EMD Millipore) were added at the time of lysis. Lysates were centrifuged at 15,000g for 10 min at 4°C. Protein concentrations were calculated based on a BCA assay-generated (Thermo Scientific) standard curve. Proteins were resolved using the NuPAGE Novex minigel system on 4%–12% Bis-Tris gels (Invitrogen). For Western blotting, equal amounts of cell lysates (15–20 µg of protein) were resolved with SDS-PAGE and transferred to membranes. The membrane was probed with primary antibodies, washed, and then incubated with corresponding fluorescent secondary antibodies and washed. The fluorescent signal was captured using a LI-COR Odyssey imaging system, and fluorescent intensity was quantified using the Odyssey software where indicated. The following antibodies were used for Western blots: p-S6 (S240/244), S6, LC3B, p-Akt(S473), p-Akt(T308), Akt, and cleaved caspase3 from Cell Signaling Technologies, and p-Stat3 (Y705), Stat3, and β-actin (AC15) from Abcam. Ki67 (Dako) and cleaved caspase 3 (Cell Signaling Technologies) were used for immunohistochemistry. MK2206 and CYT387 for in vitro and in vivo use were purchased from LC Labs and ChemieTek, respectively. BX795 and GDC0941 were purchased from Sigma.

*In vivo xenograft studies*

Six-week-old mice were used for human RCC xenografts. For both ACHN and SN12C cell lines,  $2 \times 10^6$  cells were diluted in 50 µL of PBS and 50 µL of Matrigel (BD Biosciences) and injected subcutaneously into the right and left flanks of each mouse.

Tumors were monitored until they reached an average size of 50–80 mm<sup>3</sup> (~2 wk), at which point treatments were begun. CYT387 (50 mg/kg per day) was administered by oral gavage 5 d per week. MK2206 (60 mg/kg per day) was administered by oral gavage 2–3 d per week. CYT387 was dissolved in NMP/Captisol (Cydex), and MK2206 was dissolved in Captisol (Cydex). Tumors and mouse weights were measured twice weekly. At least six to eight mice per treatment group were included. All mice were eu-

thanized using CO<sub>2</sub> inhalation followed by cervical dislocation per institutional guidelines at Oregon Health and Science University (OHSU). Experiments were approved by the Institutional Animal Care and Use Committee at OHSU.

*Phosphoproteomics screen and data analysis*

Enriched phosphopeptides were digested with trypsin and analyzed by MS following the published Cell Signaling Technology protocol (Rush et al. 2005; Moritz et al. 2010; Zhuang et al. 2013).

*MS data analysis*

MS raw files were analyzed via MaxQuant version 1.5.3.30 (Cox and Mann 2008), and MS/MS fragmentation spectra were searched using Andromeda (Cox et al. 2011) against human canonical and isoform sequences in Swiss-Prot (downloaded in September 2016 from <http://uniprot.org>; Apweiler et al. 2004). Quantitative phosphopeptide data were log<sub>10</sub> transformed, and missing data were imputed before applying quantile normalization as described previously (Drake et al. 2016). Quantitative data are in Supplemental Tables 3–8. Hierarchical clustering was performed with the Cluster 3.0 program (Eisen et al. 1998) using distance that was based on the Pearson correlation and applying pairwise average linkage analysis. Java Treeview was used to visualize clustering results (Saldanha 2004).

*KSEA*

KSEA was performed as described previously (Drake et al. 2012). Briefly, the phosphopeptides were rank-ordered by fold change, on average, between CYT387 treatment and control, and the enrichment score was calculated using the Kolmogorov-Smirnov statistic. Permutation analysis was conducted to calculate statistical significance. The normalized enrichment score was calculated by dividing the enrichment score by the average of the absolute values of all enrichment scores from the permutation analysis (Supplementary Tables 9, 10).

*DAVID pathway analysis*

To generate an appropriate list for use in DAVID (Huang da et al. 2009a, b), phosphopeptides were initially filtered with a false discovery rate of <0.20 (Supplementary Tables 11, 12). Phosphopeptides that were 1.5-fold enriched, on average, in either CYT387 treatment or no treatment were selected. Enrichment for a phosphopeptide was reversed if a functional annotation (Hornbeck et al. 2015) indicated protein activity inhibition. To reduce the complexity of this list, if multiple phosphopeptides mapped to a gene, then the most enriched phosphopeptide was selected. The only exception made was if a functional annotation existed for one or more of the phosphopeptides, in which case the most enriched annotated phosphopeptide would be selected. If multiple phosphopeptides mapped to the same gene and had enrichment values that fell into both CYT387 treatment and no treatment, then those phosphopeptides and the corresponding gene were removed from the list to be analyzed. We input into DAVID the genes in the CYT387 treatment enriched group (Supplemental Table 11) to examine KEGG pathways that were more active with CYT387 treatment (Supplemental Table 12).

*Phospho-receptor tyrosine kinase (phospho-RTK) array*

The human phospho-RTK array kit was purchased from Cell Signaling Technologies and screened according to the

manufacturer's protocol, with 150  $\mu$ g of protein being used for each experiment. Signal intensity was calculated using a LI-COR Odyssey imaging system, and fluorescent intensity was quantified using the Odyssey software where indicated.

#### *In vitro* $^{18}\text{F}$ -FDG uptake assays

$^{18}\text{F}$ -FDG was purchased from the radiopharmacy at University of California at San Francisco. SN12C or ACHN cells ( $5 \times 10^5$  cells) were plated and exposed to vehicle or drug for 24 and 48 h, whereupon the cells were incubated with 0.5  $\mu\text{Ci}$  of  $^{18}\text{F}$ -FDG for 1 h at 37°C. The  $^{18}\text{F}$ -FDG in the medium and the intracellular  $^{18}\text{F}$ -FDG were isolated and counted using a  $\gamma$  counter. The intracellular  $^{18}\text{F}$ -FDG was expressed as a percentage of the total activity added to cells normalized to the cell number.

#### *Metabolomic profiling of cancer cells*

Metabolomic data and single-reaction monitoring (SRM) transitions were analyzed as described previously (Camarda et al. 2016) and are in Supplemental Table 13. Briefly, 2 million cells were plated overnight and serum-starved for 2 h prior to harvesting, after which cells were washed twice with PBS, harvested by scraping, and flash-frozen. For nonpolar metabolomic analyses, flash-frozen cell pellets were extracted in 4 mL of 2:1:1 chloroform/methanol/PBS with internal standards: 10 nmol of dodecylglycerol and 10 nmol of pentadecanoic acid. Organic and aqueous layers were separated by centrifugation, and the organic layer was extracted. The aqueous layer was acidified with 0.1% formic acid followed by re-extraction with 2 mL of chloroform. The second organic layer was combined with the first extract and dried under nitrogen, after which lipids were resuspended in 120  $\mu\text{L}$  of chloroform. A 10- $\mu\text{L}$  aliquot was then analyzed by both SRM-based LC-MS/MS or untargeted LC-MS. For polar metabolomic analyses, frozen cell pellets were extracted in 180  $\mu\text{L}$  of 40:40:20 acetonitrile/methanol/water with internal standard: 1 nmol of d3 N15-serine. Following vortexing and bath sonication, the polar metabolite fraction (supernatant) was isolated by centrifugation. A 20- $\mu\text{L}$  aliquot was then analyzed by both SRM-based LC-MS/MS or untargeted LC-MS. For the SRM transitions where we monitored the transition of parent masses to the loss of the head group (e.g., loss of phosphocholine from PC), we ascertained the acyl chain specificities from previously described procedures (Long et al. 2011). For phospholipids such as PCs and PEs, we ascertained fatty acid acyl chain composition from phospholipids using a mobile phase containing both ammonium hydroxide and formic acid and monitored the fatty acid fragmentations from  $[\text{M} + \text{H} - \text{HCO}_2\text{H}] m/z$  at 40 V collision energy in negative ionization mode. For other phospholipids, such as PAs and PIs, we monitored the fatty acid fragmentations from  $[\text{MH}] m/z$  at 40 V collision energy in negative ionization mode in mobile phase containing just ammonium hydroxide. For the lipids that we measured in this study, the designated acyl chains represent the primary fatty acids that were on the lipid backbone. However, this method is less sensitive than monitoring the loss of head group from the phospholipid, and we therefore used SRM transitions for many phospholipids where we monitored for loss of head groups (e.g., PCs, PEs, PSs, PAs, and PIs).

Relative levels of metabolites were quantified by integrating the area under the curve for each metabolite, normalizing to internal standard values, and then normalizing to the average values of the control groups (Louie et al. 2016).

#### *ROS detection*

ROS levels were measured with CellRox deep red (Molecular Probes). Cells were plated in a 96-well clear-bottomed cell culture

plate with black sides. After adhering for 24 h, cells were treated with 2  $\mu\text{M}$  CYT387, 10  $\mu\text{M}$  MK2206, and 2  $\mu\text{M}$  CYT387 + 10  $\mu\text{M}$  MK2206. The complete medium + drug was removed after 24 h and replaced with 5  $\mu\text{M}$  CellRox deep red in medium. Cells were incubated for 30 min at 37°C and then washed with PBS. Fluorescence signal was detected using a Biotek Cytation 5 plate reader. Data were analyzed using Prism software.

#### *Cellular respiration*

OCR and ECAR were carried out in a XF96 Seahorse analyzer (Agilent/Seahorse Bioscience). Cells were plated in the wells of 96-well plates ( $8 \times 10^3$  cells per well; XF96 plates; Seahorse Bioscience) and incubated overnight at 37°C. The next day, cells were treated with the indicated drugs for 24 h, and then the medium was changed to XF assay medium and loaded with glucose, oligomycin, and 2-DG, respectively, per the manufacturer's recommendation. Similarly, Mito Fuel Flex tests were performed on an XFe96 Bioanalyzer. At 24 h after treatment, all assays were performed according to the manufacturer's protocols.

#### *Immunohistochemistry*

Immunostaining was performed following deparaffinization and rehydration of slides. Antigen retrieval was performed in a pressure cooker using citrate buffer (pH 6.0) for 4 min. Nonspecific binding was blocked using Vector mouse IgG blocking serum for 30 min at room temperature. Samples were incubated at room temperature with rabbit monoclonal antibodies pS6 (Cell Signaling Technologies, 5364), cleaved caspase 3 (Cell Signaling Technologies, 9661), and Ki67 (Dako, M7240). Slides were developed with Vector Immpress rabbit IgG (Vector Laboratories, MP7401) and Vector Immpress mouse IgG (Vector Laboratories, MP7400) for 30 min at room temperature. Chromogenic detection was performed using Vector Impact DAB (Vector Laboratories, SK4105) for 3 min. Slides were counterstained with hematoxylin. A 3DHistech MIDI scanner (Perkin Elmer) was used to capture whole-slide digital images with a 20 $\times$  objective. Images were converted to MRXS files, and computer graphic analysis was completed using inForm 1.4.0 advanced image analysis software (Perkin Elmer).

#### *Morphological and immunofluorescence evaluation*

H&E slides of formalin-fixed paraffin-embedded tissue was used to assess the morphological integrity of tumor samples. Once integrity was confirmed, immunofluorescent analysis was performed for p-S6 (1:500; Cell Signaling Technologies), p-AKT (1:200; Cell Signaling Technologies), and LC3B (1:250; Cell Signaling Technologies). Four-micron sections were cut, deparaffinized, and rehydrated. Antigen retrieval was performed using citrate for 4 min in a pressure cooker. Slides were blocked using 2.5% normal goat serum for 30 min and then incubated in primary antibody for 1 h followed by secondary antibody mouse anti-rabbit Alexa 488 (1:1000; Molecular Probes) for 30 min. Slides were rinsed in PBS, air dried, and coverslipped using Dako mounting medium with DAPI.

#### *Lipid and mitochondrial staining*

Cells were grown on coverslips and then treated with drug for 24 h. Cells were fixed in 4% paraformaldehyde for 15 min and rinsed with PBS. Cells were washed with a 1% saponin solution for 15 min at room temperature and then washed several times in PBS to remove detergent. Cells were then incubated in Bodipy



Lue et al.

(ThermoFisher, D3922) at a final concentration of 1  $\mu$ M for 10 min. Bodipy was removed, and slides were rinsed with PBS, air-dried, and mounted on slides using Dako mounting medium with DAPI.

To detect mitochondrial levels in treated cells, cells were grown on coverslips for 24 h. Mitotracker orange (ThermoFisher, M7511) was diluted in medium with drug at a final concentration of 1 M and incubated overnight. The medium was removed, and cells were fixed with 4% paraformaldehyde for 15 min. Cells were rinsed twice for 5 min in PBS and incubated in cold acetone for 10 min at  $-20^{\circ}\text{C}$ . Acetone was removed, and cells were washed in PBS, air-dried, and mounted on slides with Dako mounting medium with DAPI.

A 3DHitech MIDI scanner (Perkin Elmer) was used to capture whole-slide digital images with a 20 $\times$  objective. Images were converted to MRXS files, and computer graphic analysis was completed using inForm 1.4.0 advanced image analysis software (Perkin Elmer).

#### MDC staining

Slides were plated on coverslips and allowed to adhere for 24 h. After adherence, cells were treated with drug for 24 h. After treatment, the drug was removed, and cells were washed once in PBS. Cells were labeled with a 50 mM concentration of auto-fluorescent marker MDC (Sigma) in PBS for 10 min at  $37^{\circ}\text{C}$ . Cells were fixed in 4% formaldehyde for 15 min at room temperature. Cells were washed twice in PBS for 5 min and mounted on slides using Dako mounting medium with DAPI. Coverslips were sealed with clear nail polish and imaged with a 3DHitech MIDI scanner as described above.

#### Statistical analysis

Mouse tumor size was analyzed by two-way ANOVA with time and drug as factors using Graphpad Prism. Mouse weight during treatment was analyzed by repeated measures of two-way ANOVA with time and drug as factors. A  $P$ -value of  $<0.05$  was considered statistically significant. For immunohistochemistry,  $P$ -values were calculated using one-way ANOVA with Bonferroni's multiple comparison test ( $P < 0.05$  [\*],  $P < 0.01$  [\*\*], and  $P < 0.001$  [\*\*\*]). Metabolite fold changes were computed and visualized in Python script using the Openpyxl package (for importing Excel files) and the Matplotlib package (for visualizing fold changes).

#### Acknowledgments

We thank Andrew Thorburn, Katherine Ellwood-Yen, and Gary Thomas for helpful discussion; Jay Debnath for the *ATG5*<sup>+/+</sup> and *ATG5*<sup>-/-</sup> MEFs; Ernest Frankel, Emek Demir, and Ozgun Babur for computational advice; Steve Kazmierczak for biochemical analysis; Angela Fleischman for clinical input; Mandy Burns and Ashley Sager for administrative support; Moya Costello and Justin Lallo for artwork; the Histopathology Shared Resource for pathology support; the Massively Parallel Sequencing Shared Resource and Integrated Genomics Shared Resource for genomics support; the Bioanalytical Shared Resource/Pharmacokinetic Core for eicosanoid profiling studies; and the Oregon Translational Research and Development Institute (OTRADI) for high-throughput drug screening support. This study was supported by National Institutes of Health (NIH) grants R01 CA169172, P30 CA069533, and P30 CA069533 13S5 through the Oregon Health and Science University-Knight Cancer Institute, the

Hope Foundation (SWOG [Southwest Oncology Group]), the Oregon Translational Research and Development Institute (OTRADI), West Coast Metabolomics Core (WCMC) Pilot, and Kure It Cancer Research (G.V.T.). L.C. is supported by the National Institute of General Medical Sciences of the NIH under award number T32 GM008339. J.M.D. is supported by the Department of Defense (DOD) Prostate Cancer Research Program (W81XWH-15-1-0236), Prostate Cancer Foundation Young Investigator Award, and a grant from the New Jersey Health Foundation. V. B.O. is a European Research Council Investigator (LipidArrays) and Royal Society Wolfson Research Merit Award Holder. M.J. E. was supported by the Prostate Cancer Foundation Young Investigator Award, the DOD Prostate Cancer Research Program (W81XWH-15-1-0552), and the National Cancer Institute (R00CA172695 and R01CA176671). C.T. was supported by the DOD Prostate Cancer Research Program (W81XWH-16-1-0435).

#### References

- Amaravadi RK, Lippincott-Schwartz J, Yin XM, Weiss WA, Takebe N, Timmer W, DiPaola RS, Lotze MT, White E. 2011. Principles and current strategies for targeting autophagy for cancer treatment. *Clin Cancer Res* **17**: 654–666.
- Apweiler R, Bairoch A, Wu CH, Barker WC, Boeckmann B, Ferro S, Gasteiger E, Huang H, Lopez R, Magrane M, et al. 2004. UniProt: the Universal Protein knowledgebase. *Nucleic Acids Res* **32**: D115–D119.
- Cabodevilla AG, Sanchez-Caballero L, Nintou E, Boiadjeva VG, Picatoste F, Gubern A, Claro E. 2013. Cell survival during complete nutrient deprivation depends on lipid droplet-fueled  $\beta$ -oxidation of fatty acids. *J Biol Chem* **288**: 27777–27788.
- Camarda R, Zhou AY, Kohnz RA, Balakrishnan S, Mahieu C, Anderton B, Eyob H, Kajimura S, Tward A, Krings G, et al. 2016. Inhibition of fatty acid oxidation as a therapy for MYC-overexpressing triple-negative breast cancer. *Nat Med* **22**: 427–432.
- Cecconi F, Levine B. 2008. The role of autophagy in mammalian development: cell makeover rather than cell death. *Dev Cell* **15**: 344–357.
- Christofk HR, Vander Heiden MG, Wu N, Asara JM, Cantley LC. 2008. Pyruvate kinase M2 is a phosphotyrosine-binding protein. *Nature* **452**: 181–186.
- Chung S, Arrell DK, Faustino RS, Terzic A, Dzeja PP. 2010. Glycolytic network restructuring integral to the energetics of embryonic stem cell cardiac differentiation. *J Mol Cell Cardiol* **48**: 725–734.
- Cox J, Mann M. 2008. MaxQuant enables high peptide identification rates, individualized p.p.b.-range mass accuracies and proteome-wide protein quantification. *Nat Biotechnol* **26**: 1367–1372.
- Cox J, Neuhauser N, Michalski A, Scheltema RA, Olsen JV, Mann M. 2011. Andromeda: a peptide search engine integrated into the MaxQuant environment. *J Proteome Res* **10**: 1794–1805.
- Dangelmaier C, Manne BK, Liverani E, Jin J, Bray P, Kunapuli SP. 2014. PDK1 selectively phosphorylates Thr(308) on Akt and contributes to human platelet functional responses. *Thromb Haemost* **111**: 508–517.
- Debnath J. 2008. Detachment-induced autophagy during anoikis and lumen formation in epithelial acini. *Autophagy* **4**: 351–353.
- Dibble CC, Asara JM, Manning BD. 2009. Characterization of Rictor phosphorylation sites reveals direct regulation of mTOR complex 2 by S6K1. *Mol Cell Biol* **29**: 5657–5670.

- Drake JM, Graham NA, Stoyanova T, Sedghi A, Goldstein AS, Cai H, Smith DA, Zhang H, Komisopoulou E, Huang J, et al. 2012. Oncogene-specific activation of tyrosine kinase networks during prostate cancer progression. *Proc Natl Acad Sci* **109**: 1643–1648.
- Drake JM, Paull EO, Graham NA, Lee JK, Smith BA, Titz B, Stoyanova T, Faltermeier CM, Uzunangelov V, Carlin DE, et al. 2016. Phosphoproteome integration reveals patient-specific networks in prostate cancer. *Cell* **166**: 1041–1054.
- Duvel K, Yecies JL, Menon S, Raman P, Lipovsky AI, Souza AL, Triantafellow E, Ma Q, Gorski R, Cleaver S, et al. 2010. Activation of a metabolic gene regulatory network downstream of mTOR complex 1. *Mol Cell* **39**: 171–183.
- Eaton S. 2002. Control of mitochondrial  $\beta$ -oxidation flux. *Prog Lipid Res* **41**: 197–239.
- Eisen MB, Spellman PT, Brown PO, Botstein D. 1998. Cluster analysis and display of genome-wide expression patterns. *Proc Natl Acad Sci* **95**: 14863–14868.
- Engelman JA, Luo J, Cantley LC. 2006. The evolution of phosphatidylinositol 3-kinases as regulators of growth and metabolism. *Nat Rev Genet* **7**: 606–619.
- Finn PF, Dice JF. 2006. Proteolytic and lipolytic responses to starvation. *Nutrition* **22**: 830–844.
- Fruman DA, Rommel C. 2014. PI3K and cancer: lessons, challenges and opportunities. *Nat Rev Drug Discov* **13**: 140–156.
- Fung C, Lock R, Gao S, Salas E, Debnath J. 2008. Induction of autophagy during extracellular matrix detachment promotes cell survival. *Mol Biol Cell* **19**: 797–806.
- Galluzzi L, Pietrocola F, Bravo-San Pedro JM, Amaravadi RK, Baehrecke EH, Cecconi F, Codogno P, Debnath J, Gewirtz DA, Karantza V, et al. 2015. Autophagy in malignant transformation and cancer progression. *EMBO J* **34**: 856–880.
- Goldberg SB, Supko JG, Neal JW, Muzikansky A, Digumarthy S, Fidiias P, Temel JS, Heist RS, Shaw AT, McCarthy PO, et al. 2012. A phase I study of erlotinib and hydroxychloroquine in advanced non-small-cell lung cancer. *J Thorac Oncol* **7**: 1602–1608.
- Gwinn DM, Shackelford DB, Egan DF, Mihaylova MM, Mery A, Vasquez DS, Turk BE, Shaw RJ. 2008. AMPK phosphorylation of raptor mediates a metabolic checkpoint. *Mol Cell* **30**: 214–226.
- Hornbeck PV, Zhang B, Murray B, Kornhauser JM, Latham V, Skrzypek E. 2015. PhosphoSitePlus, 2014: mutations, PTMs and recalibrations. *Nucleic Acids Res* **43**: D512–D520.
- Hu H, Juvekar A, Lyssiotis CA, Lien EC, Albeck JG, Oh D, Varma G, Hung YP, Ullas S, Lauring J, et al. 2016. Phosphoinositide 3-kinase regulates glycolysis through mobilization of aldolase from the actin cytoskeleton. *Cell* **164**: 433–446.
- Huang da W, Sherman BT, Lempicki RA. 2009a. Bioinformatics enrichment tools: paths toward the comprehensive functional analysis of large gene lists. *Nucleic Acids Res* **37**: 1–13.
- Huang da W, Sherman BT, Lempicki RA. 2009b. Systematic and integrative analysis of large gene lists using DAVID bioinformatics resources. *Nat Protoc* **4**: 44–57.
- Inoki K, Zhu T, Guan KL. 2003. TSC2 mediates cellular energy response to control cell growth and survival. *Cell* **115**: 577–590.
- Jeon SM, Chandel NS, Hay N. 2012. AMPK regulates NADPH homeostasis to promote tumour cell survival during energy stress. *Nature* **485**: 661–665.
- Joachim J, Jiang M, McKnight NC, Howell M, Tooze SA. 2015. High-throughput screening approaches to identify regulators of mammalian autophagy. *Methods* **75**: 96–104.
- Julien LA, Carriere A, Moreau J, Roux PP. 2010. mTORC1-activated S6K1 phosphorylates Rictor on threonine 1135 and regulates mTORC2 signaling. *Mol Cell Biol* **30**: 908–921.
- Kerner J, Hoppel C. 2000. Fatty acid import into mitochondria. *Biochim Biophys Acta* **1486**: 1–17.
- Kim LC, Cook RS, Chen J. 2017. mTORC1 and mTORC2 in cancer and the tumor microenvironment. *Oncogene* **36**: 2191–2201.
- Klionsky DJ, Abdelmohsen K, Abe A, Abedin MJ, Abeliovich H, Acevedo Arozena A, Adachi H, Adams CM, Adams PD, Adeli K, et al. 2016. Guidelines for the use and interpretation of assays for monitoring autophagy (3rd edition). *Autophagy* **12**: 1–222.
- Laplanche M, Sabatini DM. 2012. mTOR signaling in growth control and disease. *Cell* **149**: 274–293.
- Leonard JT, Rowley JS, Eide CA, Traer E, Hayes-Lattin B, Loriaux M, Spurgeon SE, Druker BJ, Tyner JW, Chang BH. 2016. Targeting BCL-2 and ABL/LYN in Philadelphia chromosome-positive acute lymphoblastic leukemia. *Sci Transl Med* **8**: 354ra114.
- Long JZ, Cisar JS, Milliken D, Niessen S, Wang C, Trauger SA, Siuzdak G, Cravatt BF. 2011. Metabolomics annotates ABHD3 as a physiologic regulator of medium-chain phospholipids. *Nat Chem Biol* **7**: 763–765.
- Louie SM, Grossman EA, Crawford LA, Ding L, Camarda R, Huffman TR, Miyamoto DK, Goga A, Weerapana E, Nomura DK. 2016. GSTP1 is a driver of triple-negative breast cancer cell metabolism and pathogenicity. *Cell Chem Biol* **23**: 567–578.
- Manning BD, Cantley LC. 2007. AKT/PKB signaling: navigating downstream. *Cell* **129**: 1261–1274.
- Manning BD, Tee AR, Logsdon MN, Blenis J, Cantley LC. 2002. Identification of the tuberous sclerosis complex-2 tumor suppressor gene product tuberlin as a target of the phosphoinositide 3-kinase/akt pathway. *Mol Cell* **10**: 151–162.
- Maxson JE, Gotlib J, Pollyea DA, Fleischman AG, Agarwal A, Eide CA, Bottomly D, Wilmot B, McWeeney SK, Tognon CE, et al. 2013. Oncogenic CSF3R mutations in chronic neutrophilic leukemia and atypical CML. *N Engl J Med* **368**: 1781–1790.
- Maxson JE, Abel ML, Wang J, Deng X, Reckel S, Luty SB, Sun H, Gorenstein J, Hughes SB, Bottomly D, et al. 2016. Identification and characterization of tyrosine kinase nonreceptor 2 mutations in leukemia through integration of kinase inhibitor screening and genomic analysis. *Cancer Res* **76**: 127–138.
- Mizushima N, Yamamoto A, Hatano M, Kobayashi Y, Kabeya Y, Suzuki K, Tokuhiya T, Ohsumi Y, Yoshimori T. 2001. Dissection of autophagosome formation using Apg5-deficient mouse embryonic stem cells. *J Cell Biol* **152**: 657–668.
- Moritz A, Li Y, Guo A, Villen J, Wang Y, MacNeill J, Kornhauser J, Sprott K, Zhou J, Possemato A, et al. 2010. Akt-RSK-S6 kinase signaling networks activated by oncogenic receptor tyrosine kinases. *Sci Signal* **3**: ra64.
- Murakami M, Taketomi Y, Miki Y, Sato H, Hirabayashi T, Yamamoto K. 2011. Recent progress in phospholipase A(2) research: from cells to animals to humans. *Prog Lipid Res* **50**: 152–192.
- Patel AB, Vellore NA, Deininger MW. 2016. New strategies in myeloproliferative neoplasms: the evolving genetic and therapeutic landscape. *Clin Cancer Res* **22**: 1037–1047.
- Pearce EL, Walsh MC, Cejas PJ, Harms GM, Shen H, Wang LS, Jones RG, Choi Y. 2009. Enhancing CD8 T-cell memory by modulating fatty acid metabolism. *Nature* **460**: 103–107.
- Rambold AS, Cohen S, Lippincott-Schwartz J. 2015. Fatty acid trafficking in starved cells: regulation by lipid droplet lipolysis, autophagy, mitochondrial fusion dynamics. *Dev Cell* **32**: 678–692.

Lue et al.

- Rebecca VW, Amaravadi RK. 2016. Emerging strategies to effectively target autophagy in cancer. *Oncogene* **35**: 1–11.
- Rosenfeld MR, Ye X, Supko JG, Desideri S, Grossman SA, Brem S, Mikkelsen T, Wang D, Chang YC, Hu J, et al. 2014. A phase I/II trial of hydroxychloroquine in conjunction with radiation therapy and concurrent and adjuvant temozolomide in patients with newly diagnosed glioblastoma multiforme. *Autophagy* **10**: 1359–1368.
- Rosenson RS, Hislop C, Elliott M, Stasiv Y, Goulder M, Waters D. 2010. Effects of varespladib methyl on biomarkers and major cardiovascular events in acute coronary syndrome patients. *J Am Coll Cardiol* **56**: 1079–1088.
- Roux PP, Ballif BA, Anjum R, Gygi SP, Blenis J. 2004. Tumor-promoting phorbol esters and activated Ras inactivate the tuberous sclerosis tumor suppressor complex via p90 ribosomal S6 kinase. *Proc Natl Acad Sci* **101**: 13489–13494.
- Rush J, Moritz A, Lee KA, Guo A, Goss VL, Spek EJ, Zhang H, Zha XM, Polakiewicz RD, Comb MJ. 2005. Immunoaffinity profiling of tyrosine phosphorylation in cancer cells. *Nat Biotechnol* **23**: 94–101.
- Saldanha AJ. 2004. Java Treeview—extensible visualization of microarray data. *Bioinformatics* **20**: 3246–3248.
- Sarker D, Ang JE, Baird R, Kristeleit R, Shah K, Moreno V, Clarke PA, Raynaud FI, Levy G, Ware JA, et al. 2015. First-in-human phase I study of pictilisib (GDC-0941), a potent pan-class I phosphatidylinositol-3-kinase (PI3K) inhibitor, in patients with advanced solid tumors. *Clin Cancer Res* **21**: 77–86.
- Sehgal AR, Konig H, Johnson DE, Tang D, Amaravadi RK, Boyiadzis M, Lotze MT. 2015. You eat what you are: autophagy inhibition as a therapeutic strategy in leukemia. *Leukemia* **29**: 517–525.
- Shanware NP, Bray K, Abraham RT. 2013. The PI3K, metabolic, autophagy networks: interactive partners in cellular health and disease. *Annu Rev Pharmacol Toxicol* **53**: 89–106.
- Singh R, Kaushik S, Wang Y, Xiang Y, Novak I, Komatsu M, Tanaka K, Cuervo AM, Czaja MJ. 2009. Autophagy regulates lipid metabolism. *Nature* **458**: 1131–1135.
- Slatyer DA, Aldrovandi M, O'Connor A, Allen SM, Brasher CJ, Murphy RC, Mecklemann S, Ravi S, Darley-Usmar V, O'Donnell VB. 2016. Mapping the human platelet lipidome reveals cytosolic phospholipase A2 as a regulator of mitochondrial bioenergetics during activation. *Cell Metab* **23**: 930–944.
- Sztralny C, Kimmel AR. 2014. Perilipins: lipid droplet coat proteins adapted for tissue-specific energy storage and utilization, and lipid cytoprotection. *Biochimie* **96**: 96–101.
- Tanida I, Minematsu-Ikeguchi N, Ueno T, Kominami E. 2005. Lysosomal turnover, but not a cellular level, of endogenous LC3 is a marker for autophagy. *Autophagy* **1**: 84–91.
- Thiam AR, Farese RV Jr, Walther TC. 2013. The biophysics and cell biology of lipid droplets. *Nat Rev Mol Cell Biol* **14**: 775–786.
- Toska E, Baselga J. 2016. Pharmacology in the era of targeted therapies: the case of PI3K inhibitors. *Clin Cancer Res* **22**: 2099–2101.
- Towers CG, Thorburn A. 2016. Therapeutic targeting of autophagy. *EBioMedicine* **14**: 15–23.
- Turcotte S, Chan DA, Sutphin PD, Hay MP, Denny WA, Giaccia AJ. 2008. A molecule targeting VHL-deficient renal cell carcinoma that induces autophagy. *Cancer Cell* **14**: 90–102.
- Unger RH, Clark GO, Scherer PE, Orci L. 2010. Lipid homeostasis, lipotoxicity and the metabolic syndrome. *Biochim Biophys Acta* **1801**: 209–214.
- Vannucchi AM, Kiladjan JJ, Griesshammer M, Masszi T, Durrant S, Passamonti F, Harrison CN, Pane F, Zachee P, Mesa R, et al. 2015. Ruxolitinib versus standard therapy for the treatment of polycythemia vera. *N Engl J Med* **372**: 426–435.
- Verstovsek S, Mesa RA, Gotlib J, Levy RS, Gupta V, DiPersio JF, Catalano JV, Deininger M, Miller C, Silver RT, et al. 2012. A double-blind, placebo-controlled trial of ruxolitinib for myelofibrosis. *N Engl J Med* **366**: 799–807.
- Winton EF, Kota V. 2017. Momelotinib in myelofibrosis: JAK1/2 inhibitor with a role in treating and understanding the anemia. *Future Oncol* **13**: 395–407.
- Yap TA, Yan L, Patnaik A, Fearen I, Olmos D, Papadopoulos K, Baird RD, Delgado L, Taylor A, Lupinacci L, et al. 2011. First-in-man clinical trial of the oral pan-AKT inhibitor MK-2206 in patients with advanced solid tumors. *J Clin Oncol* **29**: 4688–4695.
- Yecies JL, Manning BD. 2011. Transcriptional control of cellular metabolism by mTOR signaling. *Cancer Res* **71**: 2815–2820.
- Zhuang G, Yu K, Jiang Z, Chung A, Yao J, Ha C, Toy K, Soriano R, Haley B, Blackwood E, et al. 2013. Phosphoproteomic analysis implicates the mTORC2–FoxO1 axis in VEGF signaling and feedback activation of receptor tyrosine kinases. *Sci Signal* **6**: ra25.



## Metabolic reprogramming ensures cancer cell survival despite oncogenic signaling blockade

Hui-wen Lue, Jennifer Podolak, Kevin Kolahi, et al.

*Genes Dev.* published online November 14, 2017  
Access the most recent version at doi:[10.1101/gad.305292.117](https://doi.org/10.1101/gad.305292.117)

---

**Supplemental Material** <http://genesdev.cshlp.org/content/suppl/2017/11/14/gad.305292.117.DC1>

Published online November 14, 2017 in advance of the full issue.

**Creative Commons License**

This article is distributed exclusively by Cold Spring Harbor Laboratory Press for the first six months after the full-issue publication date (see <http://genesdev.cshlp.org/site/misc/terms.xhtml>). After six months, it is available under a Creative Commons License (Attribution-NonCommercial 4.0 International), as described at <http://creativecommons.org/licenses/by-nc/4.0/>.

**Email Alerting Service**

Receive free email alerts when new articles cite this article - sign up in the box at the top right corner of the article or [click here](#).

---



## Video Article

# Phosphopeptide Enrichment Coupled with Label-free Quantitative Mass Spectrometry to Investigate the Phosphoproteome in Prostate Cancer

Larry C. Cheng<sup>\*1,2</sup>, Zhen Li<sup>\*3</sup>, Thomas G. Graeber<sup>4</sup>, Nicholas A. Graham<sup>5</sup>, Justin M. Drake<sup>1,2,3,6,7</sup><sup>1</sup>Graduate Program in Cellular and Molecular Pharmacology, School of Graduate Studies, Rutgers University, The State University of New Jersey<sup>2</sup>Graduate Program in Quantitative Biomedicine, School of Graduate Studies, Rutgers University, The State University of New Jersey<sup>3</sup>Department of Medicine, Division of Medical Oncology, Rutgers Robert Wood Johnson Medical School<sup>4</sup>Crump Institute for Molecular Imaging, Department of Molecular and Medical Pharmacology, Jonsson Comprehensive Cancer Center, UCLA Metabolomics Center, and California NanoSystems Institute, David Geffen School of Medicine, University of California, Los Angeles<sup>5</sup>Mork Family Department of Chemical Engineering and Materials Science, University of Southern California<sup>6</sup>Pharmacology, Rutgers Robert Wood Johnson Medical School<sup>7</sup>Cancer Metabolism and Growth Program, Rutgers Cancer Institute of New Jersey

\* These authors contributed equally

Correspondence to: Justin M. Drake at [justin.drake@cinj.rutgers.edu](mailto:justin.drake@cinj.rutgers.edu)URL: <https://www.jove.com/video/57996>DOI: [doi:10.3791/57996](https://doi.org/10.3791/57996)

Keywords: Cancer Research, Issue 138, Prostate cancer, mass spectrometry, proteomics, phosphoproteomics, phosphorylation, kinases, cell signaling

Date Published: 8/2/2018

Citation: Cheng, L.C., Li, Z., Graeber, T.G., Graham, N.A., Drake, J.M. Phosphopeptide Enrichment Coupled with Label-free Quantitative Mass Spectrometry to Investigate the Phosphoproteome in Prostate Cancer. *J. Vis. Exp.* (138), e57996, doi:10.3791/57996 (2018).

## Abstract

Phosphoproteomics involves the large-scale study of phosphorylated proteins. Protein phosphorylation is a critical step in many signal transduction pathways and is tightly regulated by kinases and phosphatases. Therefore, characterizing the phosphoproteome may provide insights into identifying novel targets and biomarkers for oncologic therapy. Mass spectrometry provides a way to globally detect and quantify thousands of unique phosphorylation events. However, phosphopeptides are much less abundant than non-phosphopeptides, making biochemical analysis more challenging. To overcome this limitation, methods to enrich phosphopeptides prior to the mass spectrometry analysis are required. We describe a procedure to extract and digest proteins from tissue to yield peptides, followed by an enrichment for phosphotyrosine (pY) and phosphoserine/threonine (pST) peptides using an antibody-based and/or titanium dioxide (TiO<sub>2</sub>)-based enrichment method. After the sample preparation and mass spectrometry, we subsequently identify and quantify phosphopeptides using liquid chromatography-mass spectrometry and analysis software.

## Video Link

The video component of this article can be found at <https://www.jove.com/video/57996/>

## Introduction

An estimated 165,000 new cases and approximately 29,000 deaths will occur in 2018 due to prostate cancer, representing the most common cancer and second leading cause of cancer-related death in men in the United States<sup>1</sup>. Early stages of prostate cancer are treatable with resection or radiation therapy of organ-confined disease, where the ten-year recurrence rate is between 20% and 40% for patients who undergo prostatectomy and between 30% and 50% for patients who receive radiation therapy<sup>2</sup>. Because prostate cancer relies on androgen signaling for growth, surgical and chemical castration therapies are also employed for high-risk patients. However, relapse occurs when the cancer no longer responds to androgen deprivation therapy as evidenced by biochemical recurrence, where the prostate-specific antigen in serum rises again. At this point in the progression, metastases are often detected as well. This advanced stage, called metastatic castration-resistant prostate cancer, represents the lethal form of the disease where the prognosis is a median survival time of less than two years<sup>3</sup>. Few treatment options are available in late-stage disease, including second-generation antiandrogens such as enzalutamide and abiraterone, as well as taxane-based chemotherapy like docetaxel. Despite available treatments, the disease often progresses. Therefore, the discovery and development of novel treatment modalities are necessary to improve the care of prostate cancer patients with advanced disease.

Mass spectrometry (MS)-based approaches provide a global analysis of the proteome through the detection of hundreds to thousands of peptide analytes<sup>4</sup>. In particular, discovery proteomics, also known as data-dependent acquisition (DDA), can yield the identification and quantitation of thousands of peptides<sup>4,5</sup>. MS-based discovery proteomics can be further delineated into top-down proteomics, where intact proteins are characterized, and bottom-up (also known as shotgun) proteomics, where peptides are analyzed to characterize proteins<sup>5</sup>. Thus, in shotgun proteomics, a proteolysis step takes place in the sample preparation preceding the MS analysis to cleave proteins into peptides. At the end, a database search is performed to map the peptides back to the proteins for identification. Label-free as well as several isotope-labeling [e.g., stable isotope labeling by amino acids in cell culture (SILAC)] methods can be used to quantitatively compare peptides between samples<sup>6,7</sup>.

While isotope labeling techniques are the gold standard, label-free methods have demonstrated similar quantification accuracies<sup>8,9</sup> and have comparable tradeoffs between sensitivity and specificity<sup>10</sup>. Label-free quantitation provides greater coverage and permits comparisons between many more samples, whereas label-based methods are limited by cost and multiplexing capacities<sup>6,7,8</sup>.

Furthermore, shotgun MS can be also used to interrogate post-translational modifications (PTMs) such as phosphorylation<sup>11</sup>. Due to the lower stoichiometric nature of phosphopeptides compared to total peptides, several methods are employed to enrich for phosphopeptides, including antibody-based immunoprecipitation of phosphotyrosine (pY) peptides, titanium dioxide (TiO<sub>2</sub>), and immobilized metal affinity chromatography (IMAC)<sup>5,12</sup>. Because protein phosphorylation is a key step in many cell signaling pathways, shotgun phosphoproteomics allows researchers to investigate cell signaling changes in different cancers, including breast<sup>13</sup>, prostate<sup>14</sup>, renal<sup>15</sup>, and ovarian<sup>16,17</sup> to better understand cancer biology and to identify potential new targets for therapy.

This label-free shotgun phosphoproteomic method was built and refined based on previous work by the Graeber group<sup>18,19,20</sup>. This protocol begins by describing the extraction and digestion of proteins and phosphoproteins from tissue into peptides. We then detail the enrichment of pY peptides using specific phosphotyrosine antibodies and TiO<sub>2</sub>. We also describe the enrichment of phosphoserine/threonine (pST) peptides using strong cation exchange (SCX) followed by TiO<sub>2</sub>. This protocol concludes with the submission of samples to an MS facility and the use of MS analysis software to identify and quantify phosphopeptides and their corresponding phosphoproteins. The application of this protocol can extend beyond prostate cancer into other cancers and fields outside of oncology.

## Protocol

Experiments using xenograft tumors were approved by the Rutgers University Institutional Animal Care and Use Committee as set forth under the guidelines of the National Institutes of Health.

### 1. Protein Extraction

1. Prepare lysis buffer (**Table 1**). (The volume depends on the number of samples to be harvested.) For *in vitro* cell samples, proceed to step 1.2. For tumor tissue, proceed to step 1.3.
2. **Harvesting cells**
  1. Collect the cells in a 50 mL conical tube and spin them at 700 x g for 5 min at 4 °C. Discard the supernatant and keep the pellet on ice. Repeat this step for all dishes to collect the cells into one pellet. (Typically, about 5 nearly confluent 15-cm dishes of cells are needed for 5 mg of protein, but this may be dependent on the cell line and needs to be determined empirically by each investigator.)
  2. Wash the pellet with 30 mL of chilled phosphate-buffered saline (PBS) and spin at 700 x g for 5 min at 4 °C before aspirating the PBS. Add 1.5 mL of lysis buffer per 5 mg of protein used to the cell pellet. Pipet up and down a couple of times. Skip to step 1.4.
3. **Harvesting tissues**
  1. Weigh the tumor and add 2 mL of ice-cold lysis buffer for every 100 mg of tissue in a culture test tube. (Typically, 50 to 150 mg of tissue wet weight is needed.)
4. Homogenize the lysate using a hand-held or benchtop homogenizer (pulse 2x for 15 s.) Clean the homogenizer before the first sample and between samples by using 10% bleach, 70% ethanol, and deionized water in succession.
5. To reduce and alkylate, heat the homogenized samples at 95 °C for 5 min. Then cool them on ice for 15 min. On ice, sonicate the lysate 3x (*i.e.*, pulse for 30 s with 60 s pauses between pulses). The sample should not be viscous or clumpy at this point. Heat the lysate at 95 °C for 5 min<sup>21</sup>.
6. Centrifuge the lysate in the same sonication tube using a swing bucket rotor at 3,500 x g at 15 °C for 15 min. Collect the supernatant and discard the pellet.
7. Determine the protein concentration by performing a Bradford assay<sup>22</sup>. If necessary, dilute the lysate to 5 mg/mL with a lysis buffer. Store it at -20 °C.  
Note: The experiment can be paused here. Freeze the samples at -80 °C and continue at a later date.

### 2. Lysate Digestion

1. Dilute the sample 12-fold by using 100 mM Tris (pH = 8.5) to reduce the amount of guanidinium. Dilute all samples to the same volume to minimize the effects of unequal digestion. Save 12.5 µg of the undigested lysate to confirm it on a Coomassie-stained gel<sup>23</sup>.
2. For 5 mg of protein, add 10 µg of Lysyl Endopeptidase (Lys-C) and incubate it at room temperature for 5 - 6 h. Adjust pH to 8.0 by adding 1 M untitrated Tris (pH ~11).
3. Prepare 1 mg/mL of L-1-tosylamido-2-phenylethyl chloromethyl ketone (TPCK)-treated trypsin in 1 mM HCl (with 20 mM CaCl<sub>2</sub>). Add the trypsin at a 1:100 trypsin:protein ratio and incubate it at 37 °C for 3 h.
4. Add the same amount of fresh trypsin as in step 2.3. Incubate it at 37 °C overnight.
5. Save 12.5 µg of the digested lysate to confirm the complete digestion on a Coomassie-stained gel<sup>23</sup>.

### 3. Reverse Phase Extraction

1. Record the lysate volume. Filter the sample by using a 15 mL 10 kDa cutoff filter. Centrifuge the sample at 3,500 x g using the swing bucket rotor (or 3,500 x g in a fixed angle rotor) at 15 °C until the retentate volume is less than 250 µL (this takes approximately 45 - 60 min). Collect the flow-through and discard the retentate.  
Note: The experiment can be paused here. Freeze the samples at -80 °C and continue at a later date.
2. To acidify the sample, add approximately 20 µL of 5% trifluoroacetic acid (TFA) per mL of lysate. Mix them well and measure the sample pH by using pH strips. Adjust pH to 2.5 using 5% TFA.

3. Connect the shorter end of a C-18 column to a vacuum manifold. Set the vacuum between 17 and 34 kPa (or according to the manufacturer's instructions). Using **glass** pipettes, wet the column with 3 mL of 100% acetonitrile (ACN). Do not let the column dry.
4. Using **glass** pipettes, equilibrate the column with 6 mL of 0.1% TFA applied as 2x 3 mL. Load the acidified sample into the column. Do not add more than 3 mL at a time. Adjust the vacuum to target about 1 to 2 drops per second.
5. Using **glass** pipettes, wash the column with 9 mL of 0.1% TFA applied as 3x 3 mL. Elute the column with 2 mL of 40% ACN, 0.1% TFA. Collect two 2 mL fractions into **glass** culture tubes. Discard the column.
6. Cover the eluate tubes with parafilm and punch 3 - 5 holes on the cover using a 20G needle. Freeze the eluate on dry ice for at least 30 min until it is completely solid.
7. Lyophilize the fractions overnight. On the following day, make sure the samples are completely dry before stopping the lyophilizer. Store the tubes in a 50 mL conical tube with delicate wipes at -80 °C.  
Note: The experiment can be paused here.

#### 4. Immunoprecipitation and Enrichment of pY Peptides<sup>24</sup>

1. Resuspend the lyophilized powder with 0.5 mL of ice-cold immunoprecipitation (IP) binding buffer in each fraction. Pool the fractions by transferring the 0.5 mL resuspension volume from the second fraction to the first fraction and save the pipette tip. Vigorously vortex (instead of pipetting up and down) to make sure the sample is completely dissolved before transferring it to a 3.6 mL screw cap cryotube.
2. As in step 4.1., rinse the lyophilization tubes with another 0.5 mL of IP binding buffer (**Table 1**) in each tube. Transfer the solution to the 3.6 mL screw cap tube using the same pipette tip to minimize any sample loss. Repeat the rinse 1x more, making the final resuspension volume 2 mL (for 5 mg of protein). Measure the sample pH to make sure it is approximately 7.4. If it is too acidic, iteratively add 10 µL of 1M Tris (untitrated, pH ~11). If it is too basic, iteratively add 10 µL of dilute HCl (1:25 or 1:100).
3. **Pre-wash the pY beads (for 5 mg of starting lysate)**
  1. 25 µg of 4G10 antibody and 12.5 µg of 27B10.4 antibody are needed per sample. After using a p200 pipette with a cut tip to transfer the antibodies into separate microcentrifuge tubes, wash the antibodies with 450 µL of ice-cold IP binding buffer 2x. Centrifuge them at 100 x g for 1 min at 4 °C and aspirate out the supernatant.
  2. Resuspend the beads to a stock concentration of 0.5 mg/mL using IP binding buffer. (Do not vortex the beads.) After aliquoting the necessary slurry (50 µL of 4G10 antibody slurry and 25 µL 27B10.4 antibody slurry per sample) into a single tube, spin down the stock centrifuge tubes at 200 x g for 1 min at 4 °C. Wash the sidewalls with supernatant before returning the beads to storage in the refrigerator.
4. Add pre-washed pY beads to the resuspended sample solution in the screw cap cryotubes. Incubate them at 4 °C on an end-over-end rotator overnight.
5. Place the screw cap cryotubes in a 50 mL centrifuge tube lined with a delicate wipe. Spin down the beads at 100 x g for 1 min. Save the supernatant, which will be used to enrich for pST peptides. (The enrichment for pST begins at step 7 and can be performed in parallel to the pY peptide processing).
6. Resuspend the beads with 300 µL of IP binding buffer. Transfer them to a 2 mL microcentrifuge tube and spin them down at 100 x g for 1 min at 4 °C.
7. Rinse the incubation tube 3x with 200 µL of IP binding buffer. Transfer the contents to the same Microcentrifuge tube each time. Then spin them down.
8. Wash the beads in the microcentrifuge tube 3x with 500 µL of IP binding buffer and spin them down at 100 x g for 1 min. Then wash the beads 4x with 450 µL of 25 mM NH<sub>4</sub>HCO<sub>3</sub>, pH 7.5, and spin them down at 100 x g for 1 min. Use a fresh 25 mM NH<sub>4</sub>HCO<sub>3</sub> solution from powder every time.
9. Centrifuge the beads at 1,500 x g for 1 min. Use a gel-loading tip to remove the supernatant completely by dipping the tip of the gel-loading tip slightly below the beads' surface.
10. Add 4x the bead volume of 0.1% TFA to the beads (*i.e.*, add 300 µL of 0.1% TFA for 75 µg of pY bead slurry). Mix them well and incubate the mixture in a thermomixer at 1,000 rpm for 15 min at 37 °C.
11. Transfer the resuspension to a 0.2 µm spin filter. Quickly spin down the elution tube and transfer the residual volume to the same spin filter using a P10 pipet. Spin down the spin filter at 850 x g for 1 min. Transfer the elution to a **low protein-binding** microcentrifuge tube. Vacuum concentrate the eluate to dryness overnight at 40 °C and with a heat time of 300 min.  
Note: The experiment can be paused here. Freeze the samples at -80 °C and continue at a later date.

#### 5. Titanium Dioxide Enrichment<sup>25</sup> of pY Peptides

1. Resuspend the dried down phosphopeptides in 200 µL of 50% ACN, 0.1% TFA. Vortex and centrifuge them at 10,000 x g for 30 s. Repeat this 1x to resuspend them well.
2. Preparing the TiO<sub>2</sub> beads contained in tips that have a capacity for 200 µL samples.
  1. Gently tap on the small tip-side of the tip to move the material to that end. Rinse the tip by adding 200 µL of 100% ACN, followed by inverting the tip and flicking the small end to move the liquid towards the cap.
  2. Using a razor blade, cut the small tip of the tip and place it over a **low protein-binding tube**. (Avoid using polystyrene tubes as the TiO<sub>2</sub> will stick to the sides of the tube.) Remove the cap and insert a micropipette to plunge out the remaining ACN. Repeat the wash with 200 µL of 100% ACN. The TiO<sub>2</sub> beads are now located in the low protein-binding tube for the following steps.
  3. Precondition TiO<sub>2</sub> with 500 µL of 100% ACN 2x. Pipet it to mix the beads with the solvent. Centrifuge them at 100 x g for 1 min.
  4. Condition TiO<sub>2</sub> with 500 µL of 0.2 M sodium phosphate buffer (pH ~7) 2x. Wash the beads with 300 µL of equilibration buffer 3x. Because TiO<sub>2</sub> is very dense, the beads will settle quickly.
3. Add 400 µL of 50% ACN, 0.1% TFA into the low protein-binding tube, followed by adding 84 µL of lactic acid. Transfer the resuspended phosphopeptides into the low protein-binding tube and incubate them for 1 h at room temperature using an end-over-end rotator.
4. Centrifuge the beads at 100 x g for 1 min to pellet them. Wash them with 300 µL of equilibration buffer (**Table 1**) 2x and spin them down at 100 x g for 1 min.

- Rinse the beads with 300  $\mu$ L of rinsing buffer 2x. Transfer them to a 0.2  $\mu$ m spin filter. Spin them at 1,500 x g for 1 min.
- Transfer the filter unit to a clean 1.5 mL low protein-binding tube. Elute the contents 2x with 200  $\mu$ L of 0.9%  $\text{NH}_3$  in  $\text{H}_2\text{O}$ . Measure the pH with pH strips, which should be between 10 and 11. Vacuum concentrate the eluate to dryness overnight to evaporate the ammonia.

## 6. Desalting pY Peptides for MS Analyses

- Reconstitute the phosphopeptides with 15  $\mu$ L of 0.1% TFA by vortexing and centrifuging them at 10,000 x g for 30 s to resuspend them. Repeat this 1x to resuspend them well. Do not pipette up and down.
- Clean the sample using a C-18 tip with a binding capacity of 5  $\mu$ g and follow the manufacturer's protocol.
- Completely dry the elution volume by vacuum concentration. This takes 1 - 2 h. Resuspend the dried phosphopeptides in 12.5  $\mu$ L of mass spectrometry solution (see **Table 1**) (or as recommended by the researcher's MS proteomics core facility). Vortex and briefly spin the solution down at 10,000 x g for 30 s. Repeat this 2x to resuspend them well. The samples are ready for submission to a mass spectrometry facility (step 11).

Note: The following steps below are related to pST peptide enrichment only.

## 7. Reverse Phase Extraction of pST Peptides

- Measure the peptide concentration of the supernatant acquired from step 4.6 by performing a peptide assay. A sufficient amount for pST mass spectrometry is 2.5 mg.
- Adjust pH to 3.5 with 5% TFA.
- Connect the shorter end of a C-18 column to a vacuum manifold. Set the vacuum between 17 and 34 kPa (or according to the manufacturer's instructions). Wet the column with 3 mL of 100% ACN. Do not let the column dry.
- Equilibrate the column with 6 mL of 0.1% TFA applied as 2x 3 mL. Load the acidified sample into the column. Do not add more than 3 mL at a time. Adjust the vacuum to target about 1 - 2 drops per second.
- Wash the column with 9 mL of 0.1% TFA applied as 3x 3 mL. Elute the column with 2 mL of 40% ACN, 0.1% TFA. Collect two 2 mL fractions into glass culture tubes. Discard the column.
- Cover the eluate tubes with parafilm and punch 3 - 5 holes on the cover using a 20G needle. Freeze the eluate on dry ice for at least 30 min until it is completely solid.
- Lyophilize the selected fractions overnight. On the following day, make sure the samples are completely dry before stopping the lyophilizer. Store the tubes in a 50 mL conical tube with delicate wipes at -80  $^{\circ}\text{C}$ .

Note: The experiment can be paused here.

## 8. Strong Cation Exchange (SCX) of pST Peptides

- Resuspend the lyophilized peptides in 2 mL of Buffer A (**Table 1**). Pool the fractions for each sample. (The solution will be cloudy.)
- Prepare the vacuum manifold. Connect an SCX column to a 3 mL syringe with the plunger removed. Set the vacuum between 17 and 34 kPa (or according to the manufacturer's instructions).
- Condition the SCX column with 4 mL of ACN, followed by 4 mL of Buffer A.
- Load the 2 mL of the sample from step 8.1 and collect the eluate immediately. Load 3 mL of A:B (80.9:19.1) buffer and collect the eluate. Pool the eluates of each sample and aliquot them into 2 mL low protein-binding tubes.
- Vacuum concentrate all samples until approximately 30% of the volume remains. (This step takes approximately 2 - 4 h.) Pool the aliquots into 1 low protein-binding tube for each sample.
- Connect the shorter end of a C-18 column to a vacuum manifold. Set the vacuum between 17 and 34 kPa (or according to the manufacturer's instructions). Wet the column with 3 mL of 100% ACN 2x. Do **not** let the column dry.
- Equilibrate the column with 3 mL of 0.1% TFA 2x. Load the sample into the column. Do not add more than 3 mL at a time. Adjust the vacuum to target about 1 - 2 drops per second.
- Wash the column with 3 mL of 0.1% TFA 2x. Elute the column with 4 mL of 50% ACN, 0.1% TFA.

## 9. Titanium Dioxide Enrichment of pST Peptides

- Preparing the  $\text{TiO}_2$  beads contained in tips that have a capacity for 200  $\mu$ L samples**
  - Gently tap on the small tip side of the tip to move the beads to that end. Remove the cap and pour the beads into a polypropylene 15 mL conical tube.
  - Rinse the tip by adding 200  $\mu$ L of 100% ACN, inverting the tip a couple times and flicking the small end to move the liquid towards the cap. Using a razor blade, cut the small tip of the tip and place it over the polypropylene 15 mL conical tube. Remove the cap and insert a micropipette to plunge out the remaining ACN. Repeat the wash with 200  $\mu$ L of 100% ACN. The  $\text{TiO}_2$  beads are now located in the 15 mL conical tube for the following steps.
  - Precondition  $\text{TiO}_2$  with 500  $\mu$ L of 100% ACN 2x. Pipet it to mix the beads with the solvent. Centrifuge them at 100 x g for 1 min.
  - Condition  $\text{TiO}_2$  with 500  $\mu$ L of 0.2 M sodium phosphate buffer (pH ~7) twice. Wash the beads with 300  $\mu$ L of equilibration buffer 3x.
- Transfer the eluted phosphopeptides into the polypropylene 15 mL conical tube. Add 560  $\mu$ L of lactic acid and incubate it for 1 h at room temperature using an end-over-end rotator.
- Centrifuge the mixture at 100 x g for 1 min to pellet the beads. Wash them with 300  $\mu$ L of equilibration buffer (**Table 1**) 3x. Spin them down at 100 x g for 1 min.
- Rinse the beads with 300  $\mu$ L of rinsing buffer 2x. Transfer them to a 0.2  $\mu$ m spin filter. Spin them down at 1,500 x g for 1 min.
- Transfer the filter unit to a clean 1.5 mL low protein-binding tube. Elute the contents 2x with 200  $\mu$ L of 0.9%  $\text{NH}_3$  in  $\text{H}_2\text{O}$ . Let the solution sit on the phosphopeptides for 2 min before eluting them. Measure the pH, which should be between 10 and 11.



- Vacuum concentrate the eluate to dryness overnight to evaporate the ammonia.

## 10. Desalting pST Peptides for MS Analyses

- Gently tap on the small tip-side of the tip to move the material to that end. Rinse the tip by adding 200  $\mu$ L of 100% ACN, followed by inverting the tip and flicking the small end to move the liquid towards the cap.
- Using a razor blade, cut the small tip of the tip and place it over a polypropylene 15 mL conical tube. Remove the cap and insert a micropipette to plunge out the remaining ACN. Repeat the wash with 200  $\mu$ L of 100% ACN. The TiO<sub>2</sub> beads are now located in the polypropylene 15 mL conical tube for the following steps.
- Clean the sample using a C-18 tip with a binding capacity of 100  $\mu$ g. (Follow the manufacturer's instructions.)
- Completely dry the elution volume by vacuum concentration. This takes 1 - 2 h.
- Resuspend the dried phosphopeptides in 12.5  $\mu$ L of mass spectrometry solution (or as recommended by the researcher's MS proteomics core facility). Vortex and centrifuge them at 10,000  $\times$  g for 30 s. Repeat 2x to resuspend them well. (Do not pipette up and down.)

## 11. Mass Spectrometry Analysis

- Submit the samples to the MS proteomics core facility to perform liquid chromatography-tandem MS (LC-MS/MS) using their recommended settings. Example settings are as follows (see **Table 2** for the summary):
  - Load 5  $\mu$ L of the samples onto a trap column (2 cm long  $\times$  75  $\mu$ m diameter) and wash them with 0.1% TFA for 5 min with a flow rate of 5  $\mu$ L/min.
  - Bring the trap in line with a nano analytical column (20 cm  $\times$  75  $\mu$ m) with a flow rate of 300 nL/min.
  - The segmented linear gradients (a percentage of 0.16% formic acid, 80% ACN in 0.2% formic acid) are different between pY and pST samples:
    - For the pY samples, elute them using a gradient of 4 - 15% in 5 min, 15 - 50% in 40 min, and 50 - 90% in 5 min.
    - For pST samples, elute them using a gradient of 4 - 15% in 30 min, 15 - 25% in 40 min, 25 - 50% in 44 min, and 50 - 90% in 11 min.
  - Acquire MS data in data-dependent acquisition mode with a cyclic series of a full scan with a resolution of 120,000 followed by MS/MS (HCD, relative collision energy of 27%) of the 20 most intense ions and a dynamic exclusion duration of 20 s.
- After the MS run completion, import the MS raw files into an MS analysis software program to identify and quantify phosphopeptides. (MaxQuant software<sup>8,26,27</sup> was used in this experiment. Unless specified in **Table 3**, the default settings were used.)

## Representative Results

This protocol describes in detail a method for protein extraction and digestion followed by phosphopeptide enrichment and subsequent MS analysis (**Figure 1**). The compositions of all the buffers and solutions that are used in this protocol are listed in **Table 1**. The sequential use of Lys-C and trypsin provides an efficient digestion. A Coomassie-stained gel of pre-digested lysate confirms the presence of proteins, while staining of post-digested lysate confirms the complete digestion (**Figure 2A**). For a complete digestion, no bands should appear above 15 kDa, except the 30 kDa and 23.3 kDa bands for Lys-C and trypsin, respectively. The addition of Lys-C also reduces the number of missed cleavages (**Figure 2B**). Because pY peptides represent only 2% of the phosphoproteome<sup>28</sup>, immunoprecipitation of the pY peptides using a pY-specific antibody is the first step of pY peptide enrichment. The resulting supernatant becomes the input for pST peptide enrichment. The pY immunoprecipitation effectively separates pY peptides from pST peptides where on average 85% of the phosphopeptides identified from the pY preparation are pY (**Figure 3A**) and over 99% of the phosphopeptides identified from the pST preparation are pST (**Figure 3B**). Titanium dioxide is used to enrich for phosphopeptides in both preparations. The expected percentage of peptides in the MS-ready preparation that are phosphorylated is between 30 - 50% (**Figure 4A**). The variability in the phosphopeptide enrichment percentage may be greater in the pY preparation as a result of there being many fewer pY peptides than pST peptides. In terms of phosphopeptide species, the majority of the phosphopeptides detected have a single or double phosphoryl group (**Figure 4B**).

After performing mass spectrometry, the MS raw files are loaded into an MS analysis software. The parameter settings used in the experiment are listed in **Table 3** but will vary from software to software and may vary from version to version. The parameters that are not listed were left as default, including an FDR cutoff of 1% for peptide-spectrum matching (PSM) with a minimum Andromeda score of 40 for the identification of modified peptides<sup>27</sup>. Setting a localization probability cutoff of greater than 0.75 filters out approximately 5% of the pY peptides and 15% and 34% of the pS and pT peptides, respectively (**Figure 5A**). After applying these filters, the expected number of phosphopeptide identifications at the end of the MS analysis is approximately 300 pY peptides (for 5 mg of the starting protein) and about 7,500 pS peptides and 640 pT peptides (for 2.5 mg of the starting peptide amount) from the respective enrichment preparations (**Figure 5B**). The number of replicates and the variability of the phosphopeptide signal intensity determines adequate powering for statistical comparisons. In four separate experiments with groups containing either biological duplicates or triplicates, the percent coefficients of variation (%CV) for detected phosphopeptides were calculated. Distributions of lower variability (e.g., pST groups 1 - 5 in **Figure 5C**) indicate that the sample collection, preparation, and mass spectrometry runs were consistent. On the other hand, distributions of higher variability (e.g., pST group 6 in **Figure 5C**) indicates noisier data that would require larger fold-changes to detect significant differences in downstream differential analyses.

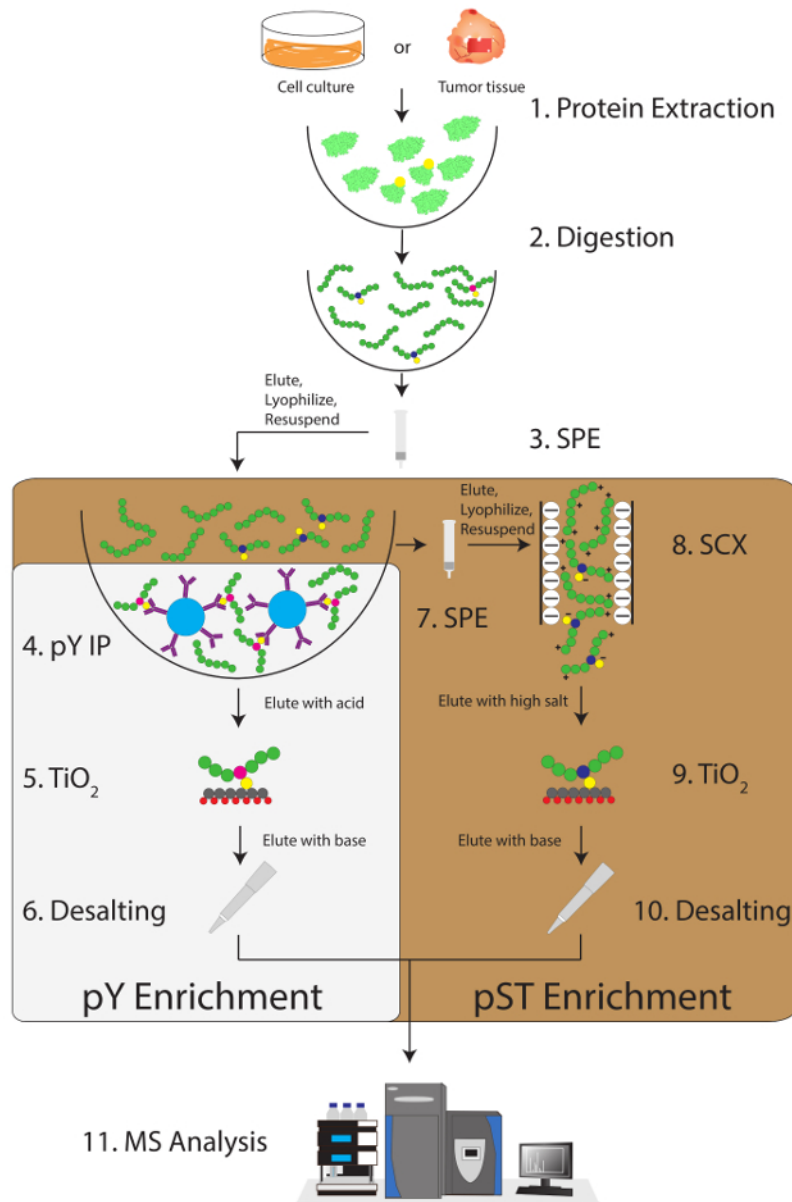


**Figure 1: Workflow diagram.** Proteins from samples are extracted and digested. Peptides are extracted by solid phase extraction (SPE), and phosphotyrosine (pY) peptides are immunoprecipitated. In parallel, the phosphoserine/threonine (pST) peptides are enriched from the supernatant in the pY immunoprecipitation step. Strong cation exchange (SCX) is performed on the supernatant to remove highly charged peptides to reduce the ion suppression<sup>12</sup>. Both preparations undergo phosphopeptide enrichment via titanium dioxide (TiO<sub>2</sub>). After sample cleanup, liquid chromatography-tandem mass spectrometry (LC-MS/MS) is performed to measure the phosphopeptide abundance. The raw data is then loaded into an MS analysis software to identify phosphopeptides. [Please click here to view a larger version of this figure.](#)

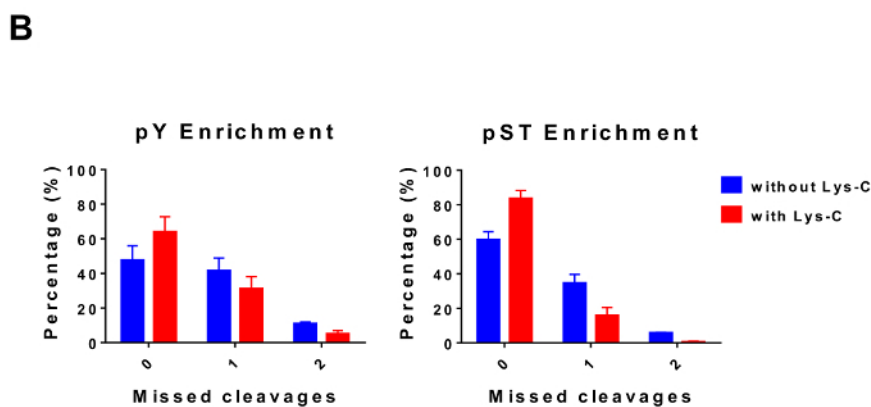
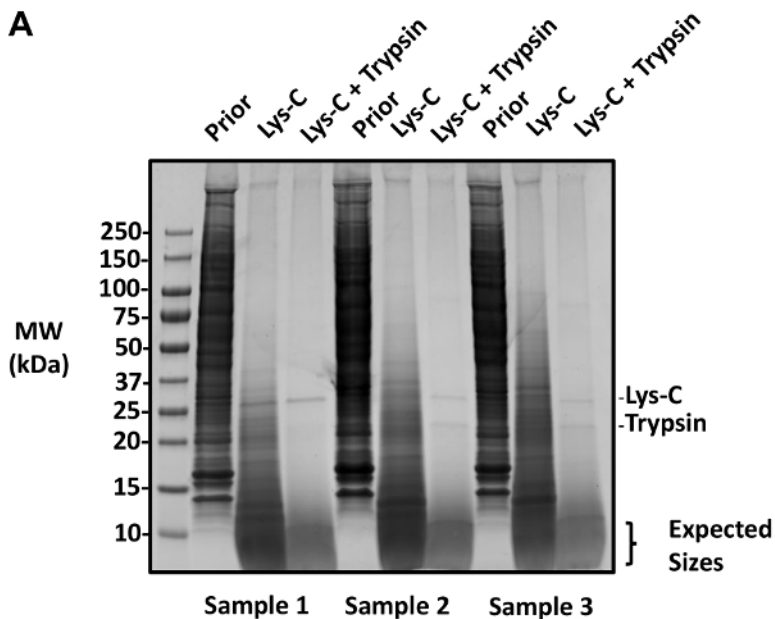
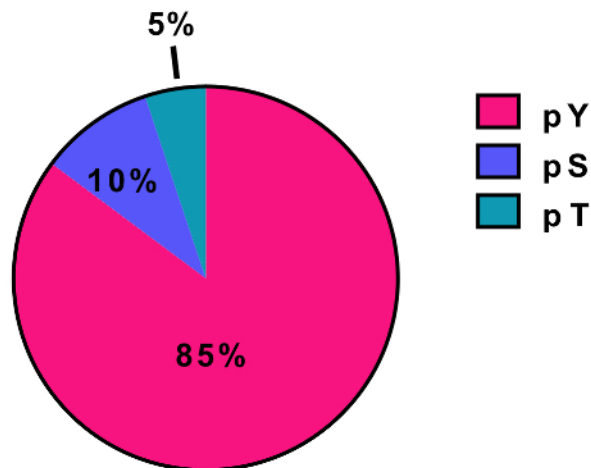


**Figure 2: Evaluation of digestion.** (A) Three samples with 12.5  $\mu$ g of lysate pre-digestion, post-Lys-C digestion, and post-trypsin digestion are shown. A Coomassie gel-stain test shows a clean digestion after sequential use of Lys-C and trypsin. The molecular weight (MW) size markers are in kilodaltons (kDa). (B) A reduction in missed cleavages is observed after Lys-C was added to the protocol. The percentage of phosphopeptides without missed cleavages increased from 48% to 64% and from 60% to 84% on average for pY and pST enrichment preparations, respectively. The graphs summarize the data obtained from two experiments performed without Lys-C and five experiments performed with Lys-C. The error bars are standard deviations representing 38 pY and 38 pST samples from 2 separate experiments (without Lys-C) and 62 pY and 60 pST samples from 5 separate experiments (with Lys-C). [Please click here to view a larger version of this figure.](#)

### A After pY Enrichment



### B After pST Enrichment

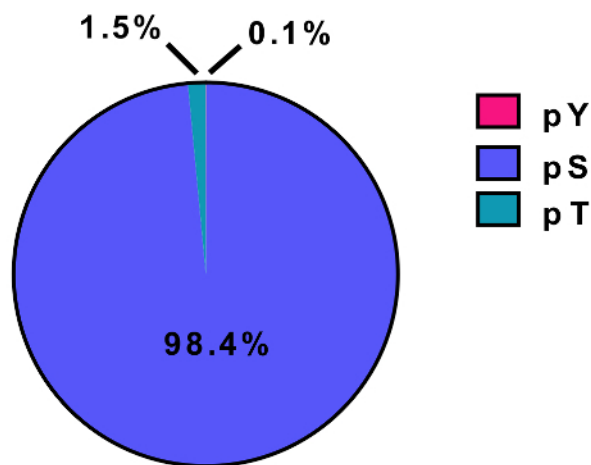


**Figure 3: Enrichment of pY and pST phosphopeptides.** These panels show the percentages of pSTY phosphopeptides from either (A) the pY or (B) the pST enrichment preparations. The pY enrichment by pY immunoprecipitation and titanium dioxide resulted in 85% phosphopeptides being for pY peptides, while only 0.1% of the phosphopeptides in the pST enrichment are pY. These values were drawn from examining the Phospho (STY)Sites.txt file of one representative experiment after filtering out contaminants, reverse sequences, and phosphopeptides with localization probabilities less than 0.75. [Please click here to view a larger version of this figure.](#)

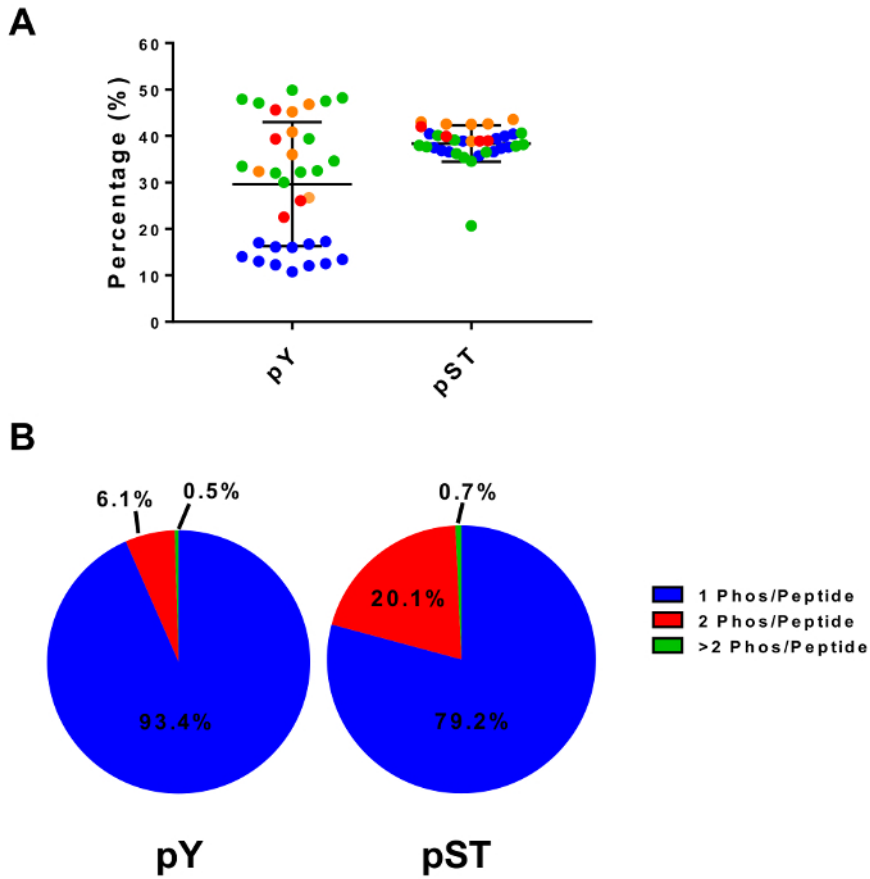


**Figure 4: Phosphopeptide enrichment with titanium dioxide.** (A) The percentage of detected phosphopeptides (relative to total peptides) from samples in four separate experiments is shown. (B) This panel shows the average composition of mono-, double-, and multi-phosphorylated peptides in four separate experiments. The error bars in panel A are standard deviations. [Please click here to view a larger version of this figure.](#)

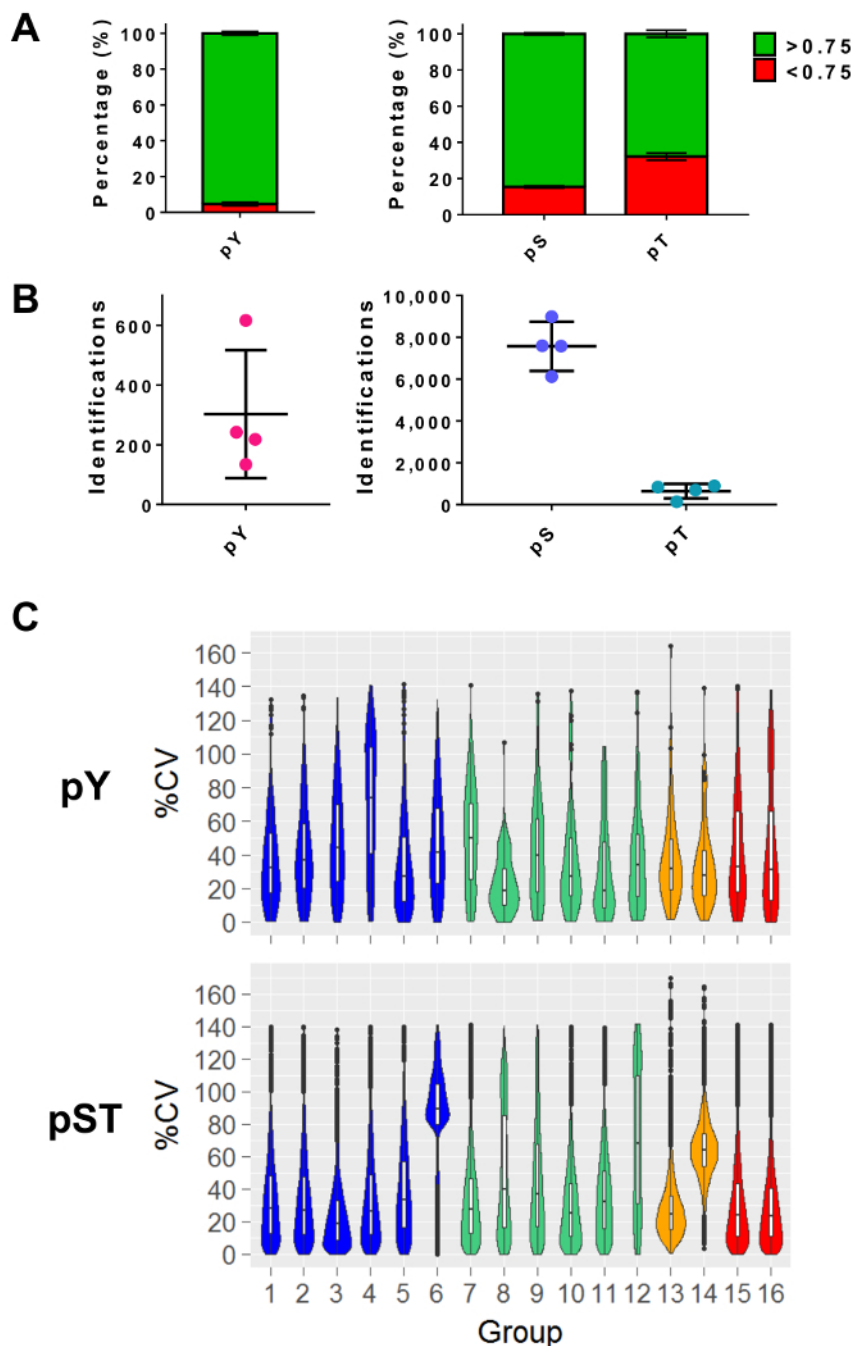


**Figure 5: Expected phosphoresidue identifications.** (A) This panel shows the phosphorylation localization probabilities of IDs from pY enrichment (left) and pST enrichment (right). The mean percentage of IDs that meet the > 0.75 probability cutoff is 93%, 75%, and 52% for pY, pS, and pT, respectively. (B) The mean number of IDs with a >0.75 localization probability is 300 for pY, 7,500 for pS, and 640 for pT. (C) This panel shows violin plots of the percent coefficient of variation (%CV) of the phosphopeptides. An evaluation of %CV was only performed if a signal intensity value was detected in each biological replicate or triplicate group. Data was taken from four separate experiments. The error bars in panels A and B are standard deviations from 34 pY and 34 pST samples from 4 separate experiments. [Please click here to view a larger version of this figure.](#)

Buffer	Volume	Composition
6 M guanidinium chloride lysis buffer	50 mL	6 M guanidinium chloride, 100 mM tris pH 8.5, 10 mM tris (2-carboxyethyl) phosphine, 40 mM chloroacetamide, 2 mM sodium orthovanadate, 2.5 mM sodium pyrophosphate, 1 mM $\beta$ -glycerophosphate, 500 mg n-octyl-glycoside, ultra-pure water to volume
100 mM sodium pyrophosphate	50 mL	2.23 g sodium pyrophosphate decahydrate, ultra-pure water to volume
1M $\beta$ -glycerophosphate	50 mL	15.31 g $\beta$ -glycerophosphate, ultra-pure water to volume
5% trifluoroacetic acid	20 mL	Add 1 mL of 100% trifluoroacetic acid into 19 mL ultra-pure water
0.1% trifluoroacetic acid	250 mL	Add 5 mL 5% trifluoroacetic acid to 245 mL ultra-pure water
pY elution buffer	250 mL	0.1% trifluoroacetic acid, 40% acetonitrile, ultra-pure water to volume
pST elution buffer	250 mL	0.1% trifluoroacetic acid, 50% acetonitrile, ultra-pure water to volume
IP binding buffer	200 mL	50 mM tris pH 7.4, 50 mM sodium chloride, ultra-pure water to volume
25 mM ammonium bicarbonate, pH 7.5	10 mL	Dissolve 19.7 mg into 10 mL sterile ultra-pure water, pH to 7.5 with 1 N hydrochloric acid (~10-15 $\mu$ L/10 ml solution), make fresh
1M phosphate buffer, pH 7	1,000 mL	423 mL 1 M sodium dihydrogen phosphate, 577 mL 1 M sodium hydrogen phosphate
Equilibration buffer	14 mL	6.3 mL acetonitrile, 280 $\mu$ L 5% trifluoroacetic acid, 1740 $\mu$ L lactic acid, 5.68 mL ultra-pure water
Rinsing buffer	20 mL	9 mL acetonitrile, 400 $\mu$ L 5% trifluoroacetic acid, 10.6 mL ultra-pure water
Mass spectrometry solution	10 mL	500 $\mu$ L acetonitrile, 200 $\mu$ L 5% trifluoroacetic acid, 9.3 mL ultra-pure water
Buffer A	250 mL	5 mM monopotassium phosphate (pH 2.65), 30% acetonitrile, 5 mM potassium chloride, ultra-pure water to volume
Buffer B	250 mL	5 mM monopotassium phosphate (pH 2.65), 30% acetonitrile, 350 mM potassium chloride, ultra-pure water to volume
0.9% ammonium hydroxide	10 mL	300 $\mu$ L 29.42% ammonium hydroxide, 9.7 mL ultra-pure water

**Table 1: Buffers and solutions.** This table shows the compositions of the buffers and solutions used in this protocol.

LC-MS/MS Settings		
Parameter	pY Setting	pST Setting
Sample loading ( $\mu$ L)	5	
Loading flow rate ( $\mu$ L/min)	5	
Gradient flow rate (nL/min)	300	
Linear gradient (percentage 0.16% formic acid, 80% ACN in 0.2% formic acid)	4 - 15% for 5 min	4 - 15% for 30 min
	15 - 50% for 40 min	15 - 25% for 40 min
	50 - 90% for 5 min	25 - 50% for 44 min
		50 - 90% for 11 min
Full scan resolution	120,000	
Number of most intense ions selected	20	
Relative collision energy (%) (HCD)	27	
Dynamic exclusion (s)	20	

**Table 2: LC-MS settings.** This is an example of LC-MS settings in a typical shotgun phosphoproteomic experiment. The samples were loaded on to a trap column. The trap was brought in-line with an analytical column. These settings were optimized for using the LC-MS system listed in the **Table of Materials and Reagents**. These settings would need to be adjusted for other LC-MS systems.

MaxQuant Parameter Settings		
Setting		Action
<b>Group-Specific Parameters</b>		
Type	Type	Select Standard
	Multiplicity	Set to 1
Digestion Mode	Enzyme	Select Trypsin/P
	Max. missed cleavages	Set to 2
Modifications	Variable modifications	Add Phospho (STY)
Label-free quantification	Label-free quantification	Select LFQ
	LFQ min. ratio count	Set to 1
	Fast LFQ	Check off
Miscellaneous	Re-quantify	Check off
<b>Global Parameters</b>		
Sequences	FASTA files	Select fasta file downloaded from UniProt
	Fixed modifications	Add Carbamidomethyl (C)
Adv. Identification	Match between runs	Check off
	Match time window	Set to 5 min
	Alignment time window	Set to 20 min
	Match unidentified features	Check off
Protein quantification	Min. ratio count	Set to 1
Folder locations		Modify accordingly

**Table 3: MS analysis software settings.** In MaxQuant, the group-specific and global parameters in this table were selected or adjusted. All other parameters remained at default. These experiments were conducted using version 1.5.3.30. The parameters may vary from version to version and from software to software.

## Discussion

Before utilizing this protocol to enrich for phosphopeptides, a careful consideration of the experimental design is critical. Using biological replicates is a more cost-effective use of mass spectrometry resources than technical replicates. The number of replicates that are necessary will depend in part on the variability of the data. A recent study demonstrated that, while increasing the number of replicates beyond three only marginally increases the number of identifications, the number of significant identifications between groups increases with more replicates<sup>10</sup>.

Due to the lower abundance of phosphoproteins in the cell, sufficient starting protein amounts are necessary to obtain a global phosphoproteome from prostate cancer samples in discovery mode. In these experiments, 5 mg of protein was used. Approximately five nearly confluent 15-cm dishes of cells provide enough protein as input into this protocol, although this will be cell line-dependent. As for tumor tissue, the expected yield of protein is about 6 - 8% of tissue weight. In the *in vitro* setting, a positive control sample to consider is the addition of 1 mM vanadate for 30 min before harvesting the cells. Vanadate, a competitive protein phosphotyrosyl phosphatase inhibitor, will preserve the tyrosine phosphorylation, thus increasing the number of pY peptide identifications<sup>29</sup>.

Clean digestion is a key step to maximize phosphopeptide identification. In addition to the Coomassie stain test, the percent of missed cleavages in the data can be used to evaluate digestion efficiency (Figure 2). Quality-control software is available that analyzes missed cleavages and other metrics to assess MS data quality<sup>30</sup>. While trypsin is the most common, alternative proteases are available<sup>5</sup> to address coverage gaps in the proteome where optimal tryptic peptides cannot be generated<sup>31</sup>. The settings of the MS analysis software would then need to be modified accordingly to adjust for changes in proteases.

The protocol employs immunoprecipitation (for pY enrichment) as well as titanium dioxide (TiO<sub>2</sub>) to enrich for phosphopeptides. Alternative approaches to enrich for peptides include immobilized metal affinity chromatography (IMAC), other metal oxides for metal oxide affinity chromatography (MOAC) such as aluminum hydroxide, and polymer-based metal ion affinity capture (PolyMAC)<sup>5,12</sup>. Previous studies have shown that different enrichment methods enrich for different populations of phosphopeptides<sup>32</sup>. For instance, IMAC enriches more multi-phosphorylated peptides while MOAC preferably enriches for mono-phosphorylated peptides<sup>33</sup>. The **Representative Results** of this protocol reflect this observation (Figure 4B). A recent publication demonstrated that combining IMAC and MOAC using a hybrid material could potentially provide greater coverage of phosphopeptide species<sup>34</sup>. Thus, this protocol could be modified to utilize other enrichment methods in parallel to allow for even more comprehensive phosphoproteomic analyses.

The MaxQuant<sup>26</sup> software suite is used to analyze the MS data in this protocol, but commercial applications<sup>35</sup> are also available for phosphopeptide identification and quantification. For phosphopeptide identification, a localization probability cutoff is applied. This filter is performed to select for phosphopeptides with a high confidence (*i.e.*, greater than 0.75) in phosphoresidue identification<sup>10,28</sup>. In other words, the summed probability of all other residues that could potentially contain the phospho-group is less than 0.25. This cutoff could be raised to



increase the stringency of the phosphopeptide selection. In regard to the number of identifications, the expected number of pY peptides is in the hundreds, while the expected number of pST peptides is in the high thousands. These values reflect previously observed phosphoproteome distribution where about 2%, 12%, and 86% of the phosphosites are pY, pT, and pS, respectively<sup>28</sup>.

If the pY and pST enrichment steps are performed in parallel, the sample preparation steps in the protocol can be completed in six days. By pairing with the powerful tool of MS, phosphopeptide enrichment protocols such as this provide a global approach for scientists to collect data to analyze the phosphoproteome in their respective research fields.

## Disclosures

The authors have nothing to disclose.

## Acknowledgements

We thank members of the Drake lab for providing advice and input on the manuscript. We also thank the members of the Biological Mass Spectrometry Facility of Robert Wood Johnson Medical School and Rutgers, The State University of New Jersey, for providing advice and performing mass spectrometry on our samples. Larry C. Cheng is supported by the National Institute of General Medical Sciences of the National Institutes of Health under award number T32 GM008339. Thomas G. Graeber is supported by the NCI/NIH (SPORE in Prostate Cancer P50 CA092131; P01 CA168585) and an American Cancer Society Research Scholar Award (RSG-12-257-01-TBE). Justin M. Drake is supported by the Department of Defense Prostate Cancer Research Program W81XWH-15-1-0236, Prostate Cancer Foundation Young Investigator Award, the New Jersey Health Foundation, and a Precision Medicine Initiative Pilot Award from the Rutgers Cancer Institute of New Jersey.

## References

1. Siegel, R. L., Miller, K. D., Jemal, A. Cancer statistics, 2018. *CA: A Cancer Journal for Clinicians*. **68** (1), 7-30 (2018).
2. Paller, C. J., Antonarakis, E. S. Management of biochemically recurrent prostate cancer after local therapy: evolving standards of care and new directions. *Clinical Advances in Hematology & Oncology*. **11** (1), 14-23 (2013).
3. Lowrance, W. T., Roth, B. J., Kirkby, E., Murad, M. H., Cookson, M. S. Castration-resistant prostate cancer: AUA guideline amendment 2015. *The Journal of Urology*. **195** (5), 1444-1452 (2016).
4. Domon, B., Aebersold, R. Options and considerations when selecting a quantitative proteomics strategy. *Nature Biotechnology*. **28** (7), 710-721 (2010).
5. Zhang, Y. Y., Fonslow, B. R., Shan, B., Baek, M. C., Yates, J. R. Protein analysis by shotgun/bottom-up proteomics. *Chemical Reviews*. **113** (4), 2343-2394 (2013).
6. Bantscheff, M., Schirle, M., Sweetman, G., Rick, J., Kuster, B. Quantitative mass spectrometry in proteomics: a critical review. *Analytical and Bioanalytical Chemistry*. **389** (4), 1017-1031 (2007).
7. Bantscheff, M., Lemeer, S., Savitski, M. M., Kuster, B. Quantitative mass spectrometry in proteomics: critical review update from 2007 to the present. *Analytical and Bioanalytical Chemistry*. **404** (4), 939-965 (2012).
8. Cox, J. *et al.* Accurate proteome-wide label-free quantification by delayed normalization and maximal peptide ratio extraction, termed MaxLFQ. *Molecular & Cellular Proteomics*. **13** (9), 2513-2526 (2014).
9. Rubbi, L. *et al.* Global phosphoproteomics reveals crosstalk between Bcr-Abl and negative feedback mechanisms controlling Src signaling. *Science Signaling*. **4** (166), ra18, (2011).
10. Högberg, A. *et al.* Benchmarking common quantification strategies for large-scale phosphoproteomics. *Nature Communications*. **9** (1), 1045 (2018).
11. Rush, J. *et al.* Immunoaffinity profiling of tyrosine phosphorylation in cancer cells. *Nature Biotechnology*. **23** (1), 94-101 (2005).
12. Fila, J., Honys, D. Enrichment techniques employed in phosphoproteomics. *Amino Acids*. **43** (3), 1025-1047 (2012).
13. Mertins, P. *et al.* Proteogenomics connects somatic mutations to signalling in breast cancer. *Nature*. **534** (7605), 55-62 (2016).
14. Drake, J. M. *et al.* Phosphoproteome integration reveals patient-specific networks in prostate cancer. *Cell*. **166** (4), 1041-1054 (2016).
15. Lue, H. W. *et al.* Metabolic reprogramming ensures cancer cell survival despite oncogenic signaling blockade. *Genes & Development*. **31** (20), 2067-2084 (2017).
16. Francavilla, C. *et al.* Phosphoproteomics of primary cells reveals druggable kinase signatures in ovarian cancer. *Cell Reports*. **18** (13), 3242-3256 (2017).
17. Zhang, H. *et al.* Integrated proteogenomic characterization of human high-grade serous ovarian cancer. *Cell*. **166** (3), 755-765 (2016).
18. Skaggs, B. J. *et al.* Phosphorylation of the ATP-binding loop directs oncogenicity of drug-resistant BCR-ABL mutants. *Proceedings of the National Academy of Sciences of the United States of America*. **103** (51), 19466-19471 (2006).
19. Zimman, A. *et al.* Activation of aortic endothelial cells by oxidized phospholipids: a phosphoproteomic analysis. *Journal of Proteome Research*. **9** (6), 2812-2824 (2010).
20. Zimman, A., Berliner, J. A., Graeber, T. G. Phosphoproteomic analysis of aortic endothelial cells activated by oxidized phospholipids. *Methods in Molecular Biology*. **1000**, 53-69 (2013).
21. Humphrey, S. J., Azimifar, S. B., Mann, M. High-throughput phosphoproteomics reveals *in vivo* insulin signaling dynamics. *Nature Biotechnology*. **33** (9), 990-995 (2015).
22. Bradford, M. M. A rapid and sensitive method for the quantitation of microgram quantities of protein utilizing the principle of protein-dye binding. *Analytical Biochemistry*. **72**, 248-254 (1976).
23. Meyer, T. S., Lamberts, B. L. Use of coomassie brilliant blue R250 for the electrophoresis of microgram quantities of parotid saliva proteins on acrylamide-gel strips. *Biochimica et Biophysica Acta*. **107** (1), 144-145 (1965).
24. Bergstrom Lind, S. *et al.* Immunoaffinity enrichments followed by mass spectrometric detection for studying global protein tyrosine phosphorylation. *Journal of Proteome Research*. **7** (7), 2897-2910 (2008).

25. Pinkse, M. W., Uitto, P. M., Hilhorst, M. J., Ooms, B., Heck, A. J. Selective isolation at the femtomole level of phosphopeptides from proteolytic digests using 2D-NanoLC-ESI-MS/MS and titanium oxide precolumns. *Analytical Chemistry*. **76** (14), 3935-3943 (2004).
26. Cox, J., Mann, M. MaxQuant enables high peptide identification rates, individualized p.p.b.-range mass accuracies and proteome-wide protein quantification. *Nature Biotechnology*. **26** (12), 1367-1372 (2008).
27. Cox, J. *et al.* Andromeda: a peptide search engine integrated into the MaxQuant environment. *Journal of Proteome Research*. **10** (4), 1794-1805 (2011).
28. Olsen, J. V. *et al.* Global, *in vivo*, and site-specific phosphorylation dynamics in signaling networks. *Cell*. **127** (3), 635-648 (2006).
29. Huyer, G. *et al.* Mechanism of inhibition of protein-tyrosine phosphatases by vanadate and pervanadate. *The Journal of Biological Chemistry*. **272** (2), 843-851 (1997).
30. Bielow, C., Mastrobuoni, G., Kempa, S. Proteomics quality control: quality control software for MaxQuant results. *Journal of Proteome Research*. **15** (3), 777-787 (2016).
31. Swaney, D. L., Wenger, C. D., Coon, J. J. Value of using multiple proteases for large-scale mass spectrometry-based proteomics. *Journal of Proteome Research*. **9** (3), 1323-1329 (2010).
32. Bodenmiller, B., Mueller, L. N., Mueller, M., Domon, B., Aebersold, R. Reproducible isolation of distinct, overlapping segments of the phosphoproteome. *Nature Methods*. **4** (3), 231-237 (2007).
33. Leitner, A., Sturm, M., Lindner, W. Tools for analyzing the phosphoproteome and other phosphorylated biomolecules: a review. *Analytica Chimica Acta*. **703** (1), 19-30 (2011).
34. Yang, D. S. *et al.* Design and synthesis of an immobilized metal affinity chromatography and metal oxide affinity chromatography hybrid material for improved phosphopeptide enrichment. *Journal of Chromatography A*. **1505**, 56-62 (2017).
35. Al Shweiki, M. R. *et al.* Assessment of label-free quantification in discovery proteomics and impact of technological factors and natural variability of protein abundance. *Journal of Proteome Research*. **16** (4), 1410-1424 (2017).

# MAPK Reliance via Acquired CDK4/6 Inhibitor Resistance in Cancer

Renée de Leeuw<sup>1</sup>, Christopher McNair<sup>1</sup>, Matthew J. Schiewer<sup>1</sup>, Neermala Poudel Neupane<sup>1</sup>, Lucas J. Brand<sup>1</sup>, Michael A. Augello<sup>1</sup>, Zhen Li<sup>2</sup>, Larry C. Cheng<sup>2,3,4</sup>, Akihiro Yoshida<sup>5</sup>, Sean M. Courtney<sup>6,7</sup>, E. Starr Hazard<sup>6,8</sup>, Gary Hardiman<sup>6,9</sup>, Maha H. Hussain<sup>10</sup>, J. Alan Diehl<sup>5</sup>, Justin M. Drake<sup>2,3,4,11</sup>, Wm. Kevin Kelly<sup>12</sup>, and Karen E. Knudsen<sup>1,12,13</sup>



## Abstract

**Purpose:** Loss of cell-cycle control is a hallmark of cancer, which can be targeted with agents, including cyclin-dependent kinase-4/6 (CDK4/6) kinase inhibitors that impinge upon the G<sub>1</sub>-S cell-cycle checkpoint via maintaining activity of the retinoblastoma tumor suppressor (RB). This class of drugs is under clinical investigation for various solid tumor types and has recently been FDA-approved for treatment of breast cancer. However, development of therapeutic resistance is not uncommon.

**Experimental Design:** In this study, palbociclib (a CDK4/6 inhibitor) resistance was established in models of early stage, RB-positive cancer.

**Results:** This study demonstrates that acquired palbociclib resistance renders cancer cells broadly resistant to CDK4/6 inhibitors. Acquired resistance was associated with aggressive *in vitro*

and *in vivo* phenotypes, including proliferation, migration, and invasion. Integration of RNA sequencing analysis and phosphoproteomics profiling revealed rewiring of the kinome, with a strong enrichment for enhanced MAPK signaling across all resistance models, which resulted in aggressive *in vitro* and *in vivo* phenotypes and prometastatic signaling. However, CDK4/6 inhibitor-resistant models were sensitized to MEK inhibitors, revealing reliance on active MAPK signaling to promote tumor cell growth and invasion.

**Conclusions:** In sum, these studies identify MAPK reliance in acquired CDK4/6 inhibitor resistance that promotes aggressive disease, while nominating MEK inhibition as putative novel therapeutic strategy to treat or prevent CDK4/6 inhibitor resistance in cancer. *Clin Cancer Res*; 1-14. ©2018 AACR.

## Introduction

Dysregulation of the cell cycle is a hallmark of cancer. Although initial attempts to target the cell cycle with nonspecific cyclin-dependent kinase (CDK) inhibitors were clinically unsuccessful, a new generation of selective CDK4/6 inhibitors has emerged that has shown clinical promise across multiple cancer types, including breast, melanoma, and colorectal cancer (1, 2). Currently, three CDK4/6 inhibitors have entered clinical trials: palbociclib (Ibrance), ribociclib (Kisqali), and abemaciclib (Verzenio) (1, 3). Notably, these three inhibitors have recently received accelerated FDA approval for treatment of hormone receptor-positive (HR<sup>+</sup>), Her2-negative breast cancer in combination with endocrine therapy based on the PALOMA-2 (palbociclib), the MONALEESA-2 (ribociclib), and the MONARCH-2 (abemaciclib) phase III clinical trials (4).

Despite evidence of clinical response, development of resistance is common, and the underlying mechanisms that lead to resistance are poorly understood. Consistent with the known functions of CDK4/6 in promoting cell-cycle progression through phosphorylation and inactivation of the retinoblastoma tumor-suppressor protein (RB), CDK4/6 inhibitors require an active RB pathway to elicit antitumor effects. As such, resistance to CDK4/6 inhibitors can occur through disruption of the RB pathway, as mediated by loss of the retinoblastoma tumor suppressor (RB), cyclin D1 and CDK6 amplification, and cyclin E-CDK2 activation (3, 5, 6). Other mechanisms of resistance have also been reported that are independent of RB

<sup>1</sup>Department of Cancer Biology, Thomas Jefferson University, Philadelphia, Pennsylvania. <sup>2</sup>Rutgers Cancer Institute of New Jersey, New Brunswick, New Jersey. <sup>3</sup>Graduate Program in Cellular and Molecular Pharmacology, School of Graduate Studies, Rutgers, The State University of New Jersey, Piscataway, New Jersey. <sup>4</sup>Graduate Program in Quantitative Biomedicine, School of Graduate Studies, Rutgers, The State University of New Jersey, Piscataway, New Jersey. <sup>5</sup>Department of Biochemistry and Molecular Biology, Hollings Cancer Center, Medical University of South Carolina, Charleston, South Carolina. <sup>6</sup>Center for Genomic Medicine Bioinformatics, Medical University of South Carolina (MUSC), Charleston, South Carolina. <sup>7</sup>Department of Pathology and Laboratory Medicine, Medical University of South Carolina, Charleston, South Carolina. <sup>8</sup>Library Science and Informatics, Medical University of South Carolina, Charleston, South Carolina. <sup>9</sup>Departments of Medicine and Public Health Sciences, Medical University of South Carolina, Charleston, South Carolina. <sup>10</sup>Division of Hematology and Oncology, Department of Medicine, Feinberg School of Medicine, Robert H. Lurie Cancer Center, Northwestern University, Chicago, Illinois. <sup>11</sup>Division of Medical Oncology, Department of Medicine, Rutgers Robert Wood Johnson Medical School, New Brunswick, New Jersey. <sup>12</sup>Department of Medical Oncology, Urology and Radiation Oncology, Thomas Jefferson University, Philadelphia, Pennsylvania. <sup>13</sup>Sidney Kimmel Cancer Center, Thomas Jefferson University, Philadelphia, Pennsylvania.

**Note:** Supplementary data for this article are available at Clinical Cancer Research Online (<http://clincancerres.aacrjournals.org/>).

**Corresponding Author:** Karen E. Knudsen, Thomas Jefferson University, 233 S. 10th St., Bluemle Bldg.- Room 1050, Philadelphia, PA 19107. Phone: 215-503-8574; Fax: 215-923-4498; E-mail: karen.knudsen@jefferson.edu

**doi:** 10.1158/1078-0432.CCR-18-0410

©2018 American Association for Cancer Research.

## Translational Relevance

In light of recent successes with the clinical application of cyclin-dependent kinase-4/6 (CDK4/6) inhibitors in breast cancer and with clinical trials underway in multiple tumor types, it is anticipated that this class of drugs will become standard of care for a variety of malignancies. Unfortunately, development of therapeutic resistance is common, and therefore, it is imperative to understand mechanisms allowing cancer progression. This study demonstrates in preclinical models that acquired CDK4/6 inhibitor resistance is associated with a rewired kinome, which includes activation of the MAPK signaling pathway as a common occurrence across models, which conferred aggressive *in vitro* phenotypes, prometastatic signaling, and enhanced tumor take *in vivo*. However, this MAPK signaling dependence resulted in sensitization to MEK inhibitors, nominating MEK inhibition as a potential therapeutic approach to treat CDK4/6 inhibitor-resistant cancers.

pathway alteration, including alterations or activation of the PI3K/AKT/mTOR pathway (7, 8). Given the promise of CDK4/6 inhibitors in the clinical setting, there is an increasing need to discern mechanisms of bypass and identify mechanisms to anticipate and prevent therapeutic resistance.

Therapeutic opportunities for implementation of CDK4/6 inhibitors in the clinical setting are widest in tumors for which RB pathway disruption is infrequent or occurs late in tumor progression. As such, studies herein were conducted using prostate adenocarcinoma as a tumor paradigm, in which a functional RB pathway is largely intact in early stage disease. Prior to androgen deprivation therapy, which is the first line of therapeutic intervention for disseminated disease, almost all tumors retain RB function, with 5% RB loss observed in primary tumors (9). By contrast, RB loss is enriched in metastatic disease, occurring in 37% of metastatic cases in a retrospective cohort, and in 21% of metastatic castration-resistant prostate cancer (CRPC; ref. 10), and is found to be causative for the transition to CRPC (11), the lethal stage of disease. Thus, CDK4/6 inhibitors are under clinical testing in both hormone-naïve metastatic prostate adenocarcinoma (NCT02059213) and metastatic CRPC (NCT02555189) as adjuvant therapy for first- and second-line hormone therapy, respectively.

As shown herein, acquired palbociclib resistance not only rendered cancer cells broadly resistant to CDK4/6 inhibitors, but also promoted aggressive phenotypes, including accelerated growth *in vitro* and *in vivo*, as well as enhanced invasion and clonogenic capacity. Unbiased global gene expression and phosphoproteomic profiling were utilized to interrogate the molecular alterations of acquired resistance to CDK4/6 inhibition in multiple models of palbociclib resistance. These integrated approaches revealed a reduction of RB function resulting in CDK4/6 inhibitor resistance. In addition, acquired CDK4/6 resistance was associated with activation of the MAPK signaling pathway, which conferred sensitization to MEK inhibitors. In sum, these studies demonstrate partially retained, hyperphosphorylated Rb in acquired CDK4/6 inhibitor resistance and nominate MEK inhibitors as a new treatment strategy for advanced cancers upon developing CDK4/6 inhibitor resistance.

## Materials and Methods

### Tissue culture and establishing resistance lines

LNCAp- and LAPC4-derived cells were cultured in improved minimum essential media (IMEM; Corning) or Iscove's modified Dulbecco media (Corning), respectively, supplemented with 5% heat-inactivated FBS (HyClone), 1% L-glutamine, and 1% penicillin/streptomycin (11). Unless otherwise described, cells were plated overnight and treated with 0.5  $\mu\text{mol/L}$  PD0233991 (PD, palbociclib, SelleckChem), LEE011 (LEE, ribociclib, Novartis), or U0126 (Promega). Palbociclib-resistant cell models were generated from LNCAp and LAPC4 cells by sustained treatment with 0.5  $\mu\text{mol/L}$  PD (schematic in Fig. 1A) and maintained under selection when resistance, measured via bromodeoxyuridine (BrdUrd) incorporation, was achieved after approximately 3 months. Cells were authenticated by the ATCC and checked for mycoplasma upon thawing and at termination of maintenance after <20 passages (ATCC 30-1012K).

### Trypan blue exclusion

Cells were treated with a dose range of indicated doses of PD, LEE, or U0126 for up to 6 days, with drugs refreshed every other day. Cells were trypsinized, counted twice on a hemacytometer using the Trypan blue exclusion method, and normalized to a drug-free control. Experiments were performed at least twice in quadruplicate.

### Flow cytometry

Cells were treated with 0.5  $\mu\text{mol/L}$  PD or LEE for 24 hours, and after a 2-hour pulse labeling of BrdUrd (Amersham, RPN201), adherent cells were harvested and fixed with 100% ethanol. Proliferation was measured by bivariate flow cytometry using BrdUrd and propidium-iodide (PI) staining. A Millipore Guava EasyCyte flow cytometer captured 10,000 BrdUrd/PI events, and the Millipore InCyte software was used to gate for the percentage of BrdUrd incorporation. Experiments were performed at least twice in biological triplicate.

### RT-PCR

Cells were treated with 0.5  $\mu\text{mol/L}$  PD or CTRL for 24 hours and processed to assess RB1 expression, as described previously (12), performed at least twice in biological triplicate.

### Immunoblotting

Protein harvesting and immunoblotting were performed as previously described (12), quantified in ImageJ. Antibodies used are mouse- $\alpha$ -RB (BD-Biosciences; 554136), rabbit- $\alpha$ -GAPDH (Santa Cruz Biotechnology; SC-25778), rabbit- $\alpha$ -CyclinA (Santa Cruz Biotechnology; SC-596), rabbit- $\alpha$ -ERK1 (Santa Cruz Biotechnology; SC-94), rabbit- $\alpha$ -phospho-p44/p42 (T202/Y204; Cell Signaling Technology, 4370S), and goat- $\alpha$ -LaminB (Santa Cruz Biotechnology; SC-6217). Phospho blots were blocked and immunoblotted in 2.5% BSA, and all other blots with 5% milk in PBS-Tween.

### Migration and invasion assays

Corning FluoroBlok 24-Multiwell and Corning BioCoat Tumor Invasion System plates were utilized for migration and invasion assays, according to protocols provided by the company, performed at least twice in quadruplicate. Bottom wells were filled with IMEM/20%FBS. A total of 50,000 cells (passed 2x, 40  $\mu\text{m}$  cell

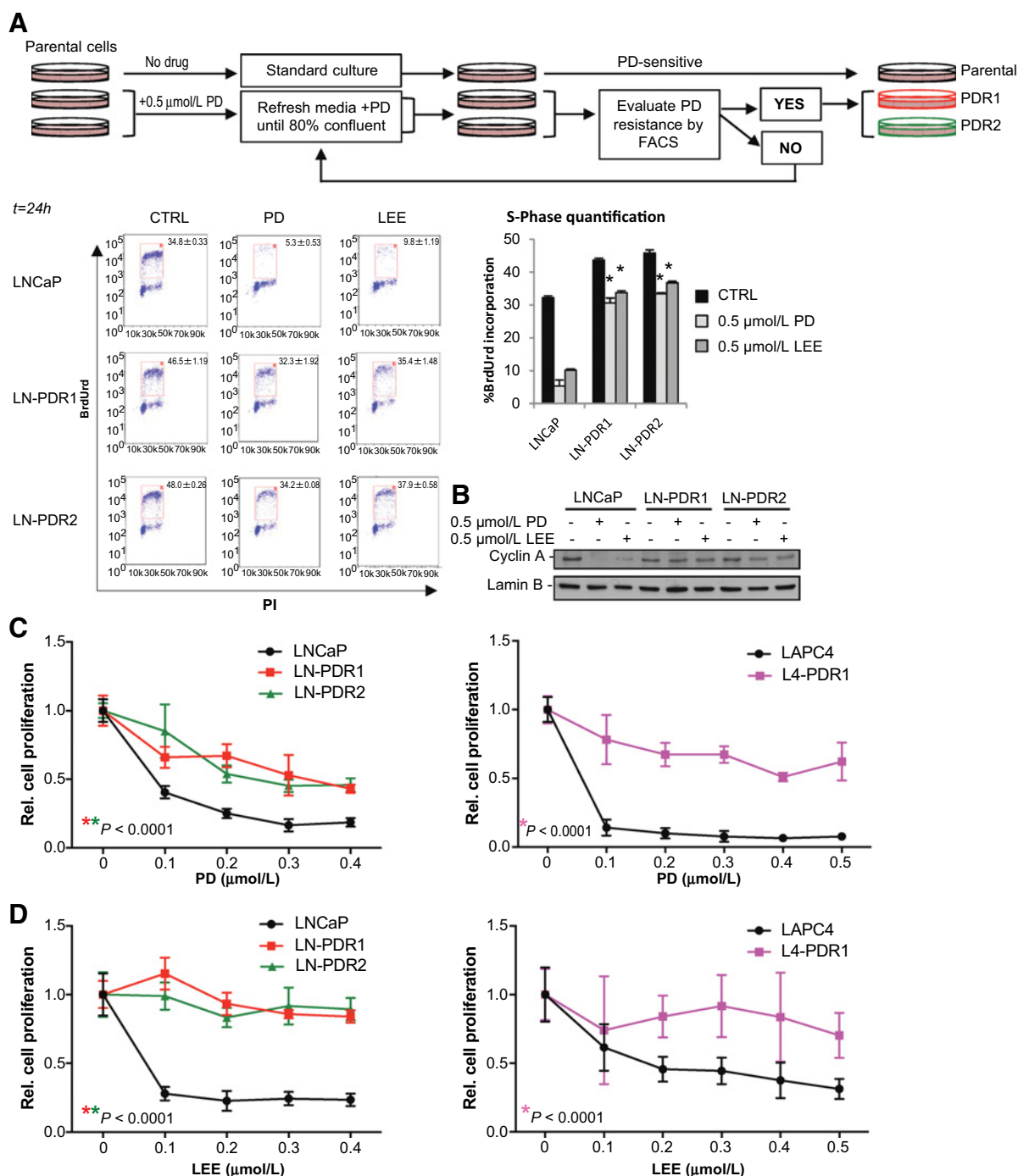


Figure 1.

Acquired resistance to palbociclib results in broad CDK4/6 inhibitor resistance. **A**, Palbociclib (PD)-resistant (PDR) prostate cancer cells were generated via continuous selection with 0.5 μmol/L PD for 2 to 3 months and evaluated regularly via flow cytometry (top). PD resistance was determined by treating biological triplicate parental or PDR cells with 0.5 μmol/L PD, LEE (ribociclib), or CTRL (no drug) for 24 hours and measuring BrdUrd incorporation with a flow cytometer after a 2-hour pulse labeling, fixation in EtOH, and staining with a secondary FITC-mouse-anti-BrdUrd antibody. FACS analysis was performed by gating for the BrdUrd+ S-phase population (representative flow traces for biological triplicates are shown on the left), quantified in a bar graph on the right as an indication of cell proliferation. FACS analysis showed that PD and ribociclib (LEE) fail to induce cell-cycle arrest in the G<sub>1</sub> phase in LNCaP PDR lines. **B**, Cells were treated for 24 hours with CTRL, 0.5 μmol/L PD, or LEE and immunoblotted for cyclin A, demonstrating a reduction in cyclin A protein upon exposure to PD or LEE only in the parental cells, indicating biochemical resistance in LNCaP PDR cells. **C**, Cell counting via Trypan blue exclusion of quadruplet samples with dose-escalation treatment with PD of *t* = 6 days (LNCaP) or *t* = 13 days (LAPC4) shows a significantly reduced response to PD in the PDR models, compared with the parental cells. **D**, Acquired resistance to PD results in broad CDK4/6 inhibitor resistance as shown by a LEE dose escalation. \*Significance for dose-response curves was determined by a two-way ANOVA analysis performing a multivariate comparison of mean per dose for PDR vs. parental data.

strainers) were seeded in the top compartment of each well in serum-free IMEM and incubated for 48 hours (migration) or 72 hours (invasion). Cells were stained with Corning Calcein AM Fluorescent Dye and measured on a BioTek SynergyHT plate reader.

### Clonogenic assays and FIJI

The bottom layer of 1% agar/PBS was mixed 1:1 with culture media supplemented with 20% FBS and poured into 6-well plates, after which a second layer with 0.6% agar/FBS mixed with a cell-media/20%FBS suspension was poured on top. Where mentioned, drugs were mixed into both agar layers. Note that 200  $\mu$ L media  $\pm$  drugs were added on top and refreshed twice a week. A total of 5,000 cells were seeded per well in triplicate. Plates were incubated for 3 weeks, after which each well was photographed. Images were analyzed with FIJI (ImageJ) as follows: select each well transform to gray scale, adjust the threshold to remove background, and detect colonies. Use the Analyze Particles algorithm to count total colonies and pixel sizes of each colony. Experiments were performed at least twice in triplicate.

### In vivo studies

Xenograft studies were performed in accordance with NIH Guidelines, and animal protocols were approved by Institutional Animal Care and Use Committee at Thomas Jefferson University. Cells ( $3 \times 10^6$  per injection) suspended in PBS were combined 1:1 with Matrigel (BD Biosciences; 354234) and injected s.c. into the flanks of 5- to 6-week-old, intact-male athymic nude mice (Charles River Laboratories). Tumor development was monitored over time by palpation. Where indicated, mice received AIN-76A diet laced with 6.7 mg/kg trametinib or control (kindly provided by the laboratory of Dr. Andrew Aplin, Thomas Jefferson University).

### RNA sequencing and gene set enrichment analyses

RNA was extracted with the RNeasy Kit (Qiagen) from PDR and parental LNCaP or LAPC4 cells pre-treated 24h with 0.5  $\mu$ mol/L PD or vehicle (CTRL). Note that 100 to 200 ng of total RNA was used to prepare RNA sequencing (RNAseq) libraries using the TruSeq RNA Sample Prep Kit V2 (Illumina), following the protocol described by the manufacturer. High-throughput sequencing (HTS) was performed using an Illumina HiSeq2500 with each sample sequenced to a minimum depth of approximately 50 million reads. A paired end  $2 \times 125$  cycle sequencing strategy was used. Data were subjected to Illumina quality control (QC) procedures (>80% of the data yielded a Phred score of 30). Secondary analysis was carried out on an OnRamp Bioinformatics Genomics Research Platform (OnRamp Bioinformatics; ref. 13). OnRamp's advanced Genomics Analysis Engine utilized an automated RNAseq workflow to process the data (13, 14), including (1) data validation and quality control, (2) read alignment to the human genome (hg19) using TopHat2 (15), which revealed >90% mapping of the paired end reads, (3) generation of gene-level count data with HTSeq, and (4) differential expression analysis with DESeq2 (15), which enabled the inference of differential signals with robust statistical power. (Genomics Research Platform with RNAseq workflow v1.0.1, including FastQValidator v0.1.1a, Fastqc v0.11.3, Bowtie2 v2.1.0, TopHat2 v2.0.9, HTSeq v0.6.0, DESeq v1.8.0.)

The resulting BAM files were sorted and input into the Python package HTSeq to generate count data for gene-level differential

expression analyses. To infer differential signal within the data sets with robust statistical power, DESeq2 was utilized (15). Transcript count data from DESeq2 analysis of the samples were sorted according to their adjusted *P* value or *q* value and the smallest FDR at which a transcript is called significant ( $q < 0.1$ ). FDR is the expected fraction of false-positive tests among significant tests and was calculated using the Benjamini-Hochberg multiple testing adjustment procedure. LNCaP (LN) and LAPC4 (L4) sequencing data are deposited using NCBI's Gene Expression Omnibus (16), accessible through GEO Series accession number GSE99675.

### Analysis of phosphotyrosine, phosphoserine, and phosphothreonine peptides by quantitative mass spectrometry

PDR and parental LNCaP or LAPC4 cells were treated for 24 hours with 0.5  $\mu$ mol/L PD or CTRL, scraped, pelleted, and snap frozen. Protein digestion and phosphopeptide enrichment were performed as previously described (17-19) with minor modifications. Briefly, cells were lysed in 6 mol/L guanidinium hydrochloride buffer (6 mol/L guanidinium chloride, 100 mmol/L Tris pH 8.5:10 mmol/L Tris (2-carboxyethyl) phosphine, 40 mmol/L 2-chloroacetamide, 2 mmol/L vanadate, 2.5 mmol/L NaPyrophosphate, 1 mmol/L Beta-glycerophosphate, 10 mg/mL N-octylglycoside). Lysates were sonicated and cleared, and protein was measured. Note that 5 mg of protein was digested with trypsin, and the resulting phosphopeptides were subjected to phosphotyrosine antibody-based enrichment via immunoprecipitation. The immunoprecipitate was washed, and phospho-Tyrosine (pY) peptides were eluted. The supernatant from the pY immunoprecipitations was kept for phospho-serine/threonine (pST) peptide enrichment. pST peptides (2.5 mg) were desalted using C18 columns and then separated using strong cation exchange chromatography. In separate reactions, the pY and pST peptides were then further enriched using titanium dioxide columns to remove existing nonphosphorylated peptides. The pY and pST peptides were then desalted using C18 tips prior to submission on the mass spectrometer. Samples were analyzed by LC-MS/MS using a dual pump nanoRSLC system (Dionex) interfaced with a Q Exactive HF (ThermoFisher). Samples were run in technical duplicates, and data were searched using MaxQuant Andromeda version 1.5.3.30 (20) against the Uniprot human reference proteome database with canonical and isoform sequences (downloaded September 2016 from <http://uniprot.org>). MaxQuant Andromeda parameters were set as previously described (21). Data are deposited in the ProteomeXchange Consortium via the PRIDE partner repository, accessible through dataset identifier PXD006561 (22).

MS data analysis was performed as previously described (23). For clustering, pY data were filtered using an FDR-corrected ANOVA *P* value of 0.2, and pS/pT data were filtered using an FDR-corrected ANOVA *P* value of 0.05. Hierarchical clustering was performed using the Cluster version 3.0 with the Pearson correlation and pairwise complete linkage analysis (24). Java TreeView version 1.1.6r4 was used to visualize clustering results (25).

### Kinase substrate enrichment analysis

Kinase substrate enrichment analysis (KSEA) was performed as previously described (18). Briefly, phosphopeptides were rank-ordered by average fold change between PDR and parental cells. The enrichment score was calculated using the Kolmogorov-Smirnov statistic. Statistical significance was calculated via permutation analysis. The normalized enrichment score (NES) was calculated by taking the enrichment score and dividing it by the

mean of the absolute values of all enrichment scores from the permutation analysis. The Benjamini–Hochberg procedure was utilized to calculate FDR for each kinase. For pY analyses, cutoffs of FDR < 0.05, hits > 4, and NES > 1.3 were used. For pST analyses, cutoffs of FDR < 0.02, hits > 5, and NES > 2 were used.

## Results

Although CDK4/6 inhibitors have shown promise in clinical trials for cancer treatment, acquired resistance is common. Thus, the present study interrogated the underpinnings of therapeutic resistance, to identify markers for therapeutic outcome and develop new strategies when resistance develops.

### Acquired resistance to palbociclib results in broad CDK4/6 inhibitor resistance

Palbociclib-resistant (PDR) prostate adenocarcinoma cell models generated from hormone therapy–sensitive prostate adenocarcinoma cells (LNCaP and LAPC4) demonstrated retained BrdUrd incorporation after PD treatment (LNCaP-parental: 5.3%; LN-PDR1: 32.3%; LN-PDR2: 34.2%), indicative of a G<sub>1</sub>–S cell-cycle checkpoint bypass (Fig. 1A; Supplementary Fig. S1A). Retained cyclin A (an RB/E2F target gene) protein levels after 24-hour treatment with 0.5 μmol/L PD confirmed acquired resistance (Fig. 1B; Supplementary Fig. S1B). Ribociclib (LEE011, LEE) is similar to PD in chemical structure and likewise targets the ATP-binding pocket, and thus it was not surprising that the PDR models were resistant to LEE, as observed via retained BrdUrd incorporation (LNCaP-parental: 9.8%; LN-PDR1: 35.4%, LN-PDR2: 37.9%) and cyclin A (Fig. 1A and B; Supplementary Fig. S1A and S1B). Dose–response curves confirmed that PDR models continued to proliferate, whereas the parental cells were arrested at submicromolar doses of PD or LEE (Fig. 1C and D). These findings indicate that acquired resistance to palbociclib confers broad resistance to this class of agents, suggestive of common mechanisms of bypass.

### Acquired CDK4/6 inhibitor resistance is associated with rewired transcriptional programs

To identify transcriptional alterations underlying CDK4/6 inhibitor resistance, PDR and parental cells were treated for 24 hours with 0.5 μmol/L PD or control (CTRL), and RNAseq was performed. The MA plots in Supplementary Figs. S2A (right) and S3A represent the log ratio (M) of the PD versus CTRL values over the average log intensity (A) of each transcript, visualizing a global reduction of differentially expressed genes in PDR models compared with the parental cells after PD treatment. Strikingly, the large cluster of downregulated genes in the parental model (indicated by the blue arrow) was absent in the resistant cells, confirming that PD is unable to significantly inhibit this gene cluster. When comparing PDR1 and PDR2 profiles with parental cells, in both PD-treated and CTRL conditions, vast transcriptomic changes were observed in both the total number of differentially expressed transcripts and log ratio amplitudes (Fig. 2A, left; Supplementary Fig. S3B). Although PD treatment showed limited impact on the transcriptome of the PDR lines compared with parental cells, these models demonstrated extensive alteration in the transcriptome to adapt to extended PD exposure. The majority of transcripts (>1.5-fold, *q* value < 0.1) were common between the two independently generated LNCaP PDR models in both CTRL and PD conditions (Fig. 2A, right). Although the PDR models

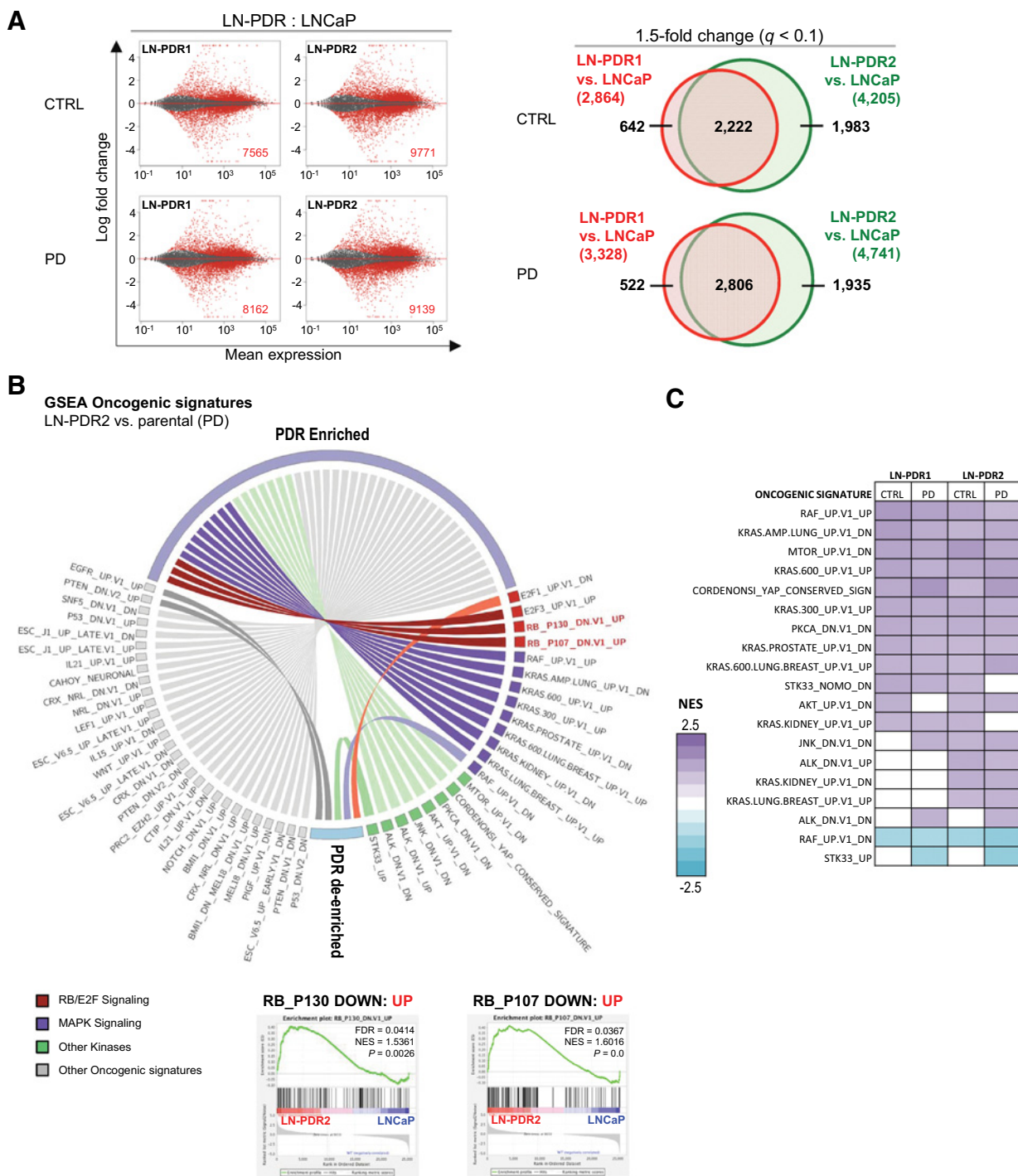
showed a few distinctions, deregulated signaling pathways common between PDR models are most likely to contribute to resistance.

To identify common pathways enriched in the PDR models, complete transcriptional profiles were utilized in Gene Set Enrichment Analyses (GSEA: [www.broadinstitute.org/GSEA](http://www.broadinstitute.org/GSEA)) interrogating the predefined Oncogenic Signatures and Hallmarks from the Molecular Signature Database (MSigDB; Fig. 2B; Supplementary Figs. S2B and S3D). Gene sets enriched in both PDR models under at least one condition were selected to highlight pathways that are most likely to contribute to acquired CDK4/6 inhibitor resistance. Enriched hallmark gene sets included G<sub>2</sub>–M checkpoint, supporting the contention that resistant cells bypass the G<sub>1</sub>–S checkpoint and progress through cell cycle. Enrichment of E2F targets in PDR lines suggests increased E2F activity, potentially mediated through a bypass of RB. Genomic RB loss has been observed in approximately 30% of advanced prostate adenocarcinoma across different patient cohorts, and as RB is the main target of CDK4/6-mediated phosphorylation, loss of this gene has been attributed to resistance to CDK4/6 inhibitors (5, 26). Concordantly, RB knockdown Oncogenic Signatures were also enriched, further highlighting that RB function may be reduced (Fig. 2B). RT-PCR and immunoblotting demonstrated that total RB mRNA and protein were retained in all PDR lines, albeit reduced to 29% to 56% (Supplementary Figs. S2C and S3C, top). Retained RB protein in the PDR models remained hyperphosphorylated [Supplementary Figs. S2C and S3C, bottom, upper band total RB (tRB)] in the presence of a CDK4/6 inhibitor, which attenuates RB function, confirming aberrant inactivation of RB in the presence of CDK4/6 inhibitors that likely cause bypass of the G<sub>1</sub>–S checkpoint and activation of E2F transcription factors. As the kinome forms an intricate network of interactions (27), it was postulated that bypass of CDK4/6 inhibition likely causes kinome rewiring. Notably, RNAseq uncovered enrichment of numerous kinase-related signatures (Fig. 2B and C; Supplementary Fig. S4A). These findings served as the impetus for further exploration to identify specific kinase pathway(s) that could present novel targets for therapeutic intervention.

### MAPK activation is a hallmark for CDK4/6 inhibitor resistance

Phosphoproteomic mass spectrometry profiling provided an unbiased approach to investigate the PDR-associated kinome. Cells were treated for 24 hours with either 0.5 μmol/L PD or control, lysed, and digested (Fig. 3A). pY peptides were immunoprecipitated with an anti-pY antibody, whereas pST peptides remained in the supernatant, allowing analysis of both peptide populations via LC-MS/MS (23). Hierarchical clustering revealed altered phosphorylation levels of peptides across models and treatments, whereas duplicate samples cluster together (Fig. 3A; Supplementary Fig. S4B). Phospho-peptide profiles were subjected to KSEA. The pY peptides unveiled multiple motifs targeted by Src and its SH2 domain (Fig. 3B; Supplementary Fig. S4C), which is linked to cancer progression (28). The pST peptides were strongly enriched for motifs targeted by ERK1 and ERK2 (aka MAPK3 and MAPK1; Fig. 3C; Supplementary Fig. S4D). To prioritize changes in the phosphoproteome most likely to link to CDK4/6 inhibitor resistance, results were compared with the gene expression data. Intriguingly, KRAS and RAF kinases, both of which were highly represented in the Oncogenic Signatures from the RNAseq data, regulate ERK1/2 via mitogen-activated protein kinase kinase, or MEK (29). These data suggest

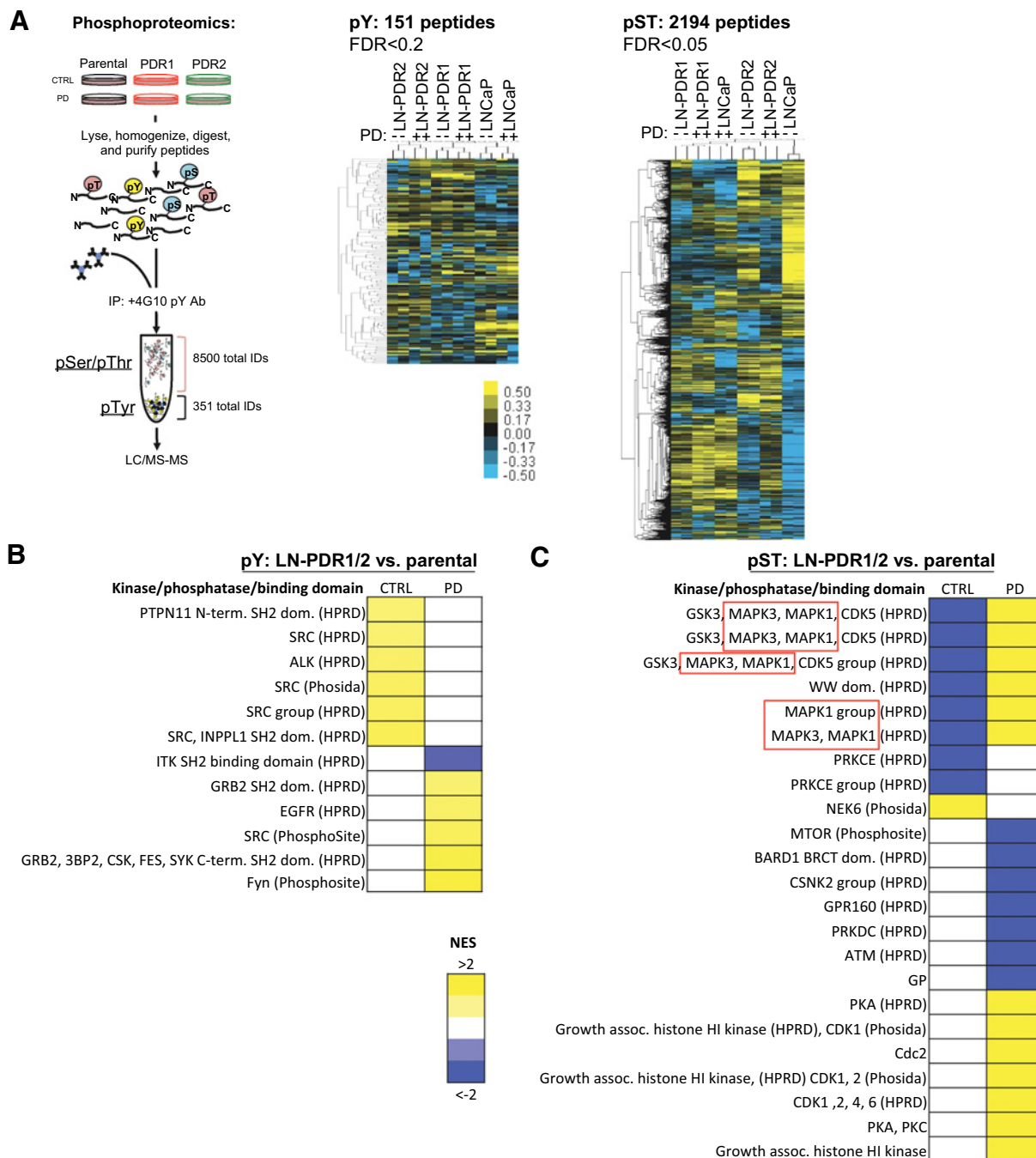
de Leeuw et al.



**Figure 2.**

Acquired CDK4/6 inhibitor resistance is associated with rewired transcriptional programs including RB function. **A**, RNAseq was performed on PDR1/2 and parental LNCaP cells treated for 24 hours with 0.5  $\mu\text{mol/L}$  PD or vehicle (CTRL). The MA plots (right) represent the log ratio (M) of PDR versus parental values over the average log intensity (A) of each transcript, which visualizes vast differences between the PDR versus parental data (red dots and inset numbers indicate significant hits,  $q$  value  $< 0.1$ ). Venn diagrams show overlap between PDR1 and PDR2 of genes  $>1.5x$  differentially expressed compared with the parental cells ( $q$  value  $< 0.1$ ; right). **B**, The complete RNAseq profiles for each PDR versus parental model comparison were subjected to unbiased GSEA (MSigDB) to determine enrichment of predefined oncogenic signatures in both PDR1 and PDR2 compared with parental cells under at least one condition (CTRL/PD) with a FDR  $< 0.25$  (complete list in Supplementary Fig. S2B). The oncogenic signatures enriched in the PDR models included two signatures defined by RB knockdown, suggesting the PDR models have upregulated genes that are induced by RB knockdown. Representative GSEA plots of the RB knockdown signatures are shown for PDR2 versus WT after PD treatment. **C**, GSEA oncogenic signature altered kinase signatures in the LNCaP PDR models for all conditions.



**Figure 3.**

Integrative transcriptome and kinome profiling identifies differential MAPK stimulus as a hallmark of CDK4/6 inhibitor resistance. **A**, LNCaP PDR and parental cells were treated for 24 hours with 0.5  $\mu\text{mol/L}$  PD or control, snap frozen, and lysed. After peptide digestion, pY peptides were immunoprecipitated, whereas pST peptides remained in the upper fraction (see schematic, more details in Materials and Methods). Duplicates of both peptide fractions were utilized in an unbiased phosphoproteomics approach to identify altered phosphorylation of tyrosine and serine/threonine peptides across PDR models compared with the parental cells, displayed by hierarchical clustering on the right. **B**, KSEA defined enriched peptide motifs for phosphorylated Tyrosine (pY) hits and mapped them to kinases that are most likely to target these motifs. This revealed enrichment for Src and Src Homology (SH2) domain target motifs in PDR1/2 compared with parental cells ( $P = 0.2$ ). **C**, KSEA analysis for pST hits showed enrichment for altered phosphorylation of MAPK3 and MAPK1 (ERK1/2) target motifs ( $P = 0.05$ ), indicative of differential MAPK signaling.

that kinase-signaling cascades play an important role in acquired CDK4/6 inhibitor resistance in these models. Moreover, the MAPK pathway is targetable with clinically tested pharmacologic

agents, such as MEK inhibitors that are already FDA approved for some cancers (e.g., melanoma; ref. 29), nominating this pathway for further study. Together, these data indicate that acquired

resistance to CDK4/6 inhibitors was associated with induced MAPK pathway activity.

#### Activated ERK is associated with aggressive phenotypes

As described above, oncogenic signatures representative of altered KRAS and RAF signaling were highly enriched as a function of acquired CDK4/6 inhibitor resistance. KRAS acts upstream of RAF family kinases, regulating their activity, and in turn, the RAF family kinases directly activate ERK1/2 kinases through phosphorylation (29). Indeed, although overall ERK1/2 levels were unchanged, ERK1/2 kinases were hyperphosphorylated in the resistance models (Fig. 4A; Supplementary Fig. S5A), which would explain the observation that ERK1/2 motifs are differentially phosphorylated in the phosphoproteomics analysis. Although canonical MAPK-activating growth factor receptors (EGFR and FGFR families; ref. 30) displayed no consensus in differential expression, EGF transcripts were consistently upregulated in the PDR models, which was associated with altered EGFR activity in the phosphoproteomic data (Fig. 3B; Supplementary Fig. S4C). Elevated EGF protein levels were confirmed via Western blotting, which likely causes MAPK activation in these models (Fig. 4B; Supplementary Fig. S5B). Combined, these data strongly suggest that acquired CDK4/6 inhibitor resistance results in increased EGF production, leading to hyperactivation of the MAPK pathway.

As activated MAPK signaling is known to induce proliferation via induction of D-type cyclins and prevent apoptosis, and thus can drive cancer progression (29, 31–33), the PDR models were further characterized biologically. Baseline growth (off PD selection) was compared with the parental cells, demonstrating an almost 3-fold higher growth rate for the LNCaP-derived models (Fig. 4C; no growth difference was observed for LAPC4 cells, data not shown). Transwell chemotaxis assays from 0% to 20% serum conditions revealed an increased migratory capacity and enhanced invasion in the PDR models (Fig. 4D; Supplementary Fig. S5C). Consonantly, transcriptome data revealed enrichment of the GSEA hallmark for epithelial–mesenchymal transition (EMT) in the PDR lines (Supplementary Figs. S2D and S3E), which could underlie the aggressive, migratory, and invasive characteristics these models have obtained upon acquiring PD resistance. To assess clonogenic growth capacity, cells were suspended at low density in agar-containing culture media and incubated for 3 weeks to allow colony formation. HRAS-transformed mouse adult fibroblasts (MAF cells) served as a positive control due to previously described capacity to grow three-dimensional (3D) colonies (34). Representative images of culture wells for each cell line are shown in Fig. 4E (left). To utilize an unbiased approach for colony formation analyses, a macro was developed for FIJI (ImageJ), which counts total colonies per well and measures the pixel size of each colony. Although there was no significant difference in total colonies formed by the LN-PDR or parental LNCaP cells (Supplementary Fig. S5D; note that LAPC4 and derivatives did not form colonies after >1 month), median colony sizes in the LN-PDR1 and LN-PDR2 models were significantly larger than the parental cells ( $P = 0.0008$  and  $P = 0.0001$ , respectively, one-way ANOVA; Fig. 4E, right). Combined, these findings reveal that acquired resistance to CDK4/6 inhibitors is associated with phenotypes linked to aggressive tumor behavior.

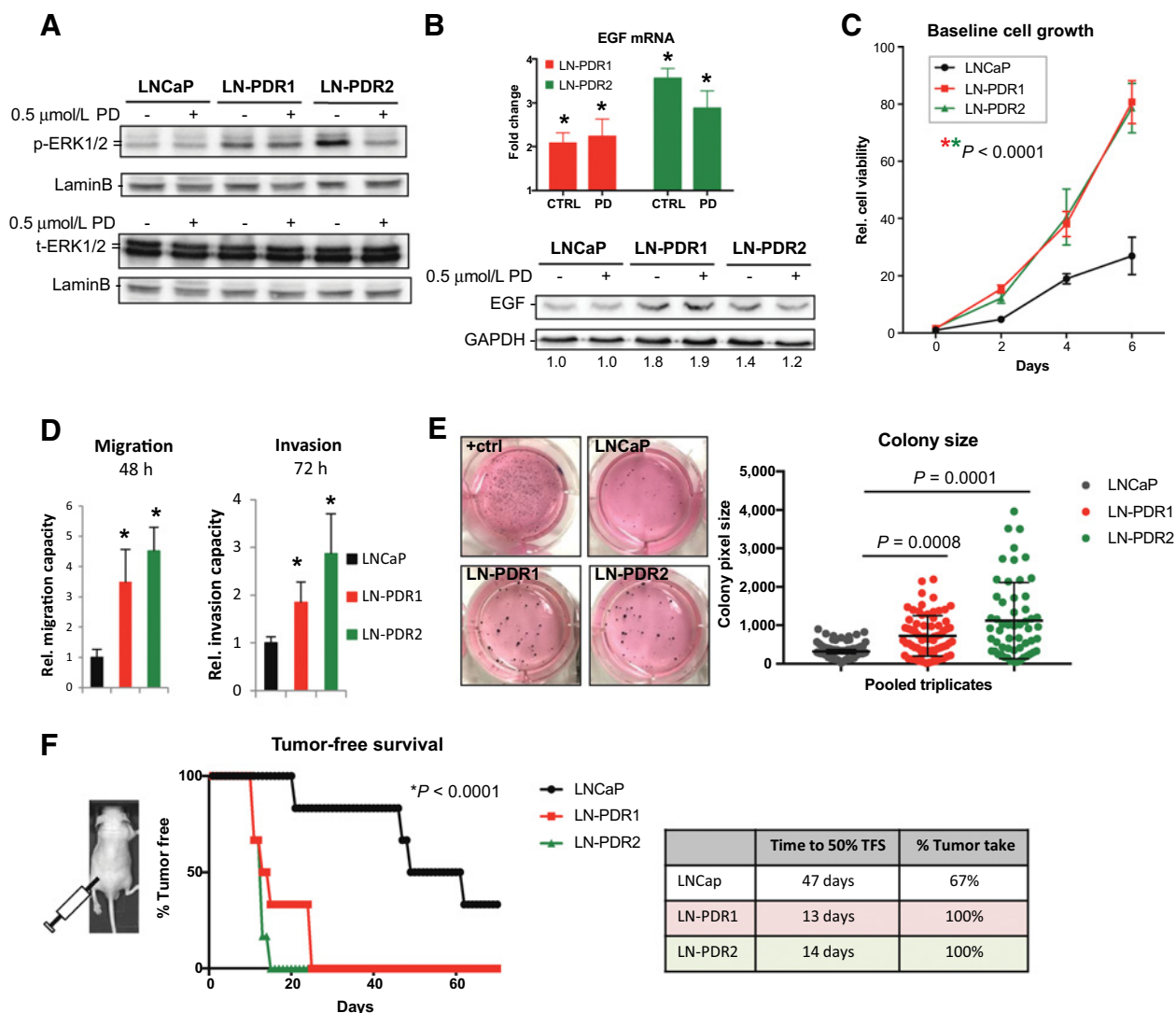
To challenge these concepts *in vivo*, cells were injected s.c. on the flanks of athymic nude mice ( $n = 6$  per group) and monitored over time for tumor take. Strikingly, the PDR models reached a

50% tumor take after only 13 to 14 days, whereas the first parental tumor formed after 20 days, and a 50% tumor take was not reached until 47 days after injection. Moreover, 100% of the mice injected with PDR cells formed palpable tumors, compared with only 67% in the parental model (Fig. 4F). Combined, acquired CDK4/6 inhibitor resistance is associated with hyperproliferation, enhanced migration and invasion, enlarged colonies, and accelerated, more efficient *in vivo* tumor take, thus promoting aggressive tumor phenotypes.

#### Acquired CDK4/6i resistance leads to dependence on MAPK signaling

With clinical trials testing an MEK inhibitor already underway for prostate adenocarcinoma (trametinib: NCT01990196, NCT02881242), and the observation that the direct downstream targets of MEK (i.e., ERK1/2) are hyperactivated upon CDK4/6 inhibitor resistance, the PDR models were assessed for sensitization to MEK inhibition. Cells treated overnight with a preclinical MEK inhibitor (U0126) showed reduction in phosphorylation of ERK1/2, the primary target proteins for MEK kinases (Fig. 5A; Supplementary Fig. S6A). To assess sensitivity to MEK inhibition, cells were treated for 6 days with U0126, and quantified via Trypan blue exclusion, demonstrating that the CDK4/6 inhibitor-resistant cells are sensitized to MEK inhibition (Fig. 5B; Supplementary Fig. S6B). In addition, MEK inhibition reduced the invasion capacity of the PDR lines, whereas the parental cells were unresponsive (Fig. 5C). The MEK inhibitor hampered the clonogenic capacity in the PDR models, reducing not only the size of the colonies, but also total numbers of colonies formed, whereas the parental cells were not affected (Fig. 5D). Combining MEK and CDK4/6 inhibitors resulted in a cooperative effect (Fig. 5E). Sensitization to MEK inhibition was validated *in vivo* (Fig. 5F), wherein mice with palpable xenograft tumors received a diet laced with trametinib (6.7 mg/kg AIN-76A diet) or control diet (AIN-76A). These data demonstrated that tumor growth of the CDK4/6 inhibitor-resistant models was reduced, whereas parental tumors were unresponsive. Together, these findings suggest that activation of the MAPK pathway promotes not only the cell growth in the PDR models, but also the more aggressive, invasive phenotypes observed. In addition, the CDK4/6i-resistant cells appear to have become more reliant on MAPK signaling and as such are sensitized to MEK inhibition.

Although KRAS-activating mutations are not commonly observed in prostate adenocarcinoma, the MAPK pathway can be activated via other mechanisms, such as RAF fusions and overexpression (35). To investigate the clinical relevance of potential MAPK activation in prostate cancer, human primary prostate adenocarcinoma [The Cancer Genome Atlas (TCGA); ref. 36] and metastatic CRPC (SU2C/PCF; ref. 10) datasets were interrogated for alterations of the following components of the MAPK signaling pathway (Fig. 6A and B): RAS family (KRAS, HRAS, NRAS), RAF family (c-RAF/RAF1, ARAF, BRAF), MEK family (MAP2K1, MAP2K2), and ERK1/2 (or MAPK3 and MAPK1). The primary prostate adenocarcinoma dataset displayed alterations (mutations, CNA, mRNA z-score:2.0) in any of these kinases in 38% of all patients, the majority of which were mRNA upregulation (Fig. 6A and B; Supplementary Fig. S7). The frequency of MAPK-related upregulation was confirmed in the metastatic CRPC cohort, in which 47% presented with alterations, including RAF amplifications and gene fusions that may lead to MAPK activation. Interestingly, RAF

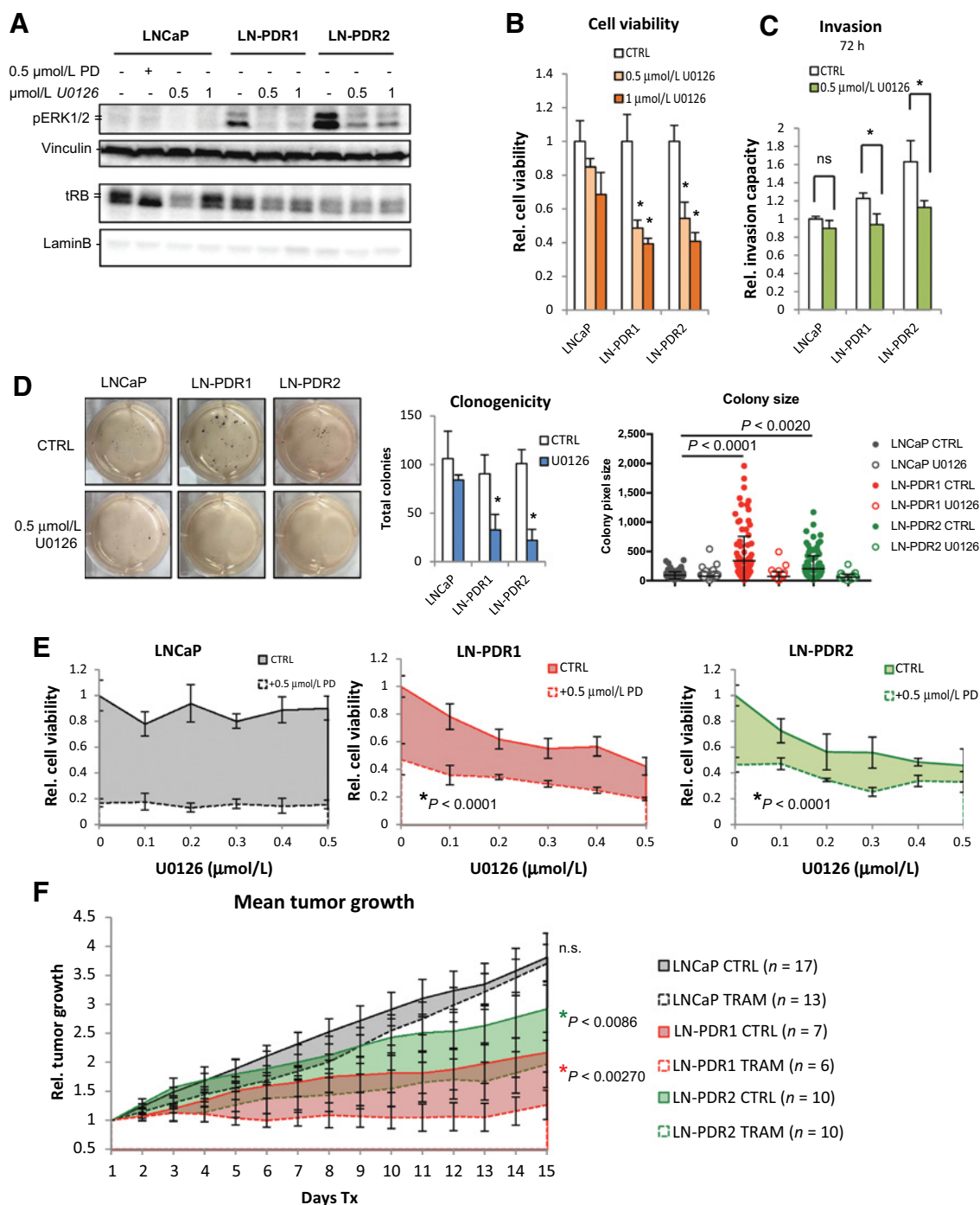


**Figure 4.**

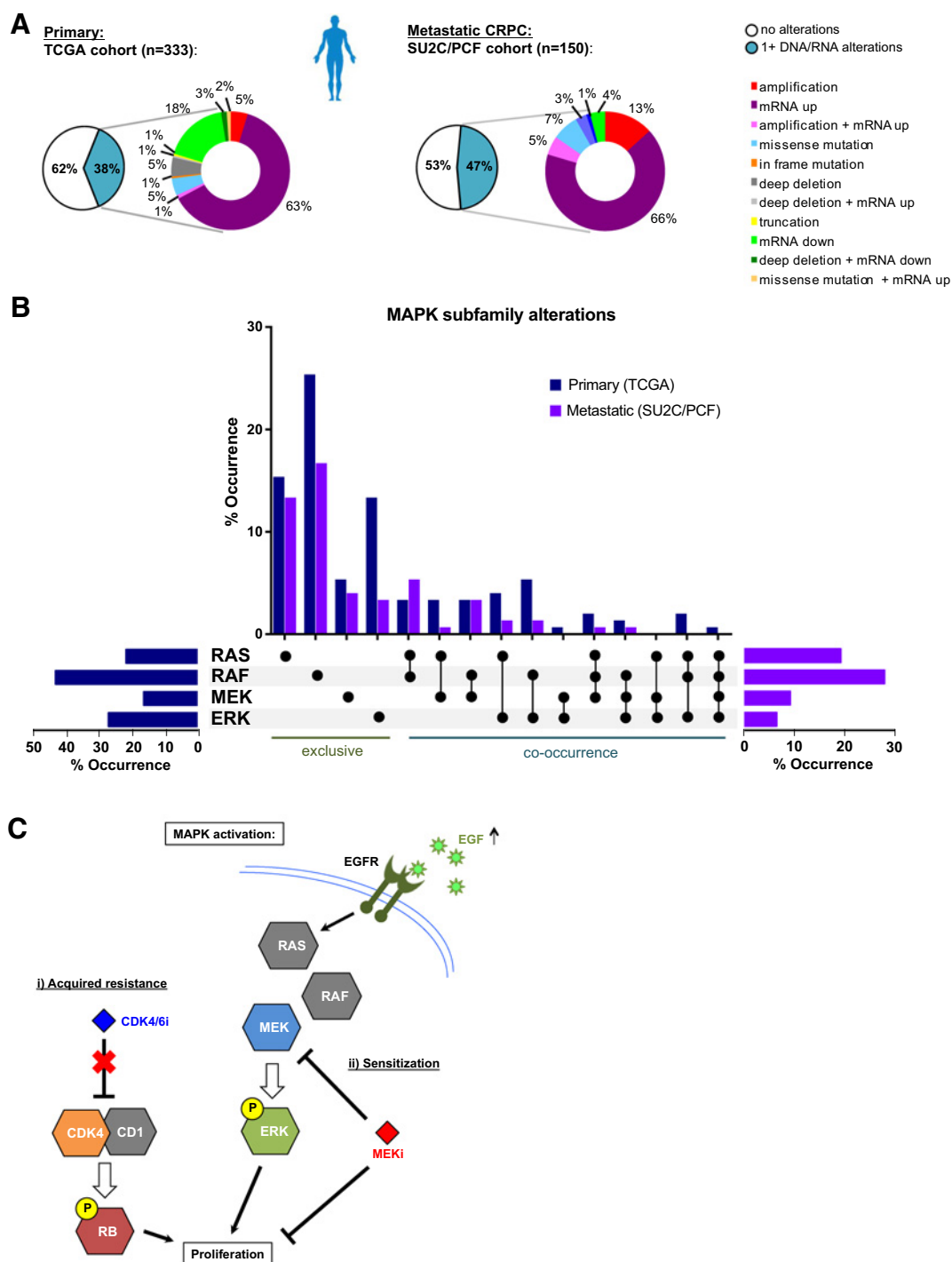
Acquired CDK4/6 inhibitor resistance promotes aggressive phenotypes. **A**, LNCaP PDR and parental cells were treated for 24 hours with 0.5  $\mu\text{mol/L}$  PD or CTRL, lysed, and immunoblotted for phospho-ERK1/2 (P-ERK1/2) and total ERK1/2 (t-ERK1/2). Results show hyperphosphorylation of ERK1/2 in the PDR lines compared with parental cells, whereas total protein levels are unchanged across the different models and conditions. These data indicate that the MAPK pathway is activated in the PDR models. **B**, EGF transcript level fold changes of LNCaP PDR1/2 relative to parental from RNAseq data (top, \* $q$  value < 0.1; error bars: standard error) show elevated EGF mRNA, resulting in increased EGF protein expression via Western blotting (bottom, numbers represent EGF quantification normalized to GAPDH, relative to parental CTRL). **C**, A time course experiment to assess cell proliferation via Trypan blue exclusion revealed that the PDR cells off PD selection are hyperproliferative compared with parental cells (\*significance was determined by a two-way ANOVA analysis performing a multivariate comparison of mean per time point for PDR vs. parental;  $P < 0.0001$ ). **D**, Cells were seeded in 6 replicates in serum-free media in a Fluoroblok transwell migration (without matrigel) or invasion (with matrigel) plates and allowed to migrate for 48 hours or invade for 72 hours to serum-rich (20%) media in the bottom of the well. PDR cells display enhanced migratory capacity and invasion through matrigel (\*Student  $t$  test:  $P < 0.05$  vs. parental). **E**, Clonogenic capacity of the PDR and parental lines was assessed by seeding cells at low density (5,000/well in a 6-well plate) in media supplemented with 0.6% agar and left to grow 3 weeks. The PDR lines displayed the ability to grow larger 3D colonies in agar. Images (left) show representative wells of triplicates. "+ctrl" are MAF cells with known clonogenicity. Colony sizes were determined via image pixel counts in FIJI (see Materials and Methods), and triplicates were pooled and plotted (right) as single dots according to size (Y axis). Line and whiskers show median and 95% confidence interval (CI). \*Statistical significance determined by a one-way ANOVA compared with parental. **F**, Subcutaneous xenograft tumor growth of LNCaP PDR and parental cells injected at  $3 \times 10^6$  cells in the flanks of athymic nude mice ( $n = 6$  per group) reveals accelerated tumor formation *in vivo*, graphed as % tumor-free survival (TFS) over time (left). \*Statistical significance determined via one-way ANOVA compared with parental. Table (right) shows reduced time to 50% tumor-free survival (TFS) and enhanced overall tumor take.

alterations are more common than RAS perturbations in either cohort (Fig. 6B). Taken together, data herein suggest that acquired CDK4/6 inhibitor resistance is associated with reduced RB expression and loss of function, and this coincides

with MAPK activation that may bypass CDK4/6-RB signaling to induce phenotypes of aggressive features and metastasis; however, this dependence confers sensitivity to MEK inhibitors that may be exploited therapeutically.

**Figure 5.**

CDK4/6i-resistant models become reliant on activated MAPK pathway and sensitized to MEK inhibition. **A**, LNCaP cells were treated for 24 hours with 0.5 or 1  $\mu\text{mol/L}$  MEK inhibitor (U0126) or CTRL and immunoblotted for p-ERK1/2, demonstrating loss of the hyperphosphorylation of ERK1/2 observed in the LNCaP PDR models when MEK is inhibited, confirming that the MAPK pathway is activated in the PDR models. MEK inhibition does not affect RB hyperphosphorylation (upper band tRB) or CDK4 phosphorylation, indicating a bypass of the RB cell-cycle checkpoint. **B**, Cell counting via Trypan blue exclusion after 6 days of 0.5 or 1  $\mu\text{mol/L}$  U0126 treatment reveals that the PDR models are sensitized to MEK inhibition (\*significant difference compared with corresponding treatment in parental cells). **C**, Invasion of PDR cells, but not parental cells, through matrigel in a Fluoroblok transwell system decreases with an MEK inhibitor (\*,  $P < 0.05$  vs. parental). **D**, Clonogenic assay shows reduction in both size (center) and total numbers of colonies (right) formed by the PDR models, whereas the parental cells are unresponsive to MEK inhibition (0.5  $\mu\text{mol/L}$  U0126). **E**, Cell counting with escalating doses of U0126 (0–0.5  $\mu\text{mol/L}$ ,  $t = 6$  days) shows a cooperative effect with 0.5  $\mu\text{mol/L}$  PD in PDR cells. **F**, LNCaP parental and PDR cells were injected sub-Q into the flanks of athymic nude mice. When tumors reached approximately 150  $\text{mm}^3$ , mice were treated with chow laced with trametinib (TRAM). Caliper measurements revealed that, although the parental tumors were unresponsive to the MEK inhibitor, the PDR models are sensitized to trametinib *in vivo* (error bars represent SEM).

**Figure 6.**

cBioportal analysis of clinical datasets reveals MAPK subfamily alterations in primary and metastatic tumors. **A**, cBioportal analyses of the TCGA clinical cohort show alterations in DNA and/or RNA for MAPK pathway genes in 128 of 333 primary prostate cancer patients (38%). Similarly, SU2C/PCF cohort reveals alterations in 71 of 150 patients with advanced prostate cancer (~47%). The majority of alterations in these patient datasets are gene amplification and/or transcriptional upregulation (~68% and ~85%, respectively). **B**, MAPK subfamily kinase analysis of alterations observed in primary (blue) and metastatic (purple) showing total percentages per subfamily (horizontal bar graphs), and exclusive versus cooccurring subfamily alterations (vertical bar graph, black dots indicate alteration, details per patient in Supplementary Fig. S7). **C**, Schematic of acquired CDK4/6 inhibitor resistance. The PDR models presented here have acquired resistance to CDK4/6 inhibition, resulting in proliferation and aggressive phenotypes. This acquired resistance is associated with MAPK pathway activation, creating a delicate reliance on this pathway that is independent of the RB cell-cycle checkpoint. This MAPK activation resulted in sensitization to MEK inhibition. EGF upregulation was observed in the PDR models, which activates the EGFR and likely activates MAPK signaling downstream. Although CDK4/6 inhibitors fail to block tumor growth in these models of acquired resistance, the sensitization to MEK inhibition provides new rationale for treating cancers that have acquired resistance to CDK4/6 inhibitors.

## Discussion

CDK4/6 inhibitors have shown clinical benefit in multiple tumor types, including breast cancer; however, these agents are unlikely to provide a durable cure, and development of resistance is anticipated. Studies herein developed preclinical models of CDK4/6 inhibitor resistance to identify major mechanisms and consequences of CDK4/6 bypass, wherein: (i) Acquired resistance to palbociclib resulted in broad CDK4/6 inhibitor resistance; (ii) Resistance was associated with MAPK activation, which (iii) conferred aggressive *in vitro* and *in vivo* phenotypes; and (iv) MAPK-activated, CDK4/6 inhibitor-resistant cancer cells are sensitized to MEK inhibitors. In summary, these studies identify MAPK induction in acquired CDK4/6 inhibitor resistance and nominate MEK inhibitors as a means to either prevent or treat CDK4/6 inhibitor-resistant cancer.

Several previous reports have approached CDK4/6 inhibitor resistance in various cancers from different perspectives, including clinical correlations with genetic alterations (6), correlation of RB loss-of-function gene signature (37), and an siRNA screen identifying PDK1 by targeting the whole kinome (7), which was not observed in the current study. To date, few studies have reported on acquired resistance modeling (8, 26, 31, 38), which largely focused on genomic alterations, gene amplifications, or deletions that could lead to CDK4/6 inhibitor resistance (including *RB1* loss and other aberrations in the CDK4/6-RB pathway). Although the observed genetic alterations are poised to affect CDK4/6 inhibitor efficacy, these may not reflect the molecular underpinnings of disease progression in patients that initially respond. Data herein suggest that cancer cells acquired resistance through aberrant inactivation of retained (albeit reduced) RB protein, likely via rewiring of the kinome to bypass CDK4/6 inhibition. Induction of the MAPK pathway was observed in CDK4/6 inhibitor resistance, determined by comparing phosphoproteomic and transcriptomic data and selecting alterations observed across PDR models. Although genomic and functional RB losses are associated with poor cancer outcomes (39) and progression to castration resistance in the context of prostate adenocarcinoma (11, 12, 40), the role for MAPK signaling in regulation of RB remains somewhat elusive. MAPK controls expression and function of D-type cyclins, and CDK4/6 requires direct binding to D-type cyclins to exert kinase function and phosphorylate RB; therefore, it could be speculated that the observed elevated MAPK signaling bypasses CDK4/6 inhibitors via cyclin D (Fig. 6C). Cyclin D1 elevation has been linked to early adaptation to palbociclib in breast cancer models, where it induced a noncanonical cyclin D1/CDK2 complex that restored RB phosphorylation under CDK4/6 inhibition (8). However, the CDK4/6 inhibitor-resistant models presented herein displayed no change in cyclin D1 levels (data not shown), and MEK inhibition did not affect hyperphosphorylation of RB (Fig. 5A; Supplementary Fig. S6A), demonstrating that MAPK activation does not mediate CDK4/6 inhibitor resistance directly, but likely presents a kinome bypass to promote tumor progression. Some studies have demonstrated intrinsic insensitivity to CDK4/6 inhibitors in cancer models with MAPK-activating mutations (41). Whole-exome sequencing revealed no reproducible alterations (data not shown), and none had relevance to MAPK signaling. Taken together, nongenomic MAPK activation, e.g., through upregulation of EGF observed in these models, likely mediates acquired resistance.

MAPK was identified as a major factor in kinome rewiring upon acquired CDK4/6 inhibitor resistance and associated with aggressive tumor phenotypes *in vitro* and *in vivo*. Activated MAPK signaling has been previously shown to promote prometastatic signaling and EMT (42). Invasion was attributed to ATF-2-mediated MMP-2 activation across various cancer models, including prostate (43). Moreover, MAPK activation has been associated with advanced stages of solid tumors (e.g. prostate, breast, lung; ref. 43), and therefore, it is not surprising that the PDR models displayed more aggressive phenotypes than the parental cells; thus, it is crucial to identify vulnerabilities of disease that progresses on CDK4/6 inhibitors and to develop alternative treatment regimens. Strikingly, activation of the MAPK pathway sensitized the CDK4/6 inhibitor-resistant cells to MEK inhibition, providing new rationale for testing MEK inhibitors in advanced prostate and other cancers that do not necessarily activate MAPK via classical KRAS mutations or RAF fusions. Moreover, phospho-ERK1/2, indicative of MAPK activity, can be determined via immunolabeling in clinical specimens from clinical trials (NCT02881242). It would be of interest to explore phospho-ERK1/2 as a clinical biomarker for resistance to CDK4/6 inhibitors. Alternatively, CDKs and MAPKs are known to form complex kinase networks that interact and regulate cellular processes involved in cell growth and death (27), and thus targeting these two nodes of the kinome would provide a novel opportunity for therapeutic intervention that could extend CDK4/6 inhibitor response or potentially prevent resistance altogether. These drug combinations are demonstrated to synergize in models of colorectal cancer (33), neuroblastoma (41), and even in MEK inhibitor-resistant melanoma models (32, 44). BRAF inhibitor-resistant melanoma may still respond to CDK4/6 inhibitors combined with mTOR inhibitors (45). One activated RAS melanoma study shows MEK and CDK4/6 inhibitors target complementary downstream networks inducing apoptosis and cell-cycle arrest, causing *in vivo* tumor regression (46). KRAS-mutant non-small cell lung cancer patients showed improved progression-free survival on palbociclib and an MEK inhibitor (PD-0325901; ref. 47). Considering the cooperative effect of a CDK4/6 and MEK inhibitor observed in the PDR models, these combinations merit prioritization for further preclinical cancer studies with the potential for future clinical trial development, either upfront to delay onset of CDK4/6 inhibitor resistance or when cancer progresses. As trametinib has already entered clinical trials in prostate adenocarcinoma (NCT02881242) and has been FDA-approved for melanoma (44), its clinical application could be considered in the context of CDK4/6 inhibitor resistance.

Clinically, MEK inhibitors are likely to be combined with AR signaling-targeted therapeutics (e.g., enzalutamide). Interestingly, the PDR models herein display a de-enrichment of the androgen response hallmark signature, suggesting a reduced reliance on AR, which could result in castration resistance. Therefore, it is paramount to assess whether acquired CDK4/6 inhibitor resistance can lead to enzalutamide resistance, and whether this can be circumvented with the addition of an MEK inhibitor, to define optimal strategies for clinical implementation.

Although induction of MAPK signaling, associated with aggressive phenotypes, was commonly observed across the PDR models, this does not rule out that other kinases identified in either of the

RNAseq and phosphoproteomics datasets may contribute to the development of resistance and cancer progression. Notably, Src motifs were highly enriched in the phosphoproteomic data alone, yet Src kinase is known to impinge on cyclin D/CDK4, and is an actionable target for which clinical agents (i.e., dasatinib) have already been developed (28). Although dasatinib in combination with abiraterone did not improve progression-free survival in metastatic CRPC (48), it merits further preclinical investigation in the context of CDK4/6 inhibitor resistance with the potential for additional therapeutic application.

In summary, the findings presented demonstrate that acquired CDK4/6 inhibitor resistance resulted in a kinase rewiring that not only promotes therapeutic resistance, but also confers aggressive phenotypes associated with tumor cell proliferation and invasion. Mechanistic investigation identified a reliance on MAPK activation and therefore nominates the MAPK signaling pathway as a potential therapeutic target for tumors bypassing CDK4/6 inhibition. These collective observations not only provide insight into the molecular underpinnings of acquired resistance to cell-cycle-targeted therapies, but also provide the basis for the next line of preclinical investigation and a rationale to develop novel combinatorial or sequential therapeutic strategies in the clinic.

### Disclosure of Potential Conflicts of Interest

No potential conflicts of interest were disclosed.

### Authors' Contributions

**Conception and design:** R. de Leeuw, M.J. Schiewer, M.A. Augello, K.E. Knudsen  
**Development of methodology:** R. de Leeuw, M.A. Augello, Z. Li, J.M. Drake, K.E. Knudsen

**Acquisition of data (provided animals, acquired and managed patients, provided facilities, etc.):** R. de Leeuw, N. Poudel Neupane, L.J. Brand, M.A. Augello, J.M. Drake, W.K. Kelly

**Analysis and interpretation of data (e.g., statistical analysis, biostatistics, computational analysis):** R. de Leeuw, C. McNair, L.J. Brand, M.A. Augello, Z. Li, L.C. Cheng, S.M. Courtney, E.S. Hazard, G. Hardiman, M.H. Hussain, J.M. Drake, W.K. Kelly, K.E. Knudsen

**Writing, review, and/or revision of the manuscript:** R. de Leeuw, C. McNair, M. J. Schiewer, L.J. Brand, Z. Li, L.C. Cheng, A. Yoshida, S.M. Courtney, E.S. Hazard, G. Hardiman, M.H. Hussain, J.A. Diehl, J.M. Drake, W.K. Kelly, K.E. Knudsen

**Administrative, technical, or material support (i.e., reporting or organizing data, constructing databases):** R. de Leeuw, M.J. Schiewer, N. Poudel Neupane, J.A. Diehl

**Study supervision:** R. de Leeuw, K.E. Knudsen

### Acknowledgments

This study was funded by the NIH R01CA176401 (K.E. Knudsen), R01CA217329 (K.E. Knudsen and W.K. Kelly), Prostate Cancer Foundation Young Investigator Awards (R. de Leeuw: Marjorie Katz Foundation 2016, J.M. Drake: 2015), Prostate Cancer Foundation Challenge Award (W.K. Kelly and K.E. Knudsen), Novartis (J.A. Diehl and K.E. Knudsen), R01CA093237 (J.A. Diehl), National Institute of General Medical Sciences of the NIH T32 GM008339 (L.C. Cheng), Department of Defense Prostate Cancer Research Program W81XWH-15-1-0236 (J.M. Drake), New Jersey Health Foundation grant (J.M. Drake), and Sidney Kimmel Cancer Center Shared Resources (5P30CA056036-17).

The costs of publication of this article were defrayed in part by the payment of page charges. This article must therefore be hereby marked *advertisement* in accordance with 18 U.S.C. Section 1734 solely to indicate this fact.

Received February 5, 2018; revised April 7, 2018; accepted May 3, 2018; published first May 8, 2018.

### References

- Barroso-Sousa R, Shapiro GI, Tolaney SM. Clinical development of the CDK4/6 inhibitors ribociclib and abemaciclib in breast cancer. *Breast Care (Basel)* 2016;11:167–73.
- Tripathy D, Bardia A, Sellers WR. Ribociclib (LEE011): mechanism of action and clinical impact of this selective cyclin-dependent kinase 4/6 inhibitor in various solid tumors. *Clin Cancer Res* 2017;23:3251–62.
- Garrido-Castro AC, Shom Goel S. CDK4/6 inhibition in breast cancer: mechanisms of response and treatment failure. *Curr Breast Cancer Rep* 2017;26–33.
- Vijayaraghavan S, Moulder S, Keyomarsi K, Layman RM. Inhibiting CDK in cancer therapy: current evidence and future directions. *Target Oncol* 2017;13:21–38.
- Comstock CE, Augello MA, Goodwin JF, de Leeuw R, Schiewer MJ, Ostrander WF Jr., et al. Targeting cell cycle and hormone receptor pathways in cancer. *Oncogene* 2013;32:5481–91.
- Gu G, Dustin D, Fuqua SA. Targeted therapy for breast cancer and molecular mechanisms of resistance to treatment. *Curr Opin Pharmacol* 2016;31:97–103.
- Jansen VM, Bholra NE, Bauer JA, Formisano L, Lee KM, Hutchinson KE, et al. Kinome-wide RNA interference screen reveals a role for PDK1 in acquired resistance to CDK4/6 inhibition in ER-positive breast cancer. *Cancer Res* 2017;77:2488–99.
- Herrera-Abreu MT, Palafox M, Asghar U, Rivas MA, Cutts RJ, Garcia-Murillas I, et al. Early adaptation and acquired resistance to CDK4/6 inhibition in estrogen receptor-positive breast cancer. *Cancer Res* 2016;76:2301–13.
- Taylor BS, Schultz N, Hieronymus H, Gopalan A, Xiao Y, Carver BS, et al. Integrative genomic profiling of human prostate cancer. *Cancer Cell* 2010;18:11–22.
- Robinson D, Van Allen EM, Wu YM, Schultz N, Lonigro RJ, Mosquera JM, et al. Integrative clinical genomics of advanced prostate cancer. *Cell* 2015;161:1215–28.
- Sharma A, Yeow WS, Ertel A, Coleman I, Clegg N, Thangavel C, et al. The retinoblastoma tumor suppressor controls androgen signaling and human prostate cancer progression. *J Clin Invest* 2010;120:4478–92.
- de Leeuw R, Berman-Booty LD, Schiewer MJ, Ciment SJ, Den RB, Dicker AP, et al. Novel actions of next-generation taxanes benefit advanced stages of prostate cancer. *Clin Cancer Res* 2015;21:795–807.
- Davis-Turak J, Courtney SM, Hazard ES, Glen WB Jr., da Silveira WA, Wesselman T, et al. Genomics pipelines and data integration: challenges and opportunities in the research setting. *Expert Rev Mol Diagn* 2017;17:225–37.
- Hardiman G, Savage SJ, Hazard ES, Wilson RC, Courtney SM, Smith MT, et al. Systems analysis of the prostate transcriptome in African-American men compared with European-American men. *Pharmacogenomics* 2016;17:1129–43.
- Love MI, Huber W, Anders S. Moderated estimation of fold change and dispersion for RNA-seq data with DESeq2. *Genome Biol* 2014;15:550.
- Edgar R, Domrachev M, Lash AE. Gene Expression Omnibus: NCBI gene expression and hybridization array data repository. *Nucleic Acids Res* 2002;30:207–10.
- Humphrey SJ, Azimifar SB, Mann M. High-throughput phosphoproteomics reveals in vivo insulin signaling dynamics. *Nat Biotechnol* 2015;33:990–5.
- Drake JM, Graham NA, Stoyanova T, Sedghi A, Goldstein AS, Cai H, et al. Oncogene-specific activation of tyrosine kinase networks during prostate cancer progression. *Proc Natl Acad Sci U S A* 2012;109:1643–8.
- Zimman A, Chen SS, Komisopoulou E, Titz B, Martinez-Pinna R, Kafi A, et al. Activation of aortic endothelial cells by oxidized phospholipids: a phosphoproteomic analysis. *J Proteome Res* 2010;9:2812–4.
- Scheltema RA, Hauschild JP, Lange O, Hornburg D, Denisov E, Damoc E, et al. The Q Exactive HF, a Benchtop mass spectrometer with a pre-filter,

- high-performance quadrupole and an ultra-high-field Orbitrap analyzer. *Mol Cell Proteomics* 2014;13:3698–708.
21. Cox J, Mann M. MaxQuant enables high peptide identification rates, individualized p.p.b.-range mass accuracies and proteome-wide protein quantification. *Nat Biotechnol* 2008;26:1367–72.
  22. Vizcaino JA, Csordas A, Del-Toro N, Dianas JA, Griss J, Lavidas I, et al. 2016 update of the PRIDE database and its related tools. *Nucleic Acids Res* 2016;44:11033.
  23. Drake JM, Paull EO, Graham NA, Lee JK, Smith BA, Titz B, et al. Phosphoproteome integration reveals patient-specific networks in prostate cancer. *Cell* 2016;166:1041–54.
  24. Eisen MB, Spellman PT, Brown PO, Botstein D. Cluster analysis and display of genome-wide expression patterns. *Proc Natl Acad Sci U S A* 1998;95:14863–8.
  25. Saldanha AJ. Java Treeview—extensible visualization of microarray data. *Bioinformatics* 2004;20:3246–8.
  26. Dean JL, Thangavel C, McClendon AK, Reed CA, Knudsen ES. Therapeutic CDK4/6 inhibition in breast cancer: key mechanisms of response and failure. *Oncogene* 2010;29:4018–32.
  27. Varjosalo M, Keskitalo S, Van Droogen A, Nurkkala H, Vichalkovski A, Aebersold R, et al. The protein interaction landscape of the human CMGC kinase group. *Cell Rep* 2013;3:1306–20.
  28. Patel A, Sabbini H, Clarke A, Somanath PR. Novel roles of Src in cancer cell epithelial-to-mesenchymal transition, vascular permeability, micro-invasion and metastasis. *Life Sci* 2016;157:52–61.
  29. Tran KA, Cheng MY, Mitra A, Ogawa H, Shi VY, Olney LP, et al. MEK inhibitors and their potential in the treatment of advanced melanoma: the advantages of combination therapy. *Drug Des Devel Ther* 2016;10:43–52.
  30. Butti R, Das S, Gunasekaran VP, Yadav AS, Kumar D, Kundu GC. Receptor tyrosine kinases (RTKs) in breast cancer: signaling, therapeutic implications and challenges. *Mol Cancer* 2018;17:34.
  31. Taylor-Harding B, Aspuria PJ, Agadjanian H, Cheon DJ, Mizuno T, Greenberg D, et al. Cyclin E1 and RTK/RAS signaling drive CDK inhibitor resistance via activation of E2F and ETS. *Oncotarget* 2015;6:696–714.
  32. Yadav V, Burke TF, Huber L, Van Horn RD, Zhang Y, Buchanan SG, et al. The CDK4/6 inhibitor LY2835219 overcomes vemurafenib resistance resulting from MAPK reactivation and cyclin D1 upregulation. *Mol Cancer Ther* 2014;13:2253–63.
  33. Lee MS, Helms TL, Feng N, Gay J, Chang QE, Tian F, et al. Efficacy of the combination of MEK and CDK4/6 inhibitors in vitro and in vivo in KRAS mutant colorectal cancer models. *Oncotarget* 2016;7:39595–608.
  34. Augello MA, Berman-Booty LD, Carr R 3rd, Yoshida A, Dean JL, Schiewer MJ, et al. Consequence of the tumor-associated conversion to cyclin D1b. *EMBO Mol Med* 2015;7:628–47.
  35. Palanisamy N, Ateeq B, Kalyana-Sundaram S, Pflueger D, Ramnarayanan K, Shankar S, et al. Rearrangements of the RAF kinase pathway in prostate cancer, gastric cancer and melanoma. *Nat Med* 2010;16:793–8.
  36. Cancer Genome Atlas Research N. The molecular taxonomy of primary prostate cancer. *Cell* 2015;163:1011–25.
  37. Malorni L, Piazza S, Ciani Y, Guarducci C, Bonechi M, Biagioni C, et al. A gene expression signature of retinoblastoma loss-of-function is a predictive biomarker of resistance to palbociclib in breast cancer cell lines and is prognostic in patients with ER positive early breast cancer. *Oncotarget* 2016;7:68012–22.
  38. Yang C, Li Z, Bhatt T, Dickler M, Giri D, Scaltriti M, et al. Acquired CDK6 amplification promotes breast cancer resistance to CDK4/6 inhibitors and loss of ER signaling and dependence. *Oncogene* 2017;36:2255–64.
  39. McNair C, Xu K, Mandigo AC, Benelli M, Leiby B, Rodrigues D, et al. Differential impact of RB status on E2F1 reprogramming in human cancer. *J Clin Invest* 2018;128:341–58.
  40. Bosco EE, Knudsen ES. RB in breast cancer: at the crossroads of tumorigenesis and treatment. *Cell Cycle* 2007;6:667–71.
  41. Hart LS, Rader J, Raman P, Batra V, Russell MR, Tsang M, et al. Preclinical therapeutic synergy of MEK1/2 and CDK4/6 inhibition in neuroblastoma. *Clin Cancer Res* 2017;23:1785–96.
  42. Mulholland DJ, Kobayashi N, Rusetti M, Zhi A, Tran LM, Huang J, et al. Pten loss and RAS/MAPK activation cooperate to promote EMT and metastasis initiated from prostate cancer stem/progenitor cells. *Cancer Res* 2012;72:1878–89.
  43. Koul HK, Pal M, Koul S. Role of p38 MAP kinase signal transduction in solid tumors. *Genes Cancer* 2013;4:342–59.
  44. Teh JL, Purwin TJ, Greenawalt EJ, Chervoneva I, Goldberg A, Davies MA, et al. An in vivo reporter to quantitatively and temporally analyze the effects of CDK4/6 inhibitor-based therapies in melanoma. *Cancer Res* 2016;76:5455–66.
  45. Yoshida A, Lee EK, Diehl JA. Induction of therapeutic senescence in vemurafenib-resistant melanoma by extended inhibition of CDK4/6. *Cancer Res* 2016;76:2990–3002.
  46. Kwong LN, Costello JC, Liu H, Jiang S, Helms TL, Langsdorf AE, et al. Oncogenic NRAS signaling differentially regulates survival and proliferation in melanoma. *Nat Med* 2012;18:1503–10.
  47. Shapiro GI, Hilton J, Gandhi L, Chau N, Cleary J, Wolansky A, et al. Phase I dose escalation study of the CDK4/6 inhibitor palbociclib in combination with the MEK inhibitor PD-0325901 in patients with RAS mutant solid tumors. Abstract in: Proceedings of the American Association for Cancer Research Annual Meeting 2017; 2017 Apr 1–5; Washington, DC. Philadelphia (PA): AACR; *Cancer Res* 2017;77(13 Suppl):Abstract nr CT046.
  48. Dorff TB, Quinn DI, Pinski JK, Goldkorn A, Sadeghi S, Tsao-Wei D, et al. Randomized phase II trial of abiraterone ± dasatinib for patients with metastatic castration-resistant prostate cancer (mCRPC). *J Clin Oncol* 2017;35:6s.



# Clinical Cancer Research

## MAPK Reliance via Acquired CDK4/6 Inhibitor Resistance in Cancer

Renée de Leeuw, Christopher McNair, Matthew J. Schiewer, et al.

*Clin Cancer Res* Published OnlineFirst May 8, 2018.

**Updated version** Access the most recent version of this article at:  
doi:[10.1158/1078-0432.CCR-18-0410](https://doi.org/10.1158/1078-0432.CCR-18-0410)

**Supplementary Material** Access the most recent supplemental material at:  
<http://clincancerres.aacrjournals.org/content/suppl/2018/05/08/1078-0432.CCR-18-0410.DC1>  
<http://clincancerres.aacrjournals.org/content/suppl/2018/07/06/1078-0432.CCR-18-0410.DC2>


**E-mail alerts** [Sign up to receive free email-alerts](#) related to this article or journal.

**Reprints and Subscriptions** To order reprints of this article or to subscribe to the journal, contact the AACR Publications Department at [pubs@aacr.org](mailto:pubs@aacr.org).

**Permissions** To request permission to re-use all or part of this article, use this link  
<http://clincancerres.aacrjournals.org/content/early/2018/06/27/1078-0432.CCR-18-0410>.  
Click on "Request Permissions" which will take you to the Copyright Clearance Center's (CCC) Rightslink site.

Review

# Nutraceutical or Pharmacological Potential of *Moringa oleifera* Lam.

Xianjuan Kou <sup>1</sup>, Biao Li <sup>1</sup>, Julia B. Olayanju <sup>2</sup>, Justin M. Drake <sup>2,3,4,\*</sup> and Ning Chen <sup>1,\*</sup> 

<sup>1</sup> Tianjiu Research and Development Center for Exercise Nutrition and Foods, Hubei Key Laboratory of Exercise Training and Monitoring, College of Health Science, Wuhan Sports University, Wuhan 430079, China; kouxianjuan@126.com (X.K.); 17375002427@163.com (B.L.)

<sup>2</sup> Rutgers Cancer Institute of New Jersey, New Brunswick, NJ 08901, USA; olayanmo@scarletmail.rutgers.edu

<sup>3</sup> Department of Medicine, Division of Medical Oncology, Rutgers Robert Wood Johnson Medical School, New Brunswick, NJ 08901, USA

<sup>4</sup> Department of Pharmacology, Rutgers Robert Wood Johnson Medical School, New Brunswick, NJ 08901, USA

\* Correspondence: jd1135@cinj.rutgers.edu (J.M.D.); nchen510@gmail.com (N.C.); Tel.: +1-732-235-7017 (J.M.D.); +86-27-6784-6140 (N.C.); Fax: +1-732-235-8681 (J.M.D.); +86-27-6784-6140 (N.C.)

Received: 8 February 2018; Accepted: 7 March 2018; Published: 12 March 2018

**Abstract:** *Moringa oleifera* Lam. (*M. oleifera*), which belongs to the Moringaceae family, is a perennial deciduous tropical tree, and native to the south of the Himalayan Mountains in northern India. *M. oleifera* is rich in proteins, vitamin A, minerals, essential amino acids, antioxidants, and flavonoids, as well as isothiocyanates. The extracts from *M. oleifera* exhibit multiple nutraceutical or pharmacological functions including anti-inflammatory, antioxidant, anti-cancer, hepatoprotective, neuroprotective, hypoglycemic, and blood lipid-reducing functions. The beneficial functions of *M. oleifera* are strongly associated with its phytochemicals such as flavonoids or isothiocyanates with bioactivity. In this review, we summarize the research progress related to the bioactivity and pharmacological mechanisms of *M. oleifera* in the prevention and treatment of a series of chronic diseases—including inflammatory diseases, neuro-dysfunctional diseases, diabetes, and cancers—which will provide a reference for its potential application in the prevention and treatment of chronic diseases or health promotion.

**Keywords:** *Moringa oleifera*; pharmacological potential; chronic disease; flavonoids; cancer; metabolism

## 1. Introduction

*Moringa oleifera* Lam. (*M. oleifera*) is a cruciferous plant that belongs to the Moringaceae family. *M. oleifera* is commonly called horseradish tree or drumstick tree by locals and is a popular staple in different parts of the world. *M. oleifera* is consumed not only for its nutritional values but also its medical benefits [1]. *M. oleifera* leaves are rich in beta-carotene, vitamin C, vitamin E, and polyphenols and are a good source of natural antioxidants [2]. Currently, *M. oleifera* is reported to enhance a broad range of biological functions including anti-inflammatory, anti-cancer, hepatoprotective, and neuroprotective functions [1,3,4]. In addition, many studies have revealed its therapeutic value including anti-diabetes, anti-rheumatoid arthritis, anti-atherosclerosis, anti-infertility, pain relief, anti-depression, and diuretic and thyroid regulation [5,6]. Due to these reported functions, the bioactivity of *M. oleifera* has gained tremendous attention over the last decade, thereby leading to the increasing exploration and understanding of its pharmacological functions and underlying mechanisms. In this review, we summarize current research progress related to its nutraceutical or

pharmacological functions and corresponding mechanism of action, as well as potential benefits for human health.

## 2. Antimicrobial Activity

A series of investigations have been conducted to evaluate the antimicrobial activity of *Moringa* species with the reports that the extracts from different parts of the *M. oleifera* plant—including seeds, stem bark, leaves, and root bark—can exert antimicrobial potential [7–12]. For example, the water-soluble lectin isolated from the extract of *M. oleifera* seeds has inhibitory effects on the growth, survival, and cell permeability of multiple species of pathological bacteria [9]. In addition, the extract of *M. oleifera* roots are reported to contain an active antibiotic pterygospermin that has powerful antibacterial and fungicidal effects [12]. The aglycone of deoxy-niazimicine isolated from the chloroform fraction of an ethanol extract of *M. oleifera* root bark is found to be responsible for antibacterial and antifungal activities [10], while the juice from the stem bark exhibits an antibacterial effect against *Staphylococcus aureus* [8]. The aqueous and ethanolic extracts from the leaves of *M. oleifera* have promising anti-bacterial properties, with strong inhibitory effects on Gram-positive species (*Staphylococcus aureus* and *Enterococcus faecalis*) over Gram-negative species (*Escherichia coli*, *Salmonella*, *Pseudomonas aeruginosa*, *Vibrio parahaemolyticus*, and *Aeromonas caviae*) [11]. In addition, the ethanol extract from leaves of *M. oleifera* has demonstrated the highest mean inhibitory zone against the growth of both *S. aureus* and *Streptococcus* mutants during the comparison between experimental toothpaste containing the extract from different parts of the *M. oleifera* plant versus mouthwash solutions [10].

## 3. Anti-Inflammation

Inflammation is a physiological response to protect the body against infection and restore tissue injury [13]. However, long-term chronic inflammation may lead to the development of chronic inflammation-associated diseases and disorders such as diabetes, cancer, autoimmune diseases, cardiovascular diseases, sepsis, colitis, and arthritis [14,15]. Inflammatory cytokines such as interleukin-1 beta (IL-1 $\beta$ ) and tumor necrosis factor alpha (TNF- $\alpha$ ) can upregulate the production of nitric oxide (NO) and prostaglandin E2 (PGE-2), thus stimulating the expression or enhancing the activity of inducible NO synthase (iNOS), cyclooxygenase-2 (COX-2), and microsomal PGE synthase-1 (mPGES-1) in target cells [16]. *M. oleifera* has been reported to not only decrease the production of TNF- $\alpha$ , IL-6, and IL-8 in response to both lipopolysaccharide (LPS) and cigarette smoke extract (CSE)-stimulated human monocyte-derived macrophages (MDM), but also inhibit the expression of RelA, a gene in nuclear factor-kappa B (NF- $\kappa$ B) p65 signaling during inflammation [17]. Moreover, in acetic acid-induced acute colitis rat models, oral administration of hydro-alcoholic extract from *M. oleifera* seeds (MSHE) at three increasing doses (50, 100, and 200 mg/kg) can reduce distal colon weight as a marker of inflammation and tissue edema, ulcer and mucosal inflammation severity, crypt damage, invasion involvement, total colitis index, and myeloperoxidase (MPO) activity when compared with the untreated groups [18]. So it can be considered as an alternative remedy for inflammatory bowel disease (IBD) and/or the preventive strategy of its recurrence in acetic acid-induced acute colitis rat models. Furthermore, previous studies have documented that *M. oleifera* can selectively inhibit the production of iNOS and COX-2 and significantly inhibit the secretion of NO and other inflammatory markers—including PGE-2, TNF- $\alpha$ , IL-6, and IL-1 $\beta$ —in lipopolysaccharide (LPS)-induced RAW264.7 cells. Meanwhile, it can induce the production of IL-10 in LPS-stimulated macrophages in a dose-dependent manner, thereby contributing to the suppression of NF- $\kappa$ B signaling pathway [19,20]. The novel bioactive phenolic glycosides 4-[(2-O-acetyl- $\alpha$ -L-rhamnosyloxy)benzyl] isothiocyanate (RBITC) from *M. oleifera* inhibited expression of COX-2 and iNOS at both the protein and mRNA levels through inhibiting major upstream signaling pathways mitogen-activated protein kinases (MAPKs) and NF- $\kappa$ B [21]. In vivo, an isothiocyanate-enriched *M. oleifera* seed extract (MSE) has shown a reduction in carrageenan-induced rat paw edema, which is comparable to aspirin. In vitro, its major isothiocyanate (MIC-1) at the dose of 5  $\mu$ M can significantly reduce inflammatory cytokines.

Further, MIC-1 at a dose of 10  $\mu\text{M}$  can also have stronger effects, when compared to curcumin, on upregulating nuclear factor (erythroid-derived 2)-like 2 (Nrf2) target genes NAD(P)H: quinone oxidoreductase 1 (NQO1), glutathione S-transferase pi 1 (GSTP1), and heme oxygenase 1 (HO-1) [22].

Finally, in a clinical study of 15 patients with urinary tract infection, Maurya and Singh observed that 66.67% of patients were completely cured of their symptoms after a three-week treatment with *M. oleifera* bark extract, while 13.33% reported moderate relief from their symptoms. However, in the control group, 46.67% of patients were cured, 26.66% of patients were relieved from their symptoms, 6.67% of patients had no symptom change, and 20% relapsed [23]. This study suggests *M. oleifera* bark extract is effective on most of the cardinal symptoms of urinary tract infection. These findings further support the traditional application of *M. oleifera* as an effective treatment for inflammation. The corresponding molecular mechanisms are summarized in Figure 1.

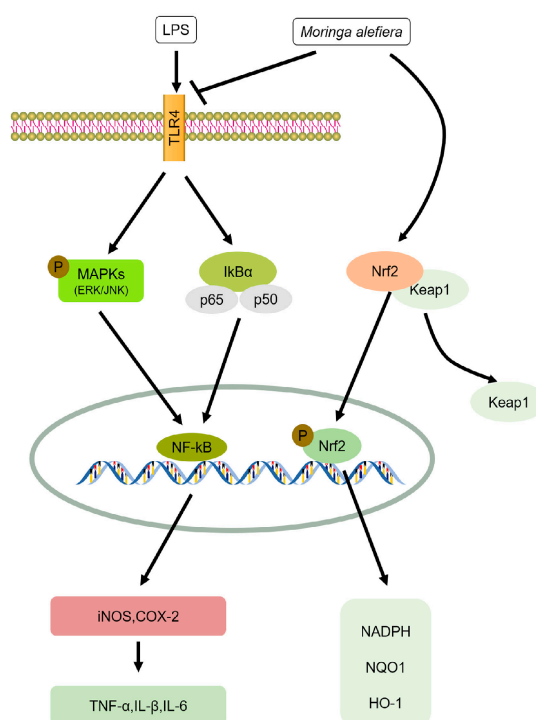


**Figure 1:** The anti-inflammatory mechanisms of *M. oleifera*. Schematic diagram illustrating the signaling pathways involved in the inhibitory effect of *M. oleifera* on proteins associated with LPS-induced inflammation summarized from a series of previous studies [17,19–22]. Toll-like receptor 4, TLR4; Nicotinamide adenine dinucleotide phosphate, NADPH; inhibitor of kappa B, IκB; IκB kinase, IKK; nuclear factor-erythroid derived 2-like 2, Nrf2; nuclear factor-κB, NF-κB; inducible NO synthase-2, iNOS; cyclooxygenase-2, COX-2; tumor necrosis factor-α, TNF-α; interleukin-1β, IL-1β; interleukin-6, IL-6; quinone oxidoreductase 1, NQO1; heme oxygenase 1, HO-1.

#### 4. Antioxidant and Hepatoprotective Effects

Usually, natural compounds rich in polyphenols have strong antioxidant properties and can decrease oxidative damage in tissues by scavenging free radical [24–26]. The methanol extract of *M. oleifera* leaves contains chlorogenic acid, rutin, quercetin glucoside, and kaempferol rhamnoglycoside, whereas in the root and stem barks, several procyanidin peaks are detected [27]. Similarly, the *Moringa* genus has high antioxidant activity mainly due to its high content of bioactive polyphenols [28,29]. Fortunately, as a medicinal plant, *M. oleifera* extracts from both mature and

Similarly, the *Moringa* genus has high antioxidant activity mainly due to its high content of bioactive polyphenols [28,29]. Fortunately, as a medicinal plant, *M. oleifera* extracts from both mature and tender leaves exhibit strong antioxidant activity against free radicals and prevent oxidative damage due to the enrichment of polyphenols [29].

Lipid peroxidation (LPO) plays an important role in the metabolism of the body, which can lead to cell lesion and nerve damage if internal and external balances are broken. In a radiation-induced Swiss albino mouse model with oxidative stress, the pre-treatment with *M. oleifera* leaf extract for 15 consecutive days can effectively restore glutathione (GSH) level and prevent lipid peroxidation in liver [30,31]. This protective effect may be related to a variety of phytochemicals such as ascorbic acid and phenols (catechin, epicatechin, ferulic acid, ellagic acid, and myricetin) through scavenging radiation-induced free radicals. Moreover, in an acute paracetamol (PCM)-induced hepatotoxicity model, the pre-administration of the hydro-ethanolic extract of *M. oleifera* before oral administration of PCM at the dose of 3 g/kg to male Sprague Dawley rats results in a significant reduction of lipid peroxidation; interestingly, the levels of glutathione-S transferase (GST), glutathione peroxidase (GPx), and glutathione reductase (GR) are restored to the normal levels in the group subjected to the pre-administration of *M. oleifera* extract [32]. These results are equivalent to the positive control silymarin (200 mg/kg; p.o.) and exhibits similar results to other research teams [33,34]. Furthermore, daily oral post-treatment with *M. oleifera* leaf extract (100, 200, and 400 mg/kg body weight) of the rats with carbon tetrachloride (CCl<sub>4</sub>)-induced lipid peroxidation and hepatic damage for 60 consecutive days can protect CCl<sub>4</sub>-induced hepatotoxicity, which may be due to the presence of total phenols and flavonoids in the extract and/or the purified compounds such as  $\beta$ -sitosterol, quercetin and kaempferol [35]. Similarly, previous finding has also demonstrated that the post-treatment of *M. oleifera* leaf extract for consecutive 28 days can protect from cadmium-induced hepatotoxicity of the rats through suppressing the elevated alkaline phosphatase (ALP), glutamic oxaloacetic transaminase (aspartate aminotransferase, AST), glutamic pyruvic transaminase (alanine aminotransferase, ALT), and LPO levels and increasing superoxide dismutase (SOD) level [36]. Furthermore, the oral administration of *M. oleifera* extract also reveals a significant protective action to the liver damage induced by anti-tubercular drug such as isoniazid (INH), rifampicin (RMP), or pyrazinamide (PZA), as evidenced by the recovered AST, ALT, ALP, and bilirubin levels in serum, as well as the reduced lipid peroxidation in liver [36]. The extract of *M. oleifera* leaves can also effectively reduce high-fat-diet (HFD)-induced liver damage of mice [37]. Compared with the model group, the treatment with the leaf extract of *M. oleifera* protects HFD-induced liver damage as indicated by recusing the abnormal histopathological change and AST, ALT, and ALP activity, and stimulates a significant increase in endogenous antioxidant parameters [37]. Overall, these data suggest that the extract of *M. oleifera* has both preventive and curative functions for liver tissue.

## 5. Neuroprotective Effect

Dementia—a serious loss of global cognitive capacity including impaired memory, attention, language, and problem-resolving capacity—is a progressive neurodegenerative disorder that is growing worldwide due to an increased aging population [38]. Alzheimer's disease (AD) is the most common cause of dementia that is an irretrievable chronic neurodegenerative disease. ROS-associated with oxidative stress can induce cell apoptosis through mitochondrial dysfunction, and result in the damage of lipids, proteins and DNA [39,40]. Previous studies have shown that oxidative stress is believed to be a primary factor in neurodegenerative diseases including AD, Parkinson's disease (PD) and Huntington's disease (HD), as well as amyotrophic lateral sclerosis (ALS) [41]. Therefore, antioxidants have gained extensive attention as promising therapeutic agents for neurodegenerative diseases. Although many efforts in the discovery of new treatments for AD have been uncovered, none of the existing treatments have been shown to slow or halt the progression of this disease [42]. Due to the high cost of synthetic anti-dementia drugs and corresponding side effects, natural products containing flavonoids have gained tremendous interest as candidates for the prevention and/or

treatment of neurodegenerative disorders [39,42]. The extract from the leaves of *M. oleifera* are thought to exhibit both antioxidant activity and nootropic effects. Indeed, the alcoholic extract of *M. oleifera* leaves can combat oxidative stress in a rat model with AD induced by colchicines [43]. In 1-methyl-4-phenyl-1,2,3,6-tetrahydropyridine (MPTP)-induced sub-acute PD mouse model, the pre-treatment with isothiocyanate isolated from the extract of *M. oleifera* seeds for one week not only modulated the signal pathway for inflammation, but also regulated the signaling pathways associated with oxidative stress and apoptosis. The efficacy of *M. oleifera* in countering inflammatory signal pathway has been corroborated by in vitro results, which can be used in clinical practice as a useful drug for the prevention or treatment of PD [44].

*M. oleifera* has been shown to stimulate neuronal outgrowth and survival under harsh treatment conditions [45,46]. For example, a concentration of 30 µg/mL ethanol extract from the leaves of *M. oleifera* can promote the outgrowth of neurites and neuronal differentiation from primary embryonic neurons in a concentration-dependent manner [45]. Similarly, *M. oleifera* leaf extract has been observed to increase the number and length of dendrites and axonal branches, the length of axons, and eventually facilitate synaptogenesis [45]. Previous studies have also demonstrated that *M. oleifera* leaf extract can successfully improve spatial memory and neurodegeneration in cornu ammonis 1 (CA1), CA2, and CA3 regions, and dentate gyrus of hippocampal tissues [46]. Mechanically, it can also decrease malondialdehyde (MDA) levels and acetylcholinesterase (AChE) activity, but can increase SOD and catalase (CAT) activity. In addition, compared with the aluminum-alone group, the administration of *M. oleifera* leaf extract at the dose of 300 mg/kg for 28 consecutive days in rats with aluminum chloride-induced temporal cortical degeneration protected against aluminum chloride-induced neurotoxicity of the temporal cortex of rats by decreasing the expression of neuron specific enolase (NSE) and glial fibrillary acidic protein (GFAP) [47].

As more people struggle with depression, a serious health problem in most countries, the need for efficient intervention or treatment options is paramount. Because of the side effects of anti-depressants during long-term application, the discovery of safer anti-depressant herbal remedies is necessary. *M. oleifera* is a potential remedy for treating nervous system disorders acting as a memory-enhancing agent. A previous study [48] in standardized mouse models with depression confirmed that the anti-depressant effect of the alcoholic extract from *M. oleifera* leaves may be invoked through the noradrenergic-serotonergic neurotransmission pathway after administering *M. oleifera* extract at the daily dose of 200 mg/kg coupled with fluoxetine at the daily dose of 10 mg/kg for 14 consecutive days. This suggests that the combinatorial administration of *M. oleifera* and fluoxetine or other selective serotonin reuptake inhibitor (SSRI) drugs seems to have promising potential.

## 6. Anticancer Property of *M. oleifera*

Cancer is the second leading cause of death in the United States and a prominent cause of death worldwide [49]. Effective therapeutic approaches have been adopted to treat various types of cancers, however, resistance and/or toxicity creates the need for more effective treatment options.

Several epidemiological studies have established a negative correlation between consumption of cruciferous vegetables and risk of breast, lung, and colon cancer [50,51]. *M. oleifera* leaf and bark extracts have been shown to effectively inhibit the growth of breast, pancreatic, and colorectal cancer cells [52,53]. Gas chromatography-mass spectroscopy (GC-MS) analysis by Alsamari and colleagues documented 12 different compounds in *M. oleifera* extract, 3 of which may have anticancer properties [52]. Isothiocyanates, which have been described as a potent anticancer compound, occur naturally in its precursor form, glucosinolates, in an intact plant. Glucosinolates are hydrolyzed in a reaction catalyzed by the enzyme myrosinase to produce isothiocyanate when the intact plant is disrupted [54].

Isothiocyanates have been extensively studied for their anticancer properties. Xiao et al. have reported that allyl isothiocyanates (AITC) inhibits the growth of androgen independent (PC-3) and androgen dependent (LNCaP) human prostate cancer cells [55]. This study also established

a correlation between the inhibition of growth of PC-3 cells in the presence of AITC and gap2/mitosis (G2/M) cell accumulation coupled with apoptosis. Reduction in the protein levels of cyclin-dependent kinase 1 (CDK1), cell division cycle protein 25B (CDC25B), and CDC25C was observed after treating PC-3 and LNCaP cells with AITC for 24 h. Boreddy and colleagues treated mice with BxPC-3 tumor xenografts with benzyl isothiocyanates (BITC) and observed a 43% reduction in tumor growth. This study also showed a reduction in phosphorylation of phosphatidylinositide 3-kinase (PI3K), protein kinase B (AKT), pyruvate dehydrogenase kinase (PDK), forkhead box O3A (FOXO3A), FOXO1, and mammalian target of rapamycin (mTOR) in response to treatment with BITC. Phenylethyl isothiocyanates (PEITC) have been shown to reduce cancer growth by inhibiting AKT [56].

While studies involving moringa isothiocyanates are limited, several studies with other isothiocyanates, along with our preliminary studies in vitro with moringa isothiocyanates, suggest that this compound may open new frontiers in cancer therapeutics.

### 6.1. Regulation of Cell Proliferation

Based on previous studies [52,57], *M. oleifera* has been confirmed to selectively inhibit the proliferation of different cell lines including lung cancer A549, human hepatocellular carcinoma HepG2, breast cancer MDA-MB-231, and colon cancer HCT-8 cells. Notably, the inhibitory rate of *M. oleifera* on the growth of neuroblastoma SH-SY5Y cells is up to 95%. In addition, *M. oleifera* leaf extract has been reported to have an anti-proliferative effect on KB cells, which is evaluated by cell morphologic change, cell viability, and internucleosomal DNA fragmentation [58].

### 6.2. Cell Cycle Arrest and Apoptosis

Apoptosis has been recognized to play an important role in maintaining cellular homeostasis through selective removal of damaged cells. The ability to induce apoptosis is a major mechanism of certain anti-tumor drugs. Previous studies have reported that isothiocyanates isolated from *M. oleifera* leaf extract are able to induce apoptosis in different cancer cells [58,59]. These studies have also reported that *M. oleifera* extract can inhibit the proliferation of cancer cells, but the molecular mechanisms are still limited. Various signaling pathways or associated mechanisms involved in apoptosis during the application of *M. oleifera* are highly correlated with the activation of caspase signaling. The extract from *M. oleifera* at different doses can lead to the increase in average sub-G1 populations during a 6 h administration in A549 lung cancer cells. Meanwhile, caspase-3 is downregulated and cleaved caspase-3 is upregulated upon the administration of *M. oleifera* leaf extract in a dose-dependent manner [60]. In addition, the administration of *M. oleifera* leaf extract resulted in a time-dependent increase of phosphor-c-Jun N-terminal kinase (p-JNK) and phosphor-extracellular signal-related kinase (p-ERK), without changes in total JNK or ERK protein, hinting at the possibility of a pro-apoptotic role of *M. oleifera* via activation of these kinases in human melanoma A2058 cells [61]. Interestingly, in cholangiocarcinoma (CCA), the phosphorylation levels of phospho-p44/42 MAPK (ERK1/2) and phospho-p38 MAPK increased in *M. oleifera* seed extract treated RMCCA1 cells, suggesting that the activity levels of anti- and pro-apoptotic signaling proteins may determine the apoptotic nature of this compound [62]. The extracts from *M. oleifera* leaves and bark also effectively arrest cell cycle progression at the G2/M phase and increase apoptosis in breast and colorectal cancer cell lines such as MDA-MB-231 and HCT-8 cells, which could be attributed to the bioactive compounds such as eugenol, isopropyl isothiocyanate, D-allose, and hexadecanoic acid ethyl ester [52].

Additionally, the checkpoint failure of cell cycle usually causes genetic mutations and genomic rearrangements, thereby causing genetic instability as one of the major factors of cancer progression. Increasing evidence suggests that a variety of anti-cancer agents can induce cell cycle arrest at a certain checkpoint, thus inducing the apoptosis of cancer cells [63,64]. Jung has also found that cyclin D1 can be significantly downregulated in *M. oleifera* aqueous leaf extract-treated cells in a dose-dependent manner. Moreover, the treatment with *M. oleifera* leaf extract can induce an elevation in the sub-G1 cell population during cell cycle in a dose-dependent manner in human pancreatic cancer cell line

(PANC-1 cells) and reduce the expression of p65, p-Ik $\beta$ , and Ik $\beta$  proteins [53], which further supports that *M. oleifera* leaf extract is a potential phytochemical to target cancer cells through arresting cell cycle.

### 6.3. Synergistic Effect on Chemotherapeutic Drugs

Multi-drug resistance (MDR) is one of the major reasons for chemotherapeutic failure. MDR to chemotherapeutic drugs often leads to reduced treatment efficacy and cancer recurrence [65]. It is well known that phytochemical compounds have the advantages of low toxicity, weak side effects, multiple targets, and less tumor resistance as well as anti-tumor and immune-regulatory functions [65]. Therefore, natural compounds with reversed MDR have become the focus of anticancer studies. Although *M. oleifera* has not yet developed into a commercial chemopreventive agent, previous findings have revealed that the chemotherapeutic drug doxorubicin combined with *M. oleifera* callus and leaf extracts produces robust synergy on the growth inhibition of HeLa cells, which is also correlated with apoptotic induction [66]. The application of currently used anticancer drugs combined with *M. oleifera* could be a novel therapeutic strategy for cancers.

### 6.4. Regulating Enzyme Activity

A balance and the induction of Phase I and II drug metabolizing enzymes is a well-known defense against chemical carcinogens [67]. The loss of GSH and GST activity can be restored by *M. oleifera* pod extract, which offers a major protective role in carcinogenesis [67,68]. The hydro-alcoholic drumstick extract from *M. oleifera* as a bifunctional inducer can induce both Phase I and Phase II enzymes and improve the levels of hepatic cytochrome b5, cytochrome P450, and GST [69]. It is also reported that the antioxidant properties of *M. oleifera* is closely correlated with its potential as a chemo preventative agent. In addition, *M. oleifera* pod extract (200 and 400 mg/kg body weight; p.o.) and its isolated saponin (50 mg/kg body weight; p.o.) can attenuate 7,12-dimethylbenz[a]anthracene (DMBA)-induced renal carcinogenesis in mice through effectively suppressing renal oxidative stress and toxicity [70].

Based on the above comprehensive analysis from several angles, *M. oleifera* may exerts its anti-tumor effects by modulating multiple signaling pathways, including inducing cell apoptosis, triggering cell cycle arrest, inhibiting cell proliferation, suppressing angiogenesis and metastasis, enhancing drug metabolism, and synergizing with chemotherapeutic agents.

## 7. Modulation of Blood Glucose

Diabetes mellitus (DM) is a chronic metabolic disorder and the pharmacological actions of the leaves of *M. oleifera* have been reported for the traditional treatment of diabetes [71]. For example, *M. oleifera* has been shown to improve plasma glucose disposal in Goto-Kakizaki (GK) Wistar DM rats [72]. Similarly, the methanol extract from its fruit powder is rich in N-benzyl thiocarbamates, N-benzyl carbamates, and benzyl nitriles which can trigger the release of insulin from pancreatic beta cells of rodents, suppress cyclooxygenase activity, and inhibit lipid peroxidation [73]. *M. oleifera* has been found to significantly reduce glucose to normal levels without any obvious cytotoxicity when compared to the alloxan-induced type 2 diabetic rats from the model group [74]. The supplementation of the aqueous extract from *M. oleifera* leaves at the dose of 100 mg/kg can improve insulin sensitivity, increase total antioxidant capacity (TAC), and improve immune tolerance [75], which is consistent with another report that *M. oleifera* can ameliorate glucose intolerance [76]. *M. oleifera* extract can also reduce diabetes-related complications. Recent studies have shown that the administration of *M. oleifera* leaf extract for six weeks plays a critical role in reducing diabetic complications by protecting diabetes-induced renal damage and inflammation in a streptozotocin-induced diabetes rat model [77]. In addition, the administration of *M. oleifera* seed powder can ameliorate diabetic nephropathy and restore normal histology of both kidney and pancreas when compared with a diabetic positive control group [78].



## 8. Future Perspectives

Autophagy is an evolutionarily conserved process whereby cytoplasm and cellular organelles are degraded in lysosomes for amino acid and energy recycling, thus executing its cytoprotective role [79]. Basal autophagy plays a critical role in cellular homeostasis. Autophagy can be induced under different conditions such as nutrient deprivation, endoplasmic reticulum (ER)-stress, and exposure to anticancer drugs. However, defective or impaired autophagy has been implicated in the pathogenesis of diverse disease states, including microbial infection, inflammation, neuronal degeneration, aging, and cancer [80–83]. The induction or upregulation of autophagy appears to decrease the susceptibility to pro-apoptotic insults, which may have further benefits [84]. Recently, the functional status of autophagy during chronic disease processes has attracted increasing attention. Notably, the upregulation of autophagy mediated by a wide range of phytochemicals such as resveratrol, curcumin, and quercetin can exert anti-inflammatory, anti-tumor and anti-aging effects. More importantly, *M. oleifera* can be treated as a nutraceutical product or food because of its safety, which will motivate the exploration of its potential to activate autophagy for the prevention and treatment of chronic diseases in the future.

## 9. Conclusions

*M. oleifera* possesses a wide range of medicinal and therapeutic properties through executing its potent anti-inflammatory activity, inhibiting the activation of NF- $\kappa$ B and PI3K/Akt pathways, mitigating oxidative stress by scavenging free radicals, and enhancing neuroprotective roles. In addition, *M. oleifera* can reduce the risk of cancer and modulate blood glucose, although the underlying mechanisms remain to be further explored. Therefore, *M. oleifera* provides the potential for the prevention or treatment of a series of chronic diseases.

**Acknowledgments:** This work was financially supported by the National Natural Science Foundation of China (No. 81601228); Natural Science Foundation from Science and Technology Department of Hubei Province (2017CFB553); and Donghu Scholar Program from Wuhan Sports University to Xianjuan Kou, as well as Hubei Superior Discipline Group of Physical Education and Health Promotion, and Outstanding Youth Scientific and Technological Innovation Team (T201624) from Hubei Provincial Department of Education; and Chutian Scholar Program and Innovative Start-Up Foundation from Wuhan Sports University to Ning Chen.

**Author Contributions:** Ning Chen and Justin M. Drake designed the outline of the manuscript. Xianjuan Kou, Biao Li, Julia B. Olayanju, and Ning Chen participated in literature collection and manuscript writing. Xianjuan Kou, Biao Li, and Ning Chen undertook figure design and construction. Ning Chen, Julia B. Olayanju, and Justin M. Drake reviewed and edited the manuscript. All authors finally reviewed and approved the manuscript.

**Conflicts of Interest:** These authors have declared no conflict of interest.

## References

1. Anwar, F.; Latif, S.; Ashraf, M.; Gilani, A.H. *Moringa oleifera*: A food plant with multiple medicinal uses. *Phytother. Res.* **2007**, *21*, 17–25. [[CrossRef](#)] [[PubMed](#)]
2. Mahmood, K.T.; Mugal, T.; Haq, I.U. *Moringa oleifera*: A natural gift—A review. *J. Pharm. Sci. Res.* **2010**, *2*, 775–781.
3. Abdull, R.A.; Ibrahim, M.D.; Kntayya, S.B. Health benefits of *Moringa oleifera*. *Asian Pac. J. Cancer Prev. APJCP* **2014**, *15*, 8571–8576. [[CrossRef](#)]
4. Posmontier, B. The medicinal qualities of *Moringa oleifera*. *Holist. Nurs. Pract.* **2011**, *25*, 80–87. [[CrossRef](#)] [[PubMed](#)]
5. Banji, O.J.; Banji, D.; Kavitha, R. Immunomodulatory effects of alcoholic and hydroalcoholic extracts of *Moringa olifera* Lam. leaves. *Indian J. Exp. Biol.* **2012**, *50*, 270–276. [[PubMed](#)]
6. Chumark, P.; Khunawat, P.; Sanvarinda, Y.; Phornchirasilp, S.; Morales, N.P.; Phivthong-Ngam, L.; Ratanachamnong, P.; Srisawat, S.; Pongrapeeporn, K.U. The in vitro and ex vivo antioxidant properties, hypolipidaemic and antiatherosclerotic activities of water extract of *Moringa oleifera* Lam. leaves. *J. Ethnopharmacol.* **2008**, *116*, 439–446. [[CrossRef](#)] [[PubMed](#)]

7. Elgamily, H.; Moussa, A.; Elborae, A.; El-Sayed, H.; Al-Moghazy, M.; Abdalla, A. Microbiological assessment of *Moringa oleifera* extracts and its incorporation in novel dental remedies against some oral pathogens. *Open Access Maced. J. Med. Sci.* **2016**, *4*, 585–590. [[CrossRef](#)] [[PubMed](#)]
8. Mehta, K.; Balaraman, R.; Amin, A.H.; Bafna, P.A.; Gulati, O.D. Effect of fruits of *Moringa oleifera* on the lipid profile of normal and hypercholesterolaemic rabbits. *J. Ethnopharmacol.* **2003**, *86*, 191–195. [[CrossRef](#)]
9. Moura, M.C.; Napoleao, T.H.; Coriolano, M.C.; Paiva, P.M.; Figueiredo, R.C.; Coelho, L.C. Water-soluble *Moringa oleifera* lectin interferes with growth, survival and cell permeability of corrosive and pathogenic bacteria. *J. Appl. Microbiol.* **2015**, *119*, 666–676. [[CrossRef](#)] [[PubMed](#)]
10. Nikkon, F.; Saud, Z.A.; Rahman, M.H.; Haque, M.E. In vitro antimicrobial activity of the compound isolated from chloroform extract of *Moringa oleifera* Lam. *Pakistan J. Biol. Sci.* **2003**, *6*, 1888–1890.
11. Peixoto, J.R.; Silva, G.C.; Costa, R.A.; de Sousa, F.J.; Vieira, G.H.; Filho, A.A.; Dos, F.V.R. In vitro antibacterial effect of aqueous and ethanolic *Moringa* leaf extracts. *Asian Pac. J. Trop. Med.* **2011**, *4*, 201–204. [[CrossRef](#)]
12. Ruckmani, K.; Kavimani, S.; Anandan, R.; Jaykar, B. Effect of *Moringa oleifera* Lam. on paracetamol induced hepatotoxicity. *Indian J. Pharm. Sci.* **1998**, *60*, 33–35.
13. Ariel, A.; Serhan, C.N. Resolvins and protectins in the termination program of acute inflammation. *Trends Immunol.* **2007**, *28*, 176–183. [[CrossRef](#)] [[PubMed](#)]
14. Bhatelia, K.; Singh, K.; Singh, R. TLRs: Linking inflammation and breast cancer. *Cell Signal.* **2014**, *26*, 2350–2357. [[CrossRef](#)] [[PubMed](#)]
15. Aggarwal, B.B. Nuclear factor-kappaB: The enemy within. *Cancer Cell* **2004**, *6*, 203–208. [[CrossRef](#)] [[PubMed](#)]
16. Kou, X.; Qi, S.; Dai, W.; Luo, L.; Yin, Z. Arctigenin inhibits lipopolysaccharide-induced iNOS expression in RAW264.7 cells through suppressing JAK-STAT signal pathway. *Int. Immunopharmacol.* **2011**, *11*, 1095–1102. [[CrossRef](#)] [[PubMed](#)]
17. Kooltheat, N.; Sranujit, R.P.; Chumark, P.; Potup, P.; Laytragoon-Lewin, N.; Usuwanthim, K. An ethyl acetate fraction of *Moringa oleifera* Lam. inhibits human macrophage cytokine production induced by cigarette smoke. *Nutrients* **2014**, *6*, 697–710. [[CrossRef](#)] [[PubMed](#)]
18. Minaiyan, M.; Asghari, G.; Taheri, D.; Saeidi, M.; Nasr-Esfahani, S. Anti-inflammatory effect of *Moringa oleifera* Lam. seeds on acetic acid-induced acute colitis in rats. *Avicenna J. Phytomed.* **2014**, *4*, 127–136. [[PubMed](#)]
19. Arulselvan, P.; Tan, W.S.; Gothai, S.; Muniandy, K.; Fakurazi, S.; Esa, N.M.; Alarfaj, A.A.; Kumar, S.S. Anti-inflammatory potential of ethyl acetate fraction of *Moringa oleifera* in downregulating the NF-kappaB signaling pathway in lipopolysaccharide-stimulated macrophages. *Molecules* **2016**, *21*, 1452. [[CrossRef](#)] [[PubMed](#)]
20. Fard, M.T.; Arulselvan, P.; Karthivashan, G.; Adam, S.K.; Fakurazi, S. Bioactive extract from *Moringa oleifera* inhibits the pro-inflammatory mediators in lipopolysaccharide stimulated macrophages. *Pharmacogn. Mag.* **2015**, *11*, S556–S563. [[PubMed](#)]
21. Park, E.J.; Cheenpracha, S.; Chang, L.C.; Kondratyuk, T.P.; Pezzuto, J.M. Inhibition of lipopolysaccharide-induced cyclooxygenase-2 and inducible nitric oxide synthase expression by 4-[(2'-O-acetyl-alpha-L-rhamnosyloxy)benzyl]isothiocyanate from *Moringa oleifera*. *Nutr. Cancer* **2011**, *63*, 971–982. [[CrossRef](#)] [[PubMed](#)]
22. Jaja-Chimedza, A.; Graf, B.L.; Simmler, C.; Kim, Y.; Kuhn, P.; Pauli, G.F.; Raskin, I. Biochemical characterization and anti-inflammatory properties of an isothiocyanate-enriched moringa (*Moringa oleifera*) seed extract. *PLoS ONE* **2017**, *12*, e0182658. [[CrossRef](#)] [[PubMed](#)]
23. Maurya, S.K.; Singh, A.K. Clinical efficacy of *Moringa oleifera* Lam. stems bark in urinary tract infections. *Int. Sch. Res. Notices* **2014**, *2014*, 906843. [[CrossRef](#)] [[PubMed](#)]
24. Niedzwiecki, A.; Roomi, M.W.; Kalinovsky, T.; Rath, M. Anticancer efficacy of polyphenols and their combinations. *Nutrients* **2016**, *8*, 552. [[CrossRef](#)] [[PubMed](#)]
25. Thapa, A.; Carroll, N.J. Dietary modulation of oxidative stress in Alzheimer's disease. *Int. J. Mol. Sci.* **2017**, *18*, 1583. [[CrossRef](#)] [[PubMed](#)]
26. Zhang, S.F.; Wang, X.L.; Yang, X.Q.; Chen, N. Autophagy-associated targeting pathways of natural products during cancer treatment. *Asian Pac. J. Cancer Prev. APJCP* **2014**, *15*, 10557–10563. [[CrossRef](#)] [[PubMed](#)]
27. Atawodi, S.E.; Atawodi, J.C.; Idakwo, G.A.; Pfundstein, B.; Haubner, R.; Wurtele, G.; Bartsch, H.; Owen, R.W. Evaluation of the polyphenol content and antioxidant properties of methanol extracts of the leaves, stem, and root barks of *Moringa oleifera* Lam. *J. Med. Food* **2010**, *13*, 710–716. [[CrossRef](#)] [[PubMed](#)]

28. Verma, A.R.; Vijayakumar, M.; Mathela, C.S.; Rao, C.V. In vitro and in vivo antioxidant properties of different fractions of *Moringa oleifera* leaves. *Food Chem. Toxicol.* **2009**, *47*, 2196–2201. [[CrossRef](#)] [[PubMed](#)]
29. Sreelatha, S.; Padma, P.R. Antioxidant activity and total phenolic content of *Moringa oleifera* leaves in two stages of maturity. *Plant Foods Hum. Nutr.* **2009**, *64*, 303–311. [[CrossRef](#)] [[PubMed](#)]
30. Sinha, M.; Das, D.K.; Bhattacharjee, S.; Majumdar, S.; Dey, S. Leaf extract of *Moringa oleifera* prevents ionizing radiation-induced oxidative stress in mice. *J. Med. Food* **2011**, *14*, 1167–1172. [[CrossRef](#)] [[PubMed](#)]
31. Sinha, M.; Das, D.K.; Datta, S.; Ghosh, S.; Dey, S. Amelioration of ionizing radiation induced lipid peroxidation in mouse liver by *Moringa oleifera* Lam. leaf extract. *Indian J. Exp. Biol.* **2012**, *50*, 209–215. [[PubMed](#)]
32. Uma, N.J.; Fakurazi, S.; Hairuszah, I. *Moringa oleifera* enhances liver antioxidant status via elevation of antioxidant enzymes activity and counteracts paracetamol-induced hepatotoxicity. *Malays. J. Nutr.* **2010**, *16*, 293–307. [[PubMed](#)]
33. Fakurazi, S.; Hairuszah, I.; Nanthini, U. *Moringa oleifera* Lam. prevents acetaminophen induced liver injury through restoration of glutathione level. *Food Chem. Toxicol.* **2008**, *46*, 2611–2615. [[CrossRef](#)] [[PubMed](#)]
34. Sharifudin, S.A.; Fakurazi, S.; Hidayat, M.T.; Hairuszah, I.; Moklas, M.A.; Arulselvan, P. Therapeutic potential of *Moringa oleifera* extracts against acetaminophen-induced hepatotoxicity in rats. *Pharm. Biol.* **2013**, *51*, 279–288. [[CrossRef](#)] [[PubMed](#)]
35. Singh, D.; Arya, P.V.; Aggarwal, V.P.; Gupta, R.S. Evaluation of antioxidant and hepatoprotective activities of *Moringa oleifera* Lam. leaves in carbon tetrachloride-intoxicated rats. *Antioxidants (Basel)* **2014**, *3*, 569–591. [[CrossRef](#)] [[PubMed](#)]
36. Pari, L.; Kumar, N.A. Hepatoprotective activity of *Moringa oleifera* on antitubercular drug-induced liver damage in rats. *J. Med. Food* **2002**, *5*, 171–177. [[CrossRef](#)] [[PubMed](#)]
37. Das, N.; Sikder, K.; Ghosh, S.; Fromenty, B.; Dey, S. *Moringa oleifera* Lam. leaf extract prevents early liver injury and restores antioxidant status in mice fed with high-fat diet. *Indian J. Exp. Biol.* **2012**, *50*, 404–412. [[PubMed](#)]
38. Prince, M.; Bryce, R.; Albanese, E.; Wimo, A.; Ribeiro, W.; Ferri, C.P. The global prevalence of dementia: A systematic review and metaanalysis. *Alzheimer's Dement. J. Alzheimer's Assoc.* **2013**, *9*, 63–75. [[CrossRef](#)] [[PubMed](#)]
39. Kou, X.; Li, J.; Bian, J.; Yang, Y.; Yang, X.; Fan, J.; Jia, S.; Chen, N. Ampelopsin attenuates 6-OHDA-induced neurotoxicity by regulating GSK-3 $\beta$ /NRF2/ARE signaling. *J. Funct. Food* **2015**, *19*, 765–774. [[CrossRef](#)]
40. Kou, X.; Liu, X.; Chen, X.; Li, J.; Yang, X.; Fan, J.; Yang, Y.; Chen, N. Ampelopsin attenuates brain aging of D-gal-induced rats through miR-34a-mediated SIRT1/mTOR signal pathway. *Oncotarget* **2016**, *7*, 74484–74495. [[CrossRef](#)] [[PubMed](#)]
41. Finkel, T.; Holbrook, N.J. Oxidants, oxidative stress and the biology of ageing. *Nature* **2000**, *408*, 239–247. [[CrossRef](#)] [[PubMed](#)]
42. Kou, X.; Chen, N. Resveratrol as a natural autophagy regulator for prevention and treatment of Alzheimer's disease. *Nutrients* **2017**, *9*, 927. [[CrossRef](#)]
43. Ganguly, R.; Guha, D. Alteration of brain monoamines & EEG wave pattern in rat model of Alzheimer's disease & protection by *Moringa oleifera*. *Indian J. Med. Res.* **2008**, *128*, 744–751. [[PubMed](#)]
44. Giacoppo, S.; Rajan, T.S.; De Nicola, G.R.; Iori, R.; Rollin, P.; Bramanti, P.; Mazzon, E. The isothiocyanate isolated from *Moringa oleifera* shows potent anti-inflammatory activity in the treatment of murine subacute Parkinson's disease. *Rejuvenat. Res.* **2017**, *20*, 50–63. [[CrossRef](#)] [[PubMed](#)]
45. Hannan, M.A.; Kang, J.Y.; Mohibullah, M.; Hong, Y.K.; Lee, H.; Choi, J.S.; Choi, I.S.; Moon, I.S. *Moringa oleifera* with promising neuronal survival and neurite outgrowth promoting potentials. *J. Ethnopharmacol.* **2014**, *152*, 142–150. [[CrossRef](#)] [[PubMed](#)]
46. Satalangka, C.; Wattanathorn, J.; Muchimapura, S.; Thukham-mee, W. *Moringa oleifera* mitigates memory impairment and neurodegeneration in animal model of age-related dementia. *Oxid. Med. Cell. Longev.* **2013**, *2013*, 695936. [[CrossRef](#)] [[PubMed](#)]
47. Ekong, M.B.; Ekpo, M.M.; Akpanyung, E.O.; Nwaokonko, D.U. Neuroprotective effect of *Moringa oleifera* leaf extract on aluminium-induced temporal cortical degeneration. *Metab. Brain Dis.* **2017**, *32*, 1437–1447. [[CrossRef](#)] [[PubMed](#)]
48. Kaur, G.; Invally, M.; Sanzagiri, R.; Buttar, H.S. Evaluation of the antidepressant activity of *Moringa oleifera* alone and in combination with fluoxetine. *J. Ayurveda Integr. Med.* **2015**, *6*, 273–279. [[CrossRef](#)] [[PubMed](#)]

49. Siegel, R.; Naishadham, D.; Jemal, A. Cancer statistics for Hispanics/Latinos, 2012. *CA Cancer J. Clin.* **2012**, *62*, 283–298. [[CrossRef](#)] [[PubMed](#)]
50. Boggs, D.A.; Palmer, J.R.; Wise, L.A.; Spiegelman, D.; Stampfer, M.J.; Adams-Campbell, L.L.; Rosenberg, L. Fruit and vegetable intake in relation to risk of breast cancer in the Black Women's Health Study. *Am. J. Epidemiol.* **2010**, *172*, 1268–1279. [[CrossRef](#)] [[PubMed](#)]
51. Fowke, J.H.; Chung, F.L.; Jin, F.; Qi, D.; Cai, Q.; Conaway, C.; Cheng, J.R.; Shu, X.O.; Gao, Y.T.; Zheng, W. Urinary isothiocyanate levels, brassica, and human breast cancer. *Cancer Res.* **2003**, *63*, 3980–3986. [[PubMed](#)]
52. Al-Asmari, A.K.; Albalawi, S.M.; Athar, M.T.; Khan, A.Q.; Al-Shahrani, H.; Islam, M. *Moringa oleifera* as an anti-cancer agent against breast and colorectal cancer cell lines. *PLoS ONE* **2015**, *10*, e0135814. [[CrossRef](#)] [[PubMed](#)]
53. Berkovich, L.; Earon, G.; Ron, I.; Rimmon, A.; Vexler, A.; Lev-Ari, S. *Moringa oleifera* aqueous leaf extract down-regulates nuclear factor-kappaB and increases cytotoxic effect of chemotherapy in pancreatic cancer cells. *BMC Complement. Altern. Med.* **2013**, *13*, 212. [[CrossRef](#)] [[PubMed](#)]
54. Fahey, J.W.; Zalcmann, A.T.; Talalay, P. The chemical diversity and distribution of glucosinolates and isothiocyanates among plants. *Phytochemistry* **2001**, *56*, 5–51. [[CrossRef](#)]
55. Xiao, D.; Srivastava, S.K.; Lew, K.L.; Zeng, Y.; Hershberger, P.; Johnson, C.S.; Trump, D.L.; Singh, S.V. Allyl isothiocyanate, a constituent of cruciferous vegetables, inhibits proliferation of human prostate cancer cells by causing G2/M arrest and inducing apoptosis. *Carcinogenesis* **2003**, *24*, 891–897. [[CrossRef](#)] [[PubMed](#)]
56. Gao, N.; Budhraj, A.; Cheng, S.; Liu, E.H.; Chen, J.; Yang, Z.; Chen, D.; Zhang, Z.; Shi, X. Phenethyl isothiocyanate exhibits antileukemic activity in vitro and in vivo by inactivation of Akt and activation of JNK pathways. *Cell Death Dis.* **2011**, *2*, e140. [[CrossRef](#)] [[PubMed](#)]
57. Karim, N.A.; Ibrahim, M.D.; Kntayya, S.B.; Rukayadi, Y.; Hamid, H.A.; Razis, A.F. *Moringa oleifera* Lam: Targeting chemoprevention. *Asian Pac. J. Cancer Prev. APJCP* **2016**, *17*, 3675–3686. [[PubMed](#)]
58. Sreelatha, S.; Jeyachitra, A.; Padma, P.R. Antiproliferation and induction of apoptosis by *Moringa oleifera* leaf extract on human cancer cells. *Food Chem. Toxicol.* **2011**, *49*, 1270–1275. [[CrossRef](#)] [[PubMed](#)]
59. Waterman, C.; Cheng, D.M.; Rojas-Silva, P.; Poulev, A.; Dreifus, J.; Lila, M.A.; Raskin, I. Stable, water extractable isothiocyanates from *Moringa oleifera* leaves attenuate inflammation in vitro. *Phytochemistry* **2014**, *103*, 114–122. [[CrossRef](#)] [[PubMed](#)]
60. Jung, I.L. Soluble extract from *Moringa oleifera* leaves with a new anticancer activity. *PLoS ONE* **2014**, *9*, e95492. [[CrossRef](#)] [[PubMed](#)]
61. Guon, T.E.; Chung, H.S. *Moringa oleifera* fruit induce apoptosis via reactive oxygen species-dependent activation of mitogen-activated protein kinases in human melanoma A2058 cells. *Oncol. Lett.* **2017**, *14*, 1703–1710. [[CrossRef](#)] [[PubMed](#)]
62. Leelawat, S.; Leelawat, K. Molecular mechanisms of cholangiocarcinoma cell inhibition by medicinal plants. *Oncol. Lett.* **2017**, *13*, 961–966. [[CrossRef](#)] [[PubMed](#)]
63. Khan, M.; Yu, B.; Rasul, A.; Al, S.A.; Yi, F.; Yang, H.; Ma, T. Jaceosidin induces apoptosis in U87 glioblastoma cells through G2/M phase arrest. *Evid. Based Complement. Altern. Med.* **2012**, *2012*, 703034. [[CrossRef](#)] [[PubMed](#)]
64. Khan, M.; Zheng, B.; Yi, F.; Rasul, A.; Gu, Z.; Li, T.; Gao, H.; Qazi, J.I.; Yang, H.; Ma, T. Pseudolaric Acid B induces caspase-dependent and caspase-independent apoptosis in u87 glioblastoma cells. *Evid. Based Complement. Altern. Med.* **2012**, *2012*, 957568. [[CrossRef](#)] [[PubMed](#)]
65. Kou, X.; Fan, J.; Chen, N. Potential molecular targets of ampelopsin in prevention and treatment of cancers. *Anti-Cancer Agents Med. Chem.* **2017**, *17*, 1610–1616. [[CrossRef](#)] [[PubMed](#)]
66. Jafarain, A.; Asghari, G.; Ghassami, E. Evaluation of cytotoxicity of *Moringa oleifera* Lam. callus and leaf extracts on Hela cells. *Adv. Biomed. Res.* **2014**, *3*, 194. [[PubMed](#)]
67. Singh, R.P.; Padmavathi, B.; Rao, A.R. Modulatory influence of *Adhatoda vesica* (*Justicia adhatoda*) leaf extract on the enzymes of xenobiotic metabolism, antioxidant status and lipid peroxidation in mice. *Mol. Cell. Biochem.* **2000**, *213*, 99–109. [[CrossRef](#)] [[PubMed](#)]
68. Sharma, V.; Paliwal, R.; Janmeda, P.; Sharma, S. Chemopreventive efficacy of *Moringa oleifera* pods against 7, 12-dimethylbenz[a]anthracene induced hepatic carcinogenesis in mice. *Asian Pac. J. Cancer Prev. APJCP* **2012**, *13*, 2563–2569. [[CrossRef](#)] [[PubMed](#)]

69. Bharali, R.; Tabassum, J.; Azad, M.R. Chemomodulatory effect of *Moringa oleifera* Lam. on hepatic carcinogen metabolising enzymes, antioxidant parameters and skin papillomagenesis in mice. *Asian Pac. J. Cancer Prev. APJCP* **2003**, *4*, 131–139. [[PubMed](#)]
70. Sharma, V.; Paliwal, R. Potential chemoprevention of 7,12-dimethylbenz[a]anthracene induced renal carcinogenesis by *Moringa oleifera* pods and its isolated saponin. *Indian J. Clin. Biochem.* **2014**, *29*, 202–209. [[CrossRef](#)] [[PubMed](#)]
71. Grover, J.K.; Yadav, S.; Vats, V. Medicinal plants of India with anti-diabetic potential. *J. Ethnopharmacol.* **2002**, *81*, 81–100. [[CrossRef](#)]
72. Kar, A.; Choudhary, B.K.; Bandyopadhyay, N.G. Comparative evaluation of hypoglycaemic activity of some Indian medicinal plants in alloxan diabetic rats. *J. Ethnopharmacol.* **2003**, *84*, 105–108. [[CrossRef](#)]
73. Mbikay, M. Therapeutic potential of *Moringa oleifera* leaves in chronic hyperglycemia and dyslipidemia: A review. *Front. Pharmacol.* **2012**, *3*, 24. [[CrossRef](#)] [[PubMed](#)]
74. Omabe, M.; Nwudele, C.; Omabe, K.N.; Okorocho, A.E. Anion gap toxicity in alloxan induced type 2 diabetic rats treated with antidiabetic noncytotoxic bioactive compounds of ethanolic extract of *Moringa oleifera*. *J. Toxicol.* **2014**, *2014*, 406242. [[CrossRef](#)] [[PubMed](#)]
75. Tuorkey, M.J. Effects of *Moringa oleifera* aqueous leaf extract in alloxan induced diabetic mice. *Interv. Med. Appl. Sci.* **2016**, *8*, 109–117. [[PubMed](#)]
76. Ndong, M.; Uehara, M.; Katsumata, S.; Suzuki, K. Effects of oral administration of *Moringa oleifera* Lam. on glucose tolerance in goto-kakizaki and wistar rats. *J. Clin. Biochem. Nutr.* **2007**, *40*, 229–233. [[CrossRef](#)] [[PubMed](#)]
77. Omodanisi, E.I.; Aboua, Y.G.; Oguntibeju, O.O. Assessment of the anti-hyperglycaemic, anti-inflammatory and antioxidant activities of the methanol extract of *Moringa oleifera* in diabetes-induced nephrotoxic male wistar rats. *Molecules* **2017**, *22*, 439. [[CrossRef](#)] [[PubMed](#)]
78. Al-Malki, A.L.; El, R.H. The antidiabetic effect of low doses of *Moringa oleifera* Lam. seeds on streptozotocin induced diabetes and diabetic nephropathy in male rats. *Biomed. Res. Int.* **2015**, *2015*, 381040. [[CrossRef](#)] [[PubMed](#)]
79. Chen, N.; Karantza-Wadsworth, V. Role and regulation of autophagy in cancer. *Biochim. Biophys. Acta* **2009**, *1793*, 1516–1523. [[CrossRef](#)] [[PubMed](#)]
80. Jin, S.V.; White, E. Tumor suppression by autophagy through the management of metabolic stress. *Autophagy* **2008**, *4*, 563–566. [[CrossRef](#)] [[PubMed](#)]
81. Orvedahl, A.; Levine, B. Eating the enemy within: Autophagy in infectious diseases. *Cell Death Differ.* **2009**, *16*, 57–69. [[CrossRef](#)] [[PubMed](#)]
82. Saitoh, T.; Fujita, N.; Jang, M.H.; Uematsu, S.; Yang, B.G.; Satoh, T.; Omori, H.; Noda, T.; Yamamoto, N.; Komatsu, M.; et al. Loss of the autophagy protein Atg16L1 enhances endotoxin-induced IL-1beta production. *Nature* **2008**, *456*, 264–268. [[CrossRef](#)] [[PubMed](#)]
83. Yen, W.L.; Klionsky, D.J. How to live long and prosper: Autophagy, mitochondria, and aging. *Physiology (Bethesda)* **2008**, *23*, 248–262. [[CrossRef](#)] [[PubMed](#)]
84. Garcia-Arencibia, M.; Hochfeld, W.E.; Toh, P.P.; Rubinsztein, D.C. Autophagy, a guardian against neurodegeneration. *Semin. Cell Dev. Biol.* **2010**, *21*, 691–698. [[CrossRef](#)] [[PubMed](#)]





# Impact of Phosphoproteomics in the Era of Precision Medicine for Prostate Cancer

Johnny R. Ramroop<sup>1</sup>, Mark N. Stein<sup>2,3</sup> and Justin M. Drake<sup>1,3,4\*</sup>

<sup>1</sup>Cancer Metabolism and Growth Program, Rutgers Cancer Institute of New Jersey, New Brunswick, NJ, United States,

<sup>2</sup>Developmental Therapeutics/Phase I Program, Rutgers Cancer Institute of New Jersey, New Brunswick, NJ, United States,

<sup>3</sup>Department of Medicine, Division of Medical Oncology and Rutgers Robert Wood Johnson Medical School,

New Brunswick, NJ, United States, <sup>4</sup>Department of Pharmacology, Rutgers Robert Wood Johnson Medical School, New Brunswick, NJ, United States

Prostate cancer is the most common malignancy in men in the United States. While androgen deprivation therapy results in tumor responses initially, there is relapse and progression to metastatic castration-resistant prostate cancer. Currently, all prostate cancer patients receive essentially the same treatment, and there is a need for clinically applicable technologies to provide predictive biomarkers toward personalized therapies. Genomic analyses of tumors are used for clinical applications, but with a paucity of obvious driver mutations in metastatic castration-resistant prostate cancer, other applications, such as phosphoproteomics, may complement this approach. Immunohistochemistry and reverse phase protein arrays are limited by the availability of reliable antibodies and evaluates a preselected number of targets. Mass spectrometry-based phosphoproteomics has been used to profile tumors consisting of thousands of phosphopeptides from individual patients after surgical resection or at autopsy. However, this approach is time consuming, and while a large number of candidate phosphopeptides are obtained for evaluation, limitations are reduced reproducibility, sensitivity, and precision. Targeted mass spectrometry can help eliminate these limitations and is more cost effective and less time consuming making it a practical platform for future clinical testing. In this review, we discuss the use of phosphoproteomics in prostate cancer and other clinical cancer tissues for target identification, hypothesis testing, and possible patient stratification. We highlight the majority of studies that have used phosphoproteomics in prostate cancer tissues and cell lines and propose ways forward to apply this approach in basic and clinical research. Overall, the implementation of phosphoproteomics *via* targeted mass spectrometry has tremendous potential to aid in the development of more rational, personalized therapies that will result in increased survival and quality of life enhancement in patients suffering from metastatic castration-resistant prostate cancer.

**Keywords:** clinical trials, kinases, kinase inhibitors, signaling pathways, phosphoproteomics, prostate cancer, mass spectrometry, targeted mass spectrometry

## CURRENT TREATMENT LANDSCAPE OF PROSTATE CANCER (PrCa)

The male prostate, as well as early stage PrCa, is dependent on androgens activating the androgen receptor (AR) for survival, growth, and proliferation (1). Prostate-specific antigen (PSA) is a serine protease that is secreted from the prostate and is transcriptionally regulated by AR. Thus, along with digital rectal exams, PSA-based screening is routinely used for early detection of PrCa (**Figure 1**)

## OPEN ACCESS

### Edited by:

Stéphane Terry,  
Institut Gustave Roussy, France

### Reviewed by:

Andrew Burgess,  
Anzac Research Institute, Australia  
Katarina Davaljeva,  
Macedonian Academy of Sciences  
and Arts, Macedonia

### \*Correspondence:

Justin M. Drake  
justin.drake@cinj.rutgers.edu

### Specialty section:

This article was submitted to  
Genitourinary Oncology,  
a section of the journal  
Frontiers in Oncology

**Received:** 08 December 2017

**Accepted:** 29 January 2018

**Published:** 16 February 2018

### Citation:

Ramroop JR, Stein MN and  
Drake JM (2018) Impact of  
Phosphoproteomics in the  
Era of Precision Medicine  
for Prostate Cancer.  
Front. Oncol. 8:28.  
doi: 10.3389/fonc.2018.00028

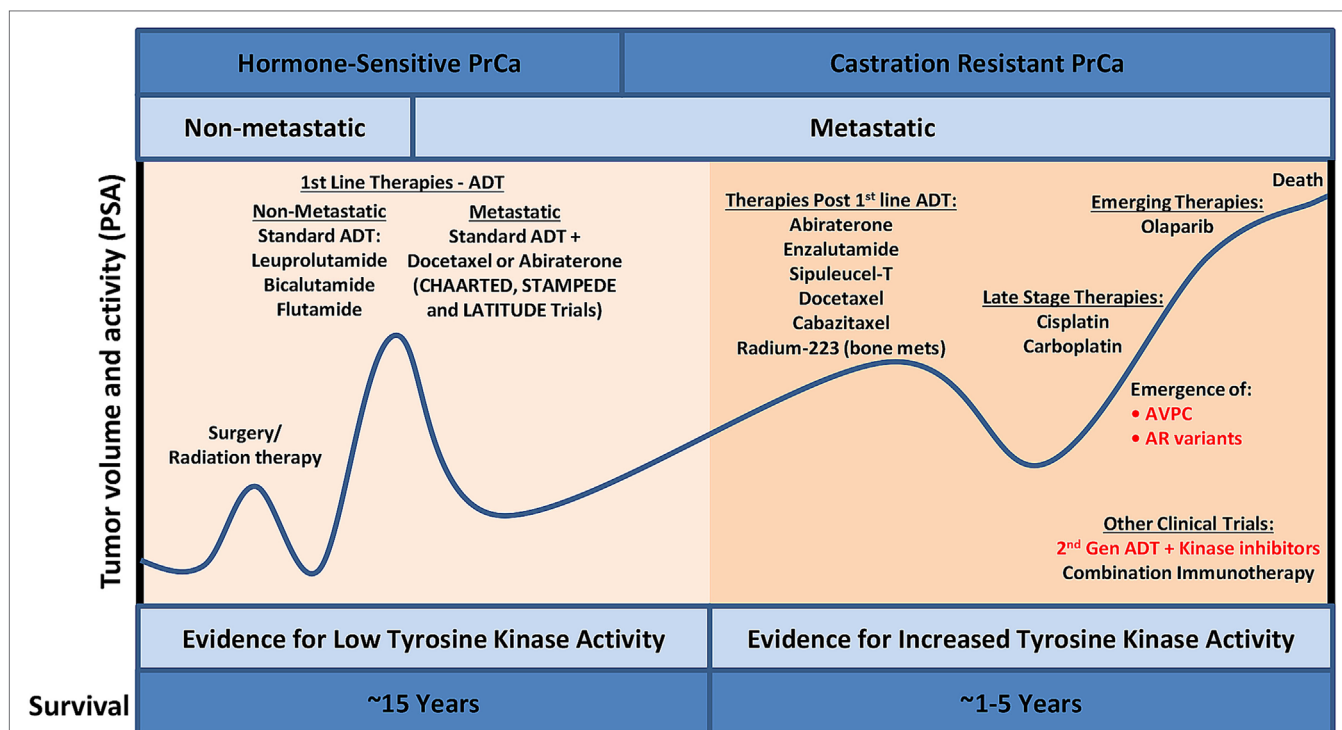


**FIGURE 1** | PrCa progression and the current treatment landscape. Despite the availability of effective treatment for PrCa in its early stages, there are constant cycles of regression and recurrence due to therapeutic resistance via bypass mechanisms. Utilizing phosphoproteomics approaches to identify activated kinases in late-stage aggressive disease and precisely targeting these kinases with FDA-approved kinase inhibitors, in combination with other standard of care treatment, will lead to increased overall survival. ADT, androgen deprivation therapy; AVPC, aggressive variant prostate cancer; FDA, Food and Drug Administration; PrCa, prostate cancer; PSA, prostate-specific antigen.

although the magnitude of benefit from PSA screening continues to be debated (2). Biopsies are typically done to confirm PrCa, and if diagnosed with clinically significant disease (3), a patient most commonly has external beam radiation therapy or radical prostatectomy. Adjuvant androgen deprivation with radiation or adjuvant radiation after surgery may be administered in the setting of tumors with high risk of recurrence. Androgen deprivation therapy (ADT) that suppresses testicular function is typically first-line therapy for androgen-sensitive PrCa. A small additional survival benefit may be seen when first-generation oral AR inhibitors such as bicalutamide and flutamide are combined with ADT. Initial positive response to ADT is common by evidence of decline PSA levels in 90% of patients (4) and duration of response to therapy varies, with 5–10% of patients surviving 10 years after initiating ADT (5). In two recent phase III clinical trials (STAMPEDE and LATITUDE), hormone naive patients with locally advanced or oligometastatic disease starting first-line long-term ADT treatment were also given abiraterone acetate and prednisone (6, 7). Abiraterone acetate is a potent, second-generation inhibitor that blocks androgen synthesis, significantly decreasing circulating androgen below levels achieved with testicular suppression alone (8). In the STAMPEDE trial, inclusion of abiraterone acetate early in the treatment protocol resulted in a lower risk of death by 37%. The 3-year survival rate was 76% with standard ADT treatment alone and 83% with the

standard care in combination with abiraterone acetate as well as a 14-month failure-free survival advantage (7). The results were also verified in a separate LATITUDE trial (6). In another phase III clinical trial (CHAARTED), patients with hormone-sensitive metastatic PrCa were given docetaxel in combination with first-line ADT treatment. The median overall survival with combination treatment was 13.6 months longer than with ADT alone (57.6 vs 44 months), nearly identical to the STAMPEDE and LATITUDE trials. A decrease in PSA to <0.2 ng/ml at 12 months was 27.7% for the combination group compared to 16.8% for the ADT only group, and the median time for development of CRPC was increased (20.2 vs 11.7 months) (9). The results of these exciting clinical trials have prompted earlier use of docetaxel or abiraterone acetate plus standard ADT to delay time of metastatic castration-resistant PrCa (mCRPC) and ultimately death.

Metastatic castration-resistant PrCa is associated with poor prognosis with a mean survival time of 16–18 months (10). The US Food and Drug Administration (FDA)-approved therapies for mCRPC include chemotherapy agents (docetaxel and cabazitaxel), second-generation hormonal therapies (abiraterone acetate and enzalutamide), immunotherapy (sipuleucel-T), and radium-223. AR point mutations and amplifications have led to resistance to first-line ADT treatments, and since AR remains active in mCRPC, these patients respond to abiraterone acetate and enzalutamide, but with a modest increase in overall survival

of 3–4 months (11). A major resistance mechanism to abiraterone acetate and enzalutamide involve the presence of AR splice variants, such as ARv7 (12), possibly explaining the modest overall survival benefit of these agents in an unselected population. AR splice variants are truncated forms of wild-type AR where the ligand-binding domain is lost, activation is ligand independent, and these variants are constitutively active (13). It was recently shown that ARv7 mRNA detection in circulating tumor cells (CTCs) correlated with poor outcomes in patients with mCRPC who were treated with abiraterone acetate and enzalutamide (14). It is still unclear if AR splice variants are functionally contributing to treatment resistance, but ARv7 has developed into an important predictive biomarker for mCRPC patients taking either abiraterone acetate or enzalutamide. Another result of resistance to prolonged administration of abiraterone acetate and enzalutamide is the development of a lethal variant of mCRPC termed aggressive variant prostate cancer (AVPC; **Figure 1**). Indeed, AVPC was classified in 15% of mCRPCs prior to the approval of abiraterone acetate and enzalutamide; however, this population shifted to 31% AVPC post-abiraterone acetate and enzalutamide (15). Several great reviews have been written on this disease variant (16–18), and recent work has classified AVPC into two distinct subtypes: AR-null expressing neuroendocrine (NE) differentiation markers and AR-null lacking markers of NE differentiation (double negative) (15). AVPC is characterized by several clinical and genetic features to include low PSA and AR protein expression, loss of retinoblastoma, *TP53* mutations, overexpression of Aurora kinase A (*AURKA*), and amplification of N-Myc (*MYCN*) (19–21). Survival is typically less than a year with limited treatment options to include platinum-based chemotherapy. Based on the recent literature, it is becoming apparent that AR-independent pathways such as activated MAPK and FGFR kinase pathways are responsible for AVPC development and progression. Indeed, several clinical trials investigating AR-independent pathways are underway in PrCa including agents that target MEK and/or SRC (NCT01990196), *AURKA* (NCT01799278), PI3K/mammalian target of rapamycin (mTOR) (NCT02407054), and DNAPK (NCT01353625), although not all of these trials focus on AVPC.

## PERSONALIZED THERAPIES IN PrCa— CLINICAL EVIDENCE

The treatment landscape of mCRPC and AVPC involve several “one-size-fits-all” approaches with no real stratification of patients or novel targeted therapies, with a few emerging exceptions. The observation that AR amplification and missense mutations are observed in nearly 70% of mCRPC cases (22) has led to the clinical paradigm where all patients are essentially treated with some form of androgen synthesis or AR function inhibitors. Other genetic alterations have been observed at high frequency (ETS gene rearrangements, *TP53* mutations, and *PTEN* deletions) in mCRPC patients but are not yet predictive for any particular targeted therapy. Recent whole-genome and transcriptome sequencing efforts have identified several genetic aberrations in mCRPC patients at lower frequency to include *TP53*, *RB1*, *PIK3CA/B*,

*BRAF/RAF1*, *BRCA2*, *BRCA1*, and *ATM* (22, 23). In another study by Barbieri et al., the exomes of over 100 primary prostate adenocarcinomas and normal tissue pairs were sequenced and led to the identification of new recurrent mutations including *MED12*, *FOXA1*, and *SPOP* (24). It was later shown that recurrent point mutations in *SPOP* in PrCa activates the PI3K/AKT/mTOR and AR signaling pathways providing functional evidence that this mutation may serve as a predictive biomarker to PI3K or AKT inhibitors in combination with antiandrogens (25, 26).

Mutations in DNA repair genes (e.g., *BRCA2*) are observed in approximately 10–15% of mCRPC cases (27). In ovarian cancer, FDA-approved poly ADP-ribose polymerase inhibitors, olaparib and rucaparib, have been used for the treatment of ovarian cancer in patients harboring the *BRCA1*, *BRCA2*, and other DNA repair gene mutations (28) and were sensitive to platinum-based chemotherapies (29). Indeed, recent clinical trials suggest that targeting these DNA repair mutations with PARP inhibitors may also be beneficial in men with mCRPC. In a phase II TOPARP-A trial, treatment with olaparib in patients who stopped responding to standard ADT treatment and who had aberrations in DNA repair genes (notably *BRCA2* and *ATM*) led to a favorable response rate in 88% of patients (30). Response included  $\geq 50\%$  reduction in PSA and reduction in CTCs to  $< 5$  per 7.5 ml of blood. Radiographic progression-free survival was longer in biomarker positive patients (median, 9.8 months) compared to biomarker negative (median, 2.7 months). Overall survival was also extended when compared between these two groups (median, 13.8 vs 7.5 months). Based on the data from this phase II TOPARP-A trial, olaparib received FDA breakthrough therapy designation in January 2016 to treat mCRPC patients with *BRCA1/2* or *ATM* mutations who have received prior abiraterone acetate or enzalutamide therapy. Another phase II study is currently underway evaluating the efficacy of rucaparib in patients with mCRPC that harbor mutations in DNA repair genes (NCT02952534). In addition, in *PTEN*-deficient and *TMPRSS2-ERG* expressing PrCa tumor cells, rucaparib addition was synergistic when combined with radiation and suggested the use of rucaparib to radiosensitize PrCa cells as a useful strategy clinically (31). Similarly, other mutations and bypass mechanisms may be targeted to re-sensitize resistant cells or make them radiosensitive. For example, expression of the transcription factor anti-programmed death ligand 1 (AP-1) is associated with mCRPC and constitutively active AP-1 is dependent on EGFR and PI3K. Interestingly, inhibition of PI3K pathway suppresses AP-1 expression, sensitizing PrCa cells to gamma radiation, suggesting a combination of AKT inhibitors with radiation therapy as a novel strategy for treatment (32). Importantly, not all mCRPC patients with mutations in DNA repair genes will respond to olaparib due to secondary mutations that restore wild-type function or other activated cell survival pathways (33). Whole exome sequencing of circulating cell-free DNA (collected during the TOPARP-A trial) suggested that germline and somatic DNA repair mutations (*BRCA2* and *PALB2*) reverted back in frame as the mechanism behind resistance to olaparib providing a novel platform for assessing predictive biomarkers in this patient cohort (28).

Currently, about 20–30% of mCRPC patients resistant to abiraterone acetate or enzalutamide may benefit from stratification



and targeted therapy trials as described above. However, the remaining 70–80% of mCRPC patients are devoid of activating mutations in genes that lead to the “smoking gun” hypothesis identifying obvious targeted therapy applications based on the genomic data alone. As we get better at targeting AR for mCRPC, it is becoming clearer that bypass kinase pathways are important mediators of treatment resistance in mCRPC and AVPC and the development of new tools or utilization of existing ones to identify these pathways are becoming necessary. Indeed, future clinical therapies may rely on the precise targeting of these select kinases in this disease in combination with other agents to prolong survival.

## TOOLS TO ASSESS KINASE SIGNALING PATHWAYS IN CANCER

### Reverse Phase Protein Arrays (RPPAs) and Immunohistochemistry (IHC)

Antibody-based methodologies for the assessment of signaling networks in CRPC (and other cancers) include both IHC (34, 35) and RPPA (36, 37). These antibody approaches are amenable to use on clinical tissues such as biopsies and do not require specialized instruments. However, these assays can be time consuming with respect to optimizing staining protocols for each antibody (IHC), and only a select few phosphosite-specific antibodies are robust enough and are commercially available, limiting the analysis to a predefined set of targets. Also, neither approach is particularly high throughput as IHC staining typically analyzes one protein at a time and RPPA can measure up to a couple hundred from a given tissue section or biopsy. Overall, RPPAs and IHC-based approaches work very well for detecting known and predefined pathways for a given tumor type and to date are better with low sample amounts. However, they are not well suited for easy customization or discovery-based investigation of a large number of cell signaling pathways such as with mass spectrometry (MS)-based approaches.

### MS-Based Phosphoproteomics

Mass spectrometry is an analytical technique that involves the ionization of a molecule and subsequent detection and identification of the fragmented ions based on its mass-to-charge ( $m/z$ ) ratio. There are two main MS-based proteomics approaches, top-down and bottom-up. The top-down approach involves analyzing whole proteins, while the bottom-up method involves measuring the peptides from digested proteins. These two approaches can be used for either shotgun or targeted platforms. In both approaches, the sample analytes are injected and eluted from a reverse-phase column, ionized, and sorted based on the  $m/z$  ratio within the mass spectrometer instrument. The fragment and parent masses are used to determine the identity of the analyte. While MS instruments are expensive, MS does provide the advantage of high data collection power and has the customizable capability of analyzing small, complex sample amounts with high sensitivity, repeatability, and resolution.

Phosphoproteomics is the identification and characterization of proteins with phosphorylation as a posttranslational

modification (PTM). Phosphoproteomics provide insight into proteins that are important for regulating essential signaling pathways and cellular processes and may lead to new potential drug targets. In shotgun phosphoproteomics, protein samples are enzymatically digested into peptides and phosphopeptides (Figure 2A). Digestion is predominantly performed using trypsin because of its high specificity, availability, and ease of use. The limitation of the use of trypsin alone in bottom-up phosphoproteomics is that a comprehensive view of the full phosphoproteome may be compromised as a result of missing particular PTM sites, missed cleavages, or too small peptides. However, LysC can be used in conjunction with trypsin to reduce some missed cleavage events, increasing PTM site coverage. The use of alternative proteases such as chymotrypsin, LysN, AspN, GluC, and ArgC may also help with limitations of trypsin digestion, but these proteases must be used in separate experimental preparations to eliminate the generation of phosphopeptides that are too small for MS detection (38). It was initially believed that up to 30% of all human proteins may be modified by phosphorylation (39). More recent findings indicate that at least approximately 75% of the proteome can be phosphorylated (40). Phosphoserine and phosphothreonine modifications represent approximately 98% of the phosphoproteome (~86 and ~12%, respectively), while tyrosine phosphorylation accounts for approximately 2% of protein phosphorylation in cells (41). Due to the low abundance of phosphopeptides in complex biological tissue, enrichment steps such as immobilized metal affinity chromatography, metal oxide surfaces using titanium oxide ( $\text{TiO}_2$ ), antibody-based enrichment (e.g., 4G10, used for phosphotyrosine enrichment), or a combination of these approaches are necessary (Figures 2B,C) (42, 43). The digested and enriched phosphopeptides are then analyzed by the mass spectrometer (Figure 2D), and the identified phosphopeptides are collected for data analysis.

While very powerful, shotgun phosphoproteomics does have some limitations. In general, higher abundant phosphopeptides are sampled more frequently, while lower abundant phosphopeptides are sampled less frequently. In addition, high variability of sampling between MS runs can exist as lower abundant phosphopeptides may be sequenced in some samples, but not in others, creating a “missing data” problem that can complicate statistical analyses (44). While thousands of phosphopeptides are identified in complex biological specimens, tool to evaluate and comprehend the large amount of phosphopeptide information is another main challenge. This has led to the development of resources providing a platform for data processing ranging from annotation and pathway enrichment to generating pathway networks and protein–protein interactions such as MaxQuant (45), Skyline (46), and kinase-substrate enrichment analysis (47, 48). A couple excellent reviews describe these software programs in more detail (49, 50) and will not be discussed in this review.

## PHOSPHOPROTEOMICS IN PrCa

Mass spectrometry-based proteomics and phosphoproteomics on cell lines, mouse xenografts, and clinical tissue samples have

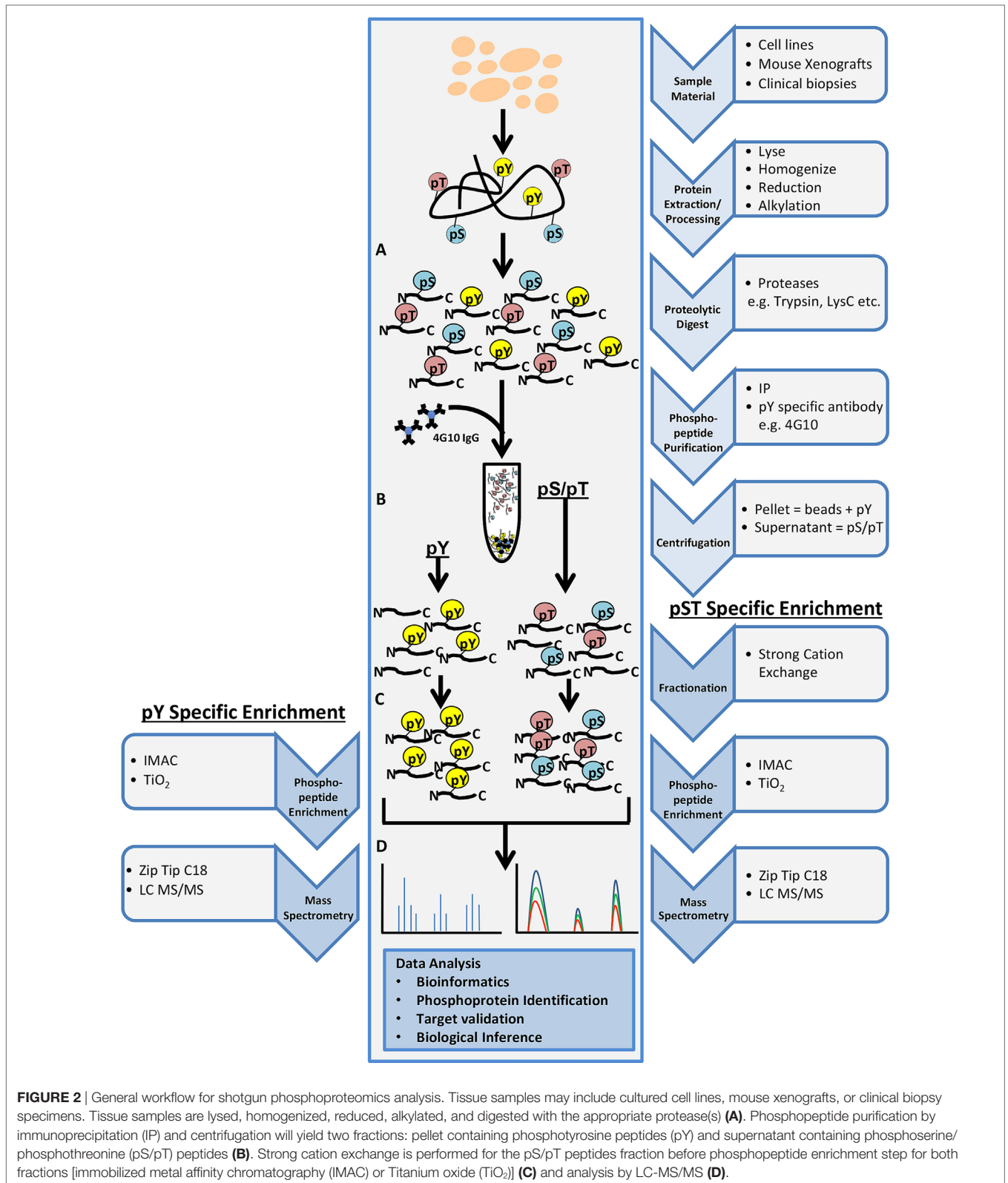


**FIGURE 2 |** General workflow for shotgun phosphoproteomics analysis. Tissue samples may include cultured cell lines, mouse xenografts, or clinical biopsy specimens. Tissue samples are lysed, homogenized, reduced, alkylated, and digested with the appropriate protease(s) (A). Phosphopeptide purification by immunoprecipitation (IP) and centrifugation will yield two fractions: pellet containing phosphotyrosine peptides (pY) and supernatant containing phosphoserine/ phosphothreonine (pS/pT) peptides (B). Strong cation exchange is performed for the pS/pT peptides fraction before phosphopeptide enrichment step for both fractions [immobilized metal affinity chromatography (IMAC) or Titanium oxide (TiO<sub>2</sub>)] (C) and analysis by LC-MS/MS (D).

been used to characterize a wide array of different cancer types as well as identify tumor associated signatures that are involved in cancer progression or resistance to standard therapies. Here, we

discuss some of the insights gained from MS-based proteomics and phosphoproteomics in PrCa as well as other cancers such as ovarian, lung, breast, and colorectal.

In a previous study by our group, nearly 50% of CRPC tissues showed increased levels of overall tyrosine phosphorylation compared to hormone naive PrCa (51), suggesting that CRPC tissues are prime candidates for investigating the role of activated kinases driving resistance to hormonal therapies. Since there are no clear common mutational drivers explaining this observed increase in tyrosine phosphorylation in CRPC, we discuss some landmark papers that utilized MS-based phosphoproteomics that identified activated kinase pathways, nominating new therapeutic targets in this disease.

Our group previously identified over 8,000 unique phosphopeptides in mCRPC patient tumors obtained at rapid autopsy using MS-based phosphoproteomics (48, 52). The phosphopeptide signatures differentiated treatment naive PrCa from mCRPC and suggested that metastatic sites within the same patient were highly similar in their signaling networks but differed across patients (52). Some of the activated kinases identified include SRC, EGFR, MEK1, JAK2, AKT, MAPK1/3, and PI3K. Further, we connected both SRC and MAPK1/3 activity to nearly 70% of the mCRPC patients who were evaluated in this study, suggesting that a combination of targeted agents to these two kinases may be beneficial clinically if administered to the correct patient population.

Our group also demonstrated that the integration of our phosphoproteomic datasets with genomic and transcriptomic data provided additional pathway information relevant to signaling networks in mCRPC. By using Tied Diffusion through Interacting Events (53) to integrate differentially expressed transcriptional regulators, genomic mutations, and activated kinases in mCRPC, a list of signaling networks with druggable kinase pathways were generated. From MSigDB gene sets, after incorporating phosphoproteomics data, six major signaling pathways were found to be upregulated in mCRPC tumors including the cell signaling pathway, DNA repair pathway, MAPK/AKT/mTOR, and nuclear receptor pathway (48). When the phosphoproteomics data were not included, these signaling pathways were not as highly enriched. Therefore, the integration of phosphoproteomic data enhanced and validated pathway networks determined by genomic and transcriptional analyses. In addition, we developed a patient-specific, rank order list of kinases predicted to drive the mCRPC tumors in each patient. Since we previously showed patterns of intrapatient similarity of kinase signaling, the collection of an easy accessible biopsy may be all that is needed to identify the activated pathways in each patient.

Our group also began to functionally assess these targets in preclinical models of metastatic development. Over 100 kinases were prioritized based on the phosphoproteomic, gene expression, or genomic information in mCRPC tissues and evaluated in a metastatic tail vein model *via* overexpression in non-metastatic mouse cell lines. We found that 20 kinases promoted metastases in an *in vivo* lung colonization screen. In a second metastatic screen, we overexpressed these 20 kinases in human RWPE-1 cells and identified RAF family (ARAF, BRAF, and CRAF), MERTK, and NTRK2 tyrosine kinases to promote bone and visceral metastases (54). These data suggested the potential contribution of wild-type kinases in PrCa metastasis and identified some candidates for future preclinical and clinical targeting.

Since our initial publications assessing the phosphoproteome of both mouse and human tumors, other groups have begun using phosphoproteomics to address different aspects of PrCa biology. By using quantitative MS-based phosphoproteomics of PrCa cell lines DU145 and PC3, an increase in activated focal adhesion kinase (FAK) at residues Y397 and Y596 was observed in docetaxel resistant DU145 (FAK Y397) and PC3 (FAK Y596) cell lines (55). The Y397 phosphosite serves as a binding site for proteins such as SRC, SHC, and the regulatory subunit of PI3K, while the Y596 site falls within the central kinase domain. Treatment with the FAK inhibitor PF-00562271 reduced phosphorylation of FAK but not AKT and had no effect on cell viability. Docetaxel alone reduced phosphorylation of FAK and AKT, and when added in combination with PF-00562271, there was an additive effect and a rescue of chemoresistance. These data suggested that in mCRPC patients who became resistant to docetaxel treatment due to increased FAK activation, combination therapy with the FAK inhibitor PF-00562271 and docetaxel may be administered to overcome chemoresistance (55).

In another study, protein phosphorylation in LNCaP PrCa cell line xenografts grown in intact and castrated mice identified hyperphosphorylation of signaling proteins including MEK, LYN, PRAS40, YAP1, and PAK2 (56). Also, analysis of CRPC clinical samples showed increased PAK2 and YAP1 levels. In androgen-independent PC3 xenografts, the PAK2 inhibitor PF-3758309 and YAP1 inhibitor verteporfin inhibited tumor growth (56). These data suggested that PAK2 and YAP1 as possible key players during the transition from a hormone naive to a castration resistance state.

Another study of parental LNCaP cells and an androgen-independent version of LNCaP revealed over 60 phosphopeptides that are involved in androgen-independent PrCa cell growth, including thyroid hormone receptor-associated protein 3 (THRAP3) (57). THRAP3 is a transcription coactivator of AR, and hypophosphorylation of residues S248 and S253 were found in androgen-independent LNCaP cells. In addition, the interacting protein partners in both phosphorylated and unphosphorylated states of THRAP3 were different. By using non-phosphorylatable mutants (S248A/S253A) and phosphomimetic forms (S248D/S253D) of THRAP3, the interacting partners were related to RNA splicing/processing, suggesting that phosphorylated THRAP3 at S248 and S253 regulates transcriptional programs leading to androgen-independent PrCa cell growth.

Other studies using the parental LNCaP PrCa cell line identified phosphopeptides corresponding to several actionable kinase targets. These included BRAF, PIK3C2G, STK39, CDK1, MAPK2, AKT1, PRKD1, casein kinase 1 and 2 (CK2A1, CK2A2), and glycogen synthase kinase 3 (GSK3B) (58–60).

The above are most of the examples of work that have demonstrated the value of utilizing phosphoproteomic profiling to reveal regulatory mechanisms and pathways crucial for drug resistance and recurrence in PrCa cell lines and tissues (**Table 1**). Interestingly, most of these kinases are not mutated at high frequencies at all in mCRPC (**Figure 3**). In addition to MS, antibody-based proteomic and phosphoproteomics analyses such as IHC (51, 56, 61–63) and RPPA (64–66) have also revealed activated kinases that are involved in disease progression and drug

**TABLE 1** | Summary of phosphoproteomic studies in prostate cancer.

Kinases and regulatory proteins altered in prostate cancer tissues and cell lines			
Regulatory protein/kinase	Kinase type/function	Source of material	Reference
SRC	Tyrosine kinase	mCRPC patient tumors at rapid autopsy vs treatment naïve primary prostate tissue	Drake et al. (52)
EGFR	Tyrosine kinase	Prostate cancer cell lines: 22Rv1, LNCaP, DU145 and C4-2	Drake et al. (48)
MEK1	Serine/threonine kinase	Prostate cancer cell line derived xenografts: 22Rv1 and LNCaP	
JAK2	Tyrosine kinase		
AKT1	Serine/threonine kinase		
MAPK1	Serine/threonine kinase		
MAPK3	Serine/threonine kinase		
FAK	Tyrosine kinase	Docetaxel resistant DU145 and PC3 prostate cell lines vs Parental DU145 and PC3 prostate cancer cell lines	Lee et al. (55)
MEK1	Serine/threonine kinase	Parental LNCaP prostate cancer cell line	Jiang et al. (56)
LYN	Tyrosine kinase		
YAP1	Transcriptional coactivator		
PAK2	Serine/threonine kinase		
THRAP3	Transcription coactivator	Parental and androgen-independent LNCaP prostate cell lines	Ino et al. (57)
AKT1	Serine/threonine kinase	Parental LNCaP prostate cancer cell line	Giorgianni et al. (58)
BRAF	Serine/threonine kinase		
CDK1	Serine/threonine kinase		
STK39	Serine/threonine kinase		
PIK3C2G	Serine/threonine kinase		
PRKD1	Serine/threonine kinase		
CK1A	Serine/threonine kinase	Parental LNCaP prostate cancer cell line	Myung and Sadar (60)
CK2A1	Serine/threonine kinase		
GSK3B	Serine/threonine kinase		
AKT1	Serine/threonine kinase	Parental LNCaP prostate cancer cell line	Chen et al. (59)
MAPK1	Serine/threonine kinase		
MAPK3	Serine/threonine kinase		

Some of the potentially key druggable targets identified via MS-based phosphoproteomics that were highlighted in this review for prostate cancer emphasizing the paucity of global phosphoproteomic studies in clinical specimens.

resistance. These identified regulatory proteins and pathways can also serve as potential therapeutic targets.

## CLINICAL TRIALS: KINASE INHIBITORS AND PrCa

Kinase pathways validated from various studies mentioned above would strongly act as clinical biomarkers for the evaluation of patients' tumor kinase activation profiles. To date, biopsy-driven, therapeutic efforts aimed at targeting wild-type kinases that are activated in mCRPC are not performed. Mounting evidence that cancer is a disease of deregulated signaling pathways has led to the development of signaling-based targeted therapies for various human tumor types based on genomic mutations of these pathways. There are a number of FDA-approved kinase inhibitors for the treatment of cancer such as non-small-cell lung cancer, myeloma, head and neck cancer, and breast cancer, just to name a few (Table 2). These agents target kinases that have also been shown to be activated or upregulated in mCRPC making these inhibitors potentially beneficial to patients with mCRPC if used in the right context or combination. Currently, there are over 900 clinical trials in progress in PrCa in the United States with 85 studies in phase III. Of these, only 21 are investigating kinase inhibitors, alone or in combination, for PrCa. Below are some examples of previous clinical trials utilizing kinase inhibitors and the outcomes.

Bevacizumab, which blocks VEGF signaling, was assessed in a phase III trial comparing the treatment of docetaxel/prednisone alone or in combination with bevacizumab in patients with mCRPC. Combination treatment resulted in a 2.4-month improvement in progression-free survival, but no difference in median survival (73). Sorafenib was shown to prevent disease progression and cause regression of bone metastases in some patients but without decreasing PSA levels (74), and sunitinib also induced a partial radiographic response but had a minimal effect on PSA levels in both treatment naïve and docetaxel-treated CRPC patients (75).

Mammalian target of rapamycin inhibitors as a single agent had minimal effect in mCRPC (76), but in combination with docetaxel, it was shown to reverse drug resistance in PrCa cell lines (77). In patients with *PTEN* and other genetic aberrations where the AKT pathway is activated, targeting the AKT pathway in combination with mTOR inhibitors was shown to induce apoptosis. The AKT inhibitor, perifosine, in a phase II trial in patients with recurrent, hormone-sensitive PrCa did not meet prespecified PSA criteria for response with only 20% of patients showing a reduction in PSA, but none had a decline greater than 50%. As a single agent, there was only modest clinical activity with perifosine but other AKT inhibitors are in clinical trials in combination studies with docetaxel (NCT02121639), bicalutamide (NCT01251861), and abiraterone (NCT01485861). Everolimus, another mTOR inhibitor, was FDA approved in 2016 for the treatment of patients with NE tumors of pancreatic origin. In a phase I study, everolimus

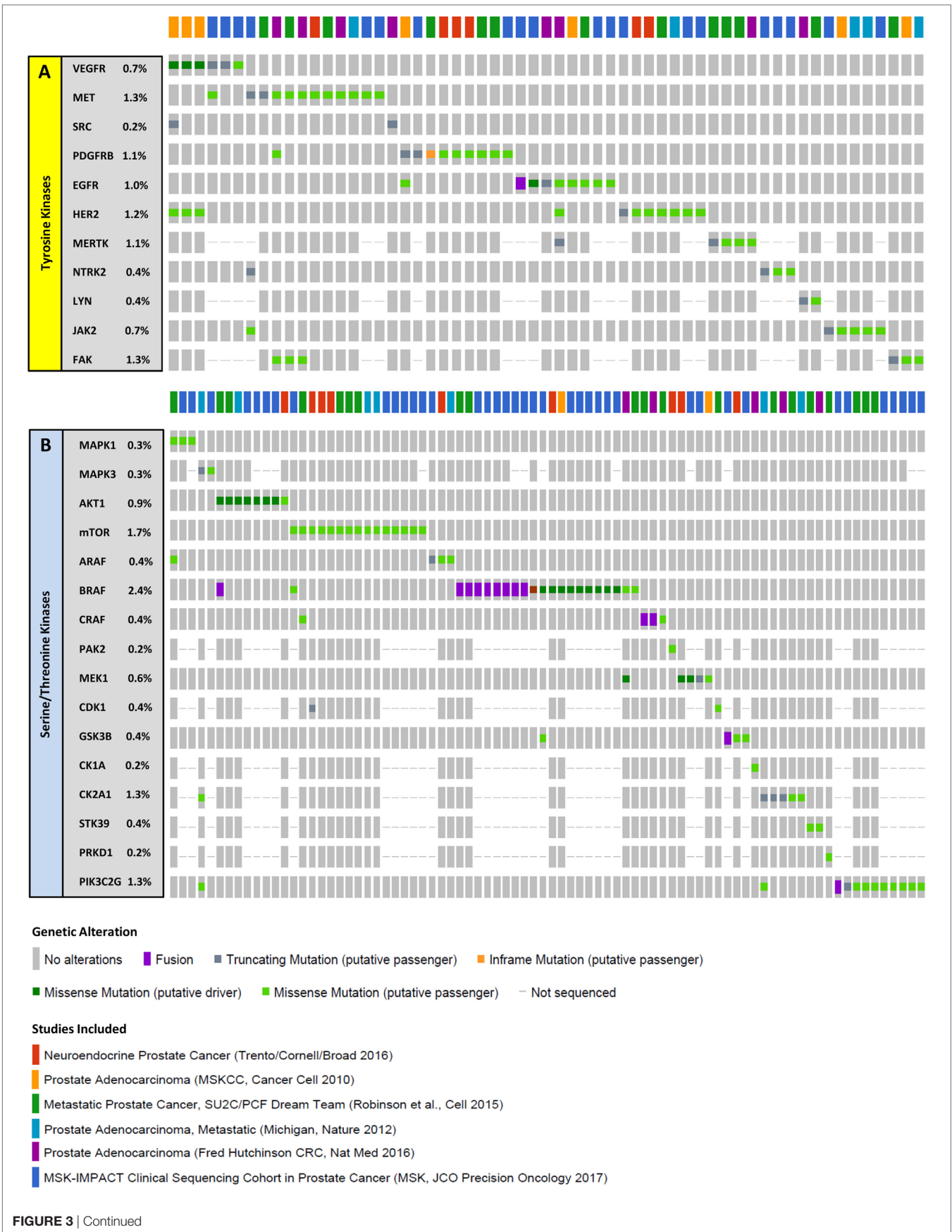


FIGURE 3 | Continued

**FIGURE 3** | Mutations in select kinases in metastatic castration-resistant prostate cancer (mCRPC). Columns represent individual patients, and rows represent genetic alterations detected in tyrosine **(A)** or serine/threonine **(B)** kinases. For the 6 studies mentioned (22, 23, 67–70), samples from a total of 900 patients were sequenced revealing mutations in 59 patients (~7%) for tyrosine kinases and in 82 patients (~9%) for serine/threonine kinases. Importantly, driver mutations were only observed in 4 patients (~0.4%) for tyrosine kinases and 19 patients (~2%) for serine/threonine kinases, suggesting that a very small fraction of the mCRPC population have genomic identifiers of kinase activity. The proportion of patients with alterations in each kinase is listed on the left. Only patients with alterations are represented. Data were extracted from cBioPortal (71, 72).

**TABLE 2** | List of FDA-approved kinase inhibitors to date with the disease and kinase targets.

Kinase inhibitor	Disease	Kinase target/s
Acalabrutinib	Mantle cell lymphoma	BTK
Afatinib	NSCLC, squamous NSCLC	EGFR, ERBB2, ERBB4
Alectinib	ALK-positive NSCLC	ALK, RET
Axitinib	Renal cell carcinoma	VEGFR1, VEGFR2, VEGFR3, PDGFR $\beta$
Bosutinib	CML	BCR-ABL, SRC, LYN, HCK
Brigatinib	ALK-positive NSCLC after crizotinib	ALK, ROS1, IGF-1R, FLT3, EGFR
Cabozantinib	Metastatic medullary thyroid carcinoma, RCC	RET, MET, VEGFR1, VEGFR2, VEGFR3, KIT, NTRK2, FLT3, AXL, TEK
Ceritinib	ALK-positive NSCLC after crizotinib	ALK, IGF-1R
Cobimetinib	Melanoma with <i>BRAF</i> V600E/K mutation with vemurafenib	MEK1/2
Crizotinib	ALK-positive NSCLC, ROS1-positive NSCLC	ALK, MET, ROS1, MST1R
Dabrafenib	Melanoma and NSCLC with <i>BRAF</i> V600E	BRAF
Dasatinib	CML, ALL	BCR-ABL, SRC, LCK, YES, FYN, KIT, EPHA2, PDGFRB
Erlotinib	NSCLC, pancreatic cancer	EGFR
Everolimus	ERBB2-negative breast cancer, PNET, RCC, RAML, SEGA	mTOR, FKBP12
Gefitinib	NSCLC	EGFR
Ibrutinib	MCL, CLL	BTK
Imatinib	CML	BCR-ABL, KIT, PDGFR
Lapatinib	Metastatic breast cancer	EGFR, ERBB2
Lenvatinib	Differentiated thyroid cancer	VEGFRs, FGFRs, PDGFR, KIT, RET
Midostaurin	AML with FLT3-positive mutation	FLT3
Neratinib	ERBB2-positive breast cancer	ERBB2
Nilotinib	CML	BCR-ABL, PDGFR, KIT, CSF1R, DDR1
Nintedanib	Idiopathic pulmonary fibrosis	FGFRs, PRGFR $\alpha/\beta$ , VEGFRs, FLT3
Osimertinib	NSCLC	EGFR T970M
Palbociclib	ER-positive/Her2-negative breast cancer	CDK4/6
Pazopanib	Renal cell carcinoma	VEGFRs, PDGFR $\alpha/\beta$ , FGFR1/3, KIT, ITK, LCK, FMS
Ponatinib	CML	BCR-ABL, VEGFR, PDGFR, FGFR, EPHR, SRC, KIT, RET, TEK, FLT3
Regorafenib	Colorectal cancer	VEGFRs, BCR-ABL, RET, KIT, FGFR1/2, PDGFR $\alpha/\beta$ , EPHA2, BRAF
Ribociclib	HR-positive/EGFR-negative breast cancer	CDK4/6
Ruxolitinib	Myelofibrosis, PV	JAK1, JAK2
Sirolimus	Renal transplant lymphangiomyomatosis	FKBP12, mTOR
Sorafenib	Hepatocellular, renal, thyroid carcinoma	BRAF, CRAF, KIT, FLT3, RET, VEGFRs, PDGFR $\beta$
Sunitinib	GIST, renal cell carcinoma, PNET	PDGFR $\alpha/\beta$ , VEGFR1, VEGFRs, KIT, FLT3, CSF1R, RET
Temsirolimus	Advanced renal cell carcinoma	mTOR
Tofacitinib	Rheumatoid arthritis	JAK1, JAK2
Trametinib	Melanoma and NSCLC with <i>BRAF</i> V600E mutation	MEK1/2
Vandantinib	Medullary thyroid carcinoma	EGFRs, RET, VEGFRs, TEK, EPHRs, SRC, BRK
Vemurafenib	Melanoma with <i>BRAF</i> V600E mutation, Erdheim–Chester disease	BRAF, ARAF, CRAF, SRMS, ACK1, MAP4K5, FGR

A current (December 2017) list of kinase inhibitors approved for the treatment of various cancer types. Some of these targets are implicated in mCRPC; however, the kinase inhibitors assessed in clinical trials for mCRPC did not demonstrate sufficient response and were not approved.

ALL, acute lymphoblastic leukemia; CML, chronic myelogenous leukemia; CLL, chronic lymphocytic leukemia; GIST, gastrointestinal stroma tumor; MCL, mantle cell lymphoma; mCRPC, metastatic castration-resistant prostate cancer; mTOR, mammalian target of rapamycin; NSCLC, non-small-cell lung cancer; PNET, progressive neuroendocrine tumor of pancreatic origin; PV, polycythemia vera; RCC, renal cell carcinoma.

in combination with docetaxel was found to be safe in CRPC patients and resulted in more than 50% reduction in PSA levels (78). Another investigational mTOR inhibitor, ridaforolimus, in phase II trials in combination with bicalutamide showed a 30% decrease in PSA response (79).

SRC non-receptor tyrosine kinase is involved in multiple signaling pathways in PrCa including cell proliferation, migration, angiogenesis, survival, and transition to androgen-independent growth (80). Dasatinib is a SRC inhibitor that was shown to

suppress cell proliferation of PrCa cell lines (81); inhibit cell adhesion, migration, and invasion (82); and reduce tumor growth in a mouse xenograft model (83). In a phase II clinical trial, dasatinib had a definite but limited activity in advanced mCRPC but was poorly tolerated, and 43% of patients discontinued treatment due to toxicity (84). In a previous phase II clinical trial, dasatinib did not show significant PSA response, and only 19% of men with mCRPC were free of disease progression at 6 months (85). In a separate phase II combination trial of dasatinib and

docetaxel, it was observed that 41% of the participants showed a PSA response and 32% of patients with bone metastases showed improvement as assessed by bone scans (86). In a phase II clinical trial with single-agent saracatinib, another SRC inhibitor, only 18% of patients with mCRPC showed a reduction of <30% in PSA (87). In a more recent phase II clinical trial, saracatinib was assessed in a subset of mCRPC patients who showed recurrence postdocetaxel treatment. Only 26% of patients had stable disease after 8 weeks with the remaining patients showing expansion of existing lesions. Fatigue was reported in 25% of patients, and this study was discontinued as it could not be determined if saracatinib would inhibit metastasis (88). Another phase II study of a SRC inhibitor, KX2-391, was closed due to prespecified futility rule and toxicities (89).

A plethora of kinase inhibitors have been assessed in phase I and phase II trials for patients with mCRPC. These include single agents such as sorafenib (74), sunitinib (90), cabozantinib (91), dasatinib (85), lapatinib (92), imatinib (93), and gefitinib (94) as well as erlotinib (95) and dasatinib (96) in combination with docetaxel. None of these agents demonstrated sufficient response or activity to advance to phase III trials, with the exception of cabozantinib and dasatinib (Table 3). Unfortunately, neither of these two inhibitors demonstrated significant overall improved survival benefits in those phase III trials (85, 91).

Most of the kinase inhibitors that entered clinical trials for mCRPC have been discontinued due to low efficacy even though they have been approved for treatment in other cancer types. This emphasizes the complexity and lack of any one dominant kinase driving the biology in mCRPC, affecting the response of any one targeted therapy in an unselected patient population. The challenge is to develop clinical trials based on biomarkers that can categorize a patient's cancer subtype to any one of several FDA-approved targeted therapies, similar to the NCI-MATCH

trials, but for protein activity. To date, only eight PrCa patients have been "matched" to any given targeted therapy in the NCI-MATCH trial (NCI Formulary, May 8, 2017). This reveals a couple concerns about implementing targeted therapies in mCRPC: (1) the paucity of activating mutations as assessed by genomic panels eliminates a majority of CRPC patients from selected targeted therapies and (2) even if the mutation is observed, information on the activity of that protein is missing. To that point, selection of a targeted agent by mutation information alone, independent of tissue type may also be misleading. Key evidence from colon cancer suggests that BRAF (V600E)-mutant tumors are not responsive to vemurafenib alone but only in combination with an EGFR inhibitor to repress the rapid feedback activation of EGFR by vemurafenib treatment (98). This example suggests that to observe prolonged, clinically significant benefits to patients with mCRPC (or other cancer types), we need to begin designing trials that not only assess the genomic aspects of the tumor but also the feedback regulation. If we can do this, we might have a better chance of inhibiting resistance and prolonging survival.

While disappointing, these clinical trial results do not mean that agents used in these failed clinical trials will not have a future role in mCRPC treatment. It is postulated that select kinase inhibitors used in combination with other targeted agents such as second-generation hormonal therapies (abiraterone acetate and enzalutamide) or checkpoint inhibitor immunotherapies may provide substantial clinical benefit. We are only starting to understand the mechanism of action of these kinase inhibitors in the tumor microenvironment and on immune cells. As this becomes clearer, we can move forward with more rationale combination treatments.

## PROTEOMICS AND PHOSPHOPROTEOMICS IN OTHER CANCERS

### Ovarian Cancer

In an effort to characterize the genome and proteome of high-grade serous ovarian cancer, Zhang et al. performed MS-based proteomic analysis on 174 ovarian tumors (169 high grade) previously characterized by The Cancer Genome Atlas (TCGA) (99). The integration of genomic and proteomic data showed an 80% positive correlation between mRNA and protein abundance with metabolic pathways and interferon response being more highly correlated than stable, abundant proteins consisting of house-keeping genes. Unbiased clustering using protein abundance data grouped tumors into mesenchymal, proliferative, immunoreactive, and differentiated subtypes, as previously defined by the TCGA transcriptome analysis. However, there was a fifth cluster of tumor-enriched proteins related to extracellular matrix interactions and erythroid and platelet functions that were not identified by genomic data alone. Interestingly, increased protein phosphorylation in high-grade serous ovarian cancer samples suggested that multiple pathways may be activated in these tumors. Indeed, the PDGFR signaling pathway important for angiogenesis, the RHOA regulatory and integrin-linked kinase pathway associated with invasion and cell mobility, and pathways

**TABLE 3** | Kinase inhibitors that have been assessed in clinical trials for mCRPC.

Kinase inhibitors	Target	Approved?	Phase reached	Reference
Cabozantinib	VEGFR, MET	No	III	Smith et al. (91)
Cediranib	VEGFR	No	II	Dahut et al. (97)
Dasatinib	SRC	No	III	Araujo et al. (96)
Dasatinib	SRC	No	II	Yu et al. (85)
Erlotinib	EGFR	No	II	Gross et al. (95)
Gefitinib	EGFR	No	II	Canil et al. (94)
Imatinib	ABL	No	II	Lin et al. (93)
Lapatinib	EGFR, HER2	No	II	Whang et al. (92)
Saracatinib	SRC	No	II	Lara et al. (87)
Saracatinib	FYN	No	II	Posadas et al. (88)
Sorafenib	PDGFR, VEGFR	No	II	Aragon-Ching et al. (74)
Sunitinib	PDGFR, VEGFR	No	II	Dror Michaelson et al. (90)

*Food and Drug Administration approved kinase inhibitors assessed in early phase I and II clinical trials for metastatic castration-resistant prostate cancer did not demonstrate sufficient response or activity to advance to phase III trials, with the exception of cabozantinib and dasatinib. However, neither inhibitor demonstrated significant overall survival benefits and both were not approved.*

associated with chemokine signaling and adaptive immune response were observed to be activated explaining the aggressive nature of this disease. In patients with activated PDGFR, for example, stratification and enrollment of patients with expected short overall survival into antiangiogenic clinical trial therapies will be beneficial. A phase II clinical trial to determine the effectiveness of imatinib, a PDGFR and KIT inhibitor, in patients with refractory ovarian cancer has been completed (NCT00039585) with no results posted to date. However, it might be promising as imatinib has been shown to be effective to inhibit the growth of ovarian cancer cells in a PDGFR-specific manner by arresting cells at the G0–G1 phase and preventing progression through the S phase (100). Other multifunctional kinase inhibitors that may be effective therapeutic agents for ovarian cancer include pazopanib (targets VEGFR, PDGFR, FGFR, and KIT), sunitinib (targets VEGFR, PDGFR, FLT3, and KIT), and sorafenib (targets VEGFR, PDGFR, and RAF kinases) (101). However, these agents did not do well in phase I and II clinical trials. With pazopanib, there was a 5.6-month progression-free survival and overall survival could not be determined because of toxicities and adverse effects (102). With sunitinib, an objective response rate of only 8.3% with a 9.9-week progression-free survival reported (103). Sorafenib showed only 3.4% partial response, no progression-free survival, or overall survival advantage and low tolerability (104).

## Lung Cancer

Previous work by Rikova et al. have analyzed 41 non-small-cell lung cancer cell lines and more than 150 tumors to identify and group samples based on the activated tyrosine kinases using phosphoproteomics (105). Robust phosphorylation was observed in known oncogenic kinases such as EGFR and c-MET, as well as novel (at the time) ALK and ROS fusion proteins (105). In addition, they identified activated tyrosine kinases not previously indicated in this disease such as PDGFR $\alpha$  and DDR1. PDGFR $\alpha$ , which was found to be aberrantly activated in the H1703 cell line and also in eight tumor samples, was nominated as a novel therapeutic target. Investigating the sensitivity of H1703 cell line to imatinib (PDGFR inhibitor) and gefitinib (EGFR inhibitor) showed that phosphorylation of AKT at serine 473 was blocked by imatinib but not gefitinib. Cell lines negative for PDGFR $\alpha$  were insensitive to imatinib, correlating kinase activity to drug sensitivity. A phase II clinical trial assessed the effectiveness of imatinib and docetaxel in patients with PDGFR expressing non-small-cell lung cancer but was terminated early due to high drug intolerance and no added clinical efficacy. The authors recommend that future studies with PDGFR inhibitors should include the measurement of PDGFR as a positive predictive biomarker prior to therapy administration (106).

Quantitative phosphoproteomics was performed on non-small-cell lung cancer tumors derived from multiple patients, and signaling networks that were known to be involved in lung cancer oncogenesis were identified (107). Activated kinases found in these tumor samples included ERBB2, c-Met, AKT, RAF, and PI3K and direct transcriptional regulators (MEF2D, TP53, ELK3, and ATF7).

## Breast Cancer

Mertins et al. utilized quantitative MS-based proteomics and phosphoproteomics to analyze over 100 genomically characterized breast cancers (108). The samples represented four main mRNA-defined PAM50 breast cancer subtypes, namely basal-like, luminal A, luminal B, and ERBB2-positive subtypes. Their results revealed a connection between loss of *CETN3* and *SKP1* to increased expression levels of EGFR and *SKP1* loss to increased SRC levels (108). They also identified a G-protein couple receptor cluster that was not identified at the mRNA level. In addition, highly phosphorylated kinases identified included ERBB2, CDK12, PAK41, RIPK2, and TLK2. The proteome subtypes identified by using the global proteomics and phosphoproteomics data included basal-enriched, luminal-enriched, and stromal-enriched, while ERBB2-enriched tumors were distributed among these three proteome subgroups (unlike with the clustering seen with the PAM50 genes, mRNA-defined subtypes). The basal and luminal groups showed a significant overlap between mRNA and proteome-defined subtypes, but the stromal-enriched proteome subgroup represented a mix of all mRNA-based subtypes. Pathway analyses showed that the luminal subtype was exclusively enriched for estradiol and ESR1-driven genes, while the basal proteome subtype was enriched for multiple gene sets including MYC target genes for cell cycle, checkpoint, and DNA repair pathway regulators including AURKA/B, ATM, ATR, CHEK1/2, and BRCA1/2 (108). This work has led to the identification of potential druggable kinases in breast cancer, other than ERBB2, and emphasized the advantage of connecting the genome to the proteome.

## Colorectal Cancer

Zhang et al. analyzed the proteomes of colorectal tumors previously characterized by the TCGA (109). They showed that somatic variants were associated with lower protein abundance compared to germline variants and that mRNA expression did not predict protein abundance between tumors. Proteomics identified five subtypes in the TCGA cohort with two overlapping the transcriptomic subtype: microsatellite instability/CpG island methylation subtype. This demonstrated that proteomic data may enable prioritization of potential driver genes. They also showed that chromosome 20q amplicon was associated with high changes at the mRNA and protein levels, some of which included HNF4 $\alpha$ , TOMM34, and SRC (109).

The data obtained from these integrative approaches provide a link from genotype to proteotype to phenotype to better understand the biology at the molecular level that lead to aggressive cancer. Insights gained from the studies mentioned above are evidence that MS-based phosphoproteomics and integration of proteomic and genomic data are advantageous for patient stratification, for identification of personalized therapies, and to understand mechanisms involved in resistance to standard treatment.

## HOW TO MEASURE PATHWAY ACTIVITY CLINICALLY: TARGETED MS

Targeted phosphoproteomic technologies are rapidly rising as key tools for the identification and quantification of highly selected



phosphopeptides in clinical samples (Figure 4). Some advantages of targeted MS are increased speed, sensitivity, reproducibility, and selectivity of your analyte. Targeted MS technology depends on the use of more expensive heavy-labeled synthetic custom phosphopeptides for assay development and absolute quantification (110–112). These phosphopeptides are designed to limit the focus to a specific subset of targets of interest, without

large-scale biomarker screening, although the targets can be highly customizable.

Limited sample amount from biopsies is a major challenge for phosphoproteomic analyses clinically. The optimization of protocols to efficiently sample biopsy amounts coupled with enrichment techniques to reduce sample complexity for reliable and reproducible detection *via* targeted MS are being

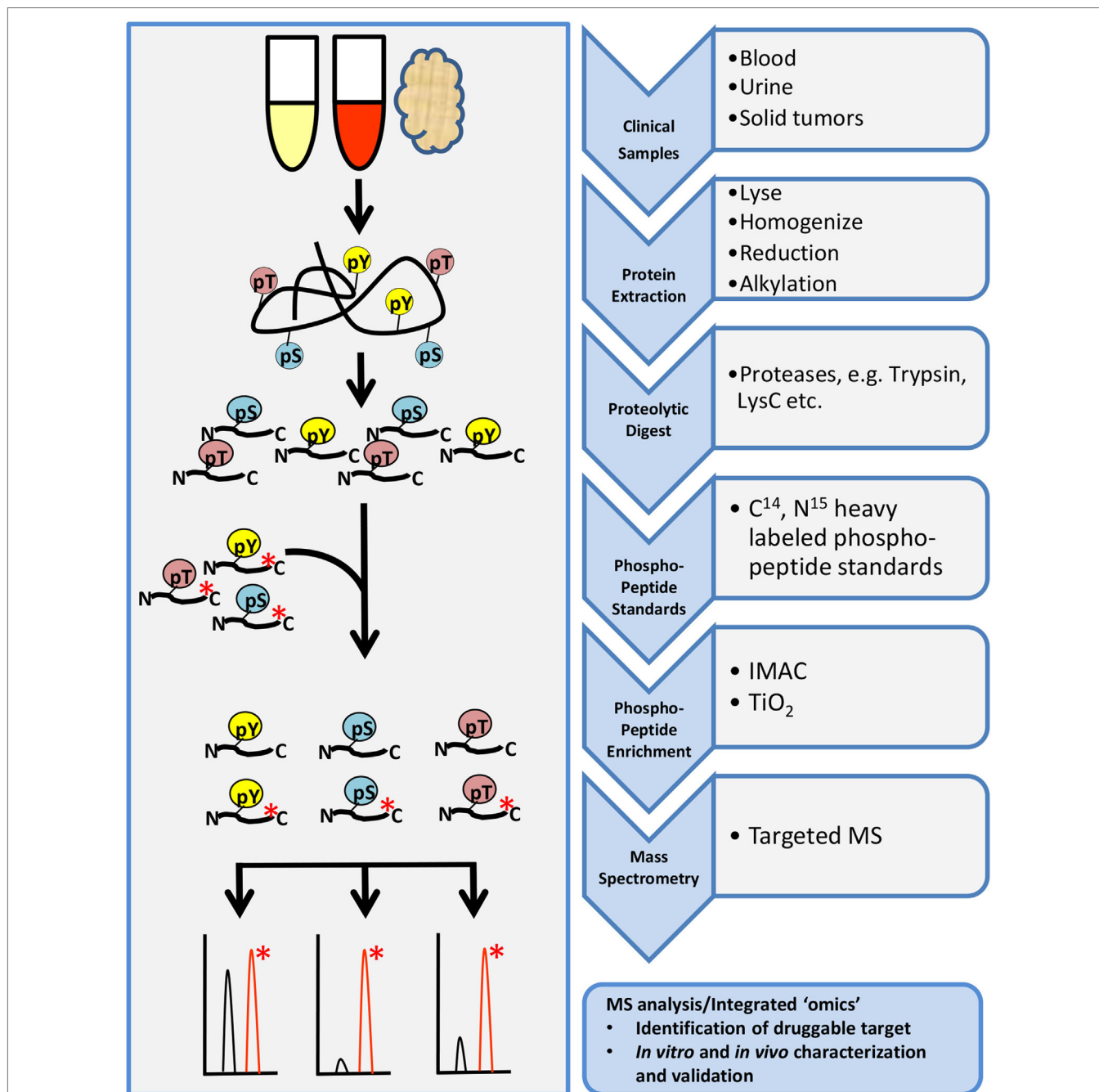


**FIGURE 4** | General workflow for targeted phosphoproteomics analysis. Tissue samples may include cultures cell lines, mouse xenografts, or clinical biopsy specimens such as blood, urine, or tumor biopsies. Samples are processed as described in the shotgun workflow up to proteolytic digestion. Custom designed heavy-labeled peptide standards to specific targets of interest are spiked in with the tryptic peptides followed by enrichment and analysis by LC-MS/MS.

investigated (42, 113). For example, a phosphoproteomic platform known as EasyPhos was shown to quantify thousands of phosphopeptides from only 1 mg of cells or tissue protein rapidly in a 96-well format (114). In addition, integrating pressure cycling technology-assisted sample preparation and SWATH-MS allowed for consistent sample preparation reproducibility as well as the quantification of thousands of proteins from biopsy level tissues (115, 116). Shao et al. evaluated minimum sample requirements from 50,000 cultured cells and as low as 0.2–0.5 mg of wet tissue weight and reported that these smaller sample sizes achieved high quantitative accuracy that were both reliable and reproducible (115). It is important to note that SWATH-MS was previously applied to the proteome and not the phosphoproteome, so other modifications to the protocol may be necessary. The capability of sample multiplexing using isobaric labeling allows the monitoring of up to 10 samples simultaneously in a single-targeted MS run, significantly reducing cost and run times (117). Overall, with significant improvements and advances in protocol optimization and sample procurement, targeted phosphoproteomic analyses will soon be a feasible and essential tool in the clinical setting for assessment of diagnostic, prognostic, or predictive biomarkers (118).

## SOURCES OF PATIENT MATERIAL FOR TARGETED MS ASSAYS

A number of studies have applied proteomics on various biological systems including tissue, serum (119), urine (120), and cell lines and conditioned media from cultured cells (121). Frozen or formalin-fixed paraffin-embedded samples represent the two major processing protocols for collecting clinical tissues and targeted MS assays are capable to detect proteins or phosphoproteins from either source depending on the assay design. The major challenges with tissue-based approaches are small amounts (biopsies), and they are not conducive for sequential assessment of pathways related to disease progression or drug resistance. Since repeated metastatic tissue biopsies are not feasible, ethical, or safe to patients with mCRPC, assessing liquid biopsies, such as blood or urine, may be an effective substitute for biomarker or pathway evaluation studies over time. Some approaches include isolation of CTCs, cell-free DNA, or exosomes in patient blood or serum.

Cell-free DNA has the capability to detect novel mutations (or loss of a mutation) after treatment, indicative of therapy success or resistance. However, cell-free DNA will generate molecular characterization at the genomic level without any information at the protein level. Several great reviews have been written on cell-free DNA and will not be discussed further (122–124). Isolation of CTCs have also garnered much interest in the PrCa community since the finding that AR splice variants can serve as potential biomarkers of resistance to abiraterone acetate or enzalutamide (14). Currently, CTCs are primarily used for RNA or DNA-based analyses and protocols are being developed to investigate proteins. Indeed, a recent study by Scher et al. identified nuclear ARv7 protein in CTCs of patients with mCRPC as

a biomarker for treatment selection (125). Importantly, patients with CTCs consisting of nuclear ARv7 were likely to have a better overall survival on taxane-based chemotherapy, suggesting that the assessment of ARv7 protein is critical for treatment selection. However, assessment of phosphoproteins in CTCs have not been reported and represents a big hurdle is the utilization of this technology to measure pathway activity. Furthermore, isolation of CTCs from blood is technically challenging and the number of CTCs in blood is quite low with counts ranging between 5 and 10 CTCs per 10 ml of blood in patients with low number metastases (126), making this approach unlikely for targeted MS assays in the current form and more suitable for immunofluorescence at the single cell level. However, if we can evaluate signaling networks in CTCs using phosphosite-specific antibodies *via* immunofluorescence, we can gain a better understanding of the heterogeneity

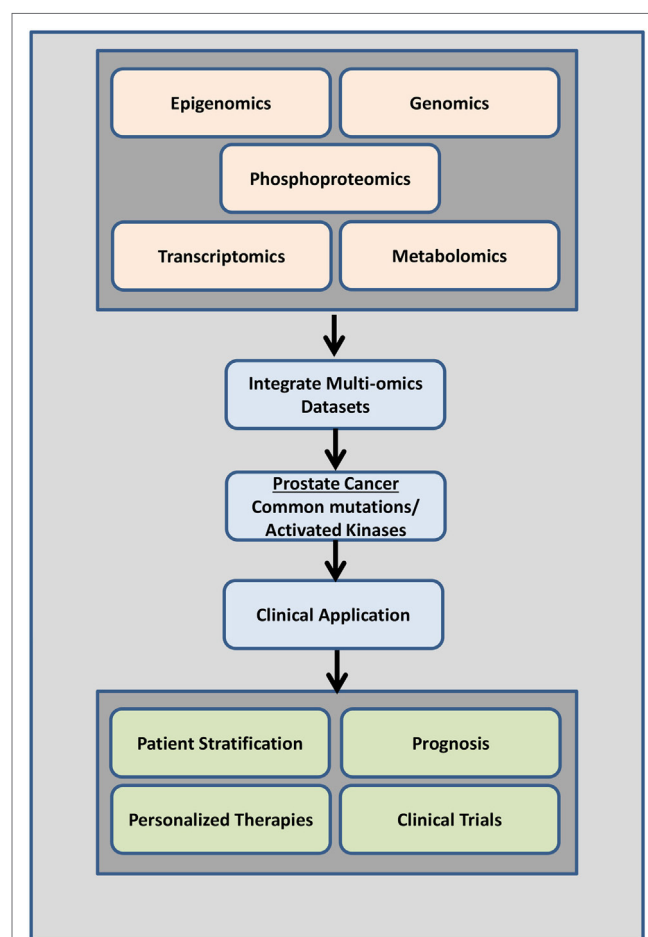


**FIGURE 5 |** Overview of data integration. Data from a combination of phosphoproteomics, genomics, transcriptomics epigenomics, and metabolomics studies investigating the mutational landscape, phosphoproteomic signature, gene expression changes, and regulation in prostate cancer tumors of individual patients can be used clinically to determine disease drivers (mutations and/or activated kinases and aberrantly regulated signaling pathways) as diagnostic tools, to predict patient outcome, to design personalized therapeutic options, and to aid in better clinical trials design.

of signaling in these cell types as well as identify possible new therapeutic targets for treatment.

An exciting new area in liquid biopsy research that has potential for MS-based assays is the isolation of extracellular vesicles or exosomes. Exosomes are an excellent source for biomarker discovery because the cargo they carry reflects the same genomic, transcriptomic, or proteomic information from parental cancer cells (127, 128). In a study where exosomes were isolated by ultracentrifugation from primary prostate epithelial and PrCa cell line supernatants, MS-based proteomic analysis revealed candidate biomarkers more abundant in PrCa cell lines, including FASN, XPO1, ALIX, and ENO1 (129). In a later MS-based study assessing the proteome of urinary exosomes, differential protein expression was observed between PrCa patients and healthy male controls (130). Some of these proteins included transmembrane protein 256 (TM256), LAMTOR, VATL, ADIRF, and RAB family. Claudin 3 was found in exosomes isolated from the plasma of patients with localized and mCRPC compared to patients with benign prostatic hyperplasia and healthy individuals (131). This demonstrated the benefits and potential clinical application of exosomes for the identification and validation of urine- and blood-based biomarkers in PrCa.

## CONCLUSION

The majority of studies have predominantly focused on the genetic signatures of cancer identifying driver mutations that confer drug resistance. Given the low mutation rates in PrCa and mCRPC relative to other cancers strongly supports the need to identify other candidate biomarkers *via* proteomic or phosphoproteomic technologies. Systems biology approaches revealed that genomic and transcriptomic data alone may be missing key players regulating cellular function and disease (132). Integrating other “omics” data sets such as metabolomics, epigenomics,

proteomics, and phosphoproteomics with genomic or gene expression data sets will reveal other key pathways, regulators, and complex signaling networks that may be involved in cell growth, proliferation, and cancer progression (Figure 5). This will give us a more comprehensive view into aberrantly regulated signaling pathways and will lead to the identification of key drug-gable regulators/molecules (Figure 5).

Our understanding of PrCa biology is rapidly increasing, as well as the availability and affordability of high-throughput technologies for comprehensive molecular characterization of PrCa and an individual's genetic and proteomic makeup. With our expanding knowledge of the key players contributing to PrCa progression and resistance to treatment, the future will provide endless possibilities for rational, personalized therapies. This can be accomplished based on the measured disease drivers (mutations and/or activated kinases and aberrantly regulated signaling pathways) *via* the integration of phosphoproteomic, genomic, and transcriptomic data sets. Continued advancement and development of proteomic and phosphoproteomic technologies will provide exciting new opportunities for molecularly targeted treatment of mCRPC.

## AUTHOR CONTRIBUTIONS

JR, MS, and JD wrote the commentary. JR and JD prepared and edited the figures.

## FUNDING

We thank members of the Drake lab for advice and input. JD is supported by the Department of Defense Prostate Cancer Research Program W81XWH-15-1-0236, Prostate Cancer Foundation Young Investigator Award, the New Jersey Health Foundation, and a Precision Medicine Initiative Pilot Award from the Rutgers Cancer Institute of New Jersey.

## REFERENCES

- Nantermet PV, Xu J, Yu Y, Hodor P, Holder D, Adamski S, et al. Identification of genetic pathways activated by the androgen receptor during the induction of proliferation in the ventral prostate gland. *J Biol Chem* (2004) 279:1310–22. doi:10.1074/jbc.M310206200
- Basch E, Oliver TK, Vickers A, Thompson I, Kantoff P, Parnes H, et al. Screening for prostate cancer with prostate-specific antigen testing: American Society of Clinical Oncology Provisional Clinical Opinion. *J Clin Oncol* (2012) 30:3020–5. doi:10.1200/JCO.2012.43.3441
- Epstein JI, Zelefsky MJ, Sjoberg DD, Nelson JB, Egevad L, Magi-Galluzzi C, et al. A contemporary prostate cancer grading system: a validated alternative to the Gleason score. *Eur Urol* (2016) 69:428–35. doi:10.1016/j.eururo.2015.06.046
- Harris WP, Mostaghel EA, Nelson PS, Montgomery B. Androgen deprivation therapy: progress in understanding mechanisms of resistance and optimizing androgen depletion. *Nat Clin Pract Urol* (2009) 6:76–85. doi:10.1038/ncpuro1296
- Tangen CM, Faulkner JR, Crawford ED, Thompson IM, Hirano D, Eisenberger M, et al. Ten-year survival in patients with metastatic prostate cancer. *Clin Prostate Cancer* (2003) 2:41–5. doi:10.3816/CGC.2003.n.011
- Fizazi K, Tran N, Fein L, Matsubara N, Rodriguez-Antolin A, Alekseev BY, et al. Abiraterone plus prednisone in metastatic, castration-sensitive prostate cancer. *N Engl J Med* (2017) 377:352–60. doi:10.1056/NEJMoa1704174
- James ND, de Bono JS, Spears MR, Clarke NW, Mason MD, Dearnaley DP, et al. Abiraterone for prostate cancer not previously treated with hormone therapy. *N Engl J Med* (2017) 377:338–51. doi:10.1056/NEJMoa1702900
- O'Donnell A, Judson I, Dowsett M, Raynaud F, Dearnaley D, Mason M, et al. Hormonal impact of the 17alpha-hydroxylase/C(17,20)-lyase inhibitor abiraterone acetate (CB7630) in patients with prostate cancer. *Br J Cancer* (2004) 90:2317–25. doi:10.1038/sj.bjc.6601879
- Sweeney CJ, Chen YH, Carducci M, Liu G, Jarrard DF, Eisenberger M, et al. Chemohormonal therapy in metastatic hormone-sensitive prostate cancer. *N Engl J Med* (2015) 373:737–46. doi:10.1056/NEJMoa1503747
- Marques RB, Dits NF, Erkens-Schulze S, van Weerden WM, Jenster G. Bypass mechanisms of the androgen receptor pathway in therapy-resistant prostate cancer cell models. *PLoS One* (2010) 5:e13500. doi:10.1371/journal.pone.0013500
- Scher HI, Fizazi K, Saad F, Taplin ME, Sternberg CN, Miller K, et al. Increased survival with enzalutamide in prostate cancer after chemotherapy. *N Engl J Med* (2012) 367:1187–97. doi:10.1056/NEJMoa1207506
- Antonarakis ES, Lu C, Wang H, Lubner B, Nakazawa M, Roeser JC, et al. AR-V7 and resistance to enzalutamide and abiraterone in prostate cancer. *N Engl J Med* (2014) 371:1028–38. doi:10.1056/NEJMoa1315815
- Guo Z, Yang X, Sun F, Jiang R, Linn DE, Chen H, et al. A novel androgen receptor splice variant is up-regulated during prostate cancer progression and promotes androgen depletion-resistant growth. *Cancer Res* (2009) 69:2305–13. doi:10.1158/0008-5472.CAN-08-3795

14. Antonarakis ES, Lu C, Lubner B, Wang H, Chen Y, Zhu Y, et al. Clinical significance of androgen receptor splice variant-7 mRNA detection in circulating tumor cells of men with metastatic castration-resistant prostate cancer treated with first- and second-line abiraterone and enzalutamide. *J Clin Oncol* (2017) 35:2149–56. doi:10.1200/JCO.2016.70.1961
15. Bluemn EG, Coleman IM, Lucas JM, Coleman RT, Hernandez-Lopez S, Tharakan R, et al. Androgen receptor pathway-independent prostate cancer is sustained through FGF signaling. *Cancer Cell* (2017) 32:474.e–89.e. doi:10.1016/j.ccell.2017.09.003
16. Aparicio A, Tzelepi V. Neuroendocrine (small-cell) carcinomas: why they teach us essential lessons about prostate cancer. *Oncology (Williston Park)* (2014) 28:831–8.
17. Beltran H, Tomlins S, Aparicio A, Arora V, Rickman D, Ayala G, et al. Aggressive variants of castration-resistant prostate cancer. *Clin Cancer Res* (2014) 20:2846–50. doi:10.1158/1078-0432.CCR-13-3309
18. Vlachostergios PJ, Puca L, Beltran H. Emerging variants of castration-resistant prostate cancer. *Curr Oncol Rep* (2017) 19:32. doi:10.1007/s11912-017-0593-6
19. Beltran H, Rickman DS, Park K, Chae SS, Sboner A, MacDonald TY, et al. Molecular characterization of neuroendocrine prostate cancer and identification of new drug targets. *Cancer Discov* (2011) 1:487–95. doi:10.1158/2159-8290.CD-11-0130
20. Tan HL, Sood A, Rahimi HA, Wang W, Gupta N, Hicks J, et al. Rb loss is characteristic of prostatic small cell neuroendocrine carcinoma. *Clin Cancer Res* (2014) 20:890–903. doi:10.1158/1078-0432.CCR-13-1982
21. Lee JK, Phillips JW, Smith BA, Park JW, Stoyanova T, McCaffrey EF, et al. N-Myc drives neuroendocrine prostate cancer initiated from human prostate epithelial cells. *Cancer Cell* (2016) 29:536–47. doi:10.1016/j.ccell.2016.03.001
22. Robinson D, Van Allen EM, Wu YM, Schultz N, Lonigro RJ, Mosquera JM, et al. Integrative clinical genomics of advanced prostate cancer. *Cell* (2015) 161:1215–28. doi:10.1016/j.cell.2015.05.001
23. Grasso CS, Wu YM, Robinson DR, Cao X, Dhanasekaran SM, Khan AP, et al. The mutational landscape of lethal castration-resistant prostate cancer. *Nature* (2012) 487:239–43. doi:10.1038/nature11125
24. Barbieri CE, Baca SC, Lawrence MS, Demicheli F, Blattner M, Theurillat JP, et al. Exome sequencing identifies recurrent SPOP, FOXA1 and MED12 mutations in prostate cancer. *Nat Genet* (2012) 44:685–9. doi:10.1038/ng.2279
25. Toren P, Zoubeidi A. Targeting the PI3K/Akt pathway in prostate cancer: challenges and opportunities (review). *Int J Oncol* (2014) 45:1793–801. doi:10.3892/ijo.2014.2601
26. Blattner M, Liu D, Robinson BD, Huang D, Poliakov A, Gao D, et al. SPOP mutation drives prostate tumorigenesis in vivo through coordinate regulation of PI3K/mTOR and AR signaling. *Cancer Cell* (2017) 31:436–51. doi:10.1016/j.ccell.2017.02.004
27. Pritchard CC, Mateo J, Walsh MF, De Sarkar N, Abida W, Beltran H, et al. Inherited DNA-repair gene mutations in men with metastatic prostate cancer. *N Engl J Med* (2016) 375:443–53. doi:10.1056/NEJMoa1603144
28. Goodall J, Mateo J, Yuan W, Mossop H, Porta N, Miranda S, et al. Circulating cell-free DNA to guide prostate cancer treatment with PARP inhibition. *Cancer Discov* (2017) 7:1006–17. doi:10.1158/2159-8290.CD-17-0261
29. Fong PC, Boss DS, Yap TA, Tutt A, Wu P, Mergui-Roelvink M, et al. Inhibition of poly(ADP-ribose) polymerase in tumors from BRCA mutation carriers. *N Engl J Med* (2009) 361:123–34. doi:10.1056/NEJMoa0900212
30. Mateo J, Carreira S, Sandhu S, Miranda S, Mossop H, Perez-Lopez R, et al. DNA-repair defects and olaparib in metastatic prostate cancer. *N Engl J Med* (2015) 373:1697–708. doi:10.1056/NEJMoa1506859
31. Chatterjee P, Choudhary GS, Sharma A, Singh K, Heston WD, Ciezki J, et al. PARP inhibition sensitizes to low dose-rate radiation TMPRSS2-ERG fusion gene-expressing and PTEN-deficient prostate cancer cells. *PLoS One* (2013) 8:e60408. doi:10.1371/journal.pone.0060408
32. Kajanne R, Miettinen P, Tenhunen M, Leppa S. Transcription factor AP-1 promotes growth and radioresistance in prostate cancer cells. *Int J Oncol* (2009) 35:1175–82. doi:10.3892/ijo\_00000434
33. Lavery A, Gilson C, Chowdhury S. PARP inhibitors and stratified treatment of prostate cancer. *Expert Rev Anticancer Ther* (2016) 16:1213–5. doi:10.1080/14737140.2016.1243474
34. Leite KR, Srougi M, Sanudo A, Dall'Oglio MF, Nesrallah A, Antunes AA, et al. The use of immunohistochemistry for diagnosis of prostate cancer. *Int Braz J Urol* (2010) 36:583–90. doi:10.1590/S1677-55382010000500008
35. Duraiyan J, Govindarajan R, Kaliyappan K, Palanisamy M. Applications of immunohistochemistry. *J Pharm Bioallied Sci* (2012) 4:S307–9. doi:10.4103/0975-7406.100281
36. Grubb RL, Calvert VS, Wulkuhler JD, Pawletz CP, Linehan WM, Phillips JL, et al. Signal pathway profiling of prostate cancer using reverse phase protein arrays. *Proteomics* (2003) 3:2142–6. doi:10.1002/pmic.200300598
37. Negm OH, Muftah AA, Aleskandarany MA, Hamed MR, Ahmad DA, Nolan CC, et al. Clinical utility of reverse phase protein array for molecular classification of breast cancer. *Breast Cancer Res Treat* (2016) 155:25–35. doi:10.1007/s10549-015-3654-2
38. Giansanti P, Tsiatsiani L, Low TY, Heck AJ. Six alternative proteases for mass spectrometry-based proteomics beyond trypsin. *Nat Protoc* (2016) 11:993–1006. doi:10.1038/nprot.2016.057
39. Cohen P. The origins of protein phosphorylation. *Nat Cell Biol* (2002) 4:E127–30. doi:10.1038/ncb0502-e127
40. Sharma K, D'Souza RC, Tyanova S, Schaab C, Wisniewski JR, Cox J, et al. Ultra-deep human phosphoproteome reveals a distinct regulatory nature of Tyr and Ser/Thr-based signaling. *Cell Rep* (2014) 8:1583–94. doi:10.1016/j.celrep.2014.07.036
41. Olsen JV, Blagoev B, Gnäd F, Macek B, Kumar C, Mortensen P, et al. Global, in vivo, and site-specific phosphorylation dynamics in signaling networks. *Cell* (2006) 127:635–48. doi:10.1016/j.cell.2006.09.026
42. Ong SE, Blagoev B, Kratchmarova I, Kristensen DB, Steen H, Pandey A, et al. Stable isotope labeling by amino acids in cell culture, SILAC, as a simple and accurate approach to expression proteomics. *Mol Cell Proteomics* (2002) 1:376–86. doi:10.1074/mcp.M200025-MCP200
43. Rush J, Moritz A, Lee KA, Guo A, Goss VL, Spek EJ, et al. Immunoaffinity profiling of tyrosine phosphorylation in cancer cells. *Nat Biotechnol* (2005) 23:94–101. doi:10.1038/nbt1046
44. Lazar C, Gatto L, Ferro M, Bruley C, Burger T. Accounting for the multiple natures of missing values in label-free quantitative proteomics data sets to compare imputation strategies. *J Proteome Res* (2016) 15:1116–25. doi:10.1021/acs.jproteome.5b00981
45. Cox J, Mann M. MaxQuant enables high peptide identification rates, individualized p.p.b.-range mass accuracies and proteome-wide protein quantification. *Nat Biotechnol* (2008) 26:1367–72. doi:10.1038/nbt.1511
46. MacLean B, Tomazela DM, Shulman N, Chambers M, Finney GL, Frewen B, et al. Skyline: an open source document editor for creating and analyzing targeted proteomics experiments. *Bioinformatics* (2010) 26:966–8. doi:10.1093/bioinformatics/btq054
47. Casado P, Rodriguez-Prados JC, Cosulich SC, Guichard S, Vanhaesebroeck B, Joel S, et al. Kinase-substrate enrichment analysis provides insights into the heterogeneity of signaling pathway activation in leukemia cells. *Sci Signal* (2013) 6:rs6. doi:10.1126/scisignal.2003573
48. Drake JM, Paull EO, Graham NA, Lee JK, Smith BA, Titz B, et al. Phosphoproteome integration reveals patient-specific networks in prostate cancer. *Cell* (2016) 166:1041–54. doi:10.1016/j.cell.2016.07.007
49. Tyanova S, Temu T, Carlson A, Sinitcyn P, Mann M, Cox J. Visualization of LC-MS/MS proteomics data in MaxQuant. *Proteomics* (2015) 15:1453–6. doi:10.1002/pmic.201400449
50. Pino LK, Searle BC, Bollinger JG, Nunn B, MacLean B, MacCoss MJ. The Skyline ecosystem: informatics for quantitative mass spectrometry proteomics. *Mass Spectrom Rev* (2017) 1–16. doi:10.1002/mas.21540
51. Drake JM, Graham NA, Stoyanova T, Sedghi A, Goldstein AS, Cai H, et al. Oncogene-specific activation of tyrosine kinase networks during prostate cancer progression. *Proc Natl Acad Sci U S A* (2012) 109:1643–8. doi:10.1073/pnas.1120985109
52. Drake JM, Graham NA, Lee JK, Stoyanova T, Faltermeier CM, Sud S, et al. Metastatic castration-resistant prostate cancer reveals intrapatient similarity and interpatient heterogeneity of therapeutic kinase targets. *Proc Natl Acad Sci U S A* (2013) 110:E4762–9. doi:10.1073/pnas.1319948110
53. Paull EO, Carlin DE, Niempel M, Sorger PK, Haussler D, Stuart JM. Discovering causal pathways linking genomic events to transcriptional states using tied diffusion through interacting events (TieDIE). *Bioinformatics* (2013) 29:2757–64. doi:10.1093/bioinformatics/btt471
54. Faltermeier CM, Drake JM, Clark PM, Smith BA, Zong Y, Volpe C, et al. Functional screen identifies kinases driving prostate cancer visceral and bone metastasis. *Proc Natl Acad Sci U S A* (2016) 113:E172–81. doi:10.1073/pnas.1521674112

55. Lee BY, Hochgräfe F, Lin HM, Castillo L, Wu J, Raftery MJ, et al. Phosphoproteomic profiling identifies focal adhesion kinase as a mediator of docetaxel resistance in castrate-resistant prostate cancer. *Mol Cancer Ther* (2014) 13:190–201. doi:10.1158/1535-7163.MCT-13-0225-T
56. Jiang N, Hjorth-Jensen K, Hekmat O, Iglesias-Gato D, Kruse T, Wang C, et al. In vivo quantitative phosphoproteomic profiling identifies novel regulators of castration-resistant prostate cancer growth. *Oncogene* (2015) 34:2764–76. doi:10.1038/ncr.2014.206
57. Ino Y, Arakawa N, Ishiguro H, Uemura H, Kubota Y, Hirano H, et al. Phosphoproteome analysis demonstrates the potential role of THRAP3 phosphorylation in androgen-independent prostate cancer cell growth. *Proteomics* (2016) 16:1069–78. doi:10.1002/pmic.201500365
58. Giorgianni F, Zhao Y, Desiderio DM, Beranova-Giorgianni S. Toward a global characterization of the phosphoproteome in prostate cancer cells: identification of phosphoproteins in the LNCaP cell line. *Electrophoresis* (2007) 28:2027–34. doi:10.1002/elps.200600782
59. Chen L, Giorgianni F, Beranova-Giorgianni S. Characterization of the phosphoproteome in LNCaP prostate cancer cells by in-gel isoelectric focusing and tandem mass spectrometry. *J Proteome Res* (2010) 9:174–8. doi:10.1021/pr900338q
60. Myung JK, Sadar MD. Large scale phosphoproteome analysis of LNCaP human prostate cancer cells. *Mol Biosyst* (2012) 8:2174–82. doi:10.1039/c2mb25151e
61. Watson K, Wang C, Yilmaz A, Bismar TA, Trpkov K. Use of immunohistochemistry in routine workup of prostate needle biopsies: a tertiary academic institution experience. *Arch Pathol Lab Med* (2013) 137:541–5. doi:10.5858/arpa.2012-0145-OA
62. Martin NE, Gerke T, Sinnott JA, Stack EC, Andrés O, Andersson SO, et al. Measuring PI3K activation: clinicopathologic, immunohistochemical, and RNA expression analysis in prostate cancer. *Mol Cancer Res* (2015) 13:1431–40. doi:10.1158/1541-7786.MCR-14-0569
63. Rizzardi AE, Zhang X, Vogel RI, Kolb S, Geybels MS, Leung Y-K, et al. Quantitative comparison and reproducibility of pathologist scoring and digital image analysis of estrogen receptor beta2 immunohistochemistry in prostate cancer. *Diagn Pathol* (2016) 11:63. doi:10.1186/s13000-016-0511-5
64. Miller JC, Zhou H, Kwekel J, Cavallo R, Burke J, Butler EB, et al. Antibody microarray profiling of human prostate cancer sera: antibody screening and identification of potential biomarkers. *Proteomics* (2003) 3:56–63. doi:10.1002/pmic.200390009
65. Cancer Genome Atlas Research Network. The molecular taxonomy of primary prostate cancer. *Cell* (2015) 163:1011–25. doi:10.1016/j.cell.2015.10.025
66. Pin E, Stratton S, Belluco C, Liotta L, Nagle R, Hodge KA, et al. A pilot study exploring the molecular architecture of the tumor microenvironment in human prostate cancer using laser capture microdissection and reverse phase protein microarray. *Mol Oncol* (2016) 10:1585–94. doi:10.1016/j.molonc.2016.09.007
67. Taylor BS, Schultz N, Hieronymus H, Gopalan A, Xiao Y, Carver BS, et al. Integrative genomic profiling of human prostate cancer. *Cancer Cell* (2010) 18:11–22. doi:10.1016/j.ccr.2010.05.026
68. Beltran H, Prandi D, Mosquera JM, Benelli M, Puca L, Cyrta J, et al. Divergent clonal evolution of castration-resistant neuroendocrine prostate cancer. *Nat Med* (2016) 22:298–305. doi:10.1038/nm.4045
69. Kumar A, Coleman I, Morrissey C, Zhang X, True LD, Gulati R, et al. Substantial interindividual and limited intraindividual genomic diversity among tumors from men with metastatic prostate cancer. *Nat Med* (2016) 22:369–78. doi:10.1038/nm.4053
70. Abida W, Armenia J, Gopalan A, Brennan R, Walsh M, Barron D, et al. Prospective genomic profiling of prostate cancer across disease states reveals germline and somatic alterations that may affect clinical decision making. *JCO Precis Oncol* (2017):2017. doi:10.1200/PO.17.00029
71. Cerami E, Gao J, Dogrusoz U, Gross BE, Sumer SO, Aksoy BA, et al. The cBio cancer genomics portal: an open platform for exploring multidimensional cancer genomics data. *Cancer Discov* (2012) 2:401–4. doi:10.1158/2159-8290.CD-12-0095
72. Gao J, Aksoy BA, Dogrusoz U, Dresdner G, Gross B, Sumer SO, et al. Integrative analysis of complex cancer genomics and clinical profiles using the cBioPortal. *Sci Signal* (2013) 6:11. doi:10.1126/scisignal.2004088
73. Kelly WK, Halabi S, Carducci M, George D, Mahoney JF, Stadler WM, et al. Randomized, double-blind, placebo-controlled phase III trial comparing docetaxel and prednisone with or without bevacizumab in men with metastatic castration-resistant prostate cancer: CALGB 90401. *J Clin Oncol* (2012) 30:1534–40. doi:10.1200/JCO.2011.39.4767
74. Aragon-Ching JB, Jain L, Gulley JL, Arlen PM, Wright JJ, Steinberg SM, et al. Final analysis of a phase II trial using sorafenib for metastatic castration-resistant prostate cancer. *BJU Int* (2009) 103:1636–40. doi:10.1111/j.1464-410X.2008.08327.x
75. Sonpavde G, Periman PO, Bernold D, Weckstein D, Fleming MT, Galsky MD, et al. Sunitinib malate for metastatic castration-resistant prostate cancer following docetaxel-based chemotherapy. *Ann Oncol* (2010) 21:319–24. doi:10.1093/annonc/mdp323
76. Figlin RA, Brown E, Armstrong AJ, Akerley W, Benson AB 3rd, Burstein HJ, et al. NCCN task force report: mTOR inhibition in solid tumors. *J Natl Compr Canc Netw* (2008) 6(Suppl 5):S1–20.
77. Morgan TM, Pitts TE, Gross TS, Poliachik SL, Vessella RL, Corey E. RAD001 (Everolimus) inhibits growth of prostate cancer in the bone and the inhibitory effects are increased by combination with docetaxel and zoledronic acid. *Prostate* (2008) 68:861–71. doi:10.1002/pros.20752
78. Courtney KD, Manola JB, Elfiky AA, Ross R, Oh WK, Yap JT, et al. A phase I study of everolimus and docetaxel in patients with castration-resistant prostate cancer. *Clin Genitourin Cancer* (2015) 13:113–23. doi:10.1016/j.clgc.2014.08.007
79. Rizzieri DA, Feldman E, Dipersio JF, Gabrail N, Stock W, Strair R, et al. A phase 2 clinical trial of deforolimus (AP23573, MK-8669), a novel mammalian target of rapamycin inhibitor, in patients with relapsed or refractory hematologic malignancies. *Clin Cancer Res* (2008) 14:2756–62. doi:10.1158/1078-0432.CCR-07-1372
80. Wheeler DL, Iida M, Dunn EF. The role of Src in solid tumors. *Oncologist* (2009) 14:667–78. doi:10.1634/theoncologist.2009-0009
81. Lombardo LJ, Lee FY, Chen P, Norris D, Barrish JC, Behnia K, et al. Discovery of N-(2-chloro-6-methyl-phenyl)-2-(6-(4-(2-hydroxyethyl)-piperazin-1-yl)-2-methylpyrimidin-4-ylamino)thiazole-5-carboxamide (BMS-354825), a dual Src/Abl kinase inhibitor with potent antitumor activity in preclinical assays. *J Med Chem* (2004) 47:6658–61. doi:10.1021/jm049486a
82. Nam S, Kim D, Cheng JQ, Zhang S, Lee JH, et al. Action of the Src family kinase inhibitor, dasatinib (BMS-354825), on human prostate cancer cells. *Cancer Res* (2005) 65:9185–9. doi:10.1158/0008-5472.CAN-05-1731
83. Park SI, Zhang J, Phillips KA, Araujo JC, Najjar AM, Volgin AY, et al. Targeting SRC family kinases inhibits growth and lymph node metastases of prostate cancer in an orthotopic nude mouse model. *Cancer Res* (2008) 68:3323–33. doi:10.1158/0008-5472.CAN-07-2997
84. Twardowski PW, Beumer JH, Chen CS, Kraft AS, Chatta GS, Mitsuhashi M, et al. A phase II trial of dasatinib in patients with metastatic castration-resistant prostate cancer treated previously with chemotherapy. *Anticancer Drugs* (2013) 24:743–53. doi:10.1097/CAD.0b013e328361feb0
85. Yu EY, Wilding G, Posadas E, Gross M, Culine S, Massard C, et al. Phase II study of dasatinib in patients with metastatic castration-resistant prostate cancer. *Clin Cancer Res* (2009) 15:7421–8. doi:10.1158/1078-0432.CCR-09-1691
86. Araujo JC, Poblenz A, Corn P, Parikh NU, Starbuck MW, Thompson JT, et al. Dasatinib inhibits both osteoclast activation and prostate cancer PC-3-cell-induced osteoclast formation. *Cancer Biol Ther* (2009) 8:2153–9. doi:10.4161/cbt.8.22.9770
87. Lara PN Jr, Longmate J, Evans CP, Quinn DI, Twardowski P, Chatta G, et al. A phase II trial of the Src-kinase inhibitor AZD0530 in patients with advanced castration-resistant prostate cancer: a California Cancer Consortium study. *Anticancer Drugs* (2009) 20:179–84. doi:10.1097/CAD.0b013e328325a867
88. Posadas EM, Ahmed RS, Karrison T, Szmulewitz RZ, O'Donnell PH, Wade JL 3rd, et al. Saracatinib as a metastasis inhibitor in metastatic castration-resistant prostate cancer: a University of Chicago Phase 2 Consortium and DOD/PCF Prostate Cancer Clinical Trials Consortium Study. *Prostate* (2016) 76:286–93. doi:10.1002/pros.23119
89. Antonarakis ES, Heath EI, Posadas EM, Yu EY, Harrison MR, Bruce JY, et al. A phase 2 study of KX2-391, an oral inhibitor of Src kinase and tubulin polymerization, in men with bone-metastatic castration-resistant prostate cancer. *Cancer Chemother Pharmacol* (2013) 71:883–92. doi:10.1007/s00280-013-2079-z
90. Dror Michaelson M, Regan MM, Oh WK, Kaufman DS, Olivier K, Michaelson SZ, et al. Phase II study of sunitinib in men with advanced prostate cancer. *Ann Oncol* (2009) 20:913–20. doi:10.1093/annonc/mdp111

91. Smith M, De Bono J, Sternberg C, Le Moulec S, Oudard S, De Giorgi U, et al. Phase III study of cabozantinib in previously treated metastatic castration-resistant prostate cancer: COMET-1. *J Clin Oncol* (2016) 34:3005–13. doi:10.1200/JCO.2015.65.5597
92. Whang YE, Armstrong AJ, Rathmell WK, Godley PA, Kim WY, Pruthi RS, et al. A phase II study of lapatinib, a dual EGFR and HER-2 tyrosine kinase inhibitor, in patients with castration-resistant prostate cancer. *Urol Oncol* (2013) 31:82–6. doi:10.1016/j.urolonc.2010.09.018
93. Lin AM, Rini BI, Weinberg V, Fong K, Ryan CJ, Rosenberg JE, et al. A phase II trial of imatinib mesylate in patients with biochemical relapse of prostate cancer after definitive local therapy. *BJU Int* (2006) 98:763–9. doi:10.1111/j.1464-410X.2006.06396.x
94. Canil CM, Moore MJ, Winquist E, Baetz T, Pollak M, Chi KN, et al. Randomized phase II study of two doses of gefitinib in hormone-refractory prostate cancer: a trial of the National Cancer Institute of Canada-Clinical Trials Group. *J Clin Oncol* (2005) 23:455–60. doi:10.1200/JCO.2005.02.129
95. Gross M, Higano C, Pantuck A, Castellanos O, Green E, Nguyen K, et al. A phase II trial of docetaxel and erlotinib as first-line therapy for elderly patients with androgen-independent prostate cancer. *BMC Cancer* (2007) 7:142. doi:10.1186/1471-2407-7-142
96. Araujo JC, Trudel GC, Saad F, Armstrong AJ, Yu EY, Bellmunt J, et al. Docetaxel and dasatinib or placebo in men with metastatic castration-resistant prostate cancer (READY): a randomised, double-blind phase 3 trial. *Lancet Oncol* (2013) 14:1307–16. doi:10.1016/S1470-2045(13)70479-0
97. Dahut WL, Madan RA, Karakunnel JJ, Adelberg D, Gulley JL, Turkbey IB, et al. Phase II clinical trial of cediranib in patients with metastatic castration-resistant prostate cancer. *BJU International* (2013) 111:1269–80. doi:10.1111/j.1464-410X.2012.11667.x
98. Prahallad A, Sun C, Huang S, Di Nicolantonio F, Salazar R, Zecchin D, et al. Unresponsiveness of colon cancer to BRAF(V600E) inhibition through feedback activation of EGFR. *Nature* (2012) 483:100–3. doi:10.1038/nature10868
99. Zhang H, Liu T, Zhang Z, Payne SH, Zhang B, McDermott JE, et al. Integrated proteogenomic characterization of human high-grade serous ovarian cancer. *Cell* (2016) 166:755–65. doi:10.1016/j.cell.2016.05.069
100. Matei D, Chang DD, Jeng MH. Imatinib mesylate (Gleevec) inhibits ovarian cancer cell growth through a mechanism dependent on platelet-derived growth factor receptor alpha and Akt inactivation. *Clin Cancer Res* (2004) 10:681–90. doi:10.1158/1078-0432.CCR-0754-03
101. Coward JI, Middleton K, Murphy F. New perspectives on targeted therapy in ovarian cancer. *Int J Womens Health* (2015) 7:189–203. doi:10.2147/IJWH.S52379
102. du Bois A, Floquet A, Kim JW, Rau J, del Campo JM, Friedlander M, et al. Incorporation of pazopanib in maintenance therapy of ovarian cancer. *J Clin Oncol* (2014) 32:3374–82. doi:10.1200/JCO.2014.55.7348
103. Campos SM, Penson RT, Matulonis U, Horowitz NS, Whalen C, Pereira L, et al. A phase II trial of Sunitinib malate in recurrent and refractory ovarian, fallopian tube and peritoneal carcinoma. *Gynecol Oncol* (2013) 128:215–20. doi:10.1016/j.ygyno.2012.07.126
104. Matei D, Sill MW, Lankes HA, DeGeest K, Bristow RE, Mutch D, et al. Activity of sorafenib in recurrent ovarian cancer and primary peritoneal carcinomatosis: a gynecologic oncology group trial. *J Clin Oncol* (2011) 29:69–75. doi:10.1200/JCO.2009.26.7856
105. Rikova K, Guo A, Zeng Q, Possemato A, Yu J, Haack H, et al. Global survey of phosphotyrosine signaling identifies oncogenic kinases in lung cancer. *Cell* (2007) 131:1190–203. doi:10.1016/j.cell.2007.11.025
106. Tsao AS, Liu S, Fujimoto J, Wistuba II, Lee JJ, Marom EM, et al. Phase II trials of imatinib mesylate and docetaxel in patients with metastatic non-small cell lung cancer and head and neck squamous cell carcinoma. *J Thorac Oncol* (2011) 6:2104–11. doi:10.1097/JTO.0b013e31822e7256
107. Schweppe DK, Rigas JR, Gerber SA. Quantitative phosphoproteomic profiling of human non-small cell lung cancer tumors. *J Proteomics* (2013) 91:286–96. doi:10.1016/j.jprot.2013.07.023
108. Mertins P, Mani DR, Ruggles KV, Gillette MA, Clauser KR, Wang P, et al. Proteogenomics connects somatic mutations to signalling in breast cancer. *Nature* (2016) 534:55–62. doi:10.1038/nature18003
109. Zhang B, Wang J, Wang X, Zhu J, Liu Q, Shi Z, et al. Proteogenomic characterization of human colon and rectal cancer. *Nature* (2014) 513:382–7. doi:10.1038/nature13438
110. Kettenbach AN, Rush J, Gerber SA. Absolute quantification of protein and post-translational modification abundance with stable isotope-labeled synthetic peptides. *Nat Protoc* (2011) 6:175–86. doi:10.1038/nprot.2010.196
111. Gillette MA, Carr SA. Quantitative analysis of peptides and proteins in biomedicine by targeted mass spectrometry. *Nat Methods* (2013) 10:28–34. doi:10.1038/nmeth.2309
112. Whiteaker JR, Zhao L, Yan P, Ivey RG, Voytovich UJ, Moore HD, et al. Peptide immunoaffinity enrichment and targeted mass spectrometry enables multiplex, quantitative pharmacodynamic studies of phospho-signaling. *Mol Cell Proteomics* (2015) 14:2261–73. doi:10.1074/mcp.O115.050351
113. Dunn JD, Reid GE, Bruening ML. Techniques for phosphopeptide enrichment prior to analysis by mass spectrometry. *Mass Spectrom Rev* (2010) 29:29–54. doi:10.1002/mas.20219
114. Humphrey SJ, Azimifar SB, Mann M. High-throughput phosphoproteomics reveals in vivo insulin signaling dynamics. *Nat Biotechnol* (2015) 33:990–5. doi:10.1038/nbt.3327
115. Shao S, Guo T, Koh CC, Gillessen S, Joerger M, Jochum W, et al. Minimal sample requirement for highly multiplexed protein quantification in cell lines and tissues by PCT-SWATH mass spectrometry. *Proteomics* (2015) 15:3711–21. doi:10.1002/pmic.201500161
116. Zhu Y, Guo T. High-throughput proteomic analysis of fresh-frozen biopsy tissue samples using pressure cycling technology coupled with SWATH mass spectrometry. *Methods Mol Biol* (2017) 1–9. doi:10.1007/978-1-4939-8787-8\_7
117. Erickson BK, Rose CM, Braun CR, Erickson AR, Knott J, McAlister GC, et al. A strategy to combine sample multiplexing with targeted proteomics assays for high-throughput protein signature characterization. *Mol Cell* (2017) 65:361–70. doi:10.1016/j.molcel.2016.12.005
118. Cheng LC, Tan VM, Ganesan S, Drake JM. Integrating phosphoproteomics into the clinical management of prostate cancer. *Clin Transl Med* (2017) 6:9. doi:10.1186/s40169-017-0138-5
119. Byrne JC, Downes MR, O'Donoghue N, Fitzpatrick JM, Dunn MJ, Watson RW. Fasting status as a consideration for human serum collection and preparation prior to depletion and analysis. *Electrophoresis* (2008) 29:3055–9. doi:10.1002/elps.200700933
120. M'Koma AE, Blum DL, Norris JL, Koyama T, Billheimer D, Motley S, et al. Detection of pre-neoplastic and neoplastic prostate disease by MALDI profiling of urine. *Biochem Biophys Res Commun* (2007) 353:829–34. doi:10.1016/j.bbrc.2006.12.111
121. Sardana G, Jung K, Stephan C, Diamandis EP. Proteomic analysis of conditioned media from the PC3, LNCaP, and 22Rv1 prostate cancer cell lines: discovery and validation of candidate prostate cancer biomarkers. *J Proteome Res* (2008) 7:3329–38. doi:10.1021/pr8003216
122. Sharma VK, Vouros P, Glick J. Mass spectrometric based analysis, characterization and applications of circulating cell free DNA isolated from human body fluids. *Int J Mass Spectrom* (2011) 304:172–83. doi:10.1016/j.ijms.2010.10.003
123. Elshimali YI, Khaddour H, Sarkissyan M, Wu Y, Vadgama JV. The clinical utilization of circulating cell free DNA (CCFDNA) in blood of cancer patients. *Int J Mol Sci* (2013) 14:18925–58. doi:10.3390/ijms140918925
124. Siravegna G, Marsoni S, Siena S, Bardelli A. Integrating liquid biopsies into the management of cancer. *Nat Rev Clin Oncol* (2017) 14:531–48. doi:10.1038/nrclinonc.2017.14
125. Scher HI, Graf RP, Schreiber NA, McLaughlin B, Lu D, Louw J, et al. Nuclear-specific AR-V7 protein localization is necessary to guide treatment selection in metastatic castration-resistant prostate cancer. *Eur Urol* (2017) 71:874–82. doi:10.1016/j.eururo.2016.11.024
126. Danila DC, Heller G, Gignac GA, Gonzalez-Espinoza R, Anand A, Tanaka E, et al. Circulating tumor cell number and prognosis in progressive castration-resistant prostate cancer. *Clin Cancer Res* (2007) 13:7053–8. doi:10.1158/1078-0432.CCR-07-1506
127. Tang MK, Wong AS. Exosomes: emerging biomarkers and targets for ovarian cancer. *Cancer Lett* (2015) 367:26–33. doi:10.1016/j.canlet.2015.07.014
128. Soung YH, Ford S, Zhang V, Chung J. Exosomes in cancer diagnostics. *Cancers (Basel)* (2017) 9. doi:10.3390/cancers9010008
129. Duijvesz D, Burnum-Johnson KE, Gritsenko MA, Hoogland AM, Vredendregt-van den Berg MS, Willemsen R, et al. Proteomic profiling of

- exosomes leads to the identification of novel biomarkers for prostate cancer. *PLoS One* (2013) 8:e82589. doi:10.1371/journal.pone.0082589
130. Øverbye A, Skotland T, Koehler CJ, Thiede B, Seierstad T, Berge V, et al. Identification of prostate cancer biomarkers in urinary exosomes. *Oncotarget* (2015) 6:30357–76. doi:10.18632/oncotarget.4851
131. Worst TS, von Hardenberg J, Gross JC, Erben P, Schnölzer M, Hausser I, et al. Database-augmented mass spectrometry analysis of exosomes identifies claudin 3 as a putative prostate cancer biomarker. *Mol Cell Proteomics* (2017) 16:998–1008. doi:10.1074/mcp.M117.068577
132. Kitano H. Computational systems biology. *Nature* (2002) 420:206–10. doi:10.1038/nature01254

**Conflict of Interest Statement:** The authors declare that the research was conducted in the absence of any commercial or financial relationships that could be construed as a potential conflict of interest.

Copyright © 2018 Ramroop, Stein and Drake. This is an open-access article distributed under the terms of the Creative Commons Attribution License (CC BY). The use, distribution or reproduction in other forums is permitted, provided the original author(s) and the copyright owner are credited and that the original publication in this journal is cited, in accordance with accepted academic practice. No use, distribution or reproduction is permitted which does not comply with these terms.